

Investigations of Excited States and Radical Ions in π -Conjugated
Polymers of Interest for Photovoltaic Applications

by

Abram J. Ledbetter

A dissertation submitted in partial fulfillment
of the requirements for the degree of
Doctor of Philosophy
(Applied Physics)
in the University of Michigan
2017

Doctoral Committee:

Professor Roy Clark, Co-Chair
John R. Miller, Brookhaven National Lab, Co-Chair
Professor Jay L. Guo
Professor Cagliyan Kurdak
Professor Stephen Maldonado

Abram J. Ledbetter

abramled@umich.edu

ORCID iD: 0000-0003-2349-4544

Dedication

To my wonderful parents whose example, strength, and support have served as a constant inspiration throughout my life.

Acknowledgments

First, I would like to thank my thesis advisor, Dr. John Miller, for helping me to grow into the scientist I am today. Without his time, support, guidance and investment the research that has culminated in this thesis would not be possible. It has been an honor and privilege to have the opportunity to benefit from your wisdom. I would also like to thank Dr. Roy Clark for whose thoughtful advice, supportiveness, and discussions have added great value to my experience as a graduate student over the years. I also owe great appreciation to Cythia McNabb and Lauren Segall who have been amazing resources for administrative support in the Applied Physics program. I would like to give a special thanks to BNL's Office of Educational Programs for their support, and to Noel Blackburn in particular, for his resourcefulness, wisdom and humor which have always been greatly appreciated.

To my father, mother, and siblings who have been a tremendous part of my growth – spiritually, personally, and professionally, I owe the greatest debt of gratitude. Thank you for being a source of love, strength and support.

Table of Contents

Dedication	ii
Acknowledgments.....	iii
List of Tables	viii
List of Figures	xi
List of Abbreviations	xxvi
Abstract.....	xxvii
1. Chapter 1: General Introduction	1
1.1 Motivation for polymer photovoltaics.....	1
1.2 Historical perspective of organic semiconductors.....	3
1.3 Aim of thesis & materials investigated	5
1.3.1 Phenylenevinylene based materials	6
1.3.2 pDPP2FT and PDI.....	9
1.4 Other materials	12
1.5 Outline of Thesis.....	12
2 Chapter 2: Theoretical Framework.....	14
2.1 Electronic structure of conjugated polymers.....	14
2.2 Radical ions.....	17
2.3 Excitons	19
2.4 Bimolecular charge & energy transfer reactions	25
2.4.1 Conditions for charge and energy transfer.....	25
2.4.2 Diffusion controlled reactions	27
2.5 Electron transfer theory.....	29
2.5.1 Classical theory	29
2.5.2 Nonclassical theories	32
2.6 Charge Transport Description	34
2.6.1 Band transport model.....	35
2.6.2 Polaron Transport Model.....	36
2.6.3 Variable Range Hopping Model	36
2.7 Operation & challenges of polymer photovoltaics	37

3	Chapter 3: Experimental Techniques	41
3.1	Absorption and Emission Spectroscopy	41
3.1.1	Preparation methods for spectrophotometric redox titrations	42
3.2	Photoinduced transient absorption spectroscopy	43
3.3	Cyclic Voltammetry	43
3.4	Pulse radiolysis	44
3.4.1	Unambiguous formation of radical ions and triplets	46
3.4.2	Laser-electron accelerator facility (LEAF)	50
4	Chapter 4: Optical signatures of radical ions and triplets	53
4.1	Introduction	53
4.2	Estimation of Reaction Radii of Compounds	53
4.3	Methodology for collection of optical signatures	56
4.4	Optical signatures of radical anions	57
4.5	Optical signatures of radical cations	78
4.6	Optical signatures of triplets	100
4.7	Discussion and Summary	114
5	Chapter 5: Extinction coefficients & energetics	118
5.1	Methodology for determination of extinction coefficients and energetics	118
5.2	Extinction coefficients of radical anions	121
5.3	Extinction coefficients & energetics of radical cations	123
5.4	Extinction coefficients of triplets	127
5.4	Extinction coefficients of ground state	129
5.4.1	Phenylenevinylene based compounds	129
5.4.2	pDPP2FT and PDI	131
5.5	Energetics of radical ions by electrochemistry	133
5.6	Energetics of radical anions determined by radiolysis	139
5.7	Energetics of radical cations determined by radiolysis	143
5.7	Energetics of triplets	144
5.7.1	Reduction potential of “n th ” excess electron of MEH-PPV	145
5.8	Summary and Discussion	148

6	Chapter 6: Spectroscopic studies of photoexcitations and charges in DBA type diblocks and at D/A interfaces	152
6.1	Introduction.....	152
6.2	Materials investigated.....	152
6.3	Delocalization length estimates	154
6.3.1	Negative polaron (Radical anion).....	155
6.3.2	Positive polaron	159
6.3.3	Triplet.....	162
6.4	Photophysical properties of moieties	164
6.4.1	Photoluminescence (PL) spectra.....	164
6.5	Determination of MWs by spectral fitting (SF) method	166
6.6	PL emission quenching	179
6.6.1	Quenching of $^1\text{fA}^*$	180
6.6.2	Quenching of $^1\text{D}^*$	186
6.7	Photoexcited ps transient absorption spectroscopy	191
6.8	$\text{D}^{\bullet-}(\text{Cn})\text{fA} \rightarrow \text{D}(\text{Cn})\text{fA}^{\bullet-}$ reactions via radiolysis	193
6.9	MEH-PPV triplet neutralization reactions in THF	208
6.10	pCVPPV/MEH-PPV type II heterojunction.....	210
6.11	Discussion and Summary	212
7	Chapter 7: Radiolytic investigations of pDPPFT and perylene-diimide (PDI) capped pDPP2FT	217
7.1	Photophysical properties of pDPP2FT _x (PDI).....	217
7.2	Redox titrations and polaron length determinations	220
7.2.1	Negative-polaron	220
7.2.2	Positive polaron	225
7.3	Investigations of electron transport in pDPP2FT _x (PDI)	229
7.3.1	Overview	230
7.3.2	Electron transport study: trials 1 and 2	232
7.3.3	Electron transport study: trial 3.....	237
7.3.4	Evidence for radiolytic degradation of PDI cap	247
7.4	Discussion and Summary	250

8 Chapter 8: Conclusion and Outlook.....	253
References	257

List of Tables

Table 1-1 Polymers investigated and compounds explored as corresponding electron acceptors	5
Table 1-2 Chemical Structures of s-PPVs investigated	7
Table 1-3 Chemical Structures of pDPP2FT and PDI based materials	10
Table 3-1 Onsager radii of select solvents.....	45
Table 3-2 Reactive solvent species, solv ^S formed by radiolysis of select solvents and their byproducts via reactions with an aromatic solute, π	46
Table 4-1 Determination of hydrodynamic radii for MEH-PPV in THF and Benzene	55
Table 4-2 Radii of select molecules	55
Table 4-3 Viscosities of solvents and dielectric constant	56
Table 4-4 Reactions following radiolysis of neat THF.....	57
Table 4-5 Radiolysis of THF solutions containing solute “Q”	57
Table 4-6 Reaction rates corresponding to radiolytic reduction of selected solutes are presented along with wavelengths associated with byproducts of the solutes. Assuming electron capture by MEH-PPV is diffusion controlled, and given the estimated hydrodynamic radius of MEH-PPV ($R_h(\text{MEH-PPV})_{\text{THF}} = 32.0 \text{ \AA}$) an effective radius for the solvated electron is $R(e^{\bullet}) = 0.25 \text{ \AA}$. Effective radii for other solutes are approximated based on the estimated effective electron radius by assuming reaction rates for radiolytic reduction are diffusion controlled.....	63
Table 4-7 Fraction of MEH-PPV \bullet^- formed by step capture at varied concentrations of MEH-PPV	69
Table 4-8 Reactions following radiolysis of a chlorinated solvent “RCl”	78
Table 4-9 Added reactions in the presence of high concentration of an arene “Q”	79
Table 4-10 Molecules and corresponding IPs.....	80
Table 4-11 Rate constants of radical cation formation via radiolytic oxidation in DCE and peak wavelengths associated with the formed radical cation.....	99
Table 4-12 Reactions following radiolysis of Benzene	100
Table 4-13 Reactions following radiolysis of Benzene solutions containing solute “S”	100
Table 4-14 Rate constants for radiolytic energy transfer from sensitizing compounds to solutes of interest, and peak wavelengths corresponding to formed triplet products. The hydrodynamic radius of pCVPPV and pDPP2FT in benzene were unknown, but that of pDPP2FT was approximated as equivalent to the estimated value obtained in THF.	102
Table 5-1 Molar extinction coefficients of species used as references.....	120

Table 5-2 Extinction coefficients of radical anions determined by electron transfer from references with known extinction coefficients	121
Table 5-3 Extinction coefficients of radical cations determined by hole transfer from references with known extinction coefficients	123
Table 5-4 Extinction coefficients of triplets determined by triplet transfer from references with known extinction coefficients	127
Table 5-5 Molar extinction coefficients at select wavelengths for the ground state absorbance of substituted p-phenylenevinylens	130
Table 5-6 Redox potentials associated with redox couples vs Ag/Ag ⁺ and Fc/Fc ⁺	136
Table 5-7 Compounds R and Q used to produce reaction: R ^{•+} + Q ← → R + Q ^{•-} and calculated Keq and ΔG for reactions (FLA = fluoranthene, 1,4-DCNB = 1,4-dicyanobenzene)	140
Table 5-8 Compounds R and Q used to produce reaction: R ^{•+} + Q ← → R + Q ^{•-} and calculated Keq and ΔG for the reactions	143
Table 5-9 Compounds R and Q used to produce reaction: ³ R* + Q ← → R + ³ Q* and calculated Keq and ΔG for the reactions	144
Table 5-10 K _{eq} and ΔG ⁰ values measured at steps of reversible MEH-PPV reduction via PERYL ^{•-}	147
Table 6-1 Maximum separation D-fA separation distance for diblock copolymers investigated	154
Table 6-2 Ratio of molar extinction coefficients (pru) for MEH-PPV neutral and fSF-PPV neutral.	165
Table 6-3 Relative quantum yields of MEH-PPV and fSF-PPV measured in THF	166
Table 6-4 Molecular weights of select diblock copolymers determined by SF method in 1 st trial	170
Table 6-5 Determined fA monomer units per chain and molecular weights of select diblocks based on application of SF method to ground state absorbance spectra in THF	174
Table 6-6 Determined fA monomer units per chain and molecular weights of select diblocks based on application of SF method to ground state absorbance spectra in chloroform ...	177
Table 6-7 Fraction of monomer units per chain and corresponding molecular weights of each diblock copolymer as determined by the spectral fit (SF) method. For diblock D(C4)fA, material limitations prevented multiple measurements and for D(C0)fA and D(C1)fA only two measurements were made and both found to be identical. Standard deviations of 5% of the mean are assumed in all of these cases.....	177
Table 6-8 Molecular weight estimates for D ₁₄ (Cn)FA determined by spectral fitting method and compared with GPC determined molecular weights	179
Table 6-9 Values of a _{theor} and b _{theor} obtained for blend and diblock solutions	181
Table 6-10 Quenching efficiencies in diblocks observed in THF	189
Table 6-11 Determination of fA _{mon} per chain and f _{fA} for diblocks D(C2)fA, D(C4)fA and D(C6)fA using a “kinetic method” based on formation rate constants for D ^{•-} based on presumed equivalence of [D _{mon}] for the D homoblock solution and D(Cn)fA solutions	199

Table 6-12 Bimolecular rate constants for electron transfer from $D^{\bullet}(Cn)fA$ to $D(Cn)fA^{\bullet-}$ based on linear fits of k_{decay} vs $[D(Cn)fA]$	201
Table 6-13 Bimolecular electron transfer rate constants, k_{Bi} determined using binary solutions of D and D(C2)fA and binary solutions of D and D(C4)fA, providing consistent estimates of $(3.52 \pm 0.20) \times 10^9 \text{ M}^{-1}\text{s}^{-1}$ per chain.	205
Table 6-14 Estimated activation energies for bimolecular $D^{\bullet}(C6)fA \rightarrow D(C6)fA^{\bullet-}$ in absence and presence of electrolyte.....	207
Table 6-15 Electron transfer rates of $D^{\bullet}(C1)fA$ at 60 μM and 120 μM	208
Table 7-1 Properties of pDPP2FT and pDPP2FT _x PDI polymers ^a Determined by GPC relative to polystyrene standard. ^b The number averaged molecular weights were determined by end group analysis using ¹ H NMR spectroscopy.	217
Table 7-2 Time constants and corresponding fraction of photoexcitation decay	219
Table 7-3 The fraction of chains with n PDI caps (f_n) calculated based on random capping process, for each batch of p _x PDI based on the measured number of PDI caps per chain (N).	231
Table 7-4 Maximum fraction of electrons captured directly by PDI caps assuming 2 PDI caps per chain.	233
Table 7-5 Fractions of slow decaying polymer radical anions (f_{slow}), fraction of uncapped chains (f_0), and fraction of defective chains ($f_{defective}$) for each p _x PDI batch.....	235
Table 7-6 Time constants of formation for pDPP2FT ^{•-} , PDI ^{•-} and calculated times of transport.....	237
Table 7-7 Values of f_{slow} determined by comparing 1400 nm yields of p _x PDI relative to pDPP2FT at $t = 1.0 \mu\text{s}$	240
Table 7-8 Estimates of $\tau_f(p_x^{\bullet}PDI)$ and $\tau_f(p_xPDI^{\bullet-})$, and calculated $\tau_{transport}$ for p _x PDI solutions in Trial 3	246
Table 7-9 Lower limits for the diffusion coefficient (D) and electron mobility (μ) of an electron on a p ₃₂ PDI chain with 2 PDI caps based on the longest possible $\tau_{transport}$ of 17 ns.	247

List of Figures

Figure 1-1 Chemical structures of polyacetylene and PPV.....	4
Figure 1-2 Orbital mixing of a strongly coupled donor and acceptor in a D-A copolymer lead to a lowered band gap.....	11
Figure 2-1: (a) An illustration of σ and π -bond formation in the sp^2 hybridized dimer, ethene. The p_z orbitals (shown dashed) interact to generate π -orbitals. (b) A molecular orbital diagram of ethene.	14
Figure 2-2 Electronic energy diagrams are shown for two isolated carbon atoms, an ethene molecule, and polyacetylene. The bandwidth (BW) associated with the spread of energies of degenerate bonding orbitals, and the electronic bandgap (E_g) are represented.....	15
Figure 2-3 Benzoid and Quinoid structural forms of phenylenevinylene	17
Figure 2-4 The spin configurations (left of dashed line) and optical transitions (right of dashed line) associated with charged excitations of a nondegenerate conjugated polymer are shown: a) negative polaron, b) positive polaron, c) negative bipolaron, and d) positive bipolaron.....	19
Figure 2-5. Illustration of spin configurations for singlet (left) and triplet (right) excitons, and the introduction of new energy levels in the forbidden gap associated with their polaronic natures.....	20
Figure 2-6 Comparative energy scale illustrating energetics of a conjugated polymer in the neutral state, charged state, and neutral excited state. (Figure adapted from [59]).	21
Figure 2-7 Configuration coordinate diagram of potential energy curves with vibration levels showing the relationship of optical transitions to the resulting absorption and emission spectra.	22
Figure 2-8 Chemical structure of PPV in ground state (a), in neutral excited state (b), in negative polaron state (c), and positive polaron state (d).....	23
Figure 2-9 Jablonski diagram indicating various photophysical processes: A=absorption, F= fluorescence, IC = internal conversion, ISC = intersystem crossing and P = phosphorescence.	24
Figure 2-10 Profile of the potential energy curves of an electron transfer reaction: R and P indicate the reactant and product states of the system.	30
Figure 2-11 Three kinetic regimes are evident by plotting the natural log of the electron transfer rate, k_{el} , versus the driving force (ΔG^0) for electron transfer reaction: the normal region, the activationless regime, and the inverted regime.....	32

Figure 2-12 Potential energy curves of product and reactant states of donor/acceptor systems with different strengths of orbital interaction between donor and acceptor, ranging from the nonadiabatic regime to a strongly adiabatic regime. Arrows indicate the likelihood of electron transfer, with upward pointing arrows in the reactant state and downward arrows in the product state.	33
Figure 2-13 Three different device architecture types for organic photovoltaics (OPVs) for which the blue phase represents an electron donor and the red phase represents an electron acceptor: a) bilayer heterojunction, b) bulk heterojunction, and c) interdigitated heterojunction.....	39
Figure 3-1 Radiolysis byproducts in the irradiated solution are probed by broadband light from a pulsed Xe lamp and the time dependence of absorbance at a wavelength selected by an optical band pass filter is detected by a silicon or InGaAs photodiode detector.	52
Figure 4-1 The transient absorption spectra of neat THF at times immediately following radiolytic pulse, giving evidence for a monotonically rising absorption band for the solvated electron that peaks in the near IR.	58
Figure 4-2 Transient absorption spectra of a THF solution containing MEH-PPV (60 μ M chain, 1.45 mM pru) at various time segments following radiolytic pulse, (a) during the growth of a 900 nm band, and (b) during the decay of the same band. Insets of both graphs correspond to the transient at 900 nm during the respective time scales shown.	59
Figure 4-3 Transient absorption spectra of a THF solution containing fSF-PPV (400 μ M chain, 1.09 mM pru) at various time segments following radiolytic pulse, (a) during the growth of a 650 nm band, and (b) during the decay of the same band. Insets of both graphs correspond to the transient at 650 nm during the respective time scales shown.	59
Figure 4-4 Transient absorption spectra of a THF solution containing pCVPPV (100 μ M chain, 0.77 mM pru) at various time segments following radiolytic pulse, (a) during the growth of a 650 nm band, and (b) during the decay of the same band. Insets of both graphs correspond to the transient at 650 nm during the respective time scales shown.	60
Figure 4-5 Transient absorbance spectra corresponding to radiolysis of pDPP2FT (30 μ M chain) in THF at varied time segments following the radiolytic pulse, (a) during growth of a \sim 1430 nm spectral band, and (b) during the decay of the same band.	60
Figure 4-6 Transient absorbance spectra corresponding to radiolysis of PDI (1 mM) in THF at varied time segments following the radiolytic pulse, (a) during growth of a 950 nm spectral band, and (b) during the decay of the same band.	61
Figure 4-7 Transient absorbance spectra corresponding to radiolysis of pDI-phenyl (1 mM) in THF at varied time segments following the radiolytic pulse, (a) during growth of a 950 nm spectral band, and (b) during the decay of the same band.	61
Figure 4-8 Transient absorption spectra corresponding to THF solutions of PDI and PDI-phenyl collected 65 ns after radiolytic pulse.....	65
Figure 4-9 Early formation kinetics of MEH-PPV $^{\bullet-}$ measured at 900 nm revealing slow diffusion controlled capture of electrons preceded by step capture of electrons.	67

Figure 4-10 Absorption transients of MEH-PPV (60 μ M chain, 1.45 mM pru) in THF at 900 nm after radiolytic pulse, shown for argon bubbled and air bubbled solutions. The transient corresponding to the air bubbled solution decays to zero suggesting no contribution of absorption from MEH-PPV ^{•+} at 900 nm.	68
Figure 4-11 A plot of fraction of MEH-PPV- formed via step capture vs. [MEH-PPV] in pru provides a linear fit with a slope of 0.065/mM.	70
Figure 4-12 Absorption transients at 650 nm corresponding to THF solutions of fSF-PPV at various monomer concentrations, collected after radiolytic pulse. Transients indicate rapid formation of electrons, and formation of fSf-PPV ^{•-} by step and diffusive capture of electrons.	71
Figure 4-13 Fraction of electrons captured via step capture plotted versus monomer concentration of fSF-PPV, showing a linear dependence with a slope of 0.140/mM.	71
Figure 4-14 Absorbance transients of MEH-PPV (1.45 mM pru) following radiolysis, collected at 570 nm and 900 nm.....	72
Figure 4-15 Radiolytic absorbance transients at 900 nm for MEH-PPV/THF at varied concentrations after pulse, shown: (a) as collected, and (b) with peak absorbances normalized.	74
Figure 4-16 Fast decay rates of MEH-PPV ^{•-} plotted versus per repeat unit concentrations of MEH-PPV.....	74
Figure 4-17 Difference absorbance transients of 1.46 mM pru of MEH-PPV/THF at 900 nm, and 1.09 mM pru of fSF-PPV/THF at 650 nm (rescaled x 2.4). Both transients follow a biphasic decay.....	75
Figure 4-18 Absorption transients of MEH-PPV in THF (60 μ M chain, 1.45 mM pru) are shown in the presence of 10 mM cryptand and in the absence of cryptand. The inset shows that despite differences in MEH-PPV ^{•-} decay, both transients exhibit nearly identical formation rates for MEH-PPV ^{•-}	76
Figure 4-19 Absorption transients of MEH-PPV in THF (60 μ M chain, 1.45 mM pru) are shown in the presence of 0.1 M TBAPF ₆ and in the absence of electrolyte.....	76
Figure 4-20 900 nm absorbance transients corresponding to THF solutions of MEH-PPV (50 μ M chain) prepared from two different batches of MEH-PPV (21.5 monomers and 24.1 monomers), showing two very different radical anion decay profiles.	77
Figure 4-21 Transient absorption spectra of aerated o-DCB at time segments ranging from 2 – 200 ns after pulse showing visible and NIR bands decaying as a UV band is formed with similar rate as the decaying bands, suggesting they are correlated. The inset shows transients at 300 nm and 1460 nm where the forming and decaying species absorb, respectively.....	81
Figure 4-22 Transient absorption spectra of aerated 1,2-dichlorethane (DCE) at times immediately following radiolytic pulse.	82
Figure 4-23 Transient absorption spectra following radiolysis of biphenyl (25 mM) in aerated DCE resulting in formation of biphenyl cation- the spectral band of which is shown here	

decaying. In the inset is shown the transient at 690 nm giving evidence of a rapid decay from geminate pairs and much slower decay due to homogenous cations.	83
Figure 4-24 Transient absorption spectra following radiolysis of biphenyl (25 mM) in aerated o-DCB, resulting in formation of biphenyl cation- the spectral band of which is shown here decaying. In the inset is shown the transient at 650 nm giving evidence of a rapid decay from geminate pairs and much slower decay due to homogenous cations.	84
Figure 4-25 Transient absorption spectra at various time segments following the radiolysis of MEH-PPV (250 μ M chain) in DCE. The inset shows the time profile of the absorbance at 1050 nm over the time range represented by the spectral transformations.	86
Figure 4-26 Absorption transients of aerated DCE only, and MEH-PPV (250 μ M chain) in aerated DCE, at 660 nm.	86
Figure 4-27 The absorbance spectra at various time segments following radiolysis of a DCE solution containing MEH-PPV (250 μ M chain): a) shown normalized to the intensity of absorbance maximum of the 100 μ s spectrum, and b) shown normalized and red-shifted relative to the absorbance maximum of the 100 μ s spectrum.	87
Figure 4-28 Transient absorption spectra corresponding to MEH-PPV (207 μ M chain, 5 mM pru) in DCE at varied time segments after radiolytic pulse, shown over two distinct time ranges: a) from 20 ns – 4 μ s, and b) from 2 ns – 29 ns.	89
Figure 4-29 Absorbance transients corresponding to radiolysis of MEH-PPV (207 μ M chain, 5 mM pru) in DCE at various wavelengths exhibit nearly identical kinetics at times < 1 μ s during conversion from biphenyl ^{•+} to MEH-PPV ^{•+} but deviate significantly over a time frame from 1 – 190 μ s as shown by normalizing the transients to the 900 nm absorbance transient at 1 μ s.	90
Figure 4-30 Transient absorption spectra at various time intervals, (a) shown normalized and (b) shown normalized with red-shifts to match the absorbance maximum of the 100 μ s spectrum.	91
Figure 4-31 Transient absorption spectra corresponding to an o-DCB solution of MEH-PPV (41.5 μ M chain, 1 mM pru) at varied time segments after radiolytic pulse, shown over two distinct time ranges: a) from 40 ns – 13 μ s, and b) from 5 ns – 50 ns.	92
Figure 4-32 Transient absorption spectra corresponding to an o-DCB solution of MEH-PPV (41.5 μ M chain, 5 mM pru) at 0.5 μ s, 9.0 μ s, and 100 μ s after radiolytic pulse: (a) normalized, and (b) normalized and red-shifted.	93
Figure 4-33 Transient absorption spectra of p-terphenyl (5 mM) during (a) growth of a visible and NIR band associated with the p-terphenyl radical cation, and (b) during their decay. .	94
Figure 4-34 Transient absorption spectra following radiolysis of a DCE solution containing terthiophene (20 mM), showing decay of terthiophene ^{•+} at 540 nm as new bands form at 580 nm and 650 nm. Absorption transients corresponding to these wavelengths are shown in the inset.	96
Figure 4-35 Transient absorption spectra following radiolysis of a DCE solution containing PDI (1 mM) and biphenyl (20 mM), showing a) growth of a 600 nm band associated with PDI ^{•+} concurrent with the decay of a 690 nm band associated biphenyl ^{•+} and b) decay of the	

same band. Insets display the 600 nm transients over the timescales of the observed transformations of the corresponding figure.....	97
Figure 4-36 Transient absorption spectra following radiolysis of an aerated DCE solution containing fSF-PPV (794 μ M, 2.5 mM pru) and biphenyl (20 mM), showing a) formation of two bands with peaks at \sim 620 nm and \sim 1450 nm associated with fSF-PPV ^{•+} which appears to be complete by 2 μ s, and b) spectral transformations at longer times which involve decay of the bands.	97
Figure 4-37 Transient absorption spectra following radiolysis of an aerated DCE solution containing pCVPPV (100 μ M, 0.7 mM pru) and biphenyl (25 mM), showing a) formation of two bands with peaks at 720 nm and \sim 1450 nm associated with pCVPPV ^{•+} which appears to be complete by 2 μ s, and b) spectral transformations at longer times which involve growth of a new band in the visible and a redshift of the high energy pCVPPV ^{•+} band.	98
Figure 4-38 Transient absorption spectra following radiolysis of an aerated DCE solution containing pDPP2FT (136 μ M, 5 mM pru) and biphenyl (20 mM), showing a) growth of a 1450 nm band associated with pDPP2FT ^{•+} and b) decay of the same band. Insets display the 1450 nm transients over the timescales of the observed transformations of the corresponding figure.	99
Figure 4-39 Transient absorption spectra at varied time segments following radiolysis of a benzene solution containing MEH-PPV (10 μ M chain, 0.241 mM pru) and anthracene (5 mM), showing, (a) formation of an 820 nm band from 500 ns – 13 μ s, and (b) decay of the same band from 13 μ s – 130 μ s.	102
Figure 4-40 Transient absorption spectra at varied time segments following radiolysis of a benzene solution containing fSF-PPV (100 μ M chain, 0.315 mM pru) and benzene (10 mM), showing formation of a 540 and 680 nm bands from 200 ns – 6 μ s.....	103
Figure 4-41 Transient absorption spectra at varied time segments following radiolysis of a benzene solution containing pCVPPV (100 μ M chain, 0.77 mM pru) and biphenyl (10 mM), showing formation of a 600 nm bands from μ s.	103
Figure 4-42 Transient absorption spectra collected at varied time segments following radiolysis of 10 μ M chain of pDPP2FT in benzene, during (a) growth of three bands (880 nm, 1150 nm, and 1450 nm) and (b) during the decay of those same bands.	104
Figure 4-43 Absorption transients collected at 880 nm, 1150 nm, and 1450 nm following radiolysis of an argon saturated benzene solution of pDPP2FT (10 μ M chain) showing similar formation kinetics within the first 2 μ s after pulse.	105
Figure 4-44 Transient absorption spectra following radiolysis of an argon-saturated benzene solution of pDPP2FT (25 μ M chain) during (a) the growth at 1150 nm, and (b) decay at 1150 nm.....	106
Figure 4-45 The 880 nm, 1150 nm, and 1450 nm absorption transients of argon saturated benzene solutions of pDPP2FT on a 100 μ s timescale, shown at chain concentrations of: (a) 10 μ M and (b) 25 μ M. For either solution, similar slow decays are exhibited at the three wavelengths suggesting a common source for each.	107

Figure 4-46 The transient absorbance spectra following radiolysis of a benzene solution containing pDPP2FT (25 μ M chain) and benzophenone (0.1 M), shown during: (a) the growth of a spectral band and (b) decay of the same band.	107
Figure 4-47 The transient absorption spectra following radiolysis of an oxygen saturated benzene solution containing pDPP2FT (25 μ M chain), shown during: (a) the growth of a spectral band and (b) decay of the same band.	108
Figure 4-48 The 1150 nm absorbance transients collected following radiolytic pulse of benzene solutions containing 25 μ M pDPP2FT collected under argon saturated condition In the absence of a cosolute (blue), argon saturated condition in the presence of 0.1 M benzophenone (red) and oxygen saturated condition in the absence of a cosolute (green).	109
Figure 4-49 Time evolution of a species “B” shown relative to two conditions where its decay rate, k_B is smaller than its observed formation rate, k (shown in red) and for which $k_B > k$ (shown in blue). The reaction scheme shown in the inset, involves conversion of the transient species A into the transient product B, with a rate of k_{AB} . The natural decay rate of A defined as k_A , leads to an observed rate of formation, $k = k_A + k_{AB}$ for B. The time evolution of B will contain a rise which reflects the rate of k or k_B , whichever is largest. In the example shown, rates were assigned as $k_A = 2.0 \times 10^7 \text{ s}^{-1}$, $k_B = 3.0 \times 10^7 \text{ s}^{-1}$, and $k_{AB} = 5.0 \times 10^6 \text{ s}^{-1}$	110
Figure 4-50 A proposed scheme for an equilibrium between a polymer triplet and ground state oxygen triplet.....	111
Figure 4-51 The absorbance transients of argon saturated and oxygen saturated benzene solutions of pDPP2FT (25 μ M chain) at 1150 nm and 1450 nm. The 1450 nm transient is presumed to be almost entirely due to a byproduct other than $^3\text{pDPP2FT}^*$ and 1150 nm is presumed to contain absorbance contribution of the 1450 nm species and 3pDPP2FT^* . Subtraction of the 1450 nm transients from the 1150 nm transients then resulted in transients which decayed to zero and approximated the time dependence of $^3\text{pDPP2FT}^*$ only.	112
Figure 4-52 The corrected spectra corresponding to $^3\text{pDPP2FT}^*$ produced by subtracting the transient at 5 μ s associated with a different species which is nearly time invariant in yield at time segments of $0.5 \mu\text{s} \leq t \leq 5 \mu\text{s}$	113
Figure 4-53 Absorption transients at 650 nm following radiolysis of DCE solutions containing 400 μ M fSF-PPV + [biphenyl], where [biphenyl] was prepared at 6.5 mM and 55 mM. The rate of formation for fSF-PPV $^{*+}$ was the same in both solutions while the yield improved at 55 mM biphenyl indicating that the hole transfer reaction involved no equilibrium.	117
Figure 5-1 An illustration of the formation and decay of species “Q” whose total and peak yields are shown as $\text{Abs}([\text{Q}]_{\text{total}}, \lambda_Q)$ and $\text{Abs}([\text{Q}]_{\text{peak}}, \lambda_Q)$, with the former acquired by a backward extrapolation of the decay back to time zero.	119
Figure 5-2 A 900 nm absorption transient corresponding to a blend solution of MEH-PPV (0.73 mM pru) and anthracene (5.0 mM) in THF, plotted with a 750 nm absorption transient of a control solution containing anthracene at 5 mM in THF.	121

Figure 5-3 A 950 nm absorption transient corresponding to a blend solution of perylene diimide (0.5 mM pru) and anthracene (5.0 mM) plotted in THF, with a 750 nm absorption transient of a control solution containing anthracene at 5 mM in THF.	122
Figure 5-4 A 650 nm absorption transient corresponding to a blend solution of MEH-PPV (0.73 mM pru) and anthracene (5.0 mM) in THF, plotted with a 750 nm absorption transient of a control solution containing anthracene at 5 mM in THF.	122
Figure 5-5 A 1400 nm absorption transient corresponding to a blend solution of pDPP2FT (25 μ M) and anthracene (5.0 mM) in THF, plotted with a 750 nm absorption transient of a control solution containing anthracene at 5 mM in THF.	123
Figure 5-6 The 900 nm absorption transient of a blend solution containing MEH-PPV (1.0 mM pru) and perylene (5.0 mM) in o-DCB, shown with the 550 nm absorption transient of a control solution containing perylene only at 5.0 mM in o-DCB.	124
Figure 5-7 The 620 nm absorption transient of a blend solution containing fSF-PPV (2.5 mM pru) and biphenyl (20 mM), shown with the 690 nm absorption transient of a control solution containing perylene only (5.0 mM).	124
Figure 5-8 The 900 nm absorption transient following radiolysis of a blend solution containing MEH-PPV (5 mM pru) and biphenyl (20 mM) in DCE, shown with the 690 nm absorption transient of a control solution in DCE containing biphenyl only at 20 mM.	125
Figure 5-9 The 1450 nm absorption transient following radiolysis of a blend solution containing MEH-PPV (5 mM pru) and biphenyl (20 mM) in DCE, shown with the 690 nm absorption transient of a control solution in DCE containing biphenyl only at 20 mM.	125
Figure 5-10 The 1400 nm absorption transient following radiolysis of a blend solution containing MEH-PPV (5 mM pru) and biphenyl (20 mM) in o-DCB, shown with the 550 nm absorption transient of a control solution in o-DCB containing perylene only at 20 mM.	126
Figure 5-11 The 720 nm absorption transient following radiolysis of a blend solution containing pCVPPV (5 mM pru) and biphenyl (20 mM) in o-DCB, shown with the 550 nm absorption transient of a control solution in o-DCB containing perylene only at 20 mM.	126
Figure 5-12 The 720 nm absorption transient of a blend solution containing pCVPPV (5 mM pru) and biphenyl (20 mM) in o-DCB, shown with the 550 nm absorption transient of a control solution in o-DCB containing perylene only at 20 mM.	127
Figure 5-13 The 820 nm absorption transient of a blend solution containing MEH-VPPV (0.241 mM pru) and anthracene (5 mM) in benzene, shown with the 430 nm absorption transient of a control solution in benzene containing anthracene only at 5 mM.	128
Figure 5-14 The 540 nm absorption transient of a blend solution containing fSF-PPV (0.3 mM pru, 100 μ M) and biphenyl (10 mM) in benzene, shown referenced against the 430 nm absorption transient of a benzene solution containing anthracene only at 10 mM.	128
Figure 5-15 The 600 nm absorption transient of a blend solution containing pCVPPV (180 μ M) and biphenyl (20 mM) in benzene, shown plotted with the 370 nm absorption transient of a benzene solution containing anthracene only at 10 mM.	129

Figure 5-16 Ground state absorbance spectra of a) MEH-PPV, fSF-PPV, and Sf-PPV in THF, and b) pCVPPV in benzene – each plotted as molar extinction coefficients per repeat unit (pru) versus wavelength.	130
Figure 5-17 Ground state spectra of SF-PPV at 5 μM per chain in chloroform and THF, shown (a) as collected, and (b) with peaks normalized.	131
Figure 5-18 Ground state absorbance spectra of pDPP2FT and PDI in chloroform at several concentrations are shown in (a) and corresponding plots of the maximum absorbances versus wavelength from which molar extinction coefficients of $9.50 \times 10^4 \text{ M}^{-1} \text{ cm}^{-1}$ and $9.14 \times 10^4 \text{ M}^{-1} \text{ cm}^{-1}$ respectively were determined, are shown in (b). (Data provided courtesy of Dr. Maxwell Robb).	132
Figure 5-19 Ground state absorbance spectra of pDPP2FT in THF at several monomer concentrations as measured in a cell with 0.1 cm pathlength cell are shown. The pru extinction coefficient at 807 nm was determined by linear fit of the absorbances at 807 nm vs concentration*pathlength.	133
Figure 5-20 An illustration of a voltammogram of an analyte with a reversible redox couple indicated by a peak cathodic current (i_{pc}) and peak anodic current (i_{pa}) whose magnitudes are equivalent. The potentials associated with these currents are the peak anodic potential (E_{pa}) and peak cathodic potential (E_{pc}). The half-wave potential ($E_{1/2} = (E_{pa} + E_{pc})/2$) is....	134
Figure 5-21 CVs of perylene, fluoranthene, and anthracene at concentrations of 1 mM vs Fc/Fc^+	136
Figure 5-22 CVs of MEH=PPV collected at 1 mM pru, 2 mM pru and 4 mM pru, shown reported vs. Fc/Fc^+	137
Figure 5-23 The i_{pc} and i_{pa} values plotted versus pru concentrations of MEH-PPV with slopes of $(2.20 \pm 0.53) \times 10^{-3} \text{ A/M}$ and $-(9.59 \pm 0.26) \times 10^{-4} \text{ A/M}$ show linearity but with values of $i_{pc} \approx 2.3 * i_{pa}$ demonstrating that the redox couple is not fully reversible.	139
Figure 5-24 The 900 nm absorption transients following radiolysis of THF solutions containing MEH-PPV at 21.4 μM and cosolutes of fluoranthene (FLA) and/or biphenyl (BP) for which FLA was varied and $[\text{FLA}] + [\text{BP}] = 10 \text{ mM}$, (a) in the absence of electrolyte, and (b) in the presence of 0.1 M TBAPF ₆	140
Figure 5-25 The 650 nm absorption transients following radiolysis of THF solutions containing fSF-PPV (30 μM) with and without 1,4-dicyanobenzene (50 mM), and the 650 nm transient corresponding to a solution of 1,4-dicyanobenzene only at 50 mM.	141
Figure 5-26 The 450 nm absorption transients following radiolysis of THF solutions containing fluoranthene (50 mM) with and without 1,4-dicyanobenzene (20 μM). An inset shows the time-dependent ratios of the absorbance transients which convey the relative ratio of the radical anions shown reaching equilibrium within 8 μs	141
Figure 5-27 The 850 nm absorption transients following radiolysis of a THF solution with pDPP2FT at 50 μM at varied concentrations of oxygen: argons saturated (0 mM O ₂), air saturated (2 mM O ₂) and oxygen saturated (10 mM O ₂).	142

Figure 5-28 The 950 nm absorption transients following radiolysis of a THF solution of perylene diimide (PDI) at 50 μ M with varied concentrations no oxygen, and with oxygen saturation (10 mM O ₂).	142
Figure 5-29 Absorption transients following radiolysis of DCE solutions containing MEH-PPV at 20 μ M and ferrocene at varied concentrations in: a) without electrolyte cosolute, and b) with 0.1 M TBAPF ₆ as cosolute.	143
Figure 5-30 The 600 nm absorption transients following radiolysis of DCE solutions containing fSF-PPV (500 μ M) and biphenyl (55 mM), with and without anthracene (58 mM), and a 600 nm transient corresponding to a solution of anthracene (58 mM) alone.	144
Figure 5-31 600 nm absorbance transients following radiolysis of benzene solutions of fSF-PPV at 50 μ M (chain) and a select cosolute (biphenyl, anthracene, and ferrocene) at 10 mM.	145
Figure 5-32 540 nm absorbance transients following radiolysis of benzene solutions of fSF-PPV at 50 μ M (chain) and a select cosolute (biphenyl, anthracene, and ferrocene) at 10 mM.	145
Figure 5-33 The absorbance spectrum of a series of spectrophotometric titrations involving a starting solution of MEH-PPV (6.7 μ M chain) and cryptand (11 mM) to which increasing concentrations of perylene ^{•-} with chelated Na ⁺ were added in aliquots.	147
Figure 5-34 ΔG^0 values corresponding to the work done by PERYL ^{•-} to create a redox state MEH-PPV ^{n•-} where “n” corresponds to the number of electrons per chain.	148
Figure 5-35 Energy diagram based on measurements of energetics of triplet and redox states of pCVPPV, MEH-PPV, and fSF-PPV. Actual experimental measurements are shown in red, while values shown in black indicate calculated values. The T ₁ energy levels indicate the lowest lying triplet levels.	149
Figure 6-1 Free energy changes for electron transfer from MEH-PPV (D) to fSF-PPV (fA) was calculated as -267 \pm 11 mV based on the free energies of electron transfer from fluoranthene (FLA) to MEH-PPV, from FLA to 1,4-dicyanobenzene (1,4-DCNB) and from 1,4-DCNB to fSF-PPV as determined in reversible electron equilibria measurements in THF. Values in indicate measurements, and the value in green indicates a calculation.	153
Figure 6-2 Absorbance spectra of MEH-PPV following varied stages of chemical reduction by Na biphenyl in THF, in the presence of 11 mM cryptand, in (a) corresponding to the formation of a radical anion band at 1.365 eV and (b) during the decay of the same band.	156
Figure 6-3 Overlaid absorbance spectra of MEH-PPV ^{•-} collected by radiolysis (rescaled) and chemical reduction in THF, showing good agreement.	157
Figure 6-4 A linear relationship was found for the magnitude of absorbance change in the 910 nm band associated with MEH-PPV ^{•-} and the corresponding magnitude of absorbance change at 500 nm band where the neutral absorbs.	158
Figure 6-5 Difference absorbance spectra obtained by subtracting the ground state neutral of MEH-PPV from a partially reduced spectrum of MEH-PPV showed good agreement.	159
Figure 6-6 Various stages of chemical oxidation of MEH-PPV via thianthrenium hexafluorophosphate (ThPF ₆) in o-DCB, shown in (a) during formation of a positive polaron band, and (b) during suppression of the band as positive bipolarons are formed.	160

Figure 6-7 A spectrum of MEH-PPV ⁺ collected by radiolysis in o-DCB, shown rescaled to overlay an absorbance spectrum of the same produced by chemical oxidation in o-DCB, showing good agreement.	161
Figure 6-8 A linear relationship was found for the magnitude of absorbance change in the 910 nm band associated with MEH-PPV ⁺ and the corresponding magnitude of absorbance change at 500 nm band where the neutral absorbs.	162
Figure 6-9 Transient absorption spectrum following radiolysis of a benzene solution containing MEH-PPV (20 μM chain) and biphenyl (5 mM) in a 1 mm pathlength cell capable of transmitting light to measure bleach.	163
Figure 6-10 Transient absorption spectrum following radiolysis of a benzene solution containing MEH-PPV (15 μM chain) and biphenyl (20 mM) in a 1 mm pathlength cell capable of transmitting light to measure bleach.	164
Figure 6-11 The absorbance and PL emission spectra of MEH-PPV and fSF-PPV in THF, plotted with absorbance spectra normalized by Abs(λ)/Abs(λ _{max}) and PL spectra normalized by PL(λ)/PL(λ _{max}).	166
Figure 6-12 The ground state spectrum of D(C2)fA in THF (green) is shown with a best spectral fit (dashed purple) based on the weighted sums of a donor reference spectrum (D _{ref}) and fA reference spectrum (fA _{ref}) defined as: m*[D _{ref}] + n*[fA _{ref}]. The spectra corresponding to m*[D _{ref}] (blue) and n*[fA _{ref}] (red) are also shown.	169
Figure 6-13 The ground state spectrum of D(C4)fA in THF (green) is shown with a best spectral fit (dashed purple) based on the weighted sums of a donor reference spectrum (D _{ref}) and fA reference spectrum (fA _{ref}) defined as: m*[D _{ref}] + n*[fA _{ref}]. The spectra corresponding to m*[D _{ref}] (blue) and n*[fA _{ref}] (red) are also shown.	169
Figure 6-14 The ground state spectrum of D(C4)fA in THF (green) is shown with a best spectral fit (dashed purple) based on the weighted sums of a donor reference spectrum (D _{ref}) and fA reference spectrum (fA _{ref}) defined as: m*[D _{ref}] + n*[fA _{ref}]. The spectra corresponding to m*[D _{ref}] (blue) and n*[fA _{ref}] (red) are also shown.	170
Figure 6-15 Plots of diblock _{ref} spectrum, D _{ref} spectrum, and A _{ref} spectrum corresponding to THF solutions of: a) D(C0)fA, b) D(C1)fA, c) D(C2)fA, and d) D(C2)A.	172
Figure 6-16 Plots of diblock _{ref} spectrum, D _{ref} spectrum, and A _{ref} spectrum corresponding to CHCl ₃ solutions of: a) D(C0)fA, b) D(C1)fA, c) D(C2)fA, and d) D(C2)A.	175
Figure 6-17 Ground state absorbance spectra of: a) D (21.5 monomers) prepared at 5 μM chain (by GPC) in THF, CHCl ₃ , and 1/6 CHCl ₃ and 5/6 THF, and b) D(C2)A at prepared at 5 μM chain (by GPC) in THF, CHCl ₃ , and 1/6 CHCl ₃ and 5/6 THF.	176
Figure 6-18 A difference spectrum between the ground state absorbance spectrum of D ₁₄ /THF and D ₁₄ (CO)fA/THF when normalized at peaks, is assumed to be equivalent to the ground state absorbance spectrum of the fA moiety from which concentration ratios of D:fA can be determined.	178
Figure 6-19 Pathways for exciton decay in a DBA system showing competing rates for recombination and dissociation to radical ion pairs.	179

Figure 6-20 Ground state absorbance spectra of THF solutions of homoblocks (D and fA), blend, and select diblocks, all prepared with an absorbance of 0.05 at 372 nm.....	181
Figure 6-21 Photoluminescence spectra following excitation at 372 nm corresponding to THF solutions of: a) D and fA homoblocks, and b) a D/fA blend, D(C2)fA, D(C4)fA, and D(C6)fA.	182
Figure 6-22 Photoluminescence spectra of blend and diblock solutions in THF corresponding to excitation at 372 nm where each contain the same absorbance.	183
Figure 6-23 The overlap integral is defined by the overlapping spectral regions of the absorbance spectrum of the energy acceptor and the fluorescence spectrum of the energy donor.	186
Figure 6-24 A plot of absorbance and PL emission versus pru concentration of MEH-PPV in THF reveals that both are linear over a range of 20 μ M pru.....	187
Figure 6-25 (a) Ground state absorbance spectra corresponding to blend solutions of D (4.82 μ M pru) and varied concentrations of fA (0 – 28.7 μ M pru). In (b) excitation at $\lambda=530$ nm where only D absorbed resulted in identical PL emission spectra suggesting no collisional quenching occurs.....	188
Figure 6-26 Photoluminescence quenching observed from MEH-PPV (D) and diblocks D(C2)fA, D(C4)fA and D(C6)fA excited at 530 nm. The inset shows the ground state absorbance spectra of each solution prepared with same absorbance at 530 nm to ensure equivalent number of photons on each when excited at that wavelength.....	189
Figure 6-27 Photoluminescence quenching observed from MEH-PPV (D) and diblocks D(C0)fA, D(C1)fA and D(C2)fA excited at 500 nm. The inset shows the ground state absorbance spectra of each solution prepared with same absorbance at 500 nm to ensure equivalent number of photons on each when excited at that wavelength.....	190
Figure 6-28 Photoluminescence (PL) yields of D ₁₄ /THF, D ₁₄ (C0)fA/THF and D ₁₄ (C1)fA/THF when controlled for number of photons absorbed at 500 nm, exhibited 9% and 5% quenching relative to the PL emission of D ₁₄ /THF.	190
Figure 6-29 Transient absorption following 530 nm photoexcitations of MEH-PPV in D and D(C2)A in CHCl ₃	192
Figure 6-30 Scheme showing charge transfer from a radical ion states of a DBA molecule: D [•] BA (a) and D ^{•+} BA (b). Charge transfer first is preceded in both cases by non-selective formation of radical ions dependent on relative concentration of the D and A moieties.	193
Figure 6-31 Radical anion decays of SF-PPV (A), MEH-PPV (D), and D(C2)A following radiolytic pulse in THF. The radical ion spectrum of DBA has the form of a linear sum of the respective radical anion components, and is found transforming from D ^{•-} (C2)A \rightarrow D(C2)A ^{•-}	194
Figure 6-32 Absorbance transients at 900 nm corresponding to radiolysis of D (1.45 mM pru) and fA (1.09 mM pru). Under these conditions, fA captures 12% more electrons suggesting the ratio of anion absorbances of D:fA are less than 20:1. This wavelength served as an effective wavelength for monitoring formation and decay kinetics of D ^{•-} in the presence of fA.....	195

Figure 6-33 Transient spectrum of D(C0)fA (1 mg/ml, purple) near maximum signal following radiolytic pulse, shown with referene spectra of $fA^{\bullet-}$ (red) and $D^{\bullet-}$ (blue) used to find a best linear sum fit of the transient spectrum of D(C0)fA, using $a \cdot D_{ref} + b \cdot fA_{ref}$, with $a=0.54$ and $b=0.13$ (dashed green).....	196
Figure 6-34 Transient spectrum of D(C0)fA (60 μM_{SF} , purple) near maximum signal following radiolytic pulse, shown with referene spectra of $fA^{\bullet-}$ (red) and $D^{\bullet-}$ (blue) used to find a best linear sum fit of the transient spectrum of D(C0)fA, using $a \cdot D_{ref} + b \cdot fA_{ref}$, with $a=0.49$ and $b=0.39$ (dashed green).....	196
Figure 6-35 Transient absorbance spectra of D(C0)fA (1 mg/ml) in THF shown: a) during the formation of the 900 nm band, and b) during the decay of the 900 nm band.....	197
Figure 6-36 Absorbance transients at 900 nm following radiolytic pulse of THF solutions for D(C2)fA, D(C4)fA, and D(C6)fA, each prepared at 60 μM_{SF} . Decay rates are found to be much slower than formation rates suggesting negligible electron transfer during the formation of $D^{\bullet-}$	198
Figure 6-37 Absorbance transients of $D^{\bullet-}$ at 900 nm corresponding to radiolysis of D, D(C0)fA, D(C1)fA, D(C2)fA and D(C6)fA. Transients of D(C2)fA and D(C6)fA were nearly identical and transients of D(C0)fA and D(C1)fA were also nearly identical.	200
Figure 6-38 The k_{decay} rates for $D^{\bullet-}$ (C0)fA plotted versus [D(C0)fA].....	202
Figure 6-39 The k_{decay} rates for $D^{\bullet-}$ (C1)fA plotted versus [D(C1)fA].....	202
Figure 6-40 The k_{decay} rates for $D^{\bullet-}$ (C2)fA plotted versus [D(C2)fA].....	203
Figure 6-41 The k_{decay} rates for $D^{\bullet-}$ (C6)fA plotted versus [D(C6)fA].....	203
Figure 6-42 Donor radical anion decay rates measured in various blend solutions of D and D(Cn)fA where $[D] \gg [D(Cn)fA]$, and for which neutralization reactions were controlled for by dividing by transients of the donor homoblock solution prepared at similar chain concentrations leading to pseudo first order rates.....	204
Figure 6-43 The absorbance decay transient associated with the rate of bimolecular electron transfer from $D^{\bullet-}$ (C6)fA \rightarrow D(C6)fA $^{\bullet-}$ in the presence of 0.1 M TBAPF ₆ . The bimolecular rate in electrolyte was determined by single exponential fit of this decay as $1.12 \times 10^4 \text{ s}^{-1}$, which is likely an underestimate given that the full transient could not be fitted due monitored exceeding the time window of observation.....	206
Figure 6-44 Absorbance transients at 900 nm following radiolysis of THF solutions of D homoblock, D(C2)fA, D(C4)fA and D(C6)fA prepared at chain concentrations of 60 μM_{SF} with 0.1 M TBAPF ₆	207
Figure 6-45 900 nm absorption transients of D ₁₄ /THF, D ₁₄ (C0)fA/THF, and D ₁₄ (C1)fA/THF shown at chain concentrations of: a) 120 μM , and b) 60 μM	208
Figure 6-46 800 nm absorbance transients following radiolysis of a THF solution of D(C6)fA (60 μM_{SF} chain): shown with an optical long pass cutoff filter (red), without an optical filter (blue) and a difference transient (blue) obtained by subtracting the green transient from the red one.	209
Figure 6-47 Formation of bleach following radiolysis of a THF solution of D(C6)fA (60 μM_{SF}) due to decay of $^3D^*$ via reaction with radical anions.	209

Figure 6-48 Transient absorption spectrum corresponding to a benzene solution of pCVPPV (450 μM chain) and MEH-PPV (15 μM chain) giving indication of a conversion of $^3\text{pCVPPV}^*$ (600 nm) to $^3\text{MEH-PPV}^*$ (820 nm).....	211
Figure 7-1 Ground state absorbance spectra of PDI and pDPP2FT _x PDI in chloroform. The spectra of pDPP2FT _x PDI are shown with normalized absorbances at 400 nm. In this way, the PDI absorbance is increased relative to the principal band of the pDPP2FT chain as chain length is decreased (Raw data provided courtesy of Dr. Maxwell Robb).	218
Figure 7-2 Transient absorption signals measured at 1150 nm corresponding to excitation of pDPP2FT, p ₁₆ PDI and p ₃₂ PDI at 850 nm.....	219
Figure 7-3 Chemical reduction of pDPP2FT (12.8 μM pru, 0.35 μM chain) via sodium biphenyl in THF results in formation of presumed (pDPP2FT ^{•-} , Na ⁺) with a peak at 1420 nm. In all but step 5, no band is observed above 1600 nm and only the neutral and 1420 nm bands are present.....	220
Figure 7-4 As the polymer is further reduced in steps 6 – 9, formation of two new bands are evident: a higher energy band with a maxima circa 1130 nm and a lower energy band that extends beyond the spectral window of observation. A difference spectrum obtained by subtracting step 9 from step 6 provides an approximate spectrum of the new optical transitions as shown in the inset.....	221
Figure 7-5 Starting with step 9 of the previous figure, a third spectral transformation is identified. Upon further reduction, the neutral is further suppressed in steps 9 – 11 with very little change in the bands associated with the 2nd charged state. In steps 12 – 14 however once the neutral is fully removed, the 2nd charged state begins to decline in yield as a 3 rd charged state forms circa 1350 nm.	222
Figure 7-6 The 4 th spectral transformation involves removal of the 2 nd charged state (evident from suppression at 2000 nm) and eventual removal of the 3 rd charged state as well (steps 17 – 19). An approximate spectrum of the 3 rd charged state is shown in the inset.....	223
Figure 7-7 The absorbance spectrum of pDPP2FT ^{•-} in THF produced via radiolysis, overlaid with a rescaled absorbance spectrum of (pDPP2FT ^{•-} , Na ⁺) produced by chemical reduction via sodium biphenyl.....	223
Figure 7-8 The magnitude of absorbance changes at 807 nm and 1400 nm corresponding to stages of partial reduction of pDPP2FT in THF exhibit linearity indicating direct conversion of the neutral into the negative polaronic species for the transitions shown.....	224
Figure 7-9 Spectrum corresponding to radiolysis of pDPP2FT (5.5 μM chain) in THF, collected at 1.0 μs after pulse, using a 0.1 cm pathlength cuvette.	225
Figure 7-10 Absorbance spectra following various states of oxidation produced chemically via Thianthrenium hexafluorophosphate (ThPF ₆) in DCE.	226
Figure 7-11 Transient absorbance spectra of pDPP2FT ^{•+} collected following radiolysis of a DCE solution with biphenyl (20 mM) and pDPP2FT (5 mM pru). Biphenyl ^{•+} is rapidly formed and converted to pDPP2FT ^{•+} via efficient hole transfer lead to the growth of a 1450 nm band in (a) and a subsequent decay process removes the band in (b)	226

Figure 7-12 A spectrum of chemically oxidized pDPP2FT overlaid by a rescaled spectrum of pDPP2FT oxidized by radiolysis of pDPP2FT in DCE shows good agreement.	227
Figure 7-13 The magnitude of absorbance changes at 807 nm and 1450 nm corresponding to stages of partial oxidation of pDPP2FT in DCE exhibit linearity.	228
Figure 7-14 A scheme for kinetic parameters involved in radiolysis of a THF solution of pDPP2FT and a THF solution of pDPP2FT _x PDI (shown with 2 PDI end caps).	229
Figure 7-15 1400 nm absorption transients immediately following radiolysis of THF solutions containing p ₃₇ , and p _x PDI at chain concentrations of 25 μM, where (a) and (b) correspond to independent experimental trials with (a) containing only p ₁₆ PDI and p ₃₂ PDI and (b) containing p ₁₄ PDI and p ₃₂ PDI as well.	232
Figure 7-16 The slow decay rate of p ₃₂ PDI/THF at 40 μM chain, associated with bimolecular electron transfer. The decay rates of all p _x PDI were found to have slow decay rates of $(1.53 \pm 0.05) \times 10^5 \text{ s}^{-1}$ corresponding to lower limiting estimates of $(3.82 \pm 0.13) \times 10^9 \text{ M}^{-1}\text{s}^{-1}$ for bimolecular electron transfer rate constants based on the assumption that the entire p _x PDI batch contains PDI caps.	235
Figure 7-17 Absorption transients at 950 nm following radiolysis corresponding to THF, and solutions of pDPP2FT, p ₁₆ PDI and p ₂₆ PDI in THF – each at chain concentrations of 25 μM, prepared for Trial 1. The transients of the p _x PDI solutions were corrected by subtracting the f _{slow} contribution.	236
Figure 7-18 Absorption transients at 950 nm following radiolysis of THF, and solutions of pDPP2FT, p ₁₄ PDI, p ₁₆ PDI and p ₂₆ PDI in THF– each at chain concentrations of 25 μM, prepared for Trial 2. The transients of the p _x PDI were corrected by subtracting the f _{slow} contribution.	237
Figure 7-19 Absorption transients at 1400 nm corresponding to radiolysis of THF solutions of pDPP2FT, p ₁₆ PDI, p ₂₆ PDI, and p ₃₂ PDI at chain concentrations of 25 μM following radiolytic pulse, shown on a time scale of (a) 6 μs, and (b) 600 ns.	239
Figure 7-20 Absorbance transients of p ₁₆ PDI/THF (25 μM chain) and THF at: (a) 1400 nm, and (b) 1600 nm.	240
Figure 7-21 Transient absorption spectrum of THF collected immediately following radiolytic pulse.	242
Figure 7-22 Transient absorption spectra of pDPP2FT/THF (25 μM chain) shown over a 7.0 μs time frame following radiolytic pulse. Transient spectra at 4.0 μs and 7.0 μs occur during the decay of pDPP2FT ^{•-} and are shown plotted with dashed fits. The decay of pDPP2FT ^{•-} by conversion to pDPP2FTH [•] is indicated by correlated growth at 950 nm associated with the decaying 1400 nm band.	243
Figure 7-23 Transient absorption spectra of p ₁₆ PDI/THF (25 μM chain) shown (a) from 30 ns – 646 ns, and (b) from 646 ns – 6 μs.	244
Figure 7-24 Transient absorption spectra of p ₂₆ PDI/THF (25 μM chain) shown (a) from 30 ns – 300 ns, and (b) from 300 ns – 5 μs.	244
Figure 7-25 Transient absorption spectra of p ₃₂ PDI/THF (25 μM chain) shown (a) from 30 ns – 300 ns, and (b) from 300 ns – 5 μs.	245

Figure 7-26 Absorbance transients at 950 nm corresponding to THF solutions of p₃₇, p₁₆PDI, p₂₆PDI, and p₃₂PDI collected immediately after radiolytic pulse. 246

Figure 7-27 Absorbance transients at 1400 nm corresponding to radiolysis of a THF solution containing p₁₆PDI (12 μM chain) following exposure to specified dosages of radiolytic pulses. 248

Figure 7-28 A plot of absorbance at t = 2 μs after radiolytic pulse are plotted relative to the number of radiolytic pulses or “shots” delivered to the p₁₆PDI sample, indicating a rise slope that is 7 times faster than the decay slope..... 249

Figure 7-29 Ground state absorbance spectra of pDPP2FT (10 μM chain) in THF following various stages of radiolytic damage according measured by number of accumulated pulses. The bands associated with PDI ground state decay completely after 300 pulses while the principal band of pDPP2FT at 807 nm decays by less than 30% during that same exposure. 250

List of Abbreviations

<u>Abbreviation</u>	<u>Full description</u>
ANTH	Anthracene
BP	Biphenyl
CV	Cyclic voltammetry
D-A	Donor-Acceptor
DCE	1,2-dichloroethane
DBA	Donor-bridge-Acceptor
D-S equation	Debye-Smoluchowski equation
FBC	Fesser, Bishop, Campbell
fSF-PPV	Fluorinated, sulfone-derivatized PPV
FCWD	Franck-Condon weighted density of states
LEAF	Laser-electron accelerator facility
MALS	Multi angle light scattering technique
MEH-PPV	Poly[2-methoxy-5-(2-ethylhexyloxy)-1,4-phenylenevinylene]
P3DT	Poly(3-dodecylthiophene-2,5-diyl)
PA	polyacetylene
pDPP2FT	Polydiketopyrrolopyrrole with 2 furans and 1 thiophene
P3DT	Poly(3-decylthiophene-2,5-diyl)
PDI	Perylene diimide
PERYL	Perylene
PPV	Polyphenylene vinylene
THF	Tetrahydrofuran

Abstract

Photovoltaics using polymer semiconductors as active materials require donor/acceptor (D/A) interfaces to convert excitons into freed charges. In the absence of chain defects, excited states and charges migrate most efficiently via intramolecular pathway. This thesis is concerned with understanding dynamics of intramolecular transport, charge transfer at intramolecular D/A interfaces, and the nature of charges and excited states which give rise to the observed phenomena.

Three conjugated polymers are investigated: MEH-PPV (typical bandgap), pDPP2FT (low bandgap), and pCVPPV (high bandgap). Compounds investigated as electron acceptors relative to these polymers were oligomers fSF-PPV and SF-PPV for MEH-PPV, perylene diimide (PDI) for pDPP2FT, and MEH-PPV for pCVPPV. As a prototypical conjugated polymer, MEH-PPV is investigated most extensively – exploring the physical and electronic properties of its charged and excited states, energetics of those states, and the rates and nature of charge and exciton capture via radiolysis. Comparisons and contrasts are made with non-conventional pCVPPV and pDPP2FT.

Radiolysis is employed as a powerful technique for obtaining optical signatures and reaction kinetics of radical ions and triplets for oligomers and polymers by ensuring a small fraction of chains in solution are injected with a single charge or excited state. This technique facilitates unambiguous assignment of specific species in contrast with other techniques for which multiple species are formed but difficult to resolve. Mistaken assignment of species have resulted from such ambiguities as well as conflicting theoretical models predicting the number of optical transitions expected for these species. Rates of formation for charged states are compared with theoretical diffusion controlled rates, and optical transitions of the optical signatures are compared with those predicted by the commonly referenced Fesser-Bishop-Campbell (FBC) model predicting two transitions for a radical ion (polaron) and one for a radical diion (bipolaron). Departures from this model included fSF-PPV and SF-PPV radical ions which

exhibited 3 transitions (one quasi-forbidden) and pDPP2FT radical ions which exhibited 1 transition while pDPP2FT diions exhibited two.

Using optical detection provided the known optical signatures, electron and exciton dynamics in acceptor-capped MEH-PPV and acceptor-capped pDPP2FT are investigated. Acceptor radical anion formation following electron or exciton capture by the chain is interpreted as rate limited by either electron transport along the chain or by electron transfer at the D/A interface. In PDI-capped pDPP2FT, a lower limit for electron mobility under zero-field conditions is estimated as $3.37 \times 10^{-3} \text{ cm}^2/\text{Vs}$, more than an order of magnitude larger than observed in polythiophene. This mobility study for a D-A copolymer under zero field conditions is the first of its kind. In a series of Donor-bridge-Acceptor (DBA) diblocks consisting of MEH-PPV and (f)SF-PPV with varying lengths of aliphatic bridges, intramolecular electron transfer rates from the radiolytically reduced MEH-PPV to neutral fSF-PPV in all cases exhibited a rate of $\geq 10^{-4} \text{ s}^{-1}$ in spite of a $\sim 270 \text{ meV}$ free energy change. Even more astonishing is that the same rate was observed when no intervening bridge was present. Improvements in power conversion efficiencies of DBA-based devices relative to D/A blend-devices have been argued to stem both from improved exciton dissociation due to intramolecular pathway and due to improved order. This study contradicts that notion that DBA diblocks should always facilitate rapid and efficient intramolecular dissociation of excitons. While a definitive reason for the inefficient intramolecular electron transfer was not determined, some contributing factors are presented.

Chapter 1: General Introduction

1.1 Motivation for polymer photovoltaics

Global demands for cheap and clean renewable energy have ignited an urgency for photovoltaic research in the past couple decades. From 1996 to 2006, funding for photovoltaic research in many developed countries more than doubled, with the U.S., Germany and Korea improving funding by more than 10 fold [1]. Photovoltaics are attractive due to their ability to convert the free and abundant optical energy of sunlight into usable electrical energy, relying on semiconductors as active optoelectronic materials. Semiconductors possess bands of energy— a lower lying valence band and a higher energy conduction band, which are separated by an energy bandgap, E_g . In the absence of defect states, electrons may occupy levels within the bands but not within the bandgap. The bandgap of a semiconductor is of a magnitude that generally lies within the range of optical energies. When photons with sufficient energy equivalent to or greater than the bandgap are absorbed by the semiconductor, the optical energy is converted into electronic energy in the form of an exciton (or electron-hole pair) which may separate into the component charges provided sufficient energy is present. Silicon has been the preferred semiconductor for photovoltaics, accounting for 86% of the solar cell market [2]. Silicon solar cells were commercialized in the 1960s for use in the space programs. Since then rapid progress has been made towards improved efficiency and reliability, while simultaneously decreasing fabrication costs, and today this technology has progressed in application as a source of household power. However, in industrialized countries this progress has only recently become competitive with the price of electricity from the electrical grid. Production of inorganic photovoltaics is very costly due either to the raw material costs, and/or processing conditions required, such as high temperature and high vacuum. Additional challenges often associated with inorganics are limitations in choice of substrate and maximum surface area of deposition.

Conjugated polymers in recent decades have been explored as semiconducting materials capable of solving these problems and other material limitations of traditional semiconductors. Conjugated polymers are organic macromolecules characterized by a backbone chain of repeat molecular units (or monomers) giving rise to degenerate molecular π -orbitals with bands of bonding and antibonding orbitals. The energy difference between the highest occupied molecular orbital (HOMO) and lowest unoccupied molecular orbital (LUMO) defines the energy bandgap, E_g . The HOMO and LUMO are analogous to the band edges of the valence and conduction bands described by band theory for crystalline inorganic semiconductors.

The key advantage of conjugated polymers lies in their potential for combining electrical properties of conventional semiconductors with the other properties typical of organics- low cost, high processability, mechanical flexibility, and the versatility of chemical synthesis. The cost reduction mainly results from the ease of processing from solution – a property that is enhanced by the attachment of side groups to the conjugated backbone. As a result, low-cost and efficient deposition techniques such as ink jet printing, [3, 4] roll to roll processing [5] and screen printing [6] have made rapid production of large area, flexible electronic devices foreseeable. These techniques have also facilitated fabrication on various substrates including plastic, paper, and even textiles [7]. Progress in material development and device designs over the last two decades have led to vast improvements in device efficiencies and stability. Further improvements however are necessary to render polymer solar cells as market viable [8-10].

To a significant extent, the short circuit current and overall efficiency of a photovoltaic, are dictated by the efficiency of charge carrier generation and charge carrier mobility. Being that excitons are intermediates in the conversion from photons into charge carriers, efficient separation of excitons is vital to photovoltaic performance. In silicon nearly all excitons dissociate via thermal energy at room temperature but polymers as materials with low dielectric constants, have more tightly bound excitons. In such cases, an interface between two semiconducting materials for which one is energetically favored to stabilize the electron (electron acceptor) while the other is energetically favored to stabilize the hole (electron donor) may be used. Such an interface is referred to as a type II heterojunction. A type I heterojunction involves an interface between two semiconductors with bandgaps of different

magnitudes for which both the electron and hole are preferentially stabilized by the lower bandgap semiconductor, leading to an energetically preferred uni-directional exciton (energy) transfer.

Once charge carriers are generated, their mobilities become a limiting factor in how rapidly they are collected at the appropriate electrodes. In polymers, charge carriers interact strongly with lattice vibrations which influence carrier mobilities. The electronic coupling between covalently bonded monomers within a chain is significantly stronger than coupling between monomers in neighboring chains, often leading to significantly better transport of charges along chains (intramolecular transport) than between chains (intermolecular transport). Intermolecular transport therefore often defines the limiting rate of carrier mobilities [11, 12]. While there is wide consensus on some physical aspects of excited and charged states of conjugated polymers, significant debate still remains, with cogent arguments to support the varied views [13]. An improved understanding of the fundamental nature of charges and excitations in conjugated polymers, the selection or design of effective donor/acceptor pairs, and the relationship between electronic structure and charge mobility are imperative to improving the prospects of market viability for polymer photovoltaics.

1.2 Historical perspective of organic semiconductors

The semiconducting properties of organic materials were first being investigated in the 1950s, and focused on small conjugated molecules such as anthracene and naphthalene in the crystalline state [14]. By the 1960s observations of electroluminescence [15] and photoconductivity [16, 17] from molecular crystals of anthracene were being reported. However, in addition to exhibiting poor semiconducting properties, these materials were difficult to handle and therefore deemed impractical for industrial application.

Interests eventually turned to the possibility of merging the mechanical properties of polymers with the semiconducting properties of conjugated molecules. This was achieved by dispersing small organic molecules into a polymer matrix. By the 1970s, these polymers were finding application as photoconductors in photocopiers and printers. These materials were preferred to previously used inorganic materials due to their lower cost and flexibility [18].

Unfortunately, the molecular doped polymers were limited to photoconductor applications, showing little value in other directions.

The modern field of plastic electronics was birthed when it was discovered in 1977 that the electrical conductivity of polyacetylene, a π -conjugated organic polymer, could be tuned over 8 orders of magnitude from intrinsic insulator to conductor by means of chemical doping. Unlike molecular doping, chemical doping is best viewed as a redox reaction in which the neutral insulating polymer is converted into an ionic complex consisting of a polymeric anion (or cation) and a counterion which is the oxidized (or reduced) form of the oxidizing agent [19]. The significance of this discovery of metallic conductivities in conjugated polymers was highlighted by the award of the Nobel Prize in Chemistry to Hideki Shirakawa, Alan MacDiarmid, and Alan Heeger in 2000.

In the 1980s and 1990s, research efforts centered primarily on demonstrating practicality of semiconducting and conducting polymers in a broad range of applications. In the 1980s the first organic field-effect transistors [20, 21], actuators, and electrochromic devices were introduced. A major breakthrough came in 1990 with the first evidence of electroluminescence from a polymer demonstrated by Burroughes et. al. using poly(p-phenylenevinylene) (PPV) [22]. PPV is not soluble so to fabricate the device required thermal conversion of a soluble precursor under vacuum. The following year a polymer light emitting diode was fabricated by spincoating a new and soluble derivative of PPV, [2-methoxy-5-(2-ethylhexyloxy)-1,4-phenylenevinylene], or MEH-PPV. The first photovoltaic effect with a 0.1% power conversion efficiency was demonstrated by Karg et. al., also using PPV in 1993 [23]. By the mid-1990s, major improvements in device fabrication followed the synthesis of new, soluble polymers. Chemical structures for trans-polyacetylene and PPV, two of the conjugated polymers involved in early breakthroughs of the field of plastic electronics, are shown in **Figure 1-1**.

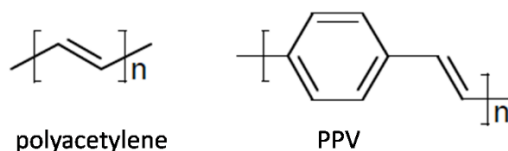


Figure 1-1 Chemical structures of polyacetylene and PPV.

In the past couple decades, research efforts in organic electronics have steadily grown, giving indication to the potential of these materials in a wide range of applications. Much of these efforts are aimed at reaching performance and stability requirements necessary for commercialization. Improvements in device design and materials have led to two orders of magnitude improvement in conversion efficiencies for photovoltaics using solely polymeric active layers, with a conversion efficiency just above 10% being reported recently based on a tandem solar cell [24]. Improving charge generation and charge transport are vital to the further improvement of device efficiencies for polymer photovoltaics. Understanding these fundamental processes remains a core goal.

1.3 Aim of thesis & materials investigated

Three polymers which collectively extend over the entire visible band were investigated to explore the nature and optical signatures of charged and excited states in conjugated polymers: a high bandgap polymer (pCVPPV), a conventional bandgap polymer (MEH-PPV) and a low bandgap polymer (pDPP2FT). In addition, optical signatures of charged and excited states of electron acceptors are collected. Sulfone-derivatized phenylenevinylenes, SF-PPV and fSF-PPV are explored as electron acceptors for MEH-PPV, perylene diimide as an electron acceptor for pDPP2FT, and MEH-PPV as an electron acceptor for pCVPPV. Through formation of type II heterojunctions between the polymers and their respective acceptors, charge and energy transfer reactions are monitored by optical detection. Important questions of these studies include: How much energy is required to separate an electron-hole pair into separated polarons? How delocalized are charges and excitons? How rapidly can they move along a chain? In this work, pulse radiolysis is used as a tool to investigate these and related questions.

A list of the polymers and their corresponding electron acceptors is shown in **Table 1-1**.

Table 1-1 *Polymers investigated and compounds explored as corresponding electron acceptors*

Polymer	Acceptor compounds
pDPP2FT	Perylene diimide (PDI)
MEH-PPV	SF-PPV & fSF-PPV
pCVPPV	MEH-PPV

The fSF-PPV electron acceptor for MEH-PPV is virtually identical to SF-PPV – differing only by the fluorination of the backbone. The intended effect of fluorination was to achieve a more positive reduction potential relative to SF-PPV. Fluorine is the most electronegative element, and having a size comparable to hydrogen, it can replace hydrogen on a polymer or oligomer backbone without introducing steric hindrance while tuning energy levels. Yu demonstrated a systematic tuning by fluorination of a donor-acceptor copolymer in which both HOMO and LUMO energy levels were reduced as a function of the number of fluorine substitutions [25]. In addition to the effect of energy level tuning, fluorination also affects the dipolar moment change in polymer repeat units between ground state and excited states [26, 27].

Diblock copolymer chains containing both MEH-PPV and the acceptors are investigated. A simplified naming scheme is used to reflect the unique constitution of each of the acceptor-capped polymers. In this naming scheme, “D” represents MEH-PPV, “A” represents SF-PPV, and “fA” represents fSF-PPV. All but one of the acceptor-capped polymers contained an intervening aliphatic bridging unit “B” between the donor and acceptor moieties, more specifically represented as “C_n” for which “n” represents the number of carbons “C”. According to this naming scheme, the set of acceptor-capped polymers investigated were: D(C₂)A, D(C₂)fA, D(C₄)fA, D(C₆)fA, and D(C₀)fA.

Polymers containing pDPP2FT covalently bonded to its electron acceptor, perylene diimide (PDI), were also synthesized. A set of PDI-capped chains were synthesized in which chain length was varied. To simplify the naming of these composites, a nomenclature of pDPP2FT_xPDI or in more abbreviated form, p_xPDI, was used where “x” indicates the number of DPP2FT monomer units with values of 14, 16, 26, 32, and 40. The ratio of PDI units per pDPP2FT chain in each p_xPDI batch was distributed among populations of 2:1, 1:1, and 0:1.

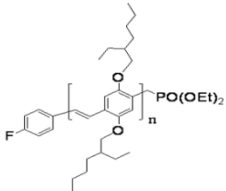
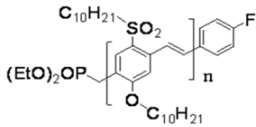
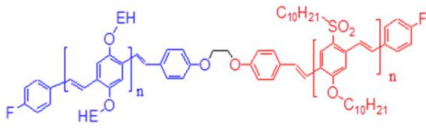
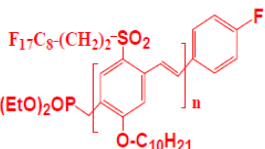
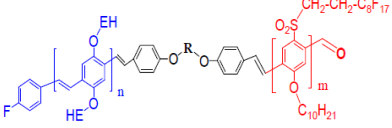
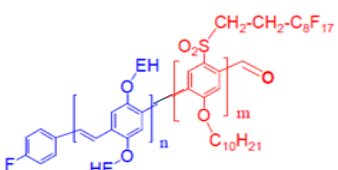
Further details of these two systems of acceptor-capped polymers are presented below.

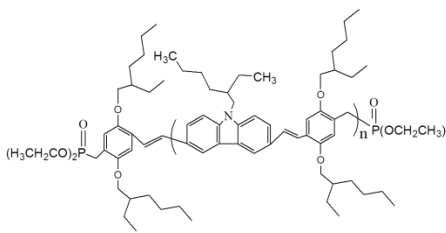
1.3.1 Phenylenevinylene based materials

All phenylenevinylene based materials were synthesized by current or former members of Dr. Sam Sun’s group in the Organic/Polymeric Materials Laboratory at Norfolk State University.

The following is a list of the materials by their designated short names, chemical structures, and collaborators who synthesized them.

Table 1-2 Chemical Structures of *s*-PPVs investigated

Polymer	Chemical Structure	Collaborator
MEH-PPV (D)		Dr. Cheng Zhang Muhammad Hasib
SF-PPV (A)		Dr. Cheng Zhang
DBA		Dr. Cheng Zhang
fSF-PPV (fA)		Muhammad Hasib
$D_x(C_n)fA_y$ $R=C_n$		Muhammad Hasib
$D_x(C_0)fA_y$		Muhammad Hasib

pCVPPV		Dr. Tanya David
--------	--	-----------------

MEH-PPV is a prototypical conjugated polymer, and has become one of the most widely explored and utilized conjugated polymers in organic electronics. For photovoltaic application, the polymer is valued as a strongly absorbing material. The idea of forming a DBA structure based on conjugated polymer as an electron donor is attractive for at least two reasons. First, given that excitons migrate more efficiently along chains than between chains, might suggest that an intrachain D/A interface might enhance the probability of charge separation in a device. Secondly, assuming the bridge length determines the closest distance between the donor and acceptor in a solid state device, an optimal bridge length will optimize retardation of electron-hole recombination once charges along a chain are separated. Thirdly, theoretical models predicting self-assembled structures from diblock copolymers based on the relative molecular weight of each block, have suggested their potential to form interdigitated structures of the material phases [28]. Such a structure based on donor/acceptor phases is ideal for photovoltaic function.

The efficiencies and rates of charge transfer reactions occurring over long distances are of great importance in light-to-chemical energy conversion and molecular electronics. Free energy differences in these reactions are an important limiting factor. The seminal work of Miller and Closs in the 1980s explored the free energy dependence and length dependence of charge transfer rates in DBA systems involving small aromatic molecules as donor and acceptor [29, 30]. This energy dependence they observed solidified the theory proposed by Rudy Marcus postulating an inverted region for which the charge transfer rates begin to decrease above some optimal free energy difference [31, 32]. Using various non-conjugated spacers, charge transfer observed over dozens of angstroms were found to exhibit nanosecond to

submicrosecond rates [29, 33]. Numerous studies regarding charge transfer in DBA systems have followed in recent decades, including studies examining the influence of the bridge [34], but nearly all have investigated donors and acceptors consisting of aromatic molecules or transition metal complexes. A study investigating a DBA system consisting of a polymeric donor has not been done. Assuming such a system facilitates electron transfer, transport of the electron must also be taken into account.

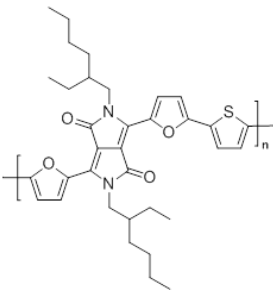
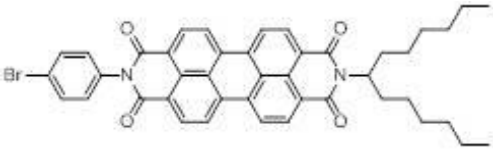
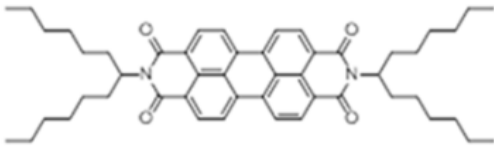
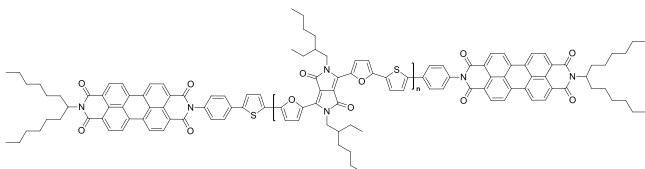
A single DBA polymer containing SF-PPV (A) was investigated which contained ~21 repeat units of D and ~14 repeat units of A. The other diblock copolymers, contained fSF-PPV (fA) as acceptor. Both SF-PPV and fSF-PPV are novel materials and naturally of interest to investigate as electron acceptors relative to MEH-PPV as they were intended. The synthesis of the DbfA polymers has been detailed elsewhere [35, 36] but in brief, was accomplished by coupling Db with fA monomer catalyzed by NaH in dry tetrahydrofuran (THF). NMR revealed that peaks associated with fA monomer prior to synthesis no longer were present following synthesis while the peaks associated with Db remained. Two sets of DBfA polymers were investigated – each set differing by the length of the D moiety. To distinguish these sets, the subscripts “x” and “y” have been used to label them generally as D_xBfA_y . In the longer chain set, “x” was ~ 24 monomers, and in the shorter chain was ~14 monomers. In each set, the homogeneity of the length of the D moiety was due to using the isolated D_x chain as a reactant in the synthesis of the DbfA diblock. The lengths of fA moiety in the diblocks were substantially shorter than those of D moiety, and estimates of their lengths were determined by methods that will be later presented. The chemical structures of each of these polymers are shown in **Table 1-2** along with their molecular weights and names. The polymer pCVPPV ($n = 7.7$) was designed to function as a wide bandgap polymer. Relative to MEH-PPV, the HOMO and LUMO levels of pCVPPV are offset to suggest a favorable conversion of $pCVPPV^* \rightarrow pCVPPV^{\bullet+} + MEH-PPV^{\bullet-}$ or $MEH-PPV^* \rightarrow pCVPPV^{\bullet+} + MEH-PPV^{\bullet-}$ [37].

1.3.2 pDPP2FT and PDI

The pDPP2FT and PDI based materials were all synthesized in the research group of Dr.

Craig Hawker at UC Santa Barbara by former member Dr. Max Robb. The chemical structures and short names of these materials are provided in **Table 1-3**.

Table 1-3 Chemical Structures of pDPP2FT and PDI based materials

Polymer	Chemical Structure	Collaborator
pDPP2FT		Dr. Max Robb
PDI-phenyl		Dr. Max Robb
PDI-hexyls		Dr. Max Robb
pDPP2FT _x PDI		Dr. Max Robb

One of the major efforts currently in the field of organic photovoltaics research is the development of low bandgap polymers that have broad absorption spectra which function as donor materials relative to commonly used acceptors such as PCBM [38-41]. Typical semiconducting polymers have bandgaps greater than 2 eV and can only harvest about 30% of the solar sunlight [42]. Lowering the bandgap is necessary to acquire better overlap with the

solar spectrum. The most common strategy towards developing a low bandgap polymer is through a D-A copolymer whose repeat units consist of alternating donor-acceptor moieties. Orbital mixing of the donor and acceptor lead to a lowered effective band gap as illustrated in **Figure 1-2**.

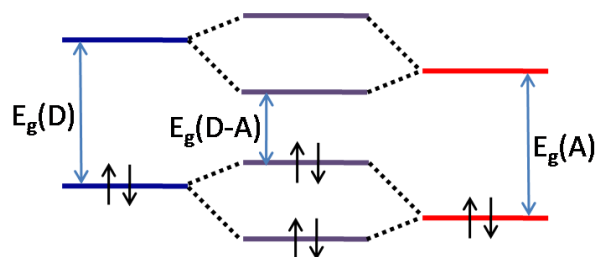


Figure 1-2 Orbital mixing of a strongly coupled donor and acceptor in a D-A copolymer lead to a lowered band gap.

The pDPP2FT polymer is a D-A copolymer for which the thiophene and furan units collectively behave as an electron donor and the diketopyrrolopyrole (DPP) unit behaves as an electron acceptor.

A survey of recent literature involving high performance polymer photovoltaics reveals that the majority utilize polymers which contain thiophene or thiophene-based heterocycles [40, 43]. This might suggest that a D-A copolymer using thiophene or thiophene-based heterocycles as donor might also provide ideal performance. Such a D-A copolymer, pDPP3T with a repeat unit structure consisting of 3 thiophene units and 1 DPP unit was synthesized [44]. However the success of this synthesis and the solubility of the polymer were found to require very long side chains. As an alternative to the thiophenes in pDPP3T, furans were explored due to their similarity in energy levels and comparable degree of aromaticity [45]. Replacing all of the thiophenes with furan to produce pDPP3F was found to significantly enhance solubility requiring shorter side chains without hindering the photovoltaic device performance. However the solubility was optimized in pDPP2FT using 2 furans and 1 thiophene as donor in conjunction with the DPP acceptor, suggesting that the ratio of furan to thiophene also impacts solubility. The nature and mobility of excess charges on isolated chains of D-A copolymers have not been well studied and was of interest here.

1.4 Other materials

Other materials were used in experimental studies presented herein. The solvents 1,2-Dichloroethane (Aldrich, HPLC grade), and benzene (Mallinckrodt, AR grade) were used as received. The compounds anthracene, fluoranthene, 9,10-dimethylanthracene, perylene, pyrene were obtained from Aldrich used as received. Biphenyl (Aldrich) was recrystallized three times from ethanol.

1.5 Outline of Thesis

In Chapter 2, a theoretical framework for the electronic structure of conjugated polymers is presented. The nature of charged and excited states of conjugated polymers were outlined within the context of electrochemical and photophysical properties. Charge transfer theory and charge transport models are provided, followed by an emphasis on the fundamental challenges of exciton dissociation and efficient charge transport in polymer photovoltaics.

In Chapter 3, descriptions of the experimental techniques used are provided – including steady state absorption and emission spectroscopies, cyclic voltammetry, photoexcited picosecond transient absorption spectroscopy, and especially radiolysis. The strengths of radiolysis for unambiguous formation and identification of radical ions and triplets are elucidated and the description of the radiolysis instrument of the Laser-electron accelerator facility (LEAF) and its unique strengths highlighted.

In Chapter 4 the methodology for acquiring unambiguous optical signatures of radical ions and triplets are detailed, and optical signatures presented. Kinetics of formation and decay are also evaluated with respect to the known radiation chemistries of the solvents and the theoretical diffusion controlled rate constants. Optical signatures are evaluated with respect to theoretical predictions according to the FBC model.

In Chapter 5, the methodology used for determining extinction coefficients and energetics of compounds via radiolysis are detailed. Energetics of redox states are determined via radiolysis and compared with results obtained via electrochemistry, and relations between the

two are drawn. The nature of multiple electron reduction in MEH-PPV is explored and potentials at various redox states determined.

In Chapter 6, electron transfer and energy transfer reactions at type-II heterojunctions in solution are investigated. The fate of excitons and excess electrons in DBfA polymers are examined with respect to bridge length dependence and donor length dependence. The fate of triplet excitons at the interface of pCVPPV/MEHPPV formed by bimolecular collision in solution, are also evaluated.

In Chapter 7, photophysical and electronic properties of pDPP2FT are explored and a lower limit for electron mobility determined. Limitations of the electron mobility measurements due to irreversible radiolytic degradation of p_x PDI chains are discussed and the effects of such degradation quantified and used to support an upper limit for chain to end cap transport on p_{16} PDI chains. Optical transitions corresponding to various redox states are explored and compared with the transitions expected by theory.

In Chapter 8 a conclusion of the pertinent findings and applications are discussed.

Chapter 2: Theoretical Framework

2.1 Electronic structure of conjugated polymers

The electrical and optical properties of organic molecules and polymers are determined by the chemical bonds between carbons. The electron configuration of carbon in the ground state is $1s^2 2s^2 2p^2$. The atomic orbitals of carbons in a molecule interact to form molecular orbitals. Specifically, the electrons in the outer orbitals of carbon, $2s^2 2p^2$, can mix in different ways to produce different hybrid orbitals, leading to a multiplicity of carbon dimer structure.

In a carbon dimer a strong σ -bond is formed by the overlap of two hybrid orbitals, and is located along the internuclear axis. If the σ -bond is formed by two sp^3 -orbitals, the dimer is sp^3 -hybridized and only contains σ -bonds. This dimer is called ethane and contains no relevant electronic properties. If the σ -bond is formed by two sp^2 -orbitals, the dimer is sp^2 -hybridized. An sp^2 -hybridized dimer has two additional sp^2 -orbitals which extend from each carbon, coplanar with the σ -bond at $+120$ and -120 degrees relative to it, and contains two p_z -orbitals oriented perpendicular to the plane of the sp^2 orbitals. This dimer is called ethene and is represented in **Figure 2-1**. The p_z -orbitals of ethene overlap to form a delocalized antibonding π^* -orbital and bonding π -orbital. Due to the weak overlap of the p_z -orbitals, π -bonds are naturally much weaker than the strongly overlapping σ -bonds.

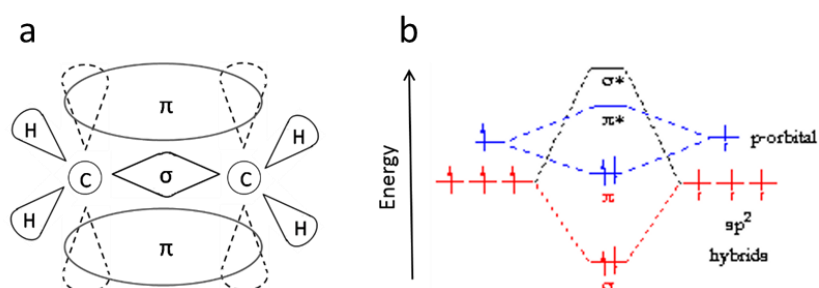


Figure 2-1: (a) An illustration of σ and π -bond formation in the sp^2 hybridized dimer, ethene. The p_z orbitals (shown dashed) interact to generate π -orbitals. (b) A molecular orbital diagram of ethene.

The energy splitting between corresponding bonding and antibonding orbitals increases with increased orbital overlap. Hence, as shown in **Figure 2-1(b)**, the π - π^* transition is significantly lower in energy than the σ - σ^* transition, indicating that the π -bonds are much easier to break than the σ -bonds which form the rigid backbone for the conjugated molecule. If ethene is treated as a repeat unit monomer in a larger chemical structure consisting of n such monomers, further splitting of degeneracies occur as n grows leading to the formation of a band of antibonding orbitals and a band of bonding orbitals. A carbon-based macromolecule with a repeat unit structure of 10 monomers or more can be considered an organic polymer. The polymer comprised of the monomer ethene is called polyacetylene (PA), and was previously shown in **Figure 1-1**. The electronic energy diagrams for two non-interacting carbon atoms, ethene, and polyacetylene are shown in **Figure 2-2**. The energy gap between the HOMO and LUMO levels was previously defined as the electronic bandgap or energy gap, E_g . The difference in the energy range of an energy band is defined as the bandwidth (BW). In **Figure 2-2**, the electronic bandgap and the bandwidth of the band of bonding orbitals are represented in relation to the polymer band structure.

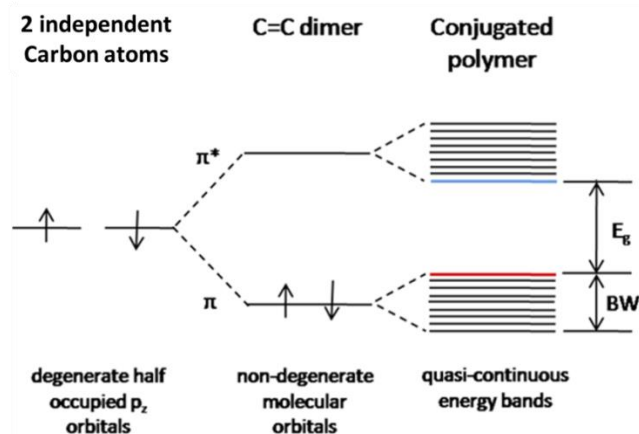


Figure 2-2 Electronic energy diagrams are shown for two isolated carbon atoms, an ethene molecule, and polyacetylene. The bandwidth (BW) associated with the spread of energies of degenerate bonding orbitals, and the electronic bandgap (E_g) are represented.

The magnitude of the bandwidth is proportional to electronic coupling. The tightly bound atoms in the crystalline lattice of an inorganic solid lead to strong electronic coupling in three

dimensions. The electronic interactions of covalently bonded monomers within an isolated polymer chain are one dimensional and less strong than in inorganic crystalline solids, but nonetheless stronger than the non-covalent interaction between segments of two neighboring polymer chains in a bulk solid. This results in an intramolecular bandwidth and an intermolecular bandwidth for conjugated polymers in the solid state, with the latter being smaller often by an order of magnitude [46]. The intermolecular bandwidth is often comparable to the energetic spread induced by disorder.

The conjugation length, defined as the average spatial extent of uninterrupted π -conjugation, increases as the chain length grows, up to some limiting length. The band gap also reduces with increasing length. This corresponds with the expected changes in energy associated with the quantum mechanical “particle in a box” description, in which the energies of eigenstates are inversely proportional to the square of the box length. In real conjugated polymer chains, the conjugation length can be limited by the presence of external impurities such as H, Cl, O, or F atoms which eliminate the double bond, or intrinsic defects such as kinks and torsional conformations. As such, a polymer chain may be viewed as an assembly of conjugated segments, or oligomers with different conjugation lengths, the average of which determines the band gap. The random variation in segment lengths is a major source of energetic disorder which leads to inhomogeneous broadening of the absorption spectrum. Conjugation lengths for polymers have been predicted by fitting the chain length dependence of optical bandgaps for corresponding oligomers by the empirical expression [47]:

$$E(n) = E_{\infty} + (E_1 - E_{\infty})\exp[-a(n - 1)] \quad 2-1$$

where E_1 and E_{∞} are the bandgaps of the monomer and infinitely long polymer, n , the number of repeat units, and a , a parameter that describes how rapidly $E(n)$ converges towards E_{∞} .

It is interesting to consider how the band structure of polyacetylene would evolve if the carbon atoms were equally spaced due to equal bond lengths. In this case, a single carbon atom would serve as the repeat unit for the structure of the polymer and would result in a half-filled band which would then function as a conductor rather than as a semiconductor. However, in 1955 Peierls postulated that the symmetry required for of a 1-D metal in the

ground state is not energetically stable and that broken symmetry is preferred [48]. As a result, the alternating single and double bonds (i.e. long and short bonds) is more energetically favorable for t-PA. This doubles the size of the unit cell and results in formation of an energy gap which makes the polymer a semiconductor.

Changing the bond alternation of single and double bonds (exchanging single bonds with double bonds and vice versa) for t-PA does not change the ground state energy, and the polymer is therefore considered degenerate. For most polymers, such as polyphenylenevinylene (PPV), the two possible bond alternation resonance forms are not energetically equivalent, and these polymers are therefore nondegenerate. The aromatic geometry is always of lower energy than the quinoid geometry. The two bond alternation structures for PPV – benzoid and quinoid - are shown in **Figure 2-3**.

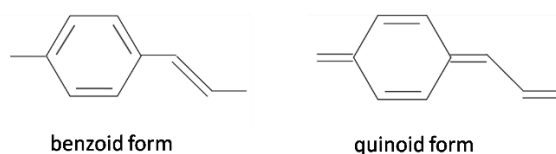


Figure 2-3 Benzoid and Quinoid structural forms of phenylenevinylene

2.2 Radical ions

The addition of an electron to the LUMO or removal of an electron from the HOMO of a nondegenerate conjugated polymer initially in the neutral state, P^0 , results in the formation of a radical anion, $P^{\bullet-}$, or radical cation, $P^{\bullet+}$, respectively. The energy released from P^0 to vacuum due to addition of an excess electron to is regarded as the electron affinity (EA) and the energy required to remove an electron from P^0 to vacuum is regarded as the ionization potential (IP). Radical ions of oligomers and polymers have been found to induce changes in the local bond lengths, which deform the one-dimensional lattice of a polymer chain. The charge and accompanying lattice deformation function as a unit described as a polaron with spin of $\frac{1}{2}$ – a negative polaron in the case of a polymer radical anion and a positive polaron in

case of a polymer radical cation. The electronic structure of polymeric charged states are qualitatively predicted by a model presented by Fesser, Bishop and Campell (FBC model) which considers single electron-phonon coupling [49]. According to the FBC model, the addition of a charge and the subsequent lattice distortion, result in a binding energy for the polaron, ϵ_p , and lead to formation of two new localized energy levels that lie within the gap between the HOMO and LUMO of the neutral polymer. The binding energies for a negative and positive polaron can be treated as equivalent which is generally a reasonable approximation. If the potential of a polymer radical anion is represented as $E^0(P^{\bullet-})$ and is equivalently represented as the reduction potential of the polymer neutral, $E_{red}(P)$, then these potentials can be defined by **Eq 2-2** as:

$$E^0(P^{\bullet-}) = E_{red}(P) = LUMO - \epsilon_p \quad 2-2$$

Similarly, if the potential of a polymer radical cation is represented as $E^0(P^{\bullet+})$ or equivalently as the oxidation potential of the polymer neutral, $E_{ox}(P)$, then these potentials can be defined by **Eq 2-3** as:

$$E^0(P^{\bullet+}) = E_{ox}(P) = HOMO + \epsilon_p \quad 2-3$$

The potentials $E^0(P^{\bullet-})$ and $E^0(P^{\bullet+})$ are believed to correspond with the insertion energies for a single electron and single hole, respectively, during an electrochemical experiment [50]. The difference in energy between $E^0(P^{\bullet-})$ and $E^0(P^{\bullet+})$ is defined as the single particle [50] energy gap, $E_{g,s}$ which is then defined as:

$$E_{g,s} = E^0(P^{\bullet-}) - E^0(P^{\bullet+}) = E_g - 2\epsilon_p \quad 2-4$$

The wavefunction of a polaron is localized over a finite length of the nondegenerate polymer chain and induces a change in the bond alternation from aromatic to quinoid over this segment. The length of this segment is referred to as the delocalization length of the charge, or polaron length. In the event that two charges of like kind are added to a nondegenerate polymer chain, there is a possibility for the charges to interact and form a spinless bipolaron - a negative bipolaron consisting of two electrons or positive bipolaron consisting of two holes. Bipolarons according to the FBC model also induce two new energy levels that are localized within the gap, and even deeper relative to the polarons. The spin configurations and optical

transitions are shown in **Figure 2-4** for the various charged states: (a) negative polaron, (b) positive polaron, (c) negative bipolaron, and (d) positive bipolaron.

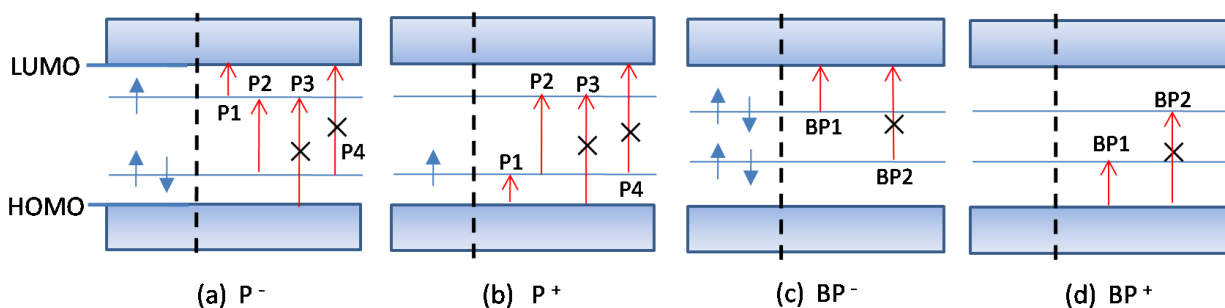


Figure 2-4 The spin configurations (left of dashed line) and optical transitions (right of dashed line) associated with charged excitations of a nondegenerate conjugated polymer are shown: **(a)** negative polaron, **(b)** positive polaron, **(c)** negative bipolaron, and **(d)** positive bipolaron.

Following the original work of Fesser and coworkers, there was confusion regarding the number of optical transitions expected for the charged states based on discrepancies between theoretical predictions and experimental observations. Upon careful quantum chemical calculations for well-controlled oligomers it was determined that P3, P4, and BP2 transitions are forbidden due to alternating symmetry of the molecular orbitals [51]. It has also been debated vigorously whether the polaron or bipolaron is most energetically stable [52-57]. Some studies have suggested that whether bipolaron formation is preferred depends strongly on the combination of chain length and density of charges. For example, if the chain length is short, as charge density is continuously increased along the chain, bipolarons may eventually become more stable than polarons due to less energy being required to form a single lattice defect for two charges. However, for a chain containing bipolarons, as length is extended Coulomb repulsion may become the dominant factor, thereby favoring dissociation of bipolarons into polarons.

2.3 Excitons

A photon with sufficient energy can be absorbed by a ground state neutral conjugated polymer, promoting an electron from the HOMO to a higher energy orbital, leaving a hole

behind. The electron and hole pair to form an exciton with a binding energy, E_b , resulting from the coulombic potential between the charges. Excitons are therefore electrically neutral. The magnitude of the binding energy is related to the relative dielectric constant ϵ_r of the semiconducting material by:

$$|E_B| = \frac{|q_1 q_2|}{4\pi\epsilon_r\epsilon_0 r_c} \quad 2-5$$

where q_1 and q_2 are the charge value of the charge carriers, ϵ_0 is the permittivity of free space, and r_c is the critical distance between both charge carriers. The critical distance indicates the difference in the spatial extension of the electron-hole pair in the bound state. In inorganic semiconductors, this binding energy is generally smaller than thermal energy, $k_B T$ at room temperature, where k_B is Boltzmann's constant and T is the temperature in Kelvin.

If the electron in the higher energy level is of antiparallel spin relative to the remaining electron in the ground state, the exciton has a total spin of zero and is called a singlet. If the electron in the higher energy level is of same spin, the total spin value of the exciton is one, and the exciton is called a triplet. The spin configurations of each are shown in **Figure 2-5**. The binding energy of a triplet is higher than that of a singlet due to the attractive exchange interaction resulting from same spin orientation between the excited and ground state electrons.

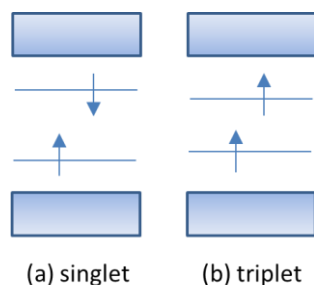


Figure 2-5. Illustration of spin configurations for singlet (left) and triplet (right) excitons, and the introduction of new energy levels in the forbidden gap associated with their polaronic natures.

To distinguish singlet and triplet energy levels by nomenclature, these levels are labeled as S_n and T_n respectively, where n indicates the order of the energy level. The ground state ($n = 0$) configuration for an aromatic molecule is always singlet in nature, and is labeled S_0 .

An exciton can separate to yield freed charge carriers by gaining energy in excess of the binding energy. If not separated, the exciton will release its potential energy by returning to the ground state via recombination of the charges to emit a photon, or through a radiationless path via loss of energy to phonons. In silicon and GaAs, the singlet exciton binding energies are 15 meV and 4 meV respectively [58]. Therefore excitons in inorganic semiconductors rapidly yield unbounded electrons and holes with efficiencies approaching unity. In organic semiconductors, the binding energies however are much stronger.

In an organic semiconductor, separation of the excitonic state results in formation of a negative polaron and positive polaron. The energy difference of these states was previously defined as the single particle energy state, $E_{g,s}$. The creation energy of the relaxed, lowest lying singlet excited state is then defined as E_{S_1} equivalent to the single particle energy gap, $E_{g,s}$, minus the binding energy, E_b :

$$E_{S_1} = E_{g,s} - E_b \quad 2-6$$

An exciton can be formed by absorption of a photon with minimum energy equivalent to E_{S_1} and a photon with energy in excess of this will ultimately relax to this energy. The magnitudes of the S_1 , T_1 , $E_{g,s}$ and $LUMO$ states of a conjugated polymer are shown on a comparative energy scale in **Figure 2-6**. The magnitudes of the ionization potential and electron affinity relative to vacuum are shown as well.

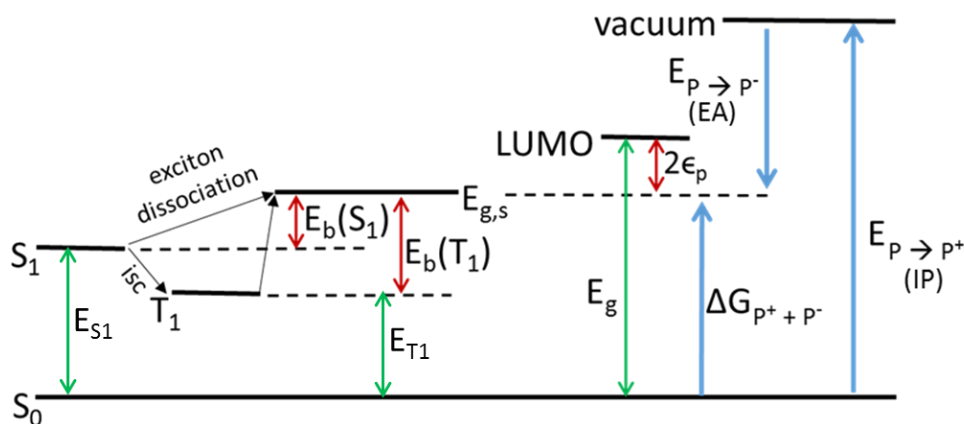


Figure 2-6 Comparative energy scale illustrating energetics of a conjugated polymer in the neutral state, charged state, and neutral excited state. (Figure adapted from [59]).

Photoexcitations from the ground state, S_0 , can only lead to the formation of singlet excited states, S_n . This is due to the fact that electron spin is an angular momentum that must be conserved but photons carry no torque and therefore do not strongly couple to electronic spin. Photoexcitation results in a redistribution of electronic configurations which shifts the equilibrium distance of the potential. The nuclear mass being much larger than the electronic mass results in far slower motion of the nuclei than the electrons such that electronic transitions can be approximated as occurring without changes in nuclei position according to the Born-Oppenheimer approximation. As a result, the electronic transitions are completed before the molecule reaches the vibrational ground state of the new electronic state. The electrons can therefore be excited to upper vibronic states.

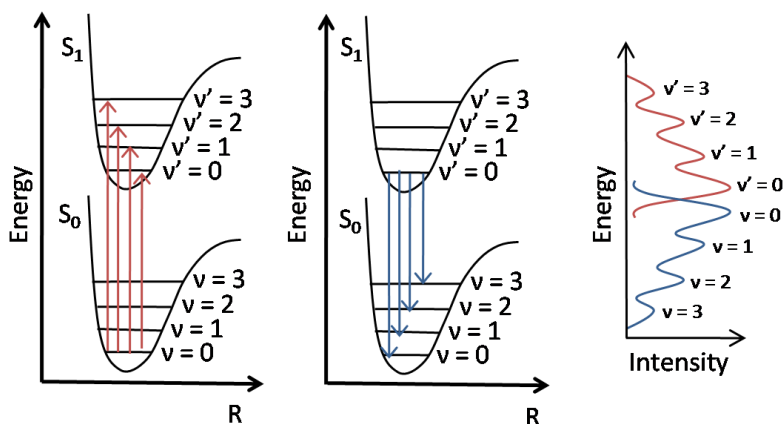


Figure 2-7 Configuration coordinate diagram of potential energy curves with vibration levels showing the relationship of optical transitions to the resulting absorption and emission spectra.

Figure 2-7 illustrates the optical transitions between the ground and first excited singlet states of a molecule, represented as potential energy curves as a function of internuclear distance. Absorption occurs from the lowest vibrational state of the ground state to vibrational levels of the excited state. The corresponding absorption spectrum can be visualized as a superposition of the excitations into all of the vibrational levels of the excited state, with a coefficient associated with each transition. The intensity of an electronic transition between two states is determined by the transition probability which is determined by the overlap of the wave functions in the initial and final states. An electron excited to a higher vibrational level of

the first excited state will relax to the lowest vibrational energy within the state via internal conversion on a time scale of $\sim 10^{-13}$. From this lowest vibrational level, the electron can transition to a vibrational level of the ground state, either by emission of a photon (fluorescence) or decay via a radiationless channel. The emission spectrum is typically mirror-symmetric to the absorption spectrum, with a red-shift in peak known as the Stokes shift. Red shift between the absorption and emission spectra can also result from energy transfer from higher energy sites to lower energy sites (Förster transfer).

The extent of delocalization for singlet excitons can be inferred by the number of monomers for which absorption and emission peaks no longer depend on oligomer size. Observations of red shifting of the absorption and emission peaks with respect to increasing lengths of oligomers suggest that the conjugation length has not yet been reached. This type of red-shifting has been demonstrated for a series of oligomeric phenylenevinyles ranging from 1 to 7 monomer units, indicating that singlets delocalize over the entire molecule in each case [60]. Similar to polarons, excitons induce a quinoid character over the region of their delocalization. In **Figure 2-8** chemical structures of PPV are shown in the neutral ground state and in the charged and neutral excited states.

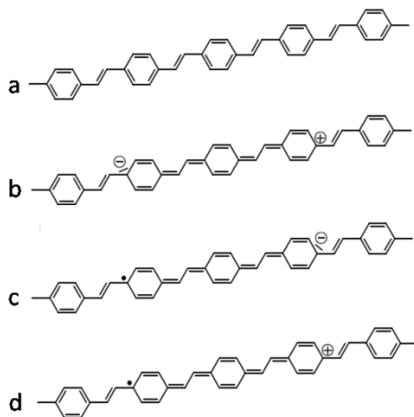


Figure 2-8 Chemical structure of PPV in ground state (**a**), in neutral excited state (**b**), in negative polaron state (**c**), and positive polaron state (**d**).

A more complete picture of the photophysical processes of an organic molecule are provided by a Jablonski diagram as shown in **Figure 2-9**, which includes triplet excited states. Triplet excitons exhibit very different properties than singlets. The triplet is much more

localized than the singlet. Experiments have shown that the triplet in PPV barely extends over a single monomer unit [61]. As mentioned, triplet excitons cannot be directly formed by photoexcitation. Hence, spin-orbit coupling and electron-phonon interactions are required for transitions between singlet and triplet states. These transitions are known as intersystem crossing. Radiative decay of a triplet excited state via Intersystem crossing to the ground state single, is called phosphorescence. Due to being spin forbidden, the timescale of phosphorescence lifetimes are much longer (μs to ms) than fluorescence (ns). Spin-orbit coupling is generally inefficient for relatively light atoms such as carbon, hydrogen, nitrogen, oxygen and sulfur and therefore intersystem crossing is largely inefficient in organic materials.

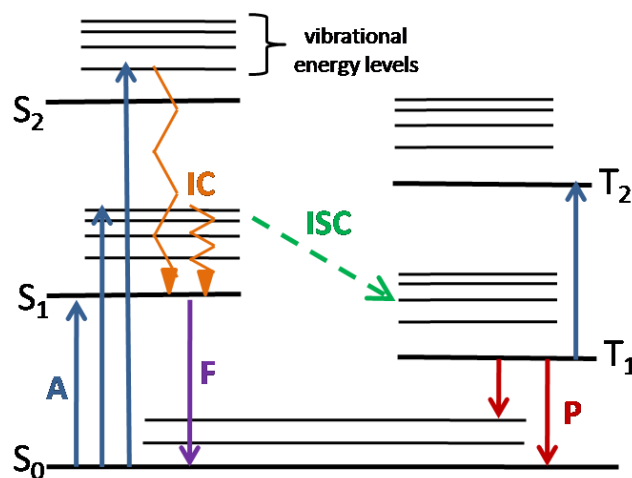


Figure 2-9 Jablonski diagram indicating various photophysical processes: A=absorption, F=fluorescence, IC = internal conversion, ISC = intersystem crossing and P = phosphorescence.

When radiative and non-radiative deactivation pathways exist for excitons of the 1st excited singlet state, the excitonic lifetime will depend on both the radiative decay rate (k_r) and the non-radiative decay (k_{nr}). The observed lifetime of the excitonic state is then defined by:

$$\tau_{fl} = (k_r + k_{nr})^{-1} \quad 2-7$$

Processes which decrease the fluorescence intensity are referred to as quenching, and result from reaction of a quencher, Q, and the fluorophore. Dynamic quenching is collisional and reduces the apparent fluorescent lifetime, while static quenching results in formation of a non-fluorescent ground state complex which reduces the apparent concentration of the fluorophore. Collisional quenching may involve either exciton dissociation or energy transfer

(Dexter energy transfer). In addition to dynamic and static quenching, at-distance quenching may also occur via fluorescence resonance energy transfer (FRET). The excitonic lifetime, $\tau_{fl'}$, in the presence of the additional deactivation pathway Q corresponds to a quenching rate, k_Q , defined as:

$$\tau_{fl'} = (k_r + k_{nr} + k_Q)^{-1} \quad 2-8$$

In the absence of all non-radiative deactivation pathways, the excitonic lifetime is referred to as the radiative lifetime, τ_r , and is dependent only on the rate of radiative decay, k_r as:

$$\tau_r = (k_r)^{-1} \quad 2-9$$

The fraction of photoexcitations which fluoresce is defined as the fluorescence quantum yield, ϕ_{fl} , and is defined as:

$$\phi_{fl} = \frac{\tau_{fl}}{\tau_r} = \frac{k_r}{k_r + k_{nr}} \quad 2-10$$

The fraction of photoexcitations which fluoresce in the presence of Q is then defined as:

$$\phi_{fl'} = \frac{k_r}{k_r + k_{nr} + k_Q} \quad 2-11$$

The rate of charge separation, k_Q , of the exciton in this case can be defined in terms of the new lifetime, $\tau_{fl'}$ as:

$$k_Q = 1/\tau_{fl'} - 1/\tau_{fl} \quad 2-12$$

2.4 Bimolecular charge & energy transfer reactions

2.4.1 Conditions for charge and energy transfer

Favorable conditions for electron transfer can be defined based on the energetic offset (ΔE) between a state of an electron donor (D), and a state of an electron acceptor (A). The energetics of these states are quantified in relation to vacuum in terms of: ionization potential (IP), electron affinity (EA), ionization potential of excited state (IP_D^*), electron affinity of

excited state (EA_A^*) and the electronic energy of an excited state, (E^{00}). Favorable conditions for electron transfer can then be described as:

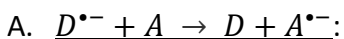
- from a reduced ground state donor, to a neutral ground state acceptor ($D^{\bullet-} + A \rightarrow D + A^{\bullet-}$) such that EA_A exceeds EA_D , and $\Delta E = EA_D - EA_A$.
- from a neutral ground state donor to oxidized ground state acceptor ($D + A^{\bullet+} \rightarrow A + D^{\bullet+}$) such that IP_A exceeds IP_D , and $\Delta E = IP_D - IP_A$.
- From a neutral excited donor to a neutral ground state acceptor ($D^* + A \rightarrow D^{\bullet-} + A^{\bullet+}$) such that EA_A exceeds IP_D^* , and $\Delta E = IP_D^* - EA_A = IP_D - EA_A - E_D^{00}$.
- From a neutral ground state donor to a neutral excited state acceptor ($D + A^* \rightarrow D^{\bullet-} + A^{\bullet+}$) such that EA_A^* exceeds IP_D , and $\Delta E = IP_D - EA_A^* = IP_D - EA_A - E_A^{00}$.

In solution, a solvation energy, ΔG_{solv} is acquired relative to vacuum. For a molecule m , a linear relationship can then be defined for the reduction potential of the molecule in solution, $E_{red}(m)$, and EA_m in vacuum. Similarly, a linearly relationship can also be defined for the oxidation potential $E_{ox}(m)$ in solution, and IP_m in vacuum. These relationships are shown in **Eq 2-13** and **Eq 2-14** :

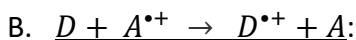
$$EA_m = E_{red}(m) + \Delta G_{solv}(m^-) \quad 2-13$$

$$IP_m = E_{ox}(m) + \Delta G_{solv}(m^+) \quad 2-14$$

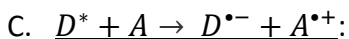
The free energy difference or “driving force”, ΔG , for an electron transfer in solution can then be defined according to the initial and final states as described below:



$$\Delta G = E_{red}(D) - E_{red}(A) \quad 2-15$$



$$\Delta G = E_{ox}(D) - E_{ox}(A) \quad 2-16$$

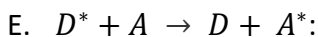


$$\Delta G = E_{ox}(D) - E_{red}(A) - E_D^{00} + w_P - w_R \quad 2-17$$



$$\Delta G = E_{ox}(D) - E_{red}(A) - E_A^{00} + w_P - w_R \quad 2-18$$

In the event of a favorable energy transfer reaction, the energy content of the excited energy donor, $E(D^*)$, is larger than the energy content of an excited energy acceptor, $E(A^*)$ and correspond to Reaction “E” below:



$$\Delta G = E(D^*) - E(A^*) \quad 2-19$$

By replacing E_D^{00} in **Eq 2-17** or E_A^{00} **Eq 2-18** with the term E^{00} to generalize the description of an excited state reactant – either donor or acceptor, an expression for the Rehm-Weller equation is obtained. The terms w_P and w_R in the Rehm-Weller equation are work terms associated with the electrostatic interactions in the product states and reactant states, respectively. The reactants of both reactions “C” and “D” above contain no electrostatic potential, and therefore, $w_R = 0$. The product states, with ions of opposite charge, solvent separated by d_{DA} will have an electrostatic potential defined by:

$$w_P = e^2/d_{DA}\epsilon_s \quad 2-20$$

The terms ϵ_s and e of and **Eq 2-20** refer to the dielectric constant of the solvent, and charge of an electron, respectively.

2.4.2 Diffusion controlled reactions

The rates of reactions can provide information about the energetics of the reactants and products as observed for reactions involving equilibria as highlighted above. Collision theory defines the rate constant for a bimolecular reaction, k_{bi} as:

$$k_{bi} = k_{diff}(t) \exp\left(-\frac{E_a}{RT}\right) \quad 2-21$$

where $k_{diff}(t)$ is the rate constant for a bimolecular, diffusion-controlled reaction, R is the gas constant, E_a is the activation energy, and T is the temperature in Kelvin. Diffusion-controlled reactions have no energy of activation, ($E_a = 0$) such that $k_{bi} = k_{diff}(t)$ and therefore occur on each encounter of the reacting species, without regard to specific reactivities. The rate

constant for a bimolecular, diffusion-controlled reaction is determined by the simplified form of the Smoluchowski equation:

$$k_{diff}(t) = 4\pi R_{eff} D N_A (1 + R_{eff}/(\pi D t))^{1/2} \quad 2-22$$

This equation gives the diffusion controlled rate constant, $k_{diff}(t)$, in terms of the effective reaction radius, R_{eff} , Avogadro's number, N_A , and the mutual diffusion coefficient, $D = D_A + D_B$, where D_A and D_B represent the diffusion coefficients of reactant A and reactant B . The "transient term" in Eq 2-22 indicates that $k_{diff}(t)$ is not strictly a constant, but decreases with $t^{-1/2}$ at short times. Nevertheless, in the infinite limit, $k_{diff}(\infty)$ can be approximated as a constant, k_{diff} which can be expressed as:

$$k_{diff} = 4\pi R_{eff} D N_A \quad 2-23$$

R_{eff} represents an average reaction distance, which for small molecules that can be approximated as spherical, can be taken as the sum of the physical radii of the reactants. Charge transfer and energy transfer reactions do not always require physical contact such that R_{eff} can be several angstroms larger than the physical sizes of the reactants at ordinary viscosities. For polymers, which are long chains that extend in one dimension when elongated, an effective radius is defined by the hydrodynamic radius, R_H which can be thought of as the radius associated with a spherical molecule with the equivalent diffusion coefficient as the polymer under observation. The hydrodynamic radius is defined in terms of its molecular weight, MW , volume, V , and density, ρ , by [62]:

$$R_H = \left[\frac{3(MW)}{4\pi N_A \rho} \right]^{1/3} \quad 2-24$$

In this work, radiolytic reactions are used to facilitate the capture of electrons, holes or triplets by aromatic compounds of interest. The time dependence suggests some fast capture may occur on very short timescales. For small molecules the transient term is significant only on the picosecond time scale, but can persist into the nanosecond time scale for large macromolecules such as polymers with large hydrodynamic radii. Another source of rapid electron and hole capture by polymers has been observed at even modest concentrations, and has been explained as capture by presolvated electrons and presolvated holes, respectively [63,

64]. Capture by presolvated species suggest that they may exhibit more extended wave functions, higher mobilities or excess kinetic energy in the first few picoseconds following their creation. Fast capture is considered to be capture that occurs on a time scale significantly faster than the time resolution of the detectors (e.g. < 2 ns). The general term “step capture” is used to describe all fast capture processes, regardless of specific mechanism.

The diffusion coefficient, D , is related to the effective radius, R_{eff} , and solvent viscosity, η , by the Stokes-Einstein equation:

$$D = k_B T / 6\pi\eta R_{eff} \quad 2-25$$

Debye derived a modification of the Smoluchowski equation in the infinite limit, which is not defined in terms of diffusion coefficient, but rather, in terms of the radii of the reacting species r_a and r_b , and the solvent viscosity, η . The Debye-Smoluchowski equation [65] is expressed as:

$$k_{diff} = (2RT/3000\eta)(2 + r_a/r_b + r_b/r_a) \quad 2-26$$

2.5 Electron transfer theory

From a kinetic point of view, electron transfer processes involving ground state molecules, as well as excited states, can be dealt with in the frame of the Marcus theory. In the case of electron transfer involving excited states, as was shown, the calculation of free energy change involves the redox potential of the excited state couple which is dependent on separation distance of the charges.

2.5.1 Classical theory

In the Marcus model, the potential energy curves of an electron transfer reaction for the reactant (R) and product (P) states of the system are represented by parabolic functions.

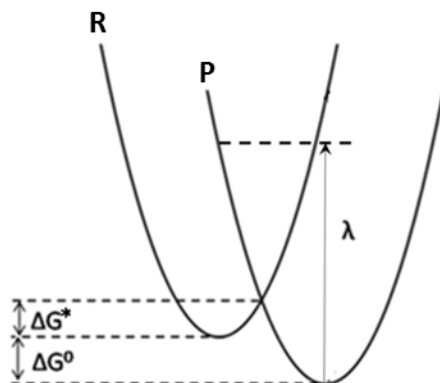


Figure 2-10 Profile of the potential energy curves of an electron transfer reaction: R and P indicate the reactant and product states of the system.

The rate limiting factors for electron transfer involve nuclear reorganization. The rate constant for electron transfer, k_{el} can be expressed as:

$$k_{el} = \nu_n \kappa_n \kappa_{el} \quad 2-27$$

where ν_n is the nuclear frequency, and κ_n and κ_{el} are the nuclear and electronic factors, respectively, which are probabilities that specific electronic or nuclear barriers can be overcome, and therefore are dimensionless constants with values between 0 and 1. For electron transfer from a reactant state to a product state, the initial nuclear geometry of the reactant state must undergo reorganization to the transition state prior to electron transfer. The reorganization energy, λ , is defined as the difference in potential energy between the reactant (product) state at its equilibrium geometry and the reactant (product) state at the equilibrium nuclear geometry of the product (reactant) state. The reorganization energy can be expressed as the sum of two components - an internal reorganization, λ_i and solvent reorganization energy, λ_s such that:

$$\lambda = \lambda_i + \lambda_s \quad 2-28$$

In electron transfer involving an excited state, the solvent reorganization energy is often the predominant term in the electron transfer process, and can be estimated as:

$$\lambda_s = e^2 \left(\frac{1}{r_D} + \frac{1}{r_A} - \frac{1}{d_{DA}} \right) \left(\frac{1}{n^2} - \frac{1}{\epsilon_s} \right) \quad 2-29$$

where e is the electronic charge, r_D and r_A are the radii of the reactants, d_{DA} is the separation distance of the donor and acceptor, n is the index of refraction, and ϵ_s is the dielectric constant of the solvent used. The energy of the transition state, ΔG^* , is gained by intermolecular collisions. At the transition state, electron transfer takes place rapidly, such that the nuclear geometry can be approximated as fixed as the much lighter electron is transferred (Franck-Condon principle). Based on the Marcus quadratic relationship, the transition state can be expressed in terms of the Gibbs free energy, ΔG^0 :

$$\Delta G^* = (\lambda + \Delta G^0)^2 / (4\lambda) \quad 2-30$$

The nuclear factor can be expressed in terms of ΔG^0 as:

$$\kappa_n = \exp(-\Delta G^* / RT) \quad 2-31$$

Substituting **Eq 2-31** into **Eq 2-27** k_{el} is then defined as:

$$k_{el} = \nu_n \kappa_{el} \exp(-\Delta G^* / RT) \quad 2-32$$

The combination of **Eq 2-30** and **Eq 2-32**, predict that for homogenous reactions for which λ and k_{el} are held constant, a bell shaped curve will result from a plot of $\ln k_{el}$ vs. ΔG^0 , as shown in **Figure 2-11**. This bell curve represents three regimes for which electron transfer processes can be distinguished:

1. The normal regime ($-\Delta G^0 < \lambda$)

The driving force is small and the electron transfer process is thermally activated, such that $\ln k_{el}$ increases with increasing driving force.

2. Activationless regime ($-\Delta G^0 \approx \lambda$)

The system is in the optimal region where electron transfer process is virtually barrierless. A change in the driving force does not cause significant changes in rate.

3. Inverted regime ($-\Delta G^0 > \lambda$)

This regime corresponds to strongly exergonic processes in which $\ln k_{el}$ decreases with increasing driving force.

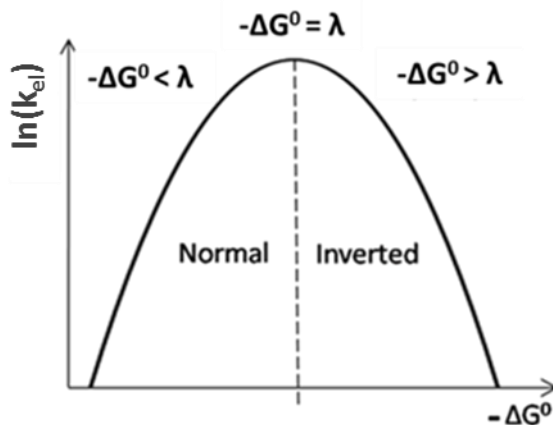


Figure 2-11 Three kinetic regimes are evident by plotting the natural log of the electron transfer rate, k_{el} , versus the driving force (ΔG^0) for electron transfer reaction: the normal region, the activationless regime, and the inverted regime.

2.5.2 Nonclassical theories

According to classical treatment described above, electron transfer occurs at a nuclear geometry midway between the reactant and product states. This treatment was formulated on the basic assumption that donor and acceptor orbitals overlap slightly at a separation distance of $\sim 7 \text{ \AA}$ within the encounter complex. There are however systems for which the distance of separation between donor and acceptor exceeds 7 \AA . In these systems, the electron transfer rate may be limited by electronic as well as nuclear barriers, such that electron transfer may occur via electron or nuclear tunneling through these energy barriers. A nonclassical treatment which emphasizes the overlap of electronic and nuclear wavefunctions in the reactant and product states is required for these systems, rather than the treatment emphasizing transition state as in the classical theory.

Two limiting conditions then can be defined for the mechanism of electron transfer in donor/acceptor systems based on the strength of electronic coupling, V_{DA} , which is related to the degree of orbital interactions between donor and acceptor. In the adiabatic limit, electronic interaction is strong, and therefore $\kappa_{el} \approx 1$. At the other extreme, where $\kappa_{el} = 0$, electron transfer occurs in the nonadiabatic limit, requiring tunneling of the electron through

an energy barrier separating the donor and acceptor. Electron transfer efficiency is illustrated in **Figure 2-12** for a series of potential curves representing reactant and product states of a donor/acceptor system, for which upward arrow represents an electron in the reactant state and a downward arrow represents an electron in the product state. A weakly adiabatic condition corresponds to $0 < \kappa_{el} \ll 1$.

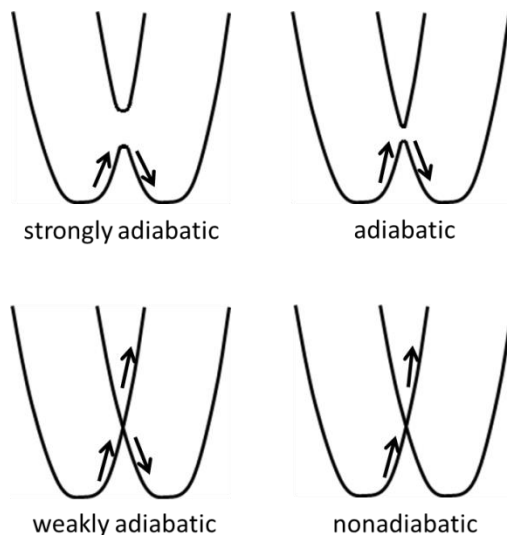


Figure 2-12 Potential energy curves of product and reactant states of donor/acceptor systems with different strengths of orbital interaction between donor and acceptor, ranging from the nonadiabatic regime to a strongly adiabatic regime. Arrows indicate the likelihood of electron transfer, with upward pointing arrows in the reactant state and downward arrows in the product state.

In the weakly adiabatic condition, the expression for the rate obtained within the Frank-Condon approximation factorizes into electronic and nuclear vibrational contribution, taking the form of the Fermi “Golden Rule”:

$$k_{el} = \frac{2\pi}{\hbar} |V_{DA}|^2 FCWD \quad 2-33$$

Here, $FCWD$ is the Franck-Condon weighted density of states. When all vibrational modes are classical, or in the high temperature limit ($h\nu \ll k_B T$), $FCWD$ can be of an Arrhenius form approximated as:

$$FCWD = \frac{1}{\sqrt{4\pi\lambda k_B T}} \exp\left[-\frac{(\Delta G^0 + \lambda)^2}{4\lambda k_B T}\right] \quad 2-34$$

When certain lattice vibrational modes of the product state are much stronger compared to the electron thermal energy ($h\nu \gg k_B T$) the transition rate constant is better represented by the Bixon and Jortner-modified Marcus equation for which *FCWD* is defined as:

$$FCWD = \sum_{n=0}^{\infty} \left\{ e^{-S_i} \frac{S_i^n}{n!} \exp \left[-\frac{(\Delta G^0 + \lambda_s + nh\nu_i)^2}{4\lambda_s T} \right] \right\}$$

Here the reorganization energy is divided into solvent contribution, λ_s , and a lattice vibrational mode, $\lambda_i = nh\nu_i$. The Huang-Rhys parameter, $S_i = nh\nu_i$, is a measure of the electron-phonon interaction.

For a donor and acceptor connected via an intervening bridge, electronic coupling is expected to be mediated both through the bonds of the bridge and through the medium. The resulting electronic coupling is a sum of the contributions of both mechanisms. Both mechanisms are typically attenuated by distance with a form:

$$V_{DA}(r) = V_0 \exp \left[-\frac{\beta}{2} (d_{DA} - d_0) \right] \quad 2-35$$

2.6 Charge Transport Description

The nature of charge propagation through molecular solids is central to the concept of organic electronics. Modeling conductivity in polymer bulk must account for: 1) charge transport along isolated chains, 2) charge transport between chains, and 3) transport across defects and chain ends. Whereas band transport describes well-ordered crystalline inorganic semiconductors, this and other models developed for inorganic semiconductors are generally inadequate for organic semiconductors. In this present work, charge transport considerations are restricted to migration along isolated chains.

In low doping conditions, charges can diffuse along a chain in the absence of a field, or drift under the influence of an applied field by hopping along with the lattice deformation. Defects occurring along a chain behave as barriers to transport, which can be surmounted. The average length bounded by such defects defines the conjugation length. A defect functions as a barrier

requiring a different activation energy than the lattice deformation to overcome. Therefore, transport along isolated chains may be considered coherent within a conjugation length, and require hopping between conjugated segments separated by a barrier [66, 67]. If the deformation energy is considered to be small compared to energetic and/or spatial disorder, the latter will determine the transport characteristics of an excess charge on a chain.

The varying degrees of disorder in many semiconducting materials are evident in the variety of models used to characterize the charge transport properties they exhibit. Three prominent models for charge transport are briefly discussed in the following sections: the band transport model, polaron transport model, and a hopping model. Each model accounts for certain physical and energetic properties of a material, such as bandwidth, polaron binding energy, and energetic and spatial disorder.

2.6.1 Band transport model

Charge transport in highly ordered inorganic crystalline semiconductors is ballistic in nature. Strong coupling between the atoms leads to large bandwidths which allow electrons promoted to the conduction band to move in highly delocalized states, and only scatter via lattice vibrations (phonons). The result is that mobility decreases with increasing temperature due to reduced mean free path of scattering. Band transport is then typified by an inverse relationship between temperature and mobility, and is feasible when the bandwidth exceeds energetic disorder.

In a molecular crystal, the coupling between molecules is defined by weak van der Waals forces or π - π interactions. This generally results in small bandwidths and a larger effective mass for charge carriers which lead to intrinsically lower mobilities and prevent band transport. Nevertheless, some examples of band-like transport in highly purified molecular single crystals have been reported in literature [68]. Conjugated polymers suffer from similarly weak intermolecular interactions leading to intermolecular bandwidths of about 0.1 eV [69]. However, due to covalent bonding within the chain, well ordered chains can have intramolecular bandwidths of 1 - 3 eV, which is smaller but more comparable to the ~ 5 eV

bandwidth of crystalline silicon. Nevertheless, the nature of phonon coupling, even if weak, will have a limiting effect on intramolecular mobility. Recently, the highest recorded mobility of $11.4 \text{ cm}^2/\text{Vs}$ was reported for a transistor using a D-A copolymer [70], which exhibited band-like transport within the high temperature regime (180 – 300 K). This mobility is still two orders of magnitude smaller than the $\sim 1500 \text{ cm}^2/\text{Vs}$ of crystalline silicon.

2.6.2 Polaron Transport Model

In the polaron-limited transport models, it is assumed that the energetic disorder energy is small compared to the lattice deformation energy. Polarons are considered to transfer from one molecular orbital to another. The activation energy for this process depends on the energy needed to overcome lattice deformation and counterion attraction if a counterion is present. The movement of a charge from one site to the next can be modeled by using the semi-classical Marcus theory. The transfer probability is proportional to the square of the overlap integral of the wave function of these orbitals. The polar models predict that the mobility is a product of a Boltzmann probability of energy coincidence and the probability that the carrier will hop between adjacent sites [71]. The most widely accepted model proposed by Emim, displays an energy dependence of the form:

$$\mu \propto \frac{\sinh(E/E_0)}{E/E_0} \quad 2-36$$

2.6.3 Variable Range Hopping Model

The Variable Range Hopping (VRH) model is a disorder model. Like other disorder models it assumes that polaronic effects are weak compared to energetic disorder. The VRH model is an extension of a disorder model presented by Miller and Abrahams which assumes that charge transport occurs via hopping between localized states. The model assumes that hopping to a higher energy site is assisted by thermal energy, while transitioning to a lower energy site is temperature independent. Between sites i and j , the hopping rate, energy difference, and distance are denoted v_{ij} , E_{ij} and r_{ij} , respectively. The hopping rate is then given by:

$$v_{ij} = v_0 \cdot e^{\frac{-E_{ij}}{k_B T}} \cdot e^{-2\alpha R_{ij}}, E_{ij} > 0 \quad 2-37$$

$$v_{ij} = v_0 \cdot e^{-2\alpha R_{ij}}, E_{ij} < 0 \quad 2-38$$

where v_0 is a phonon frequency factor and α^{-1} is the delocalization radius of a charge carrier. This model constrains the region of hopping to nearest neighbors with the term, $\exp(-2\alpha R_{ij})$. Mott later extended this model to instead constrain the hopping by the density of states at the Fermi level, which now accounted for the possibility of a charge carrier hopping over a large distance with a low activation energy or a small distance with a high activation energy. This extended model is known as the Variable Range Hopping model.

The mobility of a charge carrier using the VRH model is represented as:

$$\mu_{VRH} \propto \exp\left[-\left(\frac{T_0}{T}\right)^{1/n+1}\right] \quad 2-39$$

where T_0 is a parameter inversely proportional to the density of states at the Fermi level and n is the dimensionality of the system, with possible values of 1,2, or 3 for conjugated polymers.

2.7 Operation & challenges of polymer photovoltaics

In a photovoltaic, charge carrier generation begins with conversion of a photon into an exciton. In organic semiconductors, excitons are tightly bound and therefore have been found to most readily dissociate at a type II heterojunction between an electron donor (D) and electron acceptor (A). At the junction, dissociation of an exciton of either the donor (D^*) or the acceptor (A^*) results in the formation of two polaronic states, $D^{\bullet+}$ and $A^{\bullet-}$. This photoinduced electron transfer reaction produces an intermediate charge transfer (CT) state in which the charges are still Coulombically bound in a radical ion pair, $D^{\bullet+}/A^{\bullet-}$. The binding energy in this state is reduced due to extended spatial separation of the charges, and with sufficient energy may be overcome the coulombic potential to yield fully separated $D^{\bullet+}$ and $A^{\bullet-}$.

For photovoltaic applications, conversion of the CT state into separated charges is the most ideal transition from the CT state. Two other outcomes that lead to decay of the CT state are reverse charge transfer, and charge recombination leading to CT emission. The effectiveness of such a heterojunction at producing the CT state depends in great part on the energy offsets for the electron (hole) in the excitonic state and the energy offsets of the electron (hole) in the separated polaronic states. Although the electron and hole, both in the polaronic and excitonic states, occupy localized energy levels that are within the HOMO-LUMO bandgap, many schematics of type II heterojunctions erroneously misrepresent or approximate these energy levels as the HOMO and LUMO of the neutral polymer. A condition that energetically favors a fully charge separated state may be expressed as:

$$EA(A) - IP(D) - E_B < 0 \quad 2-40$$

where $IP(A)$ is the ionization potential of the acceptor, $EA(D)$ is the electron affinity of the donor, and E_B is the binding energy of the exciton. The probability of forming freed charge carriers will then be a product of the probability of forming a CT state and the subsequent probability of it yielding freed charges in a charge separated state. This probability therefore depends on the rate competition among the various reaction pathways for the exciton and CT state.

Once electrons and holes are freed from their binding energy, they must then be collected at electrodes – electrons at an anode and holes at a cathode. The efficient migration of these charges to their respective electrodes must be facilitated while avoiding recombination which would constitute a loss mechanism. In a solid state donor/acceptor system, the donor facilitates transport of holes, while the acceptor facilitates transport of electrons. The architecture of the donor and acceptor phases has tremendous consequence for device efficiencies. Below in **Figure 2-13**, three device architectures for organic photovoltaics are shown.

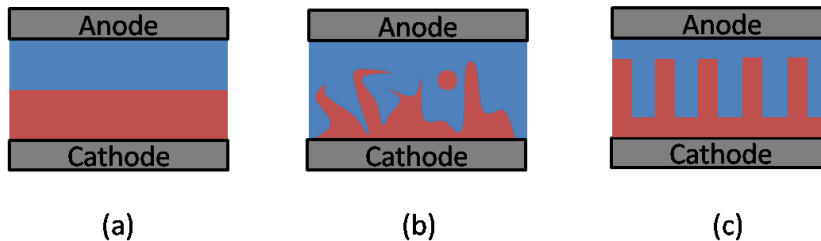


Figure 2-13 Three different device architecture types for organic photovoltaics (OPVs) for which the blue phase represents an electron donor and the red phase represents an electron acceptor: **(a)** bilayer heterojunction, **(b)** bulk heterojunction, and **(c)** interdigitated heterojunction.

In each case, the active semiconducting material consisting of a donor/acceptor system, is sandwiched by an anode and cathode. The anode (cathode) ideally has a work function comparable to the LUMO (HOMO) of the electron donor (acceptor) for efficient extraction of charges. The bilayer heterojunction device was one of the original device architectures and could be obtained by compressing two layers prepared on separate glass substrates. For such a device, increasing the active layer thickness of either the donor or acceptor up to the penetration depth of photons will have the effect of increasing the number of excitons generated, but will lead to a decline in the fraction of excitons reaching the D/A heterojunction as either layer is extended beyond the exciton diffusion length, defined as $L_{diff} = \sqrt{D\tau}$. The bulk heterojunction is the common state of the art approach to device fabrication, achieved by spincoating a blended solution of the donor and acceptor. The morphology is highly dependent on the blend ratio, solvent, and post fabrication treatment such as thermal annealing. With such a device structure, increasing the active layer thickness improves exciton yield with little effect on the fraction of excitons reaching a type II D/A heterojunction. It is possible however that pockets of either the donor or acceptor phase can be formed which are entirely bounded by the other phase rendering charges generated there as trapped and unable to reach the appropriate electrode. An ideal device architecture for polymer photovoltaics relies on an interdigitated donor/acceptor heterojunction in which the width of the donor and acceptor phases are less than or equal to the exciton diffusion length. Such a structure ensures efficient delivery of excitons to the D/A heterojunction for charge separation, eliminates the possibility of charge trapping regions, and facilitates efficient transport of the charges to their respective electrodes. A practical means for achieving such a structure has not yet been demonstrated.

The significant differences in efficiencies of charge carrier generation and charge transport between polymeric photovoltaics and inorganic photovoltaics, highlights unique differences in the semiconducting materials. The nature of conjugated polymers, which makes them amenable to facile and cheap fabrication techniques also renders them susceptible to disorder as isolated chains and as solid state bulk, unlike the ordered structure of crystalline inorganic semiconductors. Their physical description is complicated by multiple chromophores, poorly defined interfaces, and high defect content. As such, the physics of conjugated polymers differ significantly from those of inorganic semiconductor counterparts. Surprisingly, some of even the most fundamental physical properties of conjugated polymers are still strongly debated, even regarding the nature of photoexcitations and charge carriers. In the solid state, there is weak intermolecular coupling between chains which then gives rise to a strong 1-dimensional character of these species in contrast with the 3-dimensional character observed in inorganic semiconductors. The consequence of this is generally improved transport of excitons and charges along the backbone of a single conjugated polymer chain (i.e. intramolecular transport) relative to intermolecular pathways.

Chapter 3: Experimental Techniques

3.1 Absorption and Emission Spectroscopy

Steady state absorption spectroscopy was used as a tool for collecting optical signatures of the ground states as well as reduced and oxidized states of compounds investigated. Steady state absorbance measurements were collected using either an Agilent Cary 8454 UV-Vis Diode Array spectrophotometer (operating range of 190 nm – 1100 nm) or a Cary 5 UV-Vis-NIR spectrophotometer (operating range of 200 nm – 3200 nm). The diode array configuration of the Agilent permitted rapid acquisition of a full spectrum within a fraction of the time required by the Cary at similar signal to noise resolution. The tradeoff of acquisition time versus spectral range of detection is an important consideration for radical anions whose spectral bands may extend into the near IR. The accuracy of spectral measurements may be compromised if significant seepage of oxygen occurs during the timescale of measurement as may occur during an extended experiment involving redox titrations. The absorbance of a species at a given wavelength λ may be represented by the decrease in intensity of transmitted light $I(\lambda)$ at that wavelength relative to the intensity of incident light $I_0(\lambda)$ at that wavelength according to **Eq 3-1**.

$$Abs(\lambda) = -\log\left(\frac{I(\lambda)}{I_0(\lambda)}\right) \quad 3-1$$

Absorbance at a given wavelength can also be related to the optical property of molar extinction coefficient of a compound, ϵ_λ , through Beer Lambert's law as shown in **Eq 3-2**, given a concentration c of the compound, and a pathlength, l , of the cuvette.

$$Abs(\lambda) = \epsilon_\lambda cl \quad 3-2$$

Steady state emission spectroscopy measurements were also rendered using dilute solutions prepared with absorbances no greater than 0.1 at the wavelength of excitation. This restriction ensured that concentration dependent self-quenching was avoided. Beam slit

widths of 1 nm were used for both the excitation and emission, with emission measurements being collected at an angle of 90 degrees relative to the incident excitation. The PL quantum yield of fluorophore compounds were estimated relative to the PL quantum yield of known fluorophore standards. For the compound “x” of unknown quantum yield, the relative quantum yield ϕ_x , can be determined by comparison with the known quantum yield of a reference, ϕ_{ref} , by using **Eq 3-3** [72]:

$$\phi_x = \phi_{ref} \left(\frac{A_{ref}(\lambda_r)}{A_x(\lambda_x)} \right) \left(\frac{I_{ref}(\lambda_{ref})}{I_x(\lambda_x)} \right) \left(\frac{n_x^2}{n_{ref}^2} \right) \left(\frac{D_x}{D_{ref}} \right) \quad 3-3$$

Here $A(\lambda)$ is the absorbance/cm of the solution at λ , the wavelength of excitation, $I(\lambda)$ is the relative intensity of the exciting light, n is the average refractive index of the solution, and D is the integrated area under the corrected emission spectrum.

3.1.1 Preparation methods for spectrophotometric redox titrations

All absorbance measurements were made using quartz cuvettes of 0.5 cm or 0.1 cm pathlengths. These cuvettes were fused to long and hollowed pyrex stems, sometimes containing side arms attached to ~ 5 ml bulb cells for mixing of analyte and titrant. The pyrex stems contained threaded openings to be sealed by threaded Teflon stopcocks. The long stems served the dual purpose of providing handling ease intended to minimize direct contact with the cuvette, and extending the volume of solution allowable in a cell. For chemical redox titration experiments, perforated stopcocks lined with an external septum for insertion of a syringe needle were used, and careful steps were taken to prepare analyte and titrant solutions in an argon-saturated glovebox. The syringe-cuvette cells were then externally wrapped at the septum/syringe interface with parafilm to mitigate seepage of air into the solutions prior to bringing them outside of the glovebox.

Solutions prepared for chemical and radiolytic reductions, were often first prepared in 20 ml vials within the glovebox, and then transferred into the cuvette cells. In cases where added heating or sonication were needed to fully dissolve a solute, the solution vials were tightly

sealed with PTFE caps, and brought outside of the glovebox for sonication or heat treatment prior to readmission into the glovebox.

3.2 Photoinduced transient absorption spectroscopy

Photoinduced picosecond transient absorption spectroscopy was conducted at the Center for Function Nanomaterials (CFN) at Brookhaven National Lab using a commercial Ti:Sapphire laser system by SpectraPhysics. This system produced 800 nm pulses of 100 fs pulse widths at a repetition rate of 1 kHz. Excitation light was generated using a commercial optical parametric amplifier by LightConversion. By focusing the 800nm fundamental into a sapphire disc, broadband supercontinuum probe light was generated. The probe light was split into signal and reference beams, both of which were detected on a shot-by-shot basis with fibre-coupled silicon (visible) or InGaAs (infrared) diode arrays. The excitation light was used to generate a lowest lying singlet excited state, S_1 , which was then probed by the broadband light. The evolution of the optical density of the S_1 - S_n transition was monitored by the diode array detectors at varied delay times controlled by means of a mechanical delay stage by Newport. All measurements were collected on dilute solutions.

3.3 Cyclic Voltammetry

Cyclic voltammetry (CV) was performed with a standard commercial CHI Instruments Electrochemical Analyzer in a three electrode single-component cell under argon atmosphere. The supporting electrolyte used was tetrabutylammonium Hexafluorophosphate ($TBAPF_6$) used as obtained from Sigma Aldrich. Electrolyte solutions of 0.1 M ($TBAPF_6$) were prepared in sieve dried THF. Cyclic voltammetry (CV) was performed on solutions of MEH-PPV, fluoranthene, perylene and ferrocene. Analyte solutions of the small molecules were prepared by directly adding the analytes to electrolyte solution in a pyrex measurement cell after collecting CV measurements of the electrolyte solution alone. The MEH-PPV solutions were prepared by adding the polymer to electrolyte solution in vials which were sonicated until the polymer solid was fully dissolved. The solutions were prepared to achieve a volume of 10 ml. CVs were

collected under argon atmosphere by vigorously purging the solutions with argon for one minute prior to measurement. This was done by running an argon feed line through a thin sparge hole in the Teflon cap while the electrodes were assembled in position. Under these conditions evaporation was negligible and the concentrations could be considered constant before and after purging. A working electrode made of glassy carbon of 3 mm diameter was polished with 0.05 μm alumina (Baikalox), rinsed with THF and carefully wiped and dried with kimwipes before use. A Pt wire and a Ag/Ag^+ (10 mM AgNO_3 in 0.1M TBAPF_6 /THF) were used as an auxiliary and a reference electrode, respectively. The instrumental resistance compensation was turned off. For calibration of uncompensated resistances, the CVs of ferrocene were collected at varied concentrations as references.

3.4 Pulse radiolysis

Pulse radiolysis is a technique in which a material is irradiated by electron pulses with energies ranging from 1 to tens of MeV and optical detection used to monitor the subsequent formation and decay of species. The pulse width of the irradiating electrons or the speed of detection – whichever is slower, determines the time resolution of measurement in pump-probe experiments. In a solution, the energy deposited by a high energy pulse results in ionization of the most abundant material - the solvent. The initial byproducts of radiolysis immediately following ionization of the solvent are: a solvent cation, an electron, and a lesser yield of solvent excited states. The nature of the solvent dictates the reactions that follow (e.g. radiation chemistry). In some solvents, the cation is rapidly suppressed by reaction with the solvent neutral to form a non-oxidant byproduct, leaving a high yield of slow decaying electrons. Such solvents may be beneficial for radiolytic reduction. Tetrahydrofuran (THF) is an example of such a solvent and was used for radiolytic reduction. In other solvent systems, the electron is suppressed by reactions that yield non-reductant byproducts and leave a high yield of slow decaying solvent cations. Chlorinated solvents are good for these reactions. In this work, 1,2-dichloroethane (DCE) and o-dichlorobenzene (o-DCB) were used for radiolytic oxidation. In solvents where neither the solvent cation nor electron are rapidly consumed by

reactions with the solvent, the lifetime of both will depend on how rapidly the electron and cation recombine. The recombination of electron and solvent cation result in are dependent on the Onsager radius, r_c . The Onsager radius is the radial distance from an ionized solvent molecule at which the Coulombic attraction with an electron is equal to the thermal energy of the system. The Onsager radius can be expressed as $r_c = e^2/\epsilon k_B T$, where e is the charge of an electron, ϵ is the dielectric constant, k_B is the Boltzmann's constant, and T is the temperature. The probability of escape by the electron in the presence of an electric field, E was described by Onsager as:

$$P(r) = (1 + f(E)) * \exp(-r_c/r) \quad 3-4$$

where $P(r)$ is the probability of the electron's escape from the Coulomb potential of the cation at a given distance, r . Under zero field conditions, as were used in this thesis, this expression simplifies to:

$$P(r) = \exp(-r_c/r) \quad 3-5$$

The dielectric constant of the solvent has an inverse relationship with the Onsager radius. All other things being constant, the effect of increasing the Onsager radius of a solvent will lower the probability of an electron escaping the coulomb attraction to the solvent cation, and therefore increase the probability of recombination to form excited states. For rapid recombination of solvent cation and electron to produce excited states, a solvent with a large Onsager radius is required. A good solvent for rapid ion recombination is benzene, with an Onsager radius of 25.0 nm. The rapid formation of benzene excited states makes it a convenient solvent for study of energy transfer. For comparison, Onsager radii of other solvents used in this work are shown in **Table 3-1**.

Table 3-1 Onsager radii of select solvents

Solvent	Onsager radius (nm)	Reference
THF	7.2	[73]
DCE	5.4	[74]
Benzene	25.0	[75]
Water	0.70	[75]

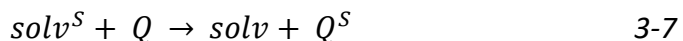
Following radiolysis of solutions, formation of some absorbing species – including, but not limited to the electron and/or solvent cation - may occur faster than the time resolution of detection and therefore appear to have formed within an instantaneous absorption “step” rather than through slower diffusional processes. The associated absorption is referred to as “step absorption”. The yields of species formed by radiolysis are generally measured in terms of G-values. The G value of a species X is expressed as the number of the species formed per 100 eV of energy absorbed by the total sample:

$$G(X) = \frac{\text{number of species } X \text{ formed}}{\text{energy absorbed in eV} \div 100} \quad 3-6$$

Alternatively, the G value is also expressed in units of micromoles per joule of absorbed energy by SI convention, where 1 molecule per 100 eV is equivalent to 0.1036 $\mu\text{M}/\text{joule}$.

3.4.1 Unambiguous formation of radical ions and triplets

Reduction, oxidation, and triplet formation of an aromatic compound of interest, Q , are all processes which require bimolecular interaction whether by contact or at a distance. To generalize the description of the transfer process, the solvent byproduct from which the intended species is transferred will be denoted as $\text{sol}v^S$ which may refer to an electron transferring agent ($\text{sol}v^{\bullet-}$), hole transferring agent ($\text{sol}v^{\bullet+}$), or triplet transferring agent (${}^3\text{sol}v^*$) of the solvent produced by radiolysis. If a sufficient concentration of an aromatic solute, Q , is present, its reaction with $\text{sol}v^S$, if energetically favorable, will yield:

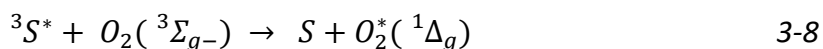


In **Table 3-2**, the solvent byproduct, $\text{sol}v^S$ according to solvent system is listed along with the reactions expected with the solute, Q .

Table 3-2 Reactive solvent species, $\text{sol}v^S$ formed by radiolysis of select solvents and their byproducts via reactions with an aromatic solute, π .

Solvent	$\text{sol}v^S$	Reactions induced by $\text{sol}v^S$
THF	$e^{\bullet-}$	$e^{\bullet-} + Q \rightarrow Q^{\bullet-}$
DCE, o-DCB	$\text{sol}v^{\bullet+}$ (solvent cations)	$\text{sol}v^{\bullet+} + Q \rightarrow Q^{\bullet+}$
Benzene	${}^3\text{Bz}^*$	${}^3\text{Bz}^* + Q \rightarrow {}^3Q^*$

An advantage of the pulse radiolytic technique is the ability to definitively form a radical ion or triplet of a compound of interest and to unambiguously determine its optical signature. While other absorbing byproducts are formed, the species of interest may be easily distinguished on the basis of yield, reactivity, and rate of formation. In some solvents a distribution of electrons, solvent cations, and triplets are produced. Even if the radiation chemistry does not naturally suppress all but one of these primary byproducts, scavenger molecules may be added which remove one or more of them. Molecular oxygen for example is an effective electron scavenger with a large electron affinity which reacts with electrons and most radical anions to produce O_2^- , a nonabsorbing product in the visible which is incapable of reducing most aromatic compounds. Oxygen is also capable of quenching triplets by two mechanisms: electron transfer (Type I reaction) and by energy transfer (Type II reaction) [76]. A Type II reaction is represented as:



Here, $O_2({}^3\Sigma_{g-})$ represents the ground electronic state of oxygen, and $O_2^*({}^1\Delta_g)$ as the electronically excited singlet state which lies at 94 kJ/mol (0.974 eV) above the ground state [77]. Although forbidden, transitions between the singlet excited state and triplet ground state of molecular oxygen have been observed in the upper atmosphere. Rate constants for quenching the triplet states of organic molecules have been found to be approximately 1/9 the diffusion controlled limit. The factor of 1/9 is due to spin multiplicity considerations [78, 79]. Other scavengers have been found to effectively convert strongly absorbing and reactive radical cations into weakly absorbing and unreactive radical cations. In this way, it is possible to obtain unambiguous optical signatures of radical ions and triplets of interest.

Several other techniques have been utilized to generate radical ions and triplets but due to the possibility of forming other species besides the one of interest and which are difficult to distinguish, ambiguities in the spectral assignments result. Optical strategies have been used to achieve reduced and oxidized states of aromatic systems by dissociation of singlet excitons via intense laser pulses, multiple pulses, or electric fields, leading to Coulomb-bound polaron pairs

(radical ion pairs) and/or free charge carriers [80-83]. Consequently, observation of different transient species or combination of species over a wide range of time domains has also led to challenges in distinguishing the spectral assignments of the one-electron reduced and oxidized states from those of other byproducts. Reduction and oxidation via electrochemical and chemical methods in solution have been more traditional methods of preparation and assignment of negative and positive charge carriers of aromatics. In these cases, there is a possibility of forming higher than single reduction or oxidation states, and effects of ion pairing can alter the spectral and chemical properties [84, 85].

Exceeding more than one excess charge per oligomer or polymer chain leads to the possibility of bipolaron formation. Experimental and theoretical studies to determine the conditions favoring conversion of individual polarons into bipolarons have been conducted, but considerable speculation and uncertainty remains. The formation of a bipolaron requires the interaction of two like charges on a single chain. This can only result if the number of charges generated per chain exceeds 1, or if two separate chains with charges interact, which requires diffusion in a solution. To mitigate possible absorbance contribution from bipolarons, unambiguous formation and measurement of the polaronic state (ionic state) should occur on a time scale shorter than the bimolecular reaction of two single polarons.

Typical spectrophotometers require a minimum integration or averaging time of at least 250 ms for absorbance measurements to achieve reasonable signal-to-noise. Assuming a diffusion controlled rate constant of $1 \times 10^{10} \text{ M}^{-1}\text{s}^{-1}$, which is reasonably low, would then require a concentration of ions no greater than 0.4 nM to limit encounters of ions to a time constant of 250 ms – a concentration far lower than the noise limit of detection. For these reasons, at concentrations of charged states (produced by chemical redox reactions for example) necessary for steady state absorbance measurements, uncertainties in the identity of the species formed are inherent.

In the pulse radiolysis method used, the concentration of $\text{sol}v^S$ produced does not exceed 3 μM . Due to the limited lifetime of $\text{sol}v^S$ a high concentration of a solute Q , is necessary to convert most of $\text{sol}v^S$ to Q^S . At very low concentrations of the solute, a small percentage of

$solv^S$ will be converted to Q^S . In either case, the fraction of solute converted to $solute^S$ is generally < 0.1 . It is worthwhile to consider the likelihood for forming bipolaron using radiolysis in LEAF. Assuming a maximum yield of 3 μM in radical ions are formed and assuming a diffusion controlled rate constant of $1 \times 10^{10} \text{ M}^{-1}\text{s}^{-1}$, two ions would encounter with a rate of $3.0 \times 10^4 \text{ s}^{-1}$ ($\tau = 33 \text{ }\mu\text{s}$). Under these conditions, formation of doubly charged species can be considered negligible at times within the first few microseconds. Additionally, formation of bipolarons if favorable could be expected to be distinguishable based on slow forming kinetics accompanied by spectral transformations.

The formation of dimer radical cations is feasible for some aromatic solutes. These species may also be distinguished by spectral and kinetic considerations, making it possible to resolve ambiguity. Equilibria of dimer and monomer radical cation have been observed for certain small aromatic molecules [86]. In such cases, the two populations were distinguished by the relative yields of each obtained at different concentrations of initial solute neutral, and isosbestic points were often evident. Due to larger entropy of macromolecules, formation of dimer radical cations might be expected to be significantly less efficient.

Triplet formation by radiolysis is also an efficient process occurring primarily by rapid recombination of geminate charges and advantageous for optical detection. Unlike photolysis which relies entirely on intersystem crossing of photoexcited states, formation of triplets by radiolysis is not limited to the intersystem crossing of the solute. Additionally, the penetration depth of absorbing photons is strongly dependent on concentration of the optically absorbing species and may prohibit homogenous distribution of excited states at significantly high concentrations and increasing the likelihood of unwanted reactions such as exciton-exciton annihilation and/or prevent an accurate measurement of the yield of the overall quantity of triplets formed. The penetration depth of the radiolytic electron pulse is much less sensitive to the concentration of the absorbing solute and may produce a more homogenous distribution of excited states for which the yield formed may be accurately determined by optical detection. The larger range of solute concentrations allowed by radiolysis makes it possible to facilitate and control rates of triplet energy reactions. Such control makes radiolysis useful for determining energetics of triplets via equilibria or irreversible triplet depletion by full transfer

to energy acceptors. Examples of triplet energy determination by phosphorescence of oligomers or polymers have been demonstrated but are very rare. An example of a polymer for which the triplet energy was found by both phosphorescence [87] and radiolytic energy transfer [88] is the ladder-type methyl-poly(*p*-phenylene). Both techniques showed very good agreement.

The 5 ps electron pulse width available in LEAF ensured that the ionization event of radiolysis occurred prior to rather than during diffusional processes and nanosecond time resolution of detection facilitated observation of both diffusional and non-diffusional charge and triplet capture. In comparison, many of the radiolytic studies of polymers in literature were conducted in facilities with pulse widths ranging from 50 ns to several microseconds long, obscuring the nature of early ion and triplet formation kinetics and limiting the time resolution of the experiment.

In this work, Q^S is formed by direct conversion from $solv^S$ and from transfer intermediates. The products are monitored by difference absorbance transients collected over a broad spectral range with intervals of ≤ 50 nm between wavelengths.

3.4.2 Laser-electron accelerator facility (LEAF)

Several pulse radiolysis facilities are operating worldwide to study the chemical kinetics of reactions on the nanosecond time scale. One of these facilities is the Laser-Electron Accelerator Facility (LEAF) in the Chemistry Department at Brookhaven National Laboratory. All radiolytic measurements in this thesis were collected in LEAF. The design of the LEAF accelerator is based on a 30 cm long radio frequency (RF) electron gun containing a magnesium photocathode. Frequency-tripled emission from a Ti-sapphire laser is used to ionize the cathode and produce a burst of electrons (~ 5 ps pulse width) that are accelerated to 9.2 MeV by RF power from a 2.856 GHz klystron. The laser pulse is synchronized with the RF to ensure that ionization occurs at the proper phase of the RF to maximize forward acceleration.

Quadrupole magnets placed at locations along the beamline ensure the electron bunch remains tightly packed during its transport down the beamline. A fraction of the electrons reaching the solution target are scattered by the solution and others are transmitted and collected by a Faraday cup which serves as a gauge of beam dosage for calibration of measurements. Provided that solvent, cuvette material, pathlength, and temperature are held constant for two independent measurements, the relative intensities of the beam dosages delivered to the samples in each measurement are equivalent to the ratio of the currents measured by the Faraday cup in each measurement. As such the dosages may be normalized by the current measurement. and can therefore be dose-normalized. The total dose per pulse was determined before each experiment by measuring the transient absorption of the hydrated electron in water at 650 nm where $\epsilon(e^-)_{650} = 18500 \text{ M}^{-1}\text{cm}^{-1}$ and a yield of $G(e^-) = 2.97$ molecules/100 eV^{-1} at 10 ns. Doses were determined for prepared solutions by correcting for the difference in electron density of the organic solvent relative to that of water.

The resulting kinetics following radiolysis were probed optically. The analyzing light source used was a pulsed Xe lamp, and the analyzing light incident on the sample was oriented collinear to the propagation path of the radiolytic pulse. Photolysis of the sample by the detection light was prevented by cutoff filters placed between the analyzing light and the sample. Transmitted wavelengths of interest were selected by using 10 nm band pass interference filters and transient absorption signals were detected with either a silicon photodiode (EG&G FND-100Q) or an InGaAs photodiode (GPD GEP-600), and were recorded with a Lecroy 8620A digitizer. The time resolutions of the measurements were determined by the silicon and InGaAs photodiodes used, with response times of 2 ns and 5 ns respectively. A fast shutter intercepting the beam and sample was used to protect the sample from continuous irradiation from the analyzing light while measurements were not being made. The fast shutter was opened less than a second before measurement and closed less than a second after.

If the time-dependent absorbance at wavelength λ for a solution in perturbed state following radiolysis is $Abs(\lambda, t)$, and time-dependent absorbance in the unperturbed state is $Abs_0(\lambda, t)$, the transient absorbance $\Delta Abs(\lambda, t)$ measures the time dependence of the absorbance difference of the at the wavelength,. For radiolytic transients, the reference beam

is the time-dependent transmitted light intensity of a solution in the unperturbed state, and the signal beam, the time-dependent transmitted light intensity of a solution in the perturbed state following radiolysis, measured as:

$$\Delta Abs(\lambda, t) = Abs(\lambda, t) - Abs_0(\lambda, t) \quad 3-9$$

Collecting $\Delta Abs(\lambda, t)$ over a range of wavelengths, and plotting them versus wavelength at a given time segment provides a difference absorbance spectrum from which spectral evolution can be monitored. A more detailed description of the LEAF facility has been published elsewhere [89].

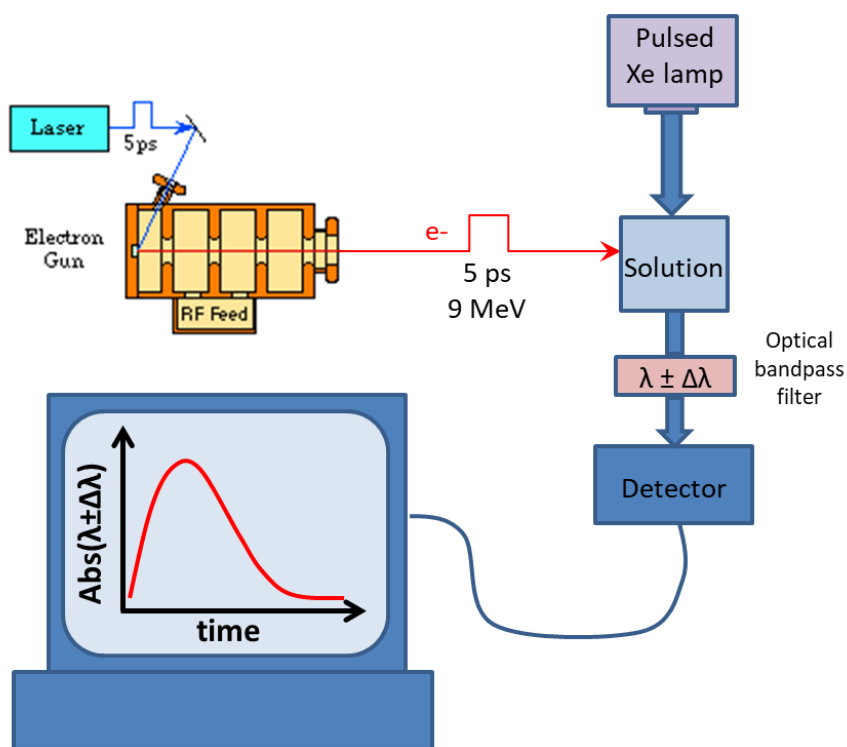


Figure 3-1 Radiolysis byproducts in the irradiated solution are probed by broadband light from a pulsed Xe lamp and the time dependence of absorbance at a wavelength selected by an optical band pass filter is detected by a silicon or InGaAs photodiode detector.

Chapter 4: Optical signatures of radical ions and triplets

4.1 Introduction

To effectively monitor charge and energy transfer reactions, the time evolving yields of the reactants and/or products must be measurable. To quantify yields of the excited and charged states, accurate optical signatures and extinction coefficients of the species must be known. Reactions of interest explored in this work involve one reactant in the ground state and the other in an excited or charged state. To unambiguously form singlet excited states, only optical excitation is required to facilitate absorption from the ground state of a compound, and the extinction coefficient at a given wavelength can easily be determined via Beer Lambert's Law. However, commonly used techniques for the formation of charged and triplet states involve ambiguities that make the assignment of optical signatures and extinction coefficients less certain. In this section, unambiguous optical signatures charged states and triplets are unambiguously determined via radiolysis using a methodology that will be detailed further below. Optical signatures of ground states are also obtained by conventional steady state absorption spectroscopy. Photoluminescence (PL) spectroscopy and photoexcited ps transient absorption spectroscopy are also used to characterize the photophysical properties of certain compounds in order to aid the interpretation of exciton and charge transfer dynamics at D/A interfaces.

4.2 Estimation of Reaction Radii of Compounds

Theoretical diffusion controlled reactions rates can be determined using the D-S equation provided the reaction radii of the reactants are known. Near diffusion controlled reactions indicate that negligible activation energy is required in a charge or energy transfer reaction. In the normal and inverted regimes, large activation energies are possible, leading to significantly

slower than diffusion controlled reactions. The theoretical diffusion controlled reaction rate constant is thus a valuable metric for evaluating the energetics of charge and energy transfer reactions. The radii of small aromatic molecules are estimated by van der Waals radii measured by bond lengths along the long axis of the molecule. For polymers however, the hydrodynamic radius is an appropriate representation for the lower limit of the reaction radius. The hydrodynamic radius depends on solvent and the molecular weight of the polymer. An approximate relationship between molecular weight and hydrodynamic radius of a polymer chain was shown in **Eq 2-24**. Provided the hydrodynamic radius of a polymer is known at a given molecular weight in a given solvent, the hydrodynamic radius at a different molecular weight in the same solvent may be obtained by defining a proportionality based on the ratio of the molecular weights. This can be shown as:

$$\left(\frac{MW_1}{MW_2}\right)^{1/3} \propto \frac{R_1}{R_2} \quad 4-1$$

Due to the solvent dependence of hydrodynamic radii for polymers, such radii must be determined according to the solvent in which the charge or energy transfer reaction is performed. The pertinent solvents in this work were: THF, Benzene, DCE, and o-DCB. From literature, hydrodynamic radii corresponding to MEH-PPV chains of known molecular weights were identified in THF [90], and benzene [91]. Using these values, the hydrodynamic radii for a 24.1 monomer MEH-PPV chain were estimated in the solvents via **Eq 4-1** as follows: THF (3.2 nm), and benzene (3.8 nm). Literature references for hydrodynamic radii of MEH-PPV in DCE and o-DCB were not be identified, however, estimates can be made based on some considerations of solubility. Nguyen et. al. [90] examined hydrodynamic radii for MEH-PPV in several solvents and found that the solvents in decreasing order by radii were p-xylene > chlorobenzene > THF. The solvent order also corresponds to increase in polarity. MEH-PPV chains are essentially non-polar, and are readily soluble in aromatic and low polarity solvents such as xylene and benzene which allow for a more open chain conformation. They are still somewhat soluble in polar non-aromatic solvents such as THF, and DCE. Dichlorobenzene is likely to be less of a good solvent as a more polar aromatic, but better than THF, and therefore the hydrodynamic radius in benzene should serve as an upper limit. The conformation of MEH-

PPV in non-aromatic and polar DCE is assumed to be similar to that in THF, and consequently the hydrodynamic radius in 1,2-DCE is assumed to be equivalent to the estimated radius in THF.

The molecular weights and average chain lengths of the reference MEH-PPV chains of known hydrodynamic radii from literature are found in **Table 4-1** along with the calculated hydrodynamic radii of the 24.1 monomer MEH-PPV in the various solvents. Hydrodynamic radii for pCVPPV and pDPP2FT were not measured and could not be effectively estimated.

Table 4-1 Determination of hydrodynamic radii for MEH-PPV in THF and Benzene

Solvent	MW of reference MEH-PPV; $R_h(\text{Ref})$	MW of 24 monomer MEH-PPV; $R_h(n=24)$	$R_h(n=24)/R_h(\text{ref})$	$R_h(\text{sample})$
Benzene (& o-DCB)	1.6×10^6 g/mol; 21.5 nm	8.9×10^3 g/mol	$\left(\frac{8.9}{1600}\right)^{1/3} = 0.177$	0.177*(21.5 nm) 3.8 nm
THF (& DCE)	5.35×10^5 g/mol; 12.5 nm	8.9×10^3 g/mol	$\left(\frac{8.9}{535}\right)^{1/3} = 0.255$	0.255*(12.5 nm) 3.2 nm

In **Table 4-2**, select molecules used as charge transfer intermediates or triplet sensitizers in experiments, and their van der Waals radii computed from bond lengths. The van der Waals radius of fSF-PPV was also computed. An effective radius for the oligomer is not clear as it is significantly larger than a small aromatic compound and yet significantly smaller than a polymer and therefore unlikely to coil significantly. In **Table 4-3**, viscosities of solvents are also presented.

Table 4-2 Radii of select molecules

Molecule	Radius (Å)
THF	1.25
Benzene	1.40
1,2-DCE	1.48
o-DCB	2.16
O ₂	3.04
Biphenyl	3.77
Anthracene	3.84

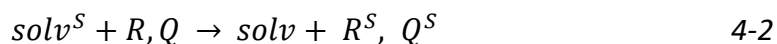
Benzophenone	4.13
Perylene diimide (PDI)	7.85
PDI-phenyl	8.43
fSF-PPV/THF	10.3
MEH-PPV/THF	32.0
MEH-PPV/DCE	32.0
MEH-PPV/Benzene	38.0
MEH-PPV/o-DCB	38.0

Table 4-3 Viscosities of solvents and dielectric constant

Molecule	Viscosity (Ns/m ²)	Dielectric constant
THF	0.00055	7.58
Benzene	0.000601	2.284
1,2-DCE	0.00079	10.36
o-DCB	0.00132	9.93

4.3 Methodology for collection of optical signatures

For an aromatic solute, Q it was shown in **Eq 3-7** that Q^S may be formed directly by conversion from $solv^S$ via the reaction: $solv^S + Q \rightarrow solv + Q^S$. A defining trait of the conversion is the equivalent rate of suppression of $solv^S$ and formation rate of Q^S . As was previously mentioned, the identity of Q^S may also be confirmed by testing its reactivity. In some cases, the spectrum of $solv^S$ is not observable due to lying out of the spectral range of detection, having a small extinction coefficient, or strong overlap with a rapidly formed byproduct. In such cases, a second aromatic solute, R may be incorporated, resulting in the following reaction:



The compound R may be considered a (hole, electron, or triplet) transfer intermediate if it satisfies the condition:



If the solubility limit of R is significantly higher than that of Q , and if the lifetime of R^S significantly exceeds that of $\text{sol}v^S$, then using the condition $[R] \gg [Q]$ may significantly improve the yield of Q^S produced relative to the yield in the absence of the transfer intermediate.

4.4 Optical signatures of radical anions

The radiation chemistry of THF is shown in **Table 4-4** and the radiation chemistry of THF solutions containing a solute in **Table 4-5**. Transient absorption spectra following radiolysis of THF are shown in **Figure 4-1** below. The solutions were prepared in an argon-saturated glovebox. As an inert gas, argon is unreactive with electrons and radical anions unlike molecular oxygen.

Table 4-4 Reactions following radiolysis of neat THF

Reaction Step	Reaction	Description
i	$\text{RH} \rightsquigarrow \text{RH}^{\bullet+} + \text{e}^-$	Ionization
ii	$\text{e}^{\bullet-} \xrightarrow{\text{thermalize}} \text{e}_s^{\bullet-}$	Solvation of electrons
iii	$\text{e}_s^{\bullet-} + (\text{impurities}, \text{RH}^{\bullet+}, \text{RH}_2^+) \rightarrow \text{products}$	Electron decay
iv	$\text{RH}^{\bullet+} + \text{RH} \rightarrow \text{RH}_2^+ + \text{R}^\bullet$	Proton transfer to neighbor

Table 4-5 Radiolysis of THF solutions containing solute "Q"

Reaction step	Reaction	Description
v	$\text{Q} + \text{e}^{\bullet-}, \text{e}_s^{\bullet-} \rightarrow \text{Q}^{\bullet-}$	Electron attachment to "Q"
vi	$\text{Q}^{\bullet-} + \text{RH}_2^+ \rightarrow \text{SH}^\bullet + \text{RH}^\bullet$	Radical anion neutralization
vii	$\text{Q}^{\bullet-} + \text{R}^\bullet, \text{impurities} \rightarrow \text{products}$	Radical anion neutralization

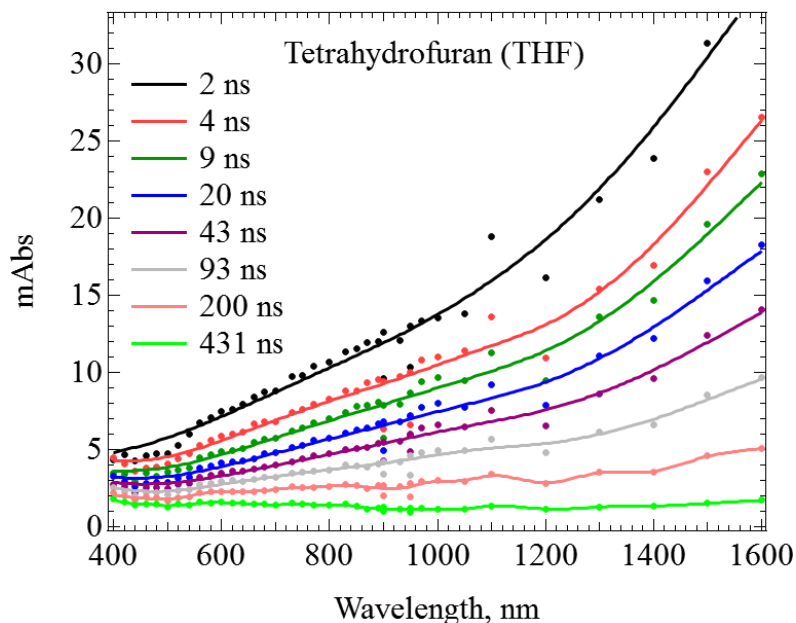


Figure 4-1 The transient absorption spectra of neat THF at times immediately following radiolytic pulse, giving evidence for a monotonically rising absorption band for the solvated electron that peaks in the near IR.

Following radiolysis of THF, electrons will decay by reaction with one of the following: geminate cation (RH^+), protonated THF (RH_2^+), or a solute. Electron decay by geminate recombination occurs within a couple nanoseconds, whereas homogenous electrons which decay via reaction with RH_2^+ have an average lifetime of ~ 500 ns in the absence of unintended solute impurities. The relatively large Onsager radius of THF results in a much higher yield of homogenous electrons which in **Figure 4-1** are shown to decay with a time constant near 100 ns, indicating some trace impurities (e.g. water, oxygen) are present. The spectrum of the electron in THF monotonically increases from the visible to the near IR and reaches a maximum circa 2100 nm and [92, 93] which was beyond the realm of detection monitored in these experiments in order to limit the number of detectors required.

Radiolytic reduction of phenylenevinylene containing compounds (MEH-PPV, fSF-PPV, and pCVPPV), pDPP2FT, and perylene diimide compounds (PDI and PDI-phenyl) were performed in THF. In all solutions except that of pCVPPV the reducing agent was the electron corresponding to a suppression of an absorption band in the near IR. The solution of pCVPPV utilized biphenyl (BP) as an electron transfer intermediate. The transient absorption spectra immediately

following radiolytic pulse of these solutions are shown below: MEH-PPV (**Figure 4-2**), fSF-PPV (**Figure 4-3**), pCVPPV (**Figure 4-4**), pDPP2FT (**Error! Reference source not found.**), PDI (**Figure 4-6**), and PDI-phenyl (**Figure 4-7**).

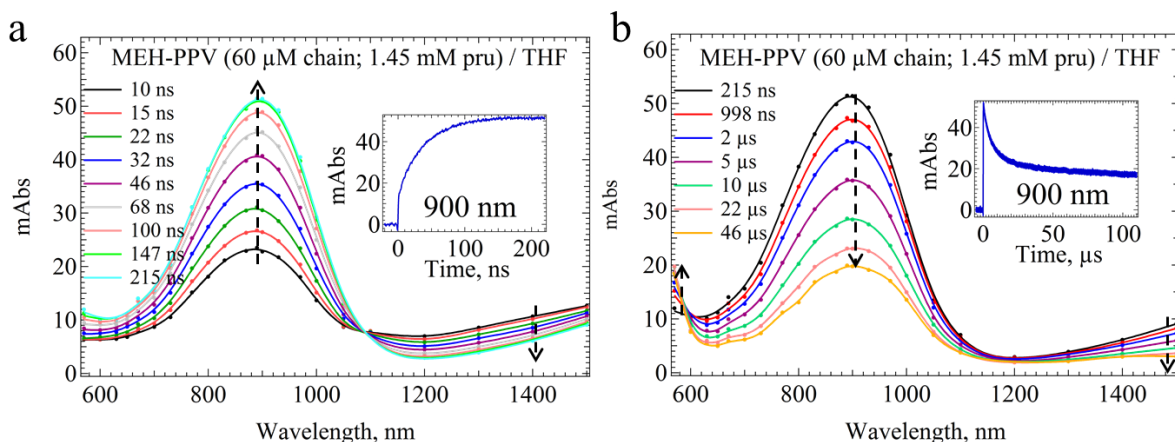


Figure 4-2 Transient absorption spectra of a THF solution containing MEH-PPV (60 μM chain, 1.45 mM pru) at various time segments following radiolytic pulse, **(a)** during the growth of a 900 nm band, and **(b)** during the decay of the same band. Insets of both graphs correspond to the transient at 900 nm during the respective time scales shown.

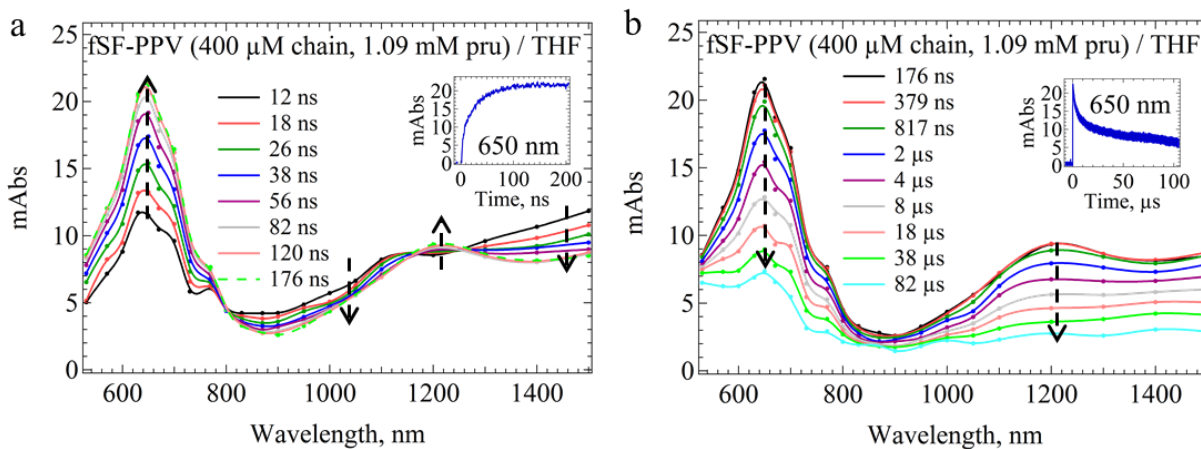


Figure 4-3 Transient absorption spectra of a THF solution containing fSF-PPV (400 μM chain, 1.09 mM pru) at various time segments following radiolytic pulse, **(a)** during the growth of a 650 nm band, and **(b)** during the decay of the same band. Insets of both graphs correspond to the transient at 650 nm during the respective time scales shown.

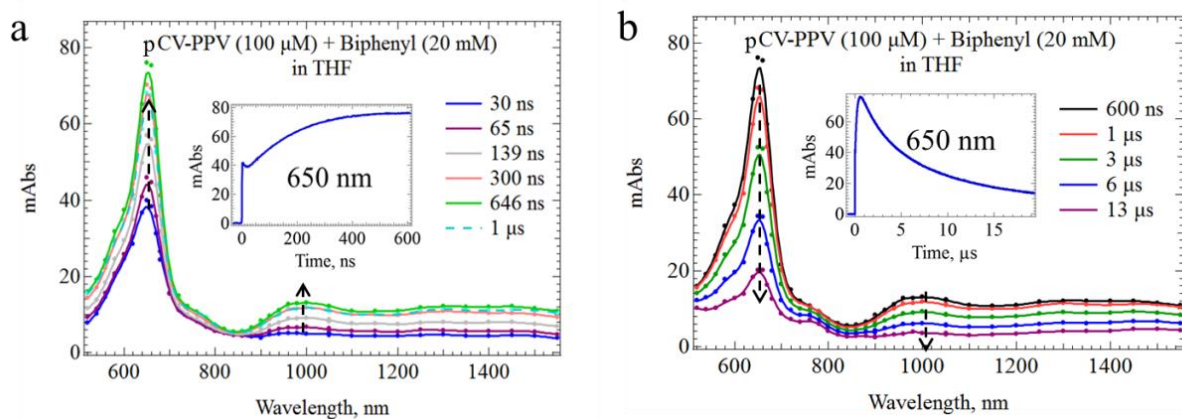


Figure 4-4 Transient absorption spectra of a THF solution containing pCVPPV (100 μM chain, 0.77 mM pru) at various time segments following radiolytic pulse, **(a)** during the growth of a 650 nm band, and **(b)** during the decay of the same band. Insets of both graphs correspond to the transient at 650 nm during the respective time scales shown.

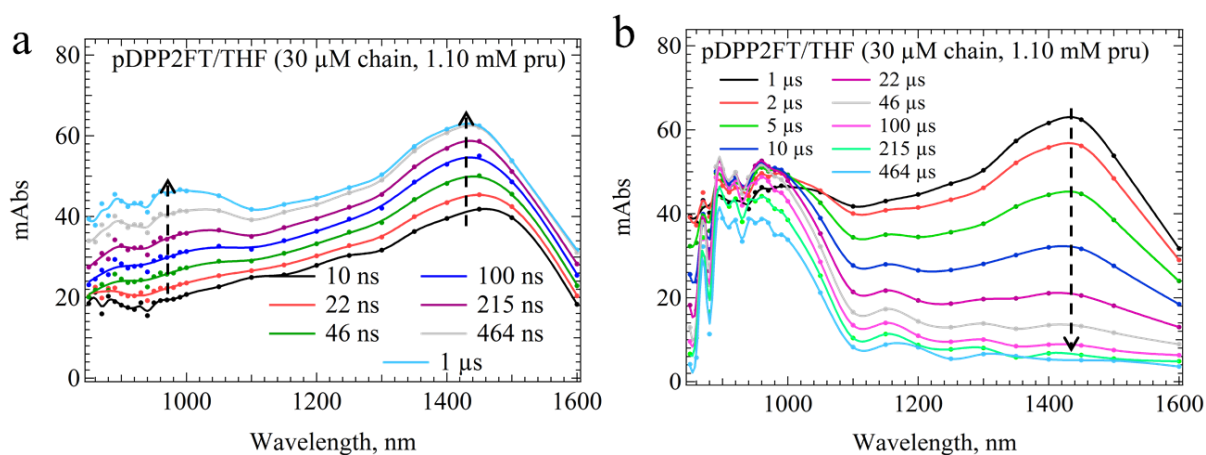


Figure 4-5 Transient absorbance spectra corresponding to radiolysis of pDPP2FT (30 μM chain) in THF at varied time segments following the radiolytic pulse, **(a)** during growth of a ~ 1430 nm spectral band, and **(b)** during the decay of the same band.

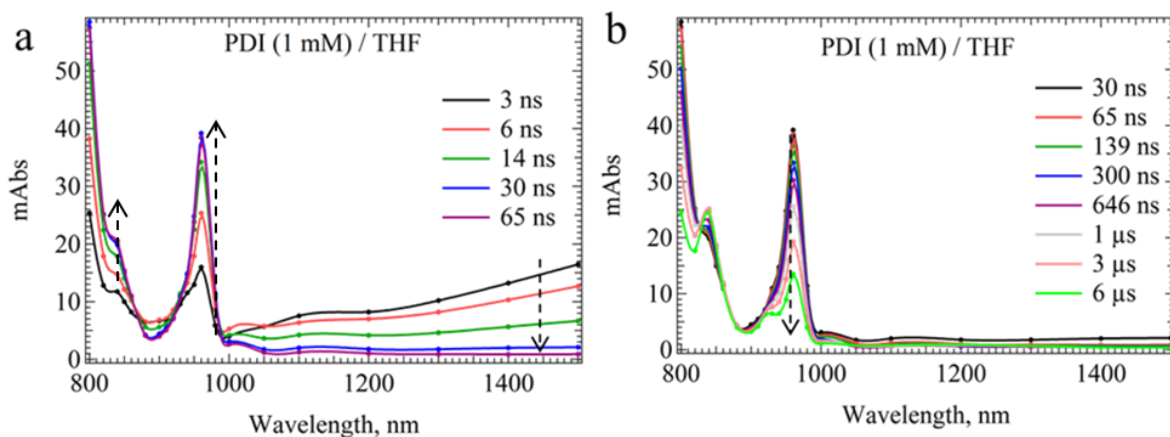


Figure 4-6 Transient absorbance spectra corresponding to radiolysis of PDI (1 mM) in THF at varied time segments following the radiolytic pulse, **(a)** during growth of a 950 nm spectral band, and **(b)** during the decay of the same band.

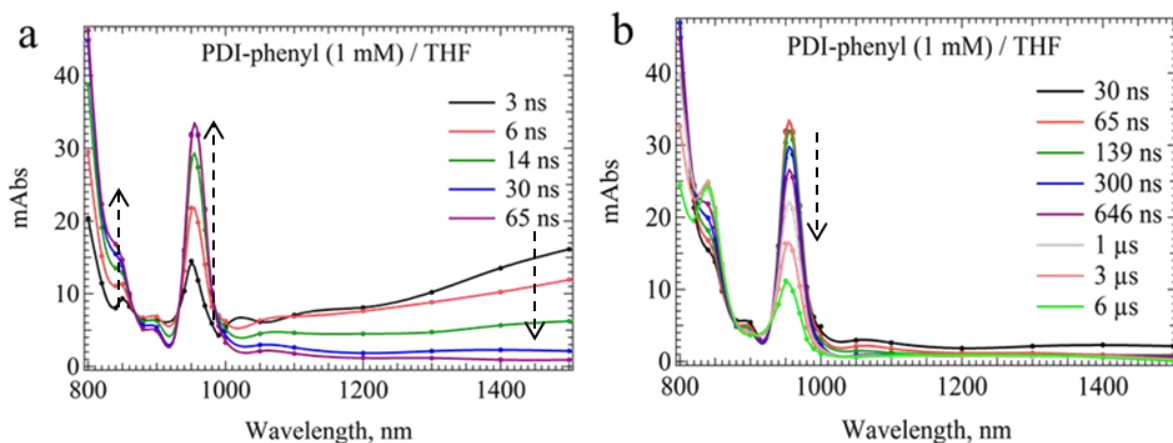


Figure 4-7 Transient absorbance spectra corresponding to radiolysis of pDI-phenyl (1 mM) in THF at varied time segments following the radiolytic pulse, **(a)** during growth of a 950 nm spectral band, and **(b)** during the decay of the same band.

For MEH-PPV, fSF-PPV, PDI, and PDI-phenyl, the spectral transformations show evidence of electron decay concomitant with growth of new spectral bands – indicating that they are byproducts of electron capture. Air bubbling the solutions resulted in very rapid (< 100 ns) suppression of the observed bands formed in the argon-saturated solutions, confirming that these bands are not due to radical cations which are unreactive with oxygen, nor triplets which

are reactive with oxygen but at slower rates of \leq one-ninth the diffusion controlled rate of encounter for the triplet species and ground state oxygen, due to spin statistics. The bands observed growing after radiolytic pulse are concomitant with electron decay are therefore definitively radical anions. The radical anion bands were observed to form in two distinct time scales – the slowest accounting for the largest fraction forming by pseudo-first order rates, and a smaller fraction on a time scale much faster than the detector response time (~ 2 ns) and therefore appear as instantaneous step absorption relative to the slower formation. Some “step absorption” in THF is due to electrons while some may also result from electrons captured by solutes within the response time of the detector - referred to here as “step captured” electrons.

To obtain rate constants of reaction for radiolytic reduction of the aforementioned solutes, the pseudo-first order rates of formation were divided by the concentrations of the solutes. These rate constants are provided in **Table 4-6**. Theoretical diffusion controlled rate constants could not be determined from the D-S equation because the effective radius of the solvated electron is unknown. To estimate the effective radius of the solvated electron, the rate of reduction for the 24 monomer MEH-PPV was assumed to be diffusion controlled. Provided a hydrodynamic radius of 3.2 nm, the effective radius of the solvated electron in THF was calculated as 0.25 Å. As a test for self-consistency, this radius was used to estimate effective radii of the other compounds reduced via the solvated electron in radiolysis. The resulting radii determined by D-S equation are also included in **Table 4-6**. The radii estimates for fSF-PPV, PDI, and PDI-phenyl were remarkably close to the values obtained by calculating van der Waals radii from bond lengths along the long axis of the compounds. Relative to the van der Waals values, the radii estimate for fSF-PPV was smaller by 30%, for PDI was larger by 11%, and for PDI-phenyl was larger by 8%. The consistency of precision for the reactions with both a polymer of known hydrodynamic radius and small molecules of known van der Waals radii suggests that each are near diffusion controlled reactions. The largest degree of discrepancy of radius size was found for fSF-PPV. It was difficult to ascertain an effective radius due to the compound being significantly larger than a small “spherical” molecule, but also significantly smaller than a lengthy polymer capable of coiling. The radius of fSF-PPV determined by this

method however suggests that the van der Waals radius is relatively close to the actual reaction radius. The van der Waals radius however will be used to estimate lower limits for the theoretical diffusional rate constant in radiolytic oxidation and energy transfer reactions in the following chapter on energetics.

Table 4-6 Reaction rates corresponding to radiolytic reduction of selected solutes are presented along with wavelengths associated with byproducts of the solutes. Assuming electron capture by MEH-PPV is diffusion controlled, and given the estimated hydrodynamic radius of MEH-PPV ($R_h(\text{MEH-PPV})_{\text{THF}} = 32.0 \text{ \AA}$) an effective radius for the solvated electron is $R(e^{\bullet-}) = 0.25 \text{ \AA}$. Effective radii for other solutes are approximated based on the estimated effective electron radius by assuming reaction rates for radiolytic reduction are diffusion controlled.

THF Solution		Species formed (λ_{max})	Rate constant of formation ($\text{M}^{-1}\text{s}^{-1}$)	Estimated effective radii for solutes
Solute of interest	$e^{\bullet-}$ transfer intermed.			
MEH-PPV	N/A	MEH-PPV $^{\bullet-}$ (900 nm) MEH-PPVH $^{\bullet}$ (<600 nm)	$4.67 \times 10^{11} \text{ M}^{-1}\text{s}^{-1}$ ($1.92 \times 10^{10} \text{ M}^{-1}\text{s}^{-1}$ pru)	32.0 \AA
fSF-PPV	N/A	fSF-PPV $^{\bullet-}$ (650, 1200)	$9.20 \times 10^{10} \text{ M}^{-1}\text{s}^{-1}$ ($2.92 \times 10^{10} \text{ M}^{-1}\text{s}^{-1}$ pru)	7.2 \AA
pCVPPV	Biphenyl	pCVPPV $^{\bullet-}$ (650 nm)	$4.36 \times 10^{10} \text{ M}^{-1}\text{s}^{-1}$ ($5.66 \times 10^9 \text{ M}^{-1}\text{s}^{-1}$ pru)	N/A
pDPP2FT	N/A	pDPP2FT $^{\bullet-}$ (~1420 nm) pDPP2FTH $^{\bullet}$ (950 nm)	$2.80 \times 10^{11} \text{ M}^{-1}\text{s}^{-1}$ ($7.63 \times 10^9 \text{ M}^{-1}\text{s}^{-1}$ pru)	22.8 \AA
PDI-hexyl	N/A	PDI $^{\bullet-}$ (950 nm)	$1.06 \times 10^{11} \text{ M}^{-1}\text{s}^{-1}$	8.8 \AA
PDI-phenyl	N/A	PDI $^{\bullet-}$ (950 nm)	$1.15 \times 10^{11} \text{ M}^{-1}\text{s}^{-1}$	9.1 \AA

Radiolytic reduction of pDPP2FT (**Figure 4-5**) was uniquely different from other reductions involving the solvated electron. The extinction coefficient of the pDPP2FT $^{\bullet-}$ appears to exceed that of the electron at all wavelengths within the allowable range monitored such that an observation of electron suppression as polymer radical anion forms was not possible. It was observed that inclusion of oxygen by air bubbling to acquire $\sim 2 \text{ mM O}_2$, significantly

suppressed the yield of the spectral band, but not to zero. By oxygen bubbling, the concentration of oxygen was increased to 10 mM O₂ and the yield further suppressed but not to zero. This observation suggests a reversible electron transfer between pDPP2FT and O₂. Due to the slightly more positive reduction potential of maleic anhydride relative to O₂, a separate test was performed to determine if electron transfer from maleic anhydride (MA) to pDPP2FT was reversible and was found to be so. These results support the assignment of the ~1400 nm NIR band observed in the solution of pDPP2FT only with polymer radical anion. Greater detail and analysis of the equilibrium measurements will be shown in the following chapter.

The spectrum of pDPP2FT^{•-} is observed to have only one band which is inconsistent with the two expected according to the FBC model [94]. While a second band at ~950 nm is observed to form its rate of formation is much slower and therefore owes to a distinctly unique species. The observed spectral transformations were akin to ones made by Das [95] in which the decay of radical anions of aromatic compounds were accompanied by formation of a new species blue-shifted relative to the higher energy band of the radical anion. The newly formed species were determined as monohydroradicals of the aromatics and were found to form by reaction of radical anions with protonated THF, and by reactions of neutral aromatics and H[•]. The broad 950 nm band observed forming partly during the growth of pDPP2FT^{•-} (with max at ~1400 nm) but even more so during its decay, is thus assigned as pDPP2FTH[•]. Similar observations were also made for the other compounds which were likewise suggestive of monohydroradical formation. In the cases of fSF-PPV and pCVPPV the observation of a new species was not direct but suggested by changes in spectral shape during the decay of the high energy radical anion bands which at later stages has a form consistent with the a composite of the spectrum of the radical anion at maximum yield and another species which monotonically decreases in intensity with increasing wavelength over the observed spectral ranges shown.

An interesting observation was made in comparing and contrasting the radical anion spectra of the perylene diimide compounds. While PDI (**Figure 4-6**) contains hexyl chains at both ends, PDI-phenyl (**Figure 4-7**) contains a hexyl chain on one side and a brominated phenyl adducted to the other. The electron attachment rate constants for PDI ($1.06 \times 10^{11} \text{ M}^{-1}\text{s}^{-1}$) and PDI-phenyl

($1.15 \times 10^{11} \text{ M}^{-1}\text{s}^{-1}$) were nearly the same and the respective radical anion yields of both were at their maxima at 65 ns. The radical anion spectra at 65 ns after pulse are shown in **Figure 4-8**. The extinction coefficient of the radical anion of PDI-phenyl was 18% smaller than that of PDI. Both appear to have low energy peaks circa 1050 nm but which are poorly resolved. The peak appears to be authentic in PDI-phenyl but is less certain in PDI, and less pronounced if real. Conceivable explanations are that the brominated phenyl adduct slightly modifies the electronic structure and/or that the electron is delocalized over the entire PDI-phenyl such that only 82% of the charge density is on the PDI unit and 18% on the phenyl adduct.

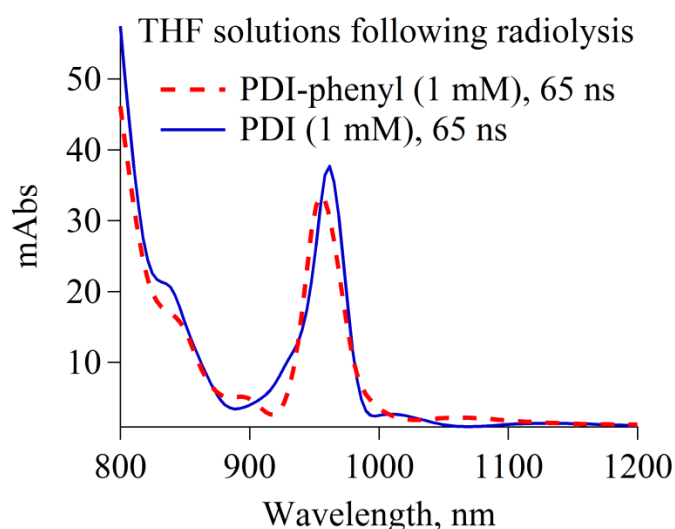


Figure 4-8 Transient absorption spectra corresponding to THF solutions of PDI and PDI-phenyl collected 65 ns after radiolytic pulse.

As a prototypical conjugated polymer, MEH-PPV is one of the most widely explored conjugated polymers in research today. According to the FBC model, radical ions should exhibit two distinct bands and this is observed for MEH-PPV^{•-} with a high energy band peaking at 900 nm and a lower energy band with a peak that could not be observed within the range of detection. Radiolytic reduction of MEH-PPV was previously examined by Burrows [96], who also found a similar maximum for the high energy band of the radical anion, but the spectrum collected by Burrows was limited and did not show evidence of a second band as does the one in **Figure 4-2(a)**. The radical anion spectra of the other two phenylenevinylene containing compounds - pCVPPV and fSF-PPV - differ from MEH-PPV in significant ways. The spectrum of

pCVPPV^{•-} shows evidence of two radical anion bands but the low energy band was very flat over a large spectral range extending out to 1500 nm. The radical anion spectrum of the oligomer fSF-PPV appears to show evidence of three bands with peaks at ~650 nm, ~1200 nm and one extending into the NIR beyond the range of measurement detectable. As will be shown later, the radical anion spectrum of SF-PPV also exhibited 3 bands at ~720 nm, ~1100 nm and one extending into the NIR.

While the spectral features of the 900 nm band formed by radiolysis of MEH-PPV in THF was reported by Burrows, no attention in his report was given to the kinetics of formation and decay of MEH-PPV^{•-}, which are herein described. The formation rate constant for MEH-PPV^{•-} was not only determined from the growth rate of the anion at 900 nm, but also from the decay rate of the solvated electron in the presence of MEH-PPV relative to its decay in neat THF. Denoting the decay rate of the electron in neat THF as $k_{decay}(e^-:THF)$ and the decay rate of the electron in the presence of a known concentration of the polymer solute as $k_{decay}(e^-:polymer/THF)$, the formation rate constant, k_{attach} was determined using the equation:

$$k_{attach} = \frac{k_{decay}(e^-:THF) - k_{decay}(e^-:polymer/THF)}{[polymer]} \quad 4-4$$

Values of $k_{decay}(e^-:THF)$ and $k_{decay}(e^-:polymer/THF)$ were determined as $3.22 \times 10^7 \text{ s}^{-1}$ and $6.15 \times 10^6 \text{ s}^{-1}$ respectively based on single exponential fits of the 1200 nm absorption transients corresponding to pristine THF and a THF solution of MEH-PPV. From these values, k_{attach} was calculated as $1.79 \times 10^{10} \text{ M}^{-1}\text{s}^{-1}$, which was less than 10% of the value of $1.92 \times 10^{10} \text{ M}^{-1}\text{s}^{-1}$, obtained using the formation rate of polymer anions at 900 nm.

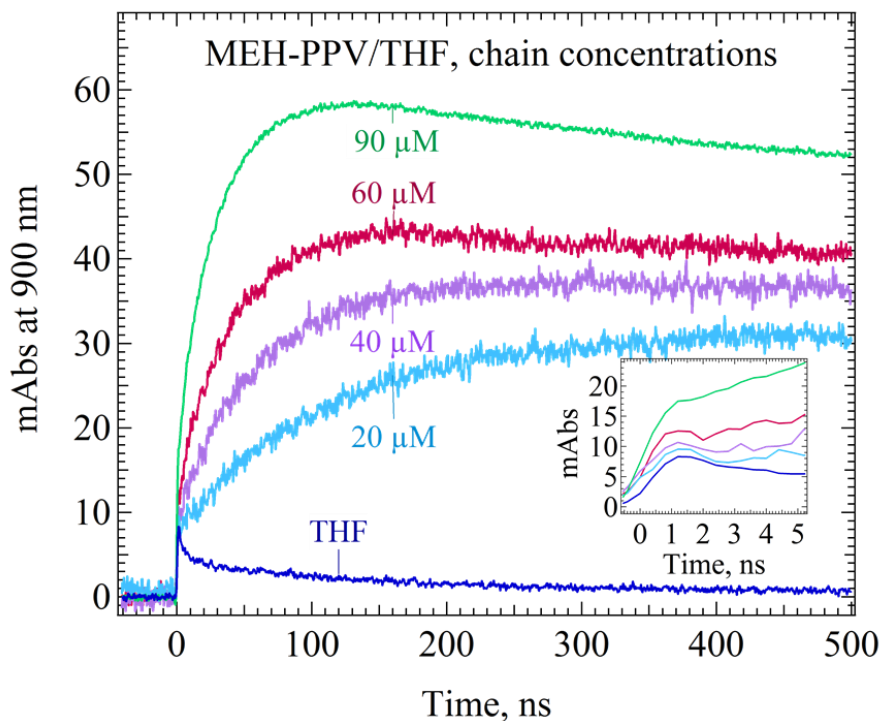


Figure 4-9 Early formation kinetics of $\text{MEH-PPV}^{\bullet-}$ measured at 900 nm revealing slow diffusion controlled capture of electrons preceded by step capture of electrons.

In addition to the 1.45 mM pru (60 μM chain) solution already evaluated, additional solutions of MEH-PPV were prepared in THF at pru concentrations of 0.482 mM (20 μM chain), 0.964 mM (40 μM chain), and 2.17 mM (90 μM chain). The 900 nm absorption transients of these solutions are shown plotted in **Figure 4-9** along with that of pristine THF. The electrons produced by radiolysis of THF are nearly all formed by the end of the radiolytic pulse (≤ 10 ps) but in the measurements made in this work, appear to form with a significantly slower time of ~ 1 ns which corresponds to the time resolution of the photodetector used. The absorption associated with the step captured electrons may be approximated by the difference in magnitudes of the step absorptions observed in solutions of THF relative the step absorption in pristine THF. As shown the inset of **Figure 4-9** the magnitude of step absorption increases with concentration of MEH-PPV indicating some electrons are captured by MEH-PPV within the rise time of the detector and that the yield of step captured electrons increases with polymer concentration. In principle, it is conceivable that triplets and holes may also be step captured, and evidence for step capture of holes such has been reported [64].

To verify that the increased step absorption corresponding to the MEH-PPV solutions is not due to triplets or holes, a spectrum of $^3\text{MEH-PPV}^*$ and $\text{MEH-PPV}^{\bullet+}$ were collected and it was found that absorption from $^3\text{MEH-PPV}^*$ is very negligible at 900 nm, while the absorption band of $\text{MEH-PPV}^{\bullet+}$ strongly overlaps that of $\text{MEH-PPV}^{\bullet-}$. These spectra will be presented later, however, spectral considerations allowed the possibility of triplet contribution to be ruled out. The possibility of radical cation contribution was tested by reactivity with molecular oxygen. A fresh argon-saturated MEH-PPV/THF solution (1.45 mM pru) was prepared and an absorbance transient collected at 900 nm immediately following radiolytic pulse. The solution was then air bubbled and an absorbance transient at 900 nm recollected. In the absence of oxygen, a growth and decay of radical anions is observed as shown in **Figure 4-10**. In the presence of ~ 2 mM of oxygen following air bubbling, the signal is found to decay entirely to zero within 100 ns.

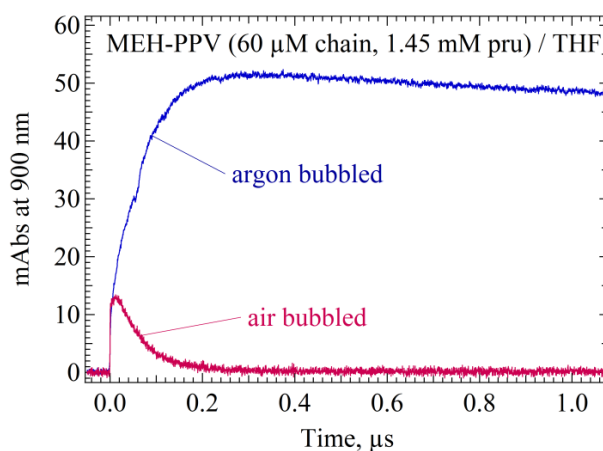


Figure 4-10 Absorption transients of MEH-PPV (60 μM chain, 1.45 mM pru) in THF at 900 nm after radiolytic pulse, shown for argon bubbled and air bubbled solutions. The transient corresponding to the air bubbled solution decays to zero suggesting no contribution of absorption from $\text{MEH-PPV}^{\bullet+}$ at 900 nm.

In spite of the low yields of triplets and cations expected to form in the radiolysis of THF solutions, valid consideration may be given to the prospect that some of the absorption signal at early times may be contributed by triplet or cation. The invariance of the spectral shape of the 900 nm band during its growth suggests negligible spectral contribution from species such as $\text{MEH-PPV}^{\bullet+}$ and $^3\text{MEH-PPV}^*$. As will be later shown, the triplet-triplet absorbance spectrum of MEH-PPV yields nearly no contribution to absorbance at 900 nm. To be certain that no cation

contributes at this wavelength, a separate solution of MEH-PPV (60 μM chain, 1.45 mM pru) in THF was prepared and absorbance transients at 900 nm were collected under argon saturated and air saturated conditions following radiolysis, as shown in **Figure 4-10**.

The absorption transient corresponding to the air saturated solution was observed to decay to zero, providing evidence that no radical cation contributes absorption at 900 nm. Assuming 2 mM of oxygen corresponding to an air saturated solution, the rate of decay measured for MEH-PPV $^{\bullet-}$ corresponds to a bimolecular reaction rate constant of $1.5 \times 10^{10} \text{ M}^{-1}\text{s}^{-1}$, which is nearly three times slower than the theoretical estimate of $4.4 \times 10^{10} \text{ M}^{-1}\text{s}^{-1}$ according to the D-S equation. This may suggest that the solution was not sufficiently bubbled to full air saturation. Nevertheless, that oxygen completely removes the entire absorption at 900 nm indicates that no radical cation is present and therefore, the step absorption formed following radiolysis of the MEH-PPV solutions in **Figure 4-9** owes entirely to step captured electrons.

If the magnitude of the step absorption of a given MEH-PPV solution at 900 nm is denoted as $Abs_{900}(\text{polymer}/\text{THF})_{step}$, the step absorption for neat THF at 900 nm, as $Abs_{900}(\text{THF})_{step}$, and the total yield of MEH-PPV $^{\bullet-}$ formed as $Abs_{900}(\text{polymer}/\text{THF})_{total}$, determined by extrapolating the absorbance decay of MEH-PPV $^{\bullet-}$ back to time zero, then the fraction of MEH-PPV $^{\bullet-}$ formed by step capture, f_{step} , can be computed as:

$$f_{step} = \frac{Abs_{900}(\text{polymer}/\text{THF})_{step} - Abs_{900}(\text{THF})_{step}}{Abs_{900}(\text{polymer}/\text{THF})_{total}} \quad 4-5$$

Using **Eq 4-5** the values of f_{step} at each of the concentration of MEH-PPV shown in **Figure 4-9** were calculated and are shown in **Table 4-7**.

Table 4-7 Fraction of MEH-PPV $^{\bullet-}$ formed by step capture at varied concentrations of MEH-PPV

[MEH-PPV] per chain	[MEH-PPV] pru	f_{step}
20 μM	0.482 mM	0.041
40 μM	0.964 mM	0.069
60 μM	1.45 mM	0.098
90 μM	2.17 mM	0.150

A plot of f_{step} versus monomer concentration of MEH-PPV reveals a linear relationship over the concentrations studied. The linear fit has a non-zero intercept which is difficult to understand, but may indicate error in overestimation of the step capture fraction due to the time resolution limit of the measurement, or may indicate that at even the lowest concentrations some limiting fraction of charges are step captured. Neglecting the y-intercept value, suggests that approximately 6.5% per of all electrons captured by MEH-PPV are captured by step formation. A linear relationship between monomer concentration of polymer and fraction of all electrons captured which are step captured is consistent with observations reported previously by our group for polyfluorene [63, 92].

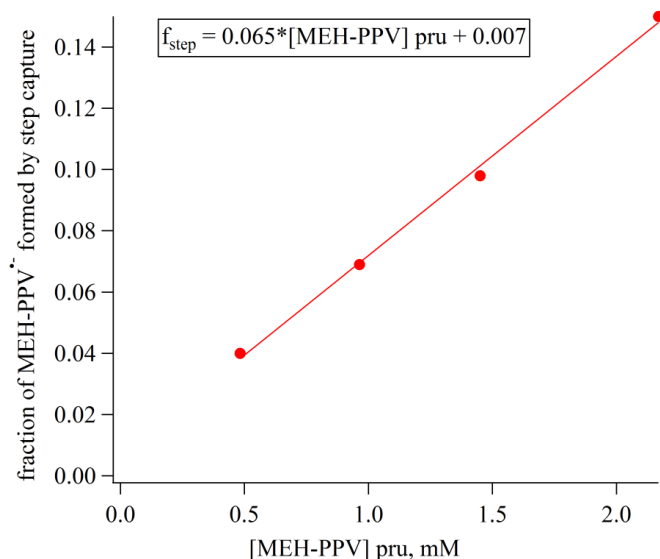


Figure 4-11 A plot of fraction of MEH-PPV- formed via step capture vs. [MEH-PPV] in pru provides a linear fit with a slope of 0.065/mM.

Similar observations in step capture of electrons were also exhibited by fSF-PPV. A plot of 650 nm absorption transients are shown in **Figure 4-12** and a partial plot of step capture fraction vs per monomer concentration of fSF-PPV is shown in **Figure 4-13**, indicating an approximate fraction of 0.14 for electrons captured by step capture relative to total electrons captured.

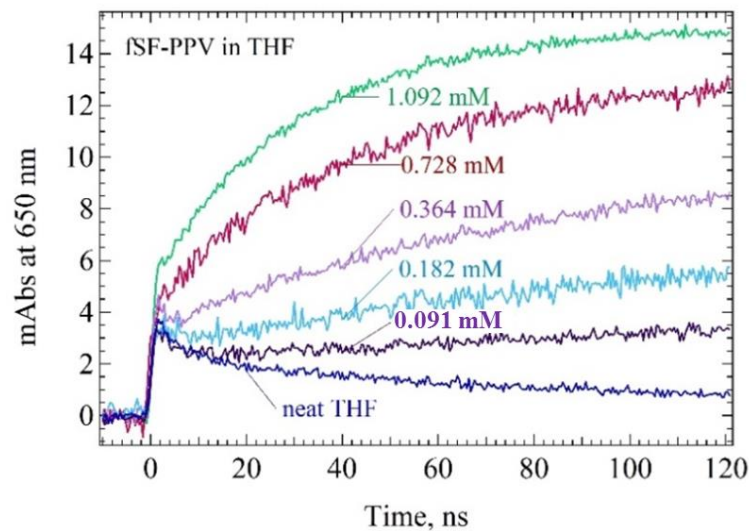


Figure 4-12 Absorption transients at 650 nm corresponding to THF solutions of *f*SF-PPV at various monomer concentrations, collected after radiolytic pulse. Transients indicate rapid formation of electrons, and formation of *f*Sf-PPV^{•-} by step and diffusive capture of electrons.

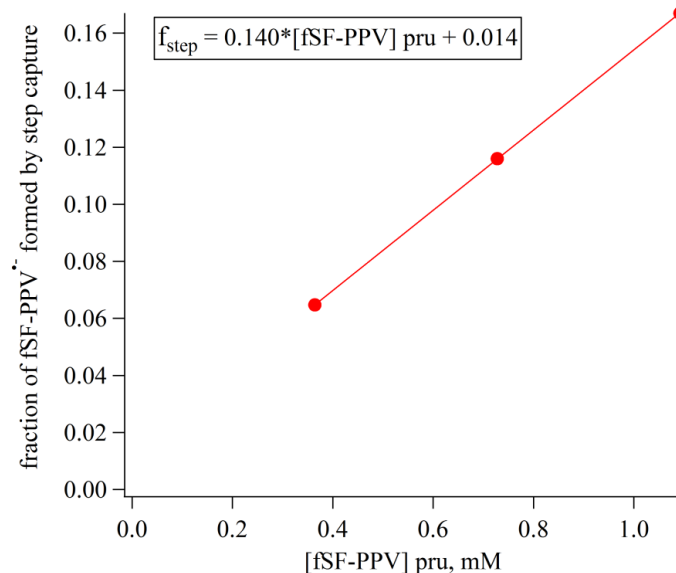


Figure 4-13 Fraction of electrons captured via step capture plotted versus monomer concentration of *f*SF-PPV, showing a linear dependence with a slope of 0.140/mM.

Unlike the pseudo first order formation rates for $\text{MEH-PPV}^{\bullet-}$, decays were observed to be biphasic as observed from the 900 nm transient shown in **Figure 4-14**. Radical anions of aromatics have been shown to react with protonated THF to produce monohydroradicals by proton transfer [95, 97], a reaction which should be second order under conditions where concentrations of anions and protons are nearly equivalent. Nevertheless, impurities such as traces of water may be introduced leading instead to observed pseudo first order rates of decay. These scenarios present two alternative rate dependent decay processes for $\text{MEH-PPV}^{\bullet-}$: 1) a slow 2nd order process if reactions with impurities such as excess water are not rate limiting, and 2) a pseudo first order decay rate due to impurities, or high excess of protons. The biphasic decay of the MEH-PPV is therefore peculiar.

It is also interesting that a new, higher energy absorption band is observed forming during the early decay of $\text{MEH-PPV}^{\bullet-}$ as evident from the 570 nm transient in **Figure 4-14**. The formation of aromatic monohydroradicals have been reported to typically absorb blue of the aromatic radical [95]. While this assignment is not conclusive, It is nonetheless clear that the species is a byproduct of either $\text{MEH-PPV}^{\bullet-}$ and/or MEH-PPV^0 . The formation of MEH-PPV^{\bullet} may result from the reaction of H atom (H^{\bullet}) with the polymer neutral (MEH-PPV^0), or by protonation of $\text{MEH-PPV}^{\bullet-}$ via reaction with RH_2^+ based on analogous radiolytic reactions reported for aromatic solutes in THF [95].

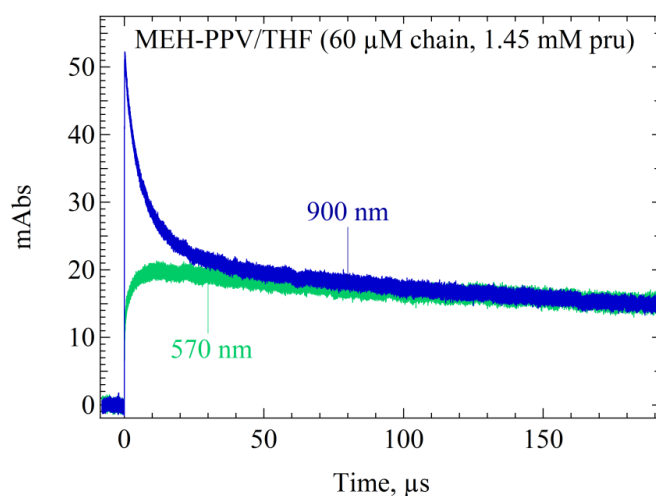


Figure 4-14 Absorbance transients of MEH-PPV (1.45 mM pru) following radiolysis, collected at 570 nm and 900 nm

A reaction involving the H^\bullet and the neutral polymer would occur with a pseudo first order rate limited by the short lifetime of H^\bullet in THF due to the competing reaction with the solvent. The rate of reaction between H^\bullet and THF might be expected to be similar to the reaction rate between H^\bullet and alkanes, reported as $\approx 10^6 \text{ M}^{-1}\text{s}^{-1}$ [98]. In THF this would lead to an estimated lifetime of $\approx 81 \text{ ns}$ for H^\bullet .

Absorbance growth at 570 nm was fit by two exponentials – $8.2 \times 10^6 \text{ s}^{-1}$ (123 ns) accounting for 46%, and $4.0 \times 10^5 \text{ s}^{-1}$ (2.50 μs) accounting for the remainder. The 900 nm transient was found to decay with rates of $1.8 \times 10^5 \text{ s}^{-1}$ (5.55 μs) and $< 1.0 \times 10^4 \text{ s}^{-1}$ ($> 100 \mu\text{s}$). The fastest decay rate of $\text{MEH-PPV}^{\bullet-}$ is nearly half that of the fastest growth rate measured at 570 nm. This would suggest that the species forming at 570 nm is formed only in part, if at all, by $\text{MEH-PPV}^{\bullet-}$ and in part by a separate reaction. The tentative assignment of MEH-PPVH^\bullet seems most plausible.

It is plausible that the 570 nm absorbing species is monohydroradical (MEH-PPVH^\bullet) formed by two reaction pathways, one of which is by protonation of the polymer radical anion which would explain the difference in the rates of formation at 570 nm and rates of decay at 900 nm. To examine the concentration dependence of $\text{MEH-PPV}^{\bullet-}$ decay, 900 nm absorbance transients over a timeframe of nearly 200 μs corresponding to MEH-PPV solutions ranging in chain concentration from 10 μM to 60 μM were collected as shown in **Figure 4-15 (a)**. At each concentration, the decay has a form that resembles a faster component by geminate recombination and a much slower component due to homogenous recombination. The timescale of geminate recombination however is typically 3 orders of magnitude faster for small aromatic compounds. A slower reacting geminate process might indicate that the protonated THF (RH_2^+) does not react immediately with $\text{MEH-PPV}^{\bullet-}$ upon encounter, but instead react to form a somewhat stable pair that reacts much more slowly. The yield of $\text{MEH-PPV}^{\bullet-}$ formed is concentration dependent within the explored range of concentrations, with lesser yields formed at lower concentrations due to less efficient capture of electrons resulting from the competing rates of electron decay and electron capture. In **Figure 4-15 (b)** the transient peaks are normalized and it can be seen that the slow decay is little affected by MEH-PPV concentration while the fast decay is more sensitive to it.

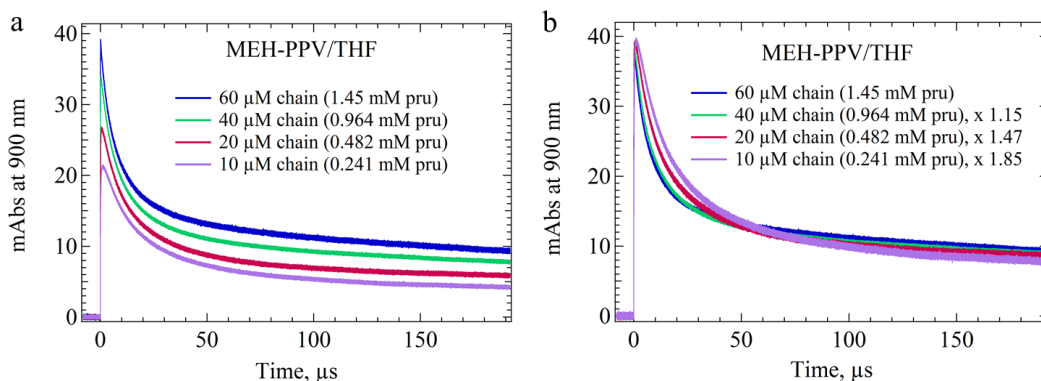


Figure 4-15 Radiolytic absorbance transients at 900 nm for MEH-PPV/THF at varied concentrations after pulse, shown: (a) as collected, and (b) with peak absorbances normalized.

Plotting the slow and fast decay rates versus concentration reveals a much stronger dependence at chain concentrations of $\leq 20 \mu\text{M}$ ($\leq 0.482 \text{ mM pru}$) indicating that decay rates at these concentrations are likely dependent on the formation rate of $\text{MEH-PPV}^{\bullet-}$ but approach independence at sufficiently high concentrations. and exponential dependence of the fast decay rate as shown in **Figure 4-16**.

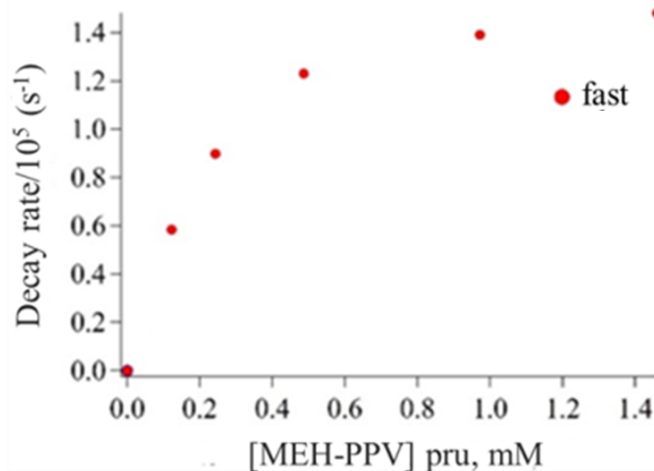


Figure 4-16 Fast decay rates of $\text{MEH-PPV}^{\bullet-}$ plotted versus per repeat unit concentrations of MEH-PPV

The biphasic decay nature of decay was not exclusive to MEH-PPV radical anions in THF but also was also evident in the decay of fSF-PPV radical anions following radiolysis of THF solutions containing fSF-PPV. An example is shown in **Figure 4-17** for which the 650 nm absorption

transient of fSF-PPV (1.09 mM pru) is normalized to match the maximum of a 900 nm absorption transient of MEH-PPV (1.46 mM pru).

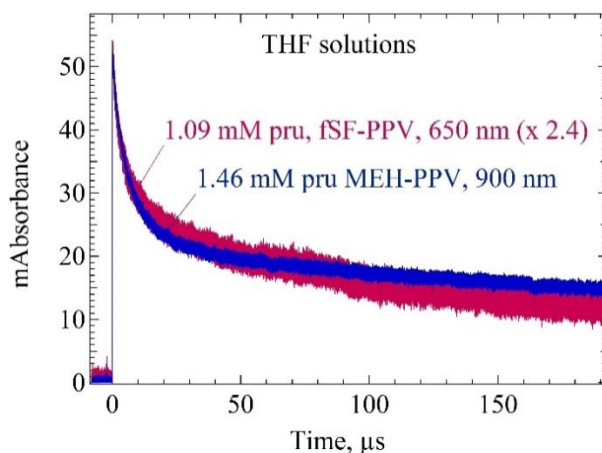


Figure 4-17 Difference absorbance transients of 1.46 mM pru of MEH-PPV/THF at 900 nm, and 1.09 mM pru of fSF-PPV/THF at 650 nm (rescaled x 2.4). Both transients follow a biphasic decay.

Some clues to the decay mechanism of MEH-PPV is elucidated by the decay kinetics of MEH-PPV radical anions in the presence of 2,2,2-cryptand and in the presence of TBAPF₆. As shown in **Figure 4-18**, 900 nm absorbance transients are shown for 60 μM chain solutions of MEH-PPV in the absence and in the presence of 2,2,2-cryptand following radiolytic pulse. In the presence of 10 mM cryptand, the lifetime of MEH-PPV^{-•} are greatly improved with respect to the solution without 2,2,2-cryptand. The inset shows the absorbance transients over a 600 ns time frame over which the radical anions in both solutions can be observed forming. The formation rate of radical anions in the presence and absence of cryptand are identical suggesting that the cryptand does not react with the solvated electron. The expected reaction of cryptand is to chelate cations. The ionized solvent molecule, RH⁺, is rapidly scavenged within 1 ps, a timescale too fast for cryptand to react at 10 mM. The reaction then must involve chelation of the proton RH₂⁺ which facilitates a higher fraction of protonated THF molecules escaping the Onsager radius to become homogeneously reactive species.

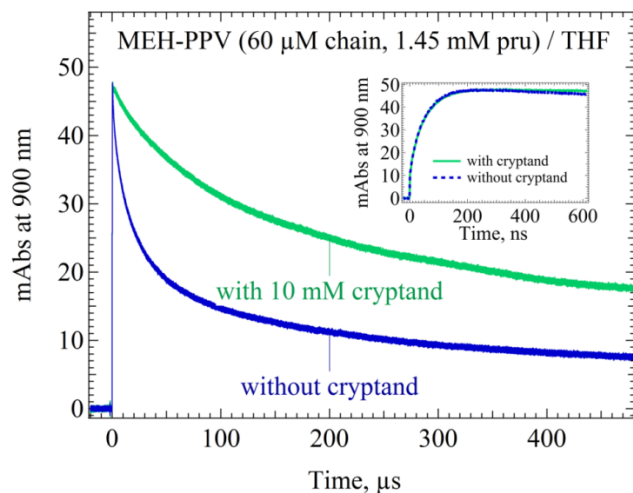


Figure 4-18 Absorption transients of MEH-PPV in THF (60 μM chain, 1.45 mM pru) are shown in the presence of 10 mM cryptand and in the absence of cryptand. The inset shows that despite differences in MEH-PPV $^{\bullet-}$ decay, both transients exhibit nearly identical formation rates for MEH-PPV $^{\bullet-}$.

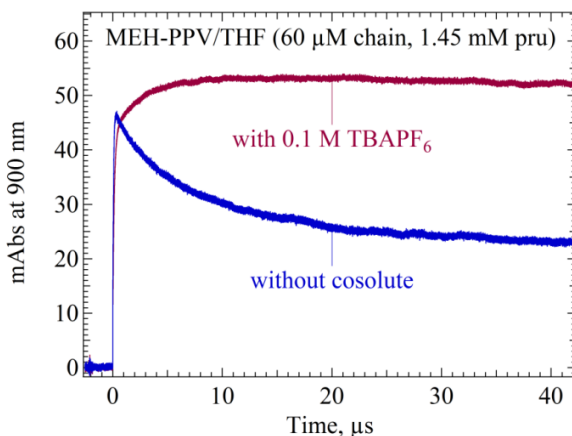


Figure 4-19 Absorption transients of MEH-PPV in THF (60 μM chain, 1.45 mM pru) are shown in the presence of 0.1 M TBAPF $_6$ and in the absence of electrolyte.

Incorporating 0.1 M TBAPF $_6$ also had an effect of improving the lifetime of MEH-PPV $^{\bullet-}$ relative to the radical anion in the absence of electrolyte as shown in **Figure 4-19**. While the lifetime of MEH-PPV radical anions have been extended in the presence of both TBAPF $_6$ (0.1 M) and 2,2,2-cryptand (10 mM), the formation rate of the radical anions in the presence of electrolyte was found to be several times slower than in the absence of electrolyte. Electrolyte cations have been observed to ion pair with electrons and anions, and stabilizing them with longer lifetimes evident [99]. The pairing of electrolyte to electrons leads to slower diffusion of

the electrons. The presence of electrolyte clearly serves to screen the Coulomb attraction between ions of opposite charges. The extended lifetime in the presence of 2,2,2-cryptand and electrolyte seems to suggest that the interaction of protons with the MEH-PPV radical anions are effectively screened, reducing their rate of reaction. The present findings suggest a geminate reaction between MEH-PPV^{•-} and protonated THF molecules at a rate orders of magnitude slower than observed for radical anions of small aromatic molecules and protons. That the reaction rate is similar for radical anions of both MEH-PPV and fSF-PPV indicates that the reaction is not dependent on reduction potential. Some dependence of the reaction on the delocalization of the electron is reasonable based on the fact that the charge density of the electron is spread and therefore Coulomb attraction between the proton and electron decreased relative to a less delocalized electron of a small aromatic compound. Nevertheless, the possibility of geminate recombination between protons and radical anions of conjugated polymers is interesting given that polymer anions have been shown to decay generally by reaction with homogenous protons or by impurities. Decay of polymer radical anions via geminate recombination to our knowledge has not previously been documented for polymers.

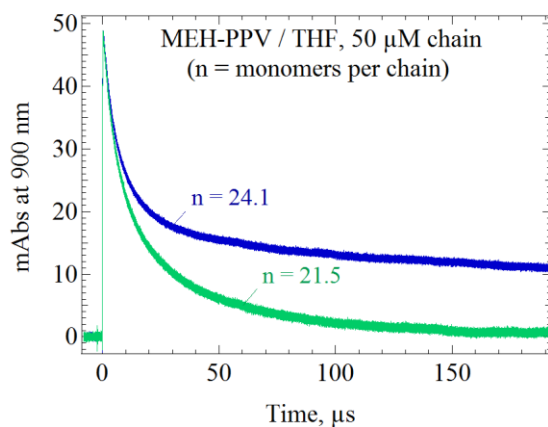


Figure 4-20 900 nm absorbance transients corresponding to THF solutions of MEH-PPV (50 μ M chain) prepared from two different batches of MEH-PPV (21.5 monomers and 24.1 monomers), showing two very different radical anion decay profiles.

The radical anion decay kinetics of a different batch of MEH-PPV ($n = 21.5$ monomers) was collected and compared with the 24.1 monomer batch. The MEH-PPV batches of both were prepared at chain concentrations of 50 μ M and the absorbance transients at 900 nm collected

as shown in **Figure 4-20**. The absorbance transients following radiolysis were found to be different, with a biphasic decay also exhibited by the 21.5 monomer unit batch but a smaller and faster decaying fraction of slower decaying anions. A possible explanation for the difference is that a low yield impurity such as oxygen was present in the n = 21.5 batch that was not present in the n = 24.1 batch. It is also possible that decay may reflect a dependence on synthetic approach or processing history which differed for the two batches of MEH-PPV. Such a dependence may suggest differences in defect yields for example.

4.5 Optical signatures of radical cations

Pulse radiolysis of chlorinated solvents has been shown to lead to one-electron oxidation of many aromatic solutes. The formation of sufficiently long-lived solvent cation and suppression of the electron both result from dissociative electron attachment to solvent resulting in production of chlorine atom which may deplete the cation with a second order reaction rate. The radiation chemistry of these solvents is complicated, and often more than one oxidizing byproduct is formed. Two chlorinated solvents were employed for radiolytic oxidation of compounds: 1,2-dichloroethane (DCE) and o-dichlorobenzene (o-DCB). Radiolytic oxidation in chlorinated solvents has been found to result from other reactants besides solvent cations, including fragment cations, chlorine atoms, chlorine complexes, and in the presence of oxygen, by chlorinated peroxy radicals [100]. According to literature references [100, 101] a partial list of reactions known to occur in chlorinated solvents following radiolysis are provided in **Table 4-8** for a pristine solvent and in **Table 4-9** for a solution containing an aromatic solute “Q”. The specific radiation chemistry of o-DCB has not been well explored while that of 1,2-DCE has been given some study [74, 102, 103].

Table 4-8 Reactions following radiolysis of a chlorinated solvent “RCl”

Reaction step	Reaction	Description
i	$RCl \xrightarrow{\gamma} e^{\bullet-} + RCl^{\bullet+}$	Ionization
ii	$e^{\bullet-} + RCl \rightarrow R^{\bullet} + Cl^-$	Dissociative capture

iii	$\text{RCl}^{\bullet+} + \text{Cl}^- \rightarrow \text{RCl} + \text{Cl}^\bullet$	Recombination
iv	$\text{RCl} + \text{Cl}^\bullet \rightarrow \text{RCl}^\bullet + \text{HCl}$	H abstraction

Table 4-9 Added reactions in the presence of high concentration of an arene "Q"

Reaction step	Reaction	Description
v	$\text{RCl}^{\bullet+} + \text{Q} \rightarrow \text{RCl} + \text{Q}^{\bullet+}$	Hole transfer to arene
vi	$\text{Q}^{\bullet+} + \text{Q} \rightarrow (\text{Q}_2)^{\bullet+}$	Dimerization
vii	$\text{Q}^{\bullet+} + \text{Cl}^- \rightarrow \text{Q} + \text{Cl}^\bullet$	Neutralization
viii	$\text{Q}^{\bullet+} + \text{Cl}^- \rightarrow (\text{Q}^{\bullet+} \text{Cl}^-)$	Non-reactive recombination
ix	$\text{Q} + \text{Cl}^\bullet \rightarrow (\text{Cl}^\bullet:\text{Q})$	Complex formation
x	$\text{Q} + \text{Cl}^\bullet \rightleftharpoons \text{Q}(-\text{H})^\bullet + \text{HCl}$	Deprotonation (H abstraction)

In chlorinated solvents, charge neutralization reactions have been reported to exhibit first order or mixed first- and second-order decay [101, 104, 105]. This suggests neutralization via reaction with Cl^- is not always the dominant decay mechanism of the solvent cation(s) in the absence of solutes. Other reactions have been proposed as explanations for neutralization reactions that fit closely to a first-order rate law such as deprotonation of the aromatic radical cation with the solvent, or reaction with an impurity. The neutralization reaction with Cl^- results in Cl^\bullet as a byproduct. The reaction may be reversible in some cases [100, 106] which would give the appearance of a long lived cation. Measurements made in this group but which have not yet been reported, have shown that Cl^\bullet complexed with toluene in chloroform is capable of oxidizing several aromatics with ionization potentials less than or equal to p-terphenyl. These observations indicate several important things about radiolysis of various chlorinated solvents: 1) that the specific knowledge of various radiation chemistries are incomplete, 2) that multiple oxidizing species may be formed, 3) oxidizing species may not only be cationic, but may involve radicals or complexes involving Cl^\bullet and aromatic molecules, and 4) degradation mechanisms are not fully understood.

Due to the limited lifetime of solvent cations generated by radiolysis, hole transfer intermediates are often utilized. The difference in gas phase ionization potentials of molecules may approximate the difference in their oxidation potentials in solution if solvation energies for the two molecules are nearly equivalent. However, solvation energies may differ significantly and even cause the difference in potentials to go from positive in the gas phase to negative in solution. In example, hole transfer from p-terphenyl to naphthalene was reported as feasible in chloroform but not in the more polar DCE, despite the ionization potential of p-terphenyl exceeding that of naphthalene by 0.6 eV [101]. Nevertheless, ionization potentials may serve as a guide for determining selection of compounds to test as oxidizing agents. In **Table 4-10** a list of gas phase ionization potentials according to NIST are provided for provided.

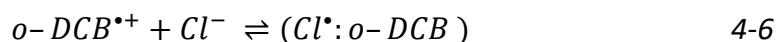
Table 4-10 Molecules and corresponding IPs

Molecule	IP	Reference
DCE	11.07	[107]
o-DCB	9.06	[107]
Biphenyl	8.16	[107]
p-terphenyl	7.80	[107]
Anthracene	7.44	[107]
Ferrocene	6.71	[107]

The specific radiation chemistry of o-DCB has not been well studied. In the present work, radiolytic oxidation was performed in both o-DCB and DCE. Understanding the detailed radiation chemistries of o-DCB and DCE were beyond the scope of these studies. Rather, the emphasis here is on uniquely identifying the optical signature of the radical cation species. In the radiolytic oxidations performed, in some cases, byproducts of side reactions or secondary reactions were evident based on transformations in the initial spectral shapes. The use of biphenyl as a hole transfer intermediate was beneficial given that the spectrum of biphenyl radical cation was known and reaction of this species with an aromatic solute of significantly less positive potential resulted in a simple hole transfer process, generally at a near-diffusion controlled rate. Therefore based on kinetic considerations, the product of the hole transfer from biphenyl radical cation to the solute of interest could be distinguished from slower forming species. Prior to providing the transient absorption spectra corresponding to radiolytic

oxidation of compounds in DCE and o-DCB, the transient absorption spectra of the pristine solvents should first be evaluated.

Transient absorption spectra of o-DCB at times immediately following radiolysis were collected as shown in **Figure 4-21**. The decay of bands in the visible and NIR are found to correlate with growth of a strong UV band. The UV band is similar to observed bands documented for complexes between Cl^{\bullet} and aromatics [74]. Given that the solvent itself is aromatic, a complex of this form is conceivable, whereas a complex should not exist in radiolysis of the nonaromatic DCE. In the inset of **Figure 4-21** absorbance transients at 300 nm and 1450 nm revealing that the conversion of one species into the other is not complete, as the 1450 nm band does not fully decay despite an initial fast decay component. This observation may indicate an equilibrium. A complexation reaction might be expected then to follow as :



If **Eq 4-6** holds true then at least two potential oxidizing species are formed, but if they are in equilibrium they will decay with the same rate.

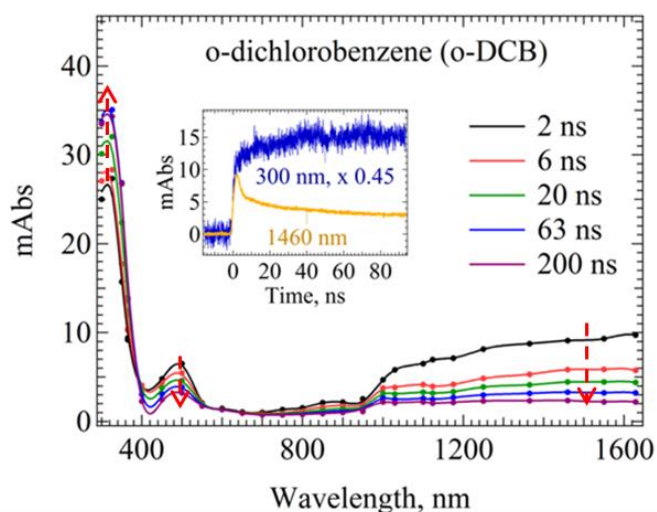


Figure 4-21 Transient absorption spectra of aerated o-DCB at time segments ranging from 2 – 200 ns after pulse showing visible and NIR bands decaying as a UV band is formed with similar rate as the decaying bands, suggesting they are correlated. The inset shows transients at 300 nm and 1460 nm where the forming and decaying species absorb, respectively.

The radiolysis of DCE has been reported to result in formation of at least two cations which are kinetically distinguishable [102, 108] and which contribute to a broad visible absorption band near 550 nm. The faster decaying cation was determined to be the solvent radical cation ($\text{CH}_2\text{ClCH}_2\text{Cl}^{+\bullet}$) and the slower decaying cation a presumed byproduct of the solvent radical cation - possibly vinylchloride cation. A UV band at 270 nm was also observed and assigned to radicals, and a 400 nm absorption owing to carbocations. The lifetimes of the solvent cations were ~ 40 ns and ~ 300 ns, respectively. Carbocations exhibited a lifetime of nearly $2 \mu\text{s}$ and a fraction of radicals absorbing at 280 nm remained after $20 \mu\text{s}$. Transient absorption spectra of DCE collected in LEAF are shown in **Figure 4-22** and are consistent with the spectral observations previously reported [102].

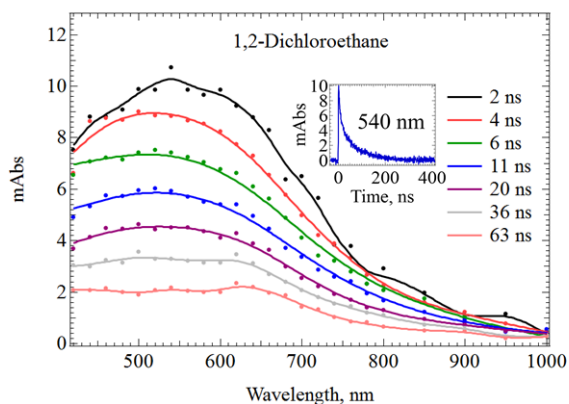


Figure 4-22 Transient absorption spectra of aerated 1,2-dichloroethane (DCE) at times immediately following radiolytic pulse.

The 550 nm absorbance transient of pristine DCE was fitted by two exponentials and found to have time constants of $1.6 \times 10^8 \text{ s}^{-1}$ and $2.1 \times 10^7 \text{ s}^{-1}$, but could also be approximately fitted by a single exponential fit with a time constant of $4.0 \times 10^7 \text{ s}^{-1}$. A new batch of solvent was purchased and dried with alumina sieve. This drying improved the lifetimes marginally indicating that while water was present the lifetimes are naturally short in DCE and that longer reported lifetimes were due to the length of the electron pulse width.

Biphenyl was used as a hole transfer intermediate in both DCE and o-DCB. Solution of biphenyl at 25 mM were prepared in DCE and o-DCB and the transient absorption spectra collected as shown in **Figure 4-23** and **Figure 4-24** respectively.

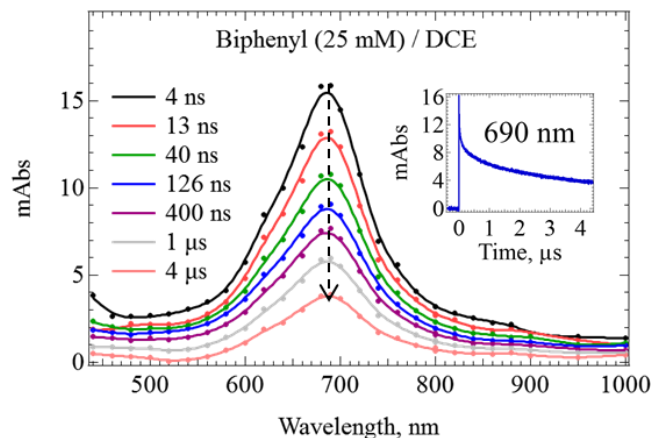


Figure 4-23 Transient absorption spectra following radiolysis of biphenyl (25 mM) in aerated DCE resulting in formation of biphenyl cation- the spectral band of which is shown here decaying. In the inset is shown the transient at 690 nm giving evidence of a rapid decay from geminate pairs and much slower decay due to homogenous cations.

In both solvents, cation formation of biphenyl appears nearly instantaneous following radiolysis, due to the high concentration of biphenyl used. A large fraction of cations decay rapidly due to recombination of geminate pairs of biphenyl cations and electrons, while the other fraction associated with homogenous biphenyl radical cations, remain for microseconds as seen in the insets of **Figure 4-23** and **Figure 4-24**. Biphenyl was utilized as a hole transfer intermediate due to the lifetime of its homogenous radical cations and because its oxidation potential is significantly more positive than most aromatics compounds. In DCE, the transient absorption spectrum of biphenyl radical cation as shown in **Figure 4-23** is well defined with a 690 nm peak in agreement with previous reports [101, 104]. The transient absorption spectrum in o-DCB as shown in **Figure 4-24** is less well defined and broad making unclear how much of the spectrum owes to biphenyl radical cation ($\text{BP}^{\bullet+}$). It is possible that the spectrum contains contribution from both $\text{BP}^{\bullet+}$ and the solvent cation, in which case the single decay rate observed along the spectrum might suggest an equilibrium.

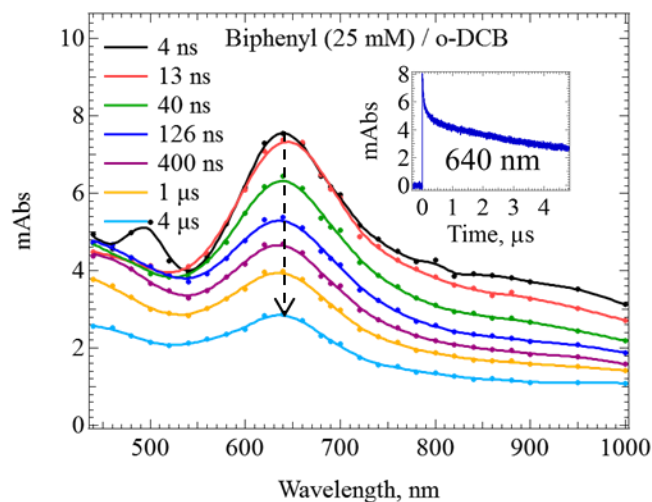


Figure 4-24 Transient absorption spectra following radiolysis of biphenyl (25 mM) in aerated o-DCB, resulting in formation of biphenyl cation- the spectral band of which is shown here decaying. In the inset is shown the transient at 650 nm giving evidence of a rapid decay from geminate pairs and much slower decay due to homogenous cations.

Studies of radiolytic redox reactions involving conjugated polymers in literature are limited in number but are important for elucidating differences in the nature and stability of injected charges in conjugated polymers relative to those of small aromatic molecules. A report by Burrows [96] identified an optical signatures by radiolytic oxidation for the polymer MEH-PPV, which was also investigated in this work. The transient spectrum was collected over a limited range extending enough to see evidence for a single polaron band, but a second is expected based on the FBC model and was not observed within the measured range. The reported oxidation was performed in chloroform, and spectra at select times presented, indicate that growth of MEH-PPV^{•+} continued for more than 500 μs – much longer than the lifetime of the ionized chloroform molecule and the long electron pulse of 50 ns, indicating that a different oxidant, was responsible. Similar observations of extremely slow radiolytic oxidation rates in chloroform were observed in this group which in part motivated the selection of other chlorinated solvents - namely DCE and o-DCB.

In this work, radiolytic oxidation was performed on MEH-PPV and other compounds of interest. Due to uncertainty about the specific radiation chemistries of DCE and o-DCB – for example, the number of oxidizing species produced and their oxidation potentials, radiolytic oxidations of MEH-PPV were performed in three different experimental conditions to establish

certainty about the optical signature of MEH-PPV^{•+}: 1) in aerated DCE without hole transfer intermediate, 2) in aerated DCE with biphenyl as hole transfer intermediate, and 3) in aerated o-DCB with biphenyl as hole transfer intermediate. Aeration of solutions results in ~ 2 mM of oxygen. Assuming a bimolecular reaction rate of $1 \times 10^{10} \text{ M}^{-1}\text{s}^{-1}$ as a lower limit for oxygen and radical anions, would a lifetime of $\leq 50 \text{ ns}$ for radical anions in aerated solutions. The transient absorption spectra obtained under these various conditions are compared with that obtained by Burrows in chloroform and used to confirm the optical signature in each. The radiolytic oxidation conditions used for MEH-PPV were then used to determine the best conditions for performing radiolytic oxidation of the other compounds as will be shown.

The initial trial of radiolytic oxidation of MEH-PPV was performed in aerated DCE without hole transfer intermediate. To compensate for the short lifetime of the solvent cations in DCE, a high concentration of MEH-PPV was required in the absence of a hole transfer intermediate. The transient absorption spectra immediately following radiolysis of a DCE solution containing MEH-PPV at 250 μM (6.0 mM pru) is shown in **Figure 4-25**. The spectrum by 100 ns is nearly identical to the one assigned to MEH-PPV^{•+} by Burrow et al [96]. Growth of MEH-PPV^{•+} occurs in several rate steps within a 100 μs timeframe suggesting the likelihood of multiple oxidants at work. Such oxidants require lifetimes on the timescales of the observed growths which is difficult to reconcile with the fact that no absorbing byproducts of DCE radiolysis are reported to live on a timescale even close to 10 μs , except for radical byproducts. In **Figure 4-26** the 660 nm transients of pristine DCE and the 250 μM MEH-PPV solution in DCE show similitude in the decay rate of DCE^{•+} and the fastest growth of MEH-PPV^{•+}, as well as step captured cation by comparing the instantaneous absorption rise of the solvent and solution. The kinetics of the MEH-PPV^{•+} formation is observed to form via step capture (~20%) followed by three rate steps: $1.12 \times 10^7 \text{ s}^{-1}$ (~15%), $4.20 \times 10^5 \text{ s}^{-1}$ (~15%), and $4.00 \times 10^4 \text{ s}^{-1}$ (~50%).

Assuming that each rate of MEH-PPV^{•+} formation is pseudo first order with respect to chain concentration provides rate constants of $4.48 \times 10^{10} \text{ M}^{-1}\text{s}^{-1}$, $1.68 \times 10^9 \text{ M}^{-1}\text{s}^{-1}$, and $1.60 \times 10^8 \text{ M}^{-1}\text{s}^{-1}$ per chain, respectively. The solvent cation, DCE^{•+}, is a strong oxidant which is expected to react via a diffusion controlled rate with MEH-PPV, and therefore would be the most probable oxidant responsible for the fastest rate – both due to its short lifetime and strong oxidizing

power. The slower reaction rates are far slower than diffusion controlled and may signify slow oxidation reactions due to an equilibrium, inverted region or high reorganization energy.

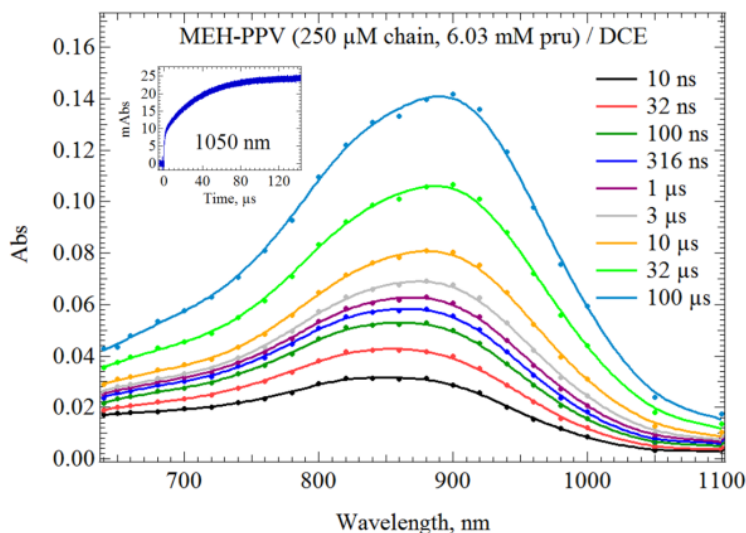


Figure 4-25 Transient absorption spectra at various time segments following the radiolysis of MEH-PPV (250 μM chain) in DCE. The inset shows the time profile of the absorbance at 1050 nm over the time range represented by the spectral transformations.

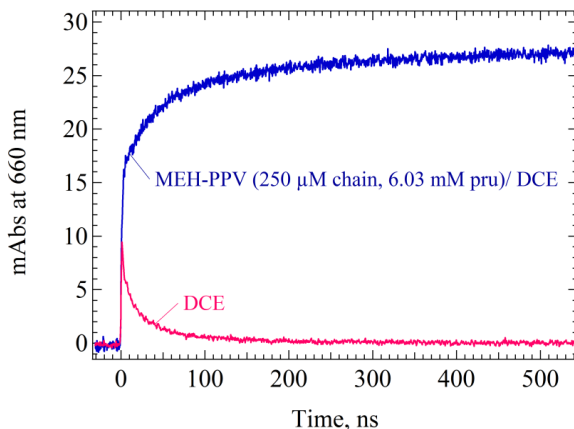


Figure 4-26 Absorption transients of aerated DCE only, and MEH-PPV (250 μM chain) in aerated DCE, at 660 nm.

The observation of non-decaying radical cations on such a long time scale are in stark contrast with nearly first order decay rates reported by Arai et. al. for radical cations of several aromatic molecules in oxygenated DCE, with lifetimes not exceeding several microseconds in the absence of impurities. The lifetimes in the absence of impurities were associated with the neutralization of radical cations via reaction with Cl^- . The absence of decay for MEH-PPV $^{\bullet+}$ over

such long time frames suggest a non-reactive recombination with Cl^- . In addition to the peculiar slow growth of polymer cations, another peculiar observation is an observed redshift in the spectrum from 10 ns to 100 μs .

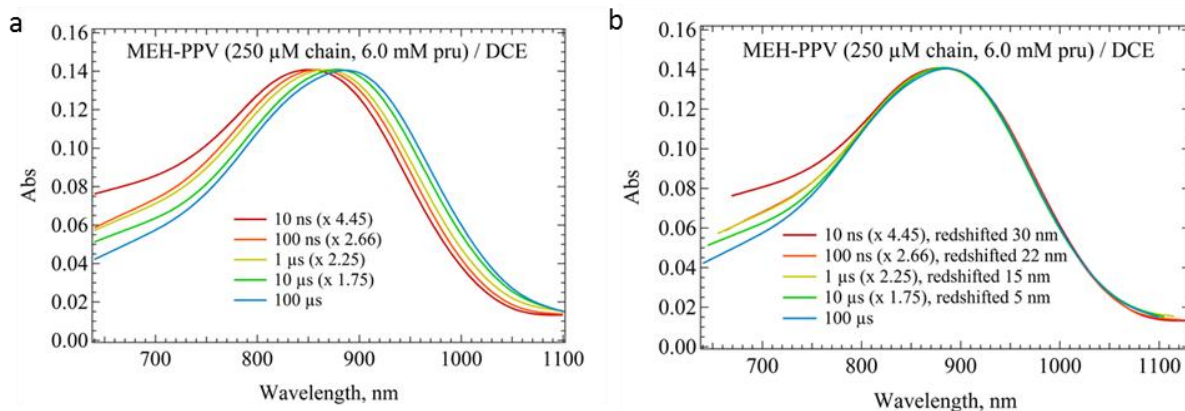


Figure 4-27 The absorbance spectra at various time segments following radiolysis of a DCE solution containing MEH-PPV (250 μM chain): a) shown normalized to the intensity of absorbance maximum of the 100 μs spectrum, and b) shown normalized and red-shifted relative to the absorbance maximum of the 100 μs spectrum.

Figure 4-27(a), spectra at various time segments after pulse are normalized to the peak intensity of the 100 μs spectrum. By redshifting the normalized spectra to match the peak of the 100 μs spectrum as is done in **Figure 4-27(b)**, suggests a redshift of 30 nm from 10 ns to 100 μs . Although the spectral resolution in each spectrum is 20 nm, the redshifts were instead determined by the shift necessary to overlap the low energy rising edge of the normalized absorption bands. The spectral shapes of the red-shifted and normalized spectra in **Figure 4-27(b)** are nearly identical in the low energy portion of the bands but deviate at the higher energies. The divergence decreases with time after pulse and suggests that its contribution may stem from a radiolytic solvent byproduct or impurity whose concentration decreases relative to that of the forming polymer radical cation.

It is unclear whether the observed red shift may be related to the slow forming cations and if so, what mechanism might give rise to such a phenomenon. While blue shifting has been observed for radical cations and radical anions due to ion pairing in the presence of electrolyte, [97] observations of red shifts in the spectra of polymer radical cations after radiolysis have not to our knowledge been previously reported.

It was of interest to examine whether the use of biphenyl as a hole transfer intermediate might mitigate the slow forming oxidation reactions observed in the absence of a hole transfer intermediate. The mitigation of slow oxidation reactions would indicate that the oxidizing species are radical cations or radicals with oxidation potentials more positive than biphenyl. For this purpose, a blend solution containing MEH-PPV at 207 μM (5 mM pru) and biphenyl at 20 mM was prepared. Spectral transformations of the blend solution after pulse are shown in **Figure 4-28(a)** from 20 ns - 4 μs after pulse, and in **Figure 4-28(b)** from 2 ns – 20 ns.

Unlike the prior radiolytic oxidation spectrum, or the one reported by Burrows, the growing spectra are displayed over a more extended spectral range revealing a low energy band which forms with the same rate as the higher energy one. The presence of $\text{BP}^{\bullet+}$ is evident at early times from the sharp peak at 690 nm, and in spite of the high concentration of BP a step capture of holes by MEH-PPV is also evident as early as 2 ns after pulse. Accounting for the contribution of $\text{BP}^{\bullet+}$ to the absorption at 900 nm indicates that ~ 8 mAbs is contributed by $\text{MEH-PPV}^{\bullet+}$. A bimolecular formation rate constant of $2.22 \times 10^{10} \text{ M}^{-1}\text{s}^{-1}$ per chain was calculated based on single exponential fit of the $\text{MEH-PPV}^{\bullet+}$ growth which was identical to the theoretical value of $2.23 \times 10^{10} \text{ M}^{-1}\text{s}^{-1}$ determined from the Debye-Smoluchowski equation. The absorption yield of $\text{MEH-PPV}^{\bullet+}$ at 900 nm, just following completion of the hole transfer reaction at 1 μs is 118 mAbs, indicating that $\sim 7\%$ of the $\text{MEH-PPV}^{\bullet+}$ formation by 1 μs was via step capture of holes, and the other 93% via conversion from $\text{BP}^{\bullet+}$.

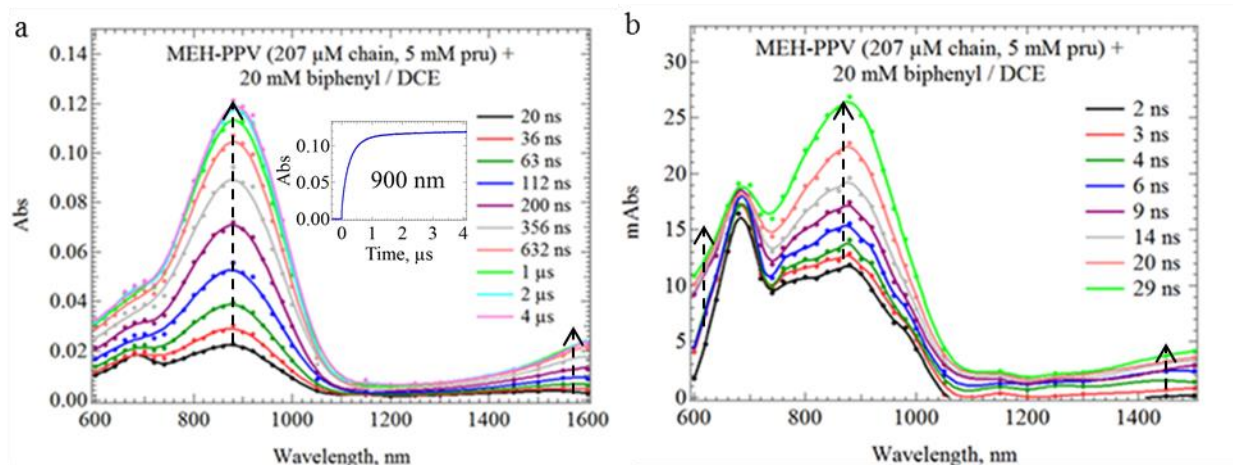


Figure 4-28 Transient absorption spectra corresponding to MEH-PPV (207 μM chain, 5 mM pru) in DCE at varied time segments after radiolytic pulse, shown over two distinct time ranges: a) from 20 ns – 4 μs , and b) from 2 ns – 29 ns.

As is observed in the inset of **Figure 4-28(a)** continued growth at 900 nm is observed beyond 1 μs and after all BP^{*+} has been converted, but at a much slower rate. At other wavelengths, while the kinetics prior to 1 μs were nearly identical, peculiar growths and/or decays in the dozens of microseconds beyond 1 μs suggest a new product is formed.

In **Figure 4-29** absorbance transients at various wavelengths are normalized at 1 μs to highlight the varied changes occurring at longer timescales. In spite of these growths and/or decays, the change to the overall spectrum is subtle suggesting little if any of the original MEH-PPV^{*+} is lost in the process. A slow absorption growth is most evident at 1150 nm and a single exponential fit indicates it forms with a rate of $3.4 \times 10^4 \text{ s}^{-1}$ ($\sim 30 \mu\text{s}$) which was nearly the same as the slow forming growth of MEH-PPV^{*+} observed in the absence of biphenyl. A test was performed to determine if the slow growth rate at 1150 nm was concentration dependent and it was found to be insensitive to concentration.

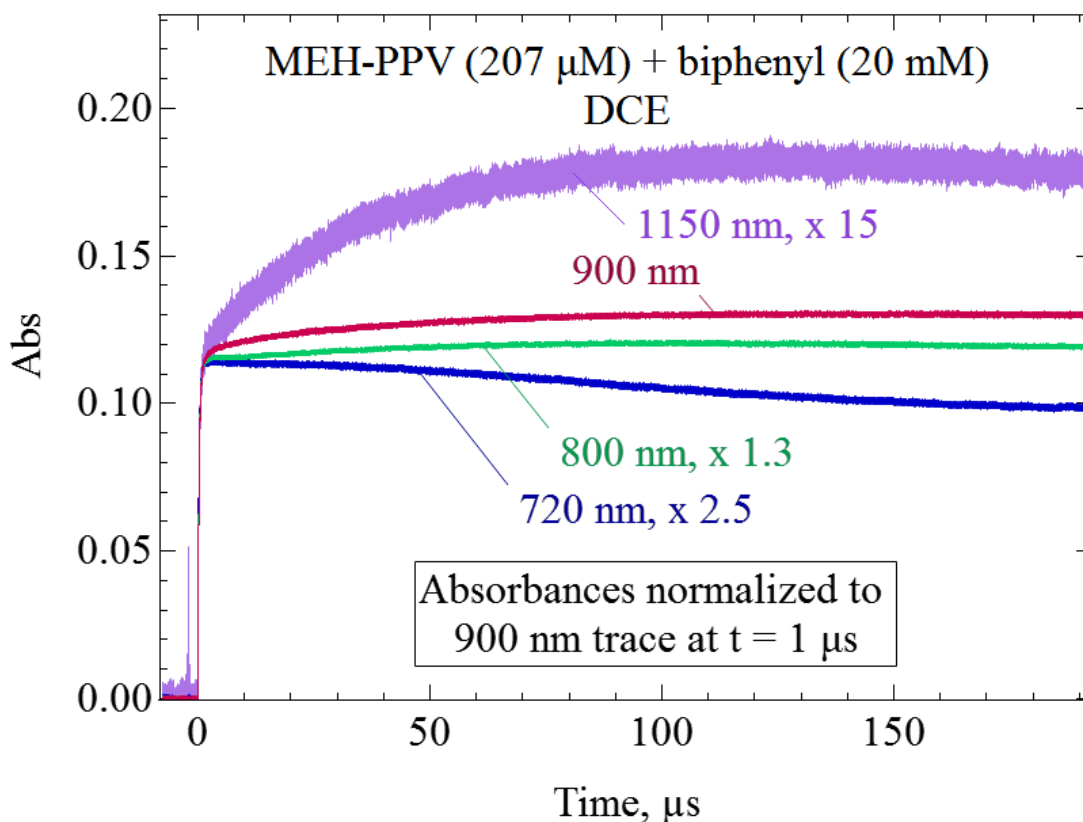


Figure 4-29 Absorbance transients corresponding to radiolysis of MEH-PPV (207 μM chain, 5 mM pru) in DCE at various wavelengths exhibit nearly identical kinetics at times $< 1 \mu\text{s}$ during conversion from biphenyl^{•+} to MEH-PPV^{•+} but deviate significantly over a time frame from 1 – 190 μs as shown by normalizing the transients to the 900 nm absorbance transient at 1 μs .

By comparing normalized spectra at varied times following radiolysis of the blend solution, a redshift was once again discernible. In **Figure 4-30(a)** spectra at 63 ns, 0.5 μs , 9.0 μs were several time segments after pulse are shown normalized to the peak intensity of the spectral band at 100 μs . In **Figure 4-30(b)** the normalized spectra are shown redshifted to match the band of the 100 μs spectrum after pulse, suggesting a redshift of 16 nm from 63 ns to 100 μs after pulse. Substantial contribution from BP^{•+} at 63 ns, may limit the certainty of this estimate, but a more sound estimate by 0.5 μs suggests a redshift of ≥ 10 nm.

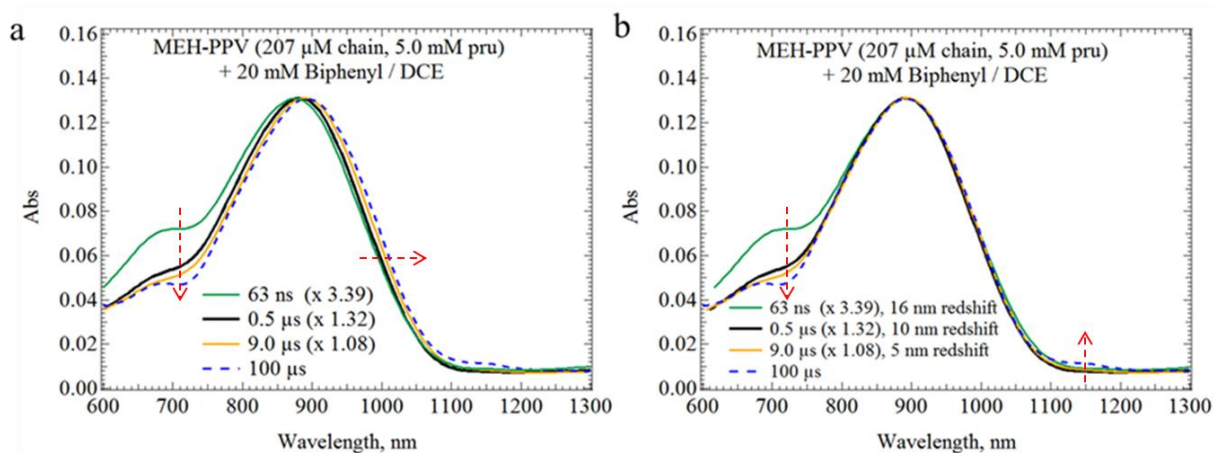


Figure 4-30 Transient absorption spectra at various time intervals, (a) shown normalized and (b) shown normalized with red-shifts to match the absorbance maximum of the 100 μs spectrum.

Based on the unambiguous spectrum of $\text{BP}^{\bullet+}$ in DCE which does not undergo a spectral shift with time, and based on a hole transfer from biphenyl to MEH-PPV which appears to be otherwise reactively innocent, the optical signature of $\text{MEH-PPV}^{\bullet+}$ is best defined near the completion of the hole transfer reaction, which in the blend solution represented in **Figure 4-28** occurs at ~ 600 ns. The peak of the spectrum in this time range is ~ 880 nm.

To determine if slow growth and red shifting spectrum was solvent dependent, a solution of MEH-PPV (41.5 μM chain, 1 mM pru) and biphenyl (10 mM) was prepared in o-DCB. In **Figure 4-31** transient absorption spectra are shown during the growth and partial decay of the MEH-PPV $^{\bullet+}$ bands. The spectral transformations in o-DCB are similar. The presence of $\text{BP}^{\bullet+}$ is evident with a sharp peak at 640 nm which becomes less prominent as MEH-PPV $^{\bullet+}$ grows in. At maximum yield, the spectrum of MEH-PPV $^{\bullet+}$ is virtually identical to the one obtained in DCE after conversion from $\text{BP}^{\bullet+}$.

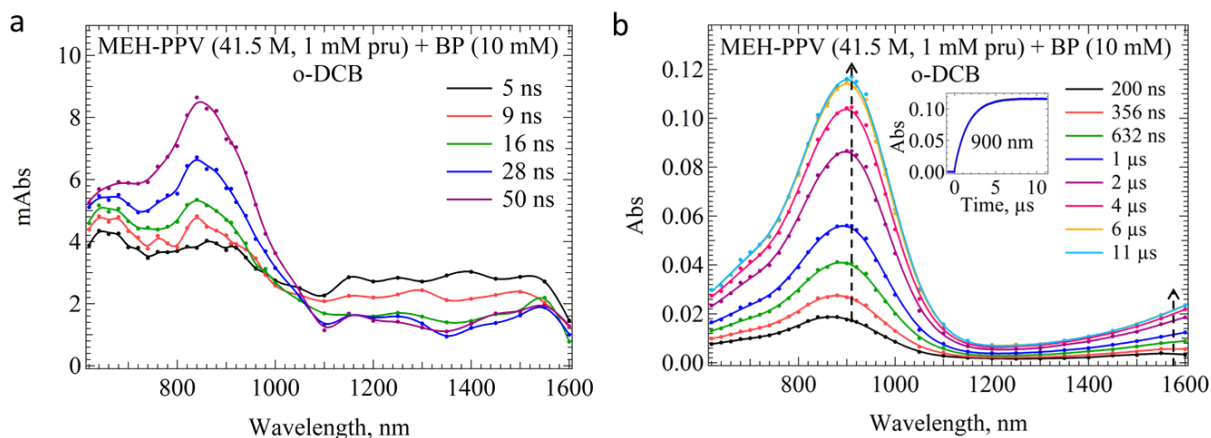


Figure 4-31 Transient absorption spectra corresponding to an *o*-DCB solution of MEH-PPV (41.5 μ M chain, 1 mM pru) at varied time segments after radiolytic pulse, shown over two distinct time ranges: a) from 40 ns – 13 μ s, and b) from 5 ns – 50 ns.

Using a two exponential fit of the growth and decay, a hole transfer rate constant of $1.49 \times 10^{10} \text{ M}^{-1}\text{s}^{-1}$ per chain was determined for conversion of $\text{BP}^{*\cdot}$ to $\text{MEH-PPV}^{*\cdot}$. This rate constant was virtually identical to the theoretical value of $1.52 \times 10^{10} \text{ M}^{-1}\text{s}^{-1}$ determined from the Debye-Smoluchowski equation. The slow decay of $\text{MEH-PPV}^{*\cdot}$ suggests a lifetime in excess of 200 μ s which is nearly 3 orders of magnitude longer than the lifetimes reported for radical cations of small aromatics. While the nature of $\text{BP}^{*\cdot}$ formed radiolytically in *o*-DCB is uncertain, the single rate of formation may suggest a single oxidizing species or an equilibrium between two or more.

Comparing normalized spectra at various times after pulse revealed a redshift consistent with the observation in DCE. Normalizing spectra at 0.2 μ s, 1.0 μ s, 20 μ s and 80 μ s, to the intensity of the 8.0 μ s spectrum, reveals offsets in the spectral peaks in **Figure 4-32 (b)**. Redshifting the spectra to match the peak at 80 μ s as shown in **Figure 4-32 (b)** reveals a redshift of roughly 30 nm from 0.2 μ s to 80 μ s. Due to strong contribution from biphenyl cation at 200 ns, the calculated redshift may be less reliable from this time, but at 1 μ s the contribution is not significant, and a lower limit for the redshift observed between can be estimated as ≥ 10 nm. Unlike the redshifted spectra observed in DCE, no other spectral transformations are observed in *o*-DCB which are difficult to associate with reactions.

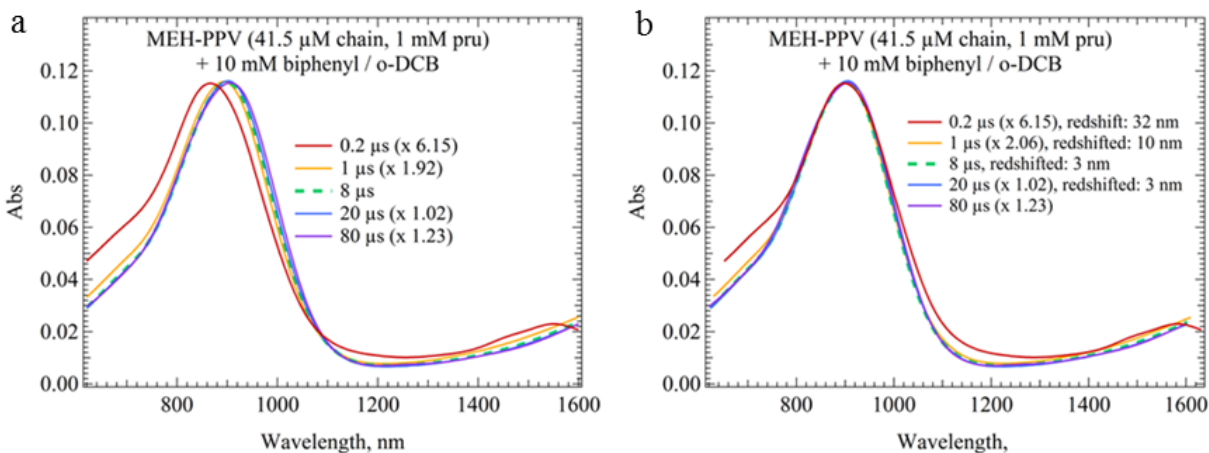


Figure 4-32 Transient absorption spectra corresponding to an *o*-DCB solution of MEH-PPV (41.5 μM chain, 5 mM pru) at 0.5 μs, 9.0 μs, and 100 μs after radiolytic pulse: **(a)** normalized, and **(b)** normalized and red-shifted.

The results signify that a charge neutralization reaction of MEH-PPV^{•+} in *o*-DCB is more efficient in *o*-DCB than in DCE and that redshifts in the spectrum of MEH-PPV^{•+} is not unique to radiolytic oxidation in DCE. This observation suggest two possibilities: 1) that the redshift is due to a solvent effect, or 2) that the redshift is an attribute of the polymer. If the latter is true, it might be a phenomenon relating to systems with delocalized charges. Two aromatic systems with delocalized charges were selected to evaluate comparatively – *p*-terphenyl and terthiophene. The first order kinetics of radical cation formation and decay in *o*-DCB suggest it is preferable for obtaining unambiguous assignments of optical signatures but uncertainty regarding the nature of the biphenyl radical cation and its molar extinction coefficient in *o*-DCB indicates that it cannot be utilized as a good extinction coefficient reference in *o*-DCB. In DCE however, the nature and extinction coefficient of BP^{•+} are clear, and the optical signature determinable based on completion of the hole transfer reaction from the hole transfer intermediate.

Solutions of *p*-terphenyl at 5 mM and of terthiophene at 20 mM were prepared in DCE – without hole transfer intermediate, and their transient absorption spectra investigated.

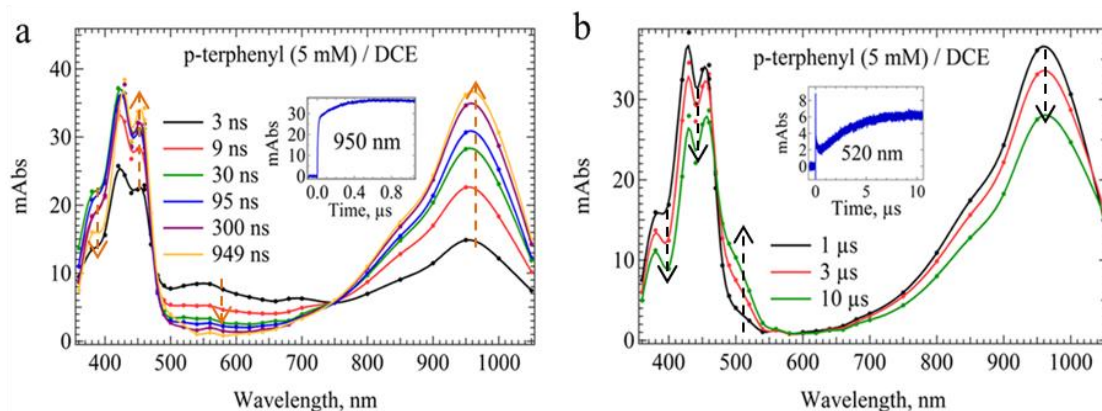


Figure 4-33 Transient absorption spectra of *p*-terphenyl (5 mM) during (a) growth of a visible and NIR band associated with the *p*-terphenyl radical cation, and (b) during their decay.

Transient absorption spectra of *p*-terphenyl in DCE immediately following radiolytic pulse are shown in **Figure 4-33**. Two absorption bands at 450 nm and 950 nm were found to grow in with a fast rate of $1.41 \times 10^8 \text{ s}^{-1}$ (7.1 ns). A second growth rate of $3.00 \times 10^6 \text{ s}^{-1}$ (333 ns) was observed at 950 nm. That a secondary growth rate is not apparent at 450 nm may be the result of an overlapping spectrum of a species decaying as the band grows. This interpretation seems consistent with the observation of absorption decay at 400 nm in the timeframe of 30 ns – 949 ns during which the absorption at 450 nm is virtually constant. While the transient absorption spectrum at the high energy band transforms slightly due to a contribution from two species, that of the lower energy band goes unchanged during the two rates of growth, suggesting that the same species is formed by two oxidizing species which react with the different rates. Interestingly these two formation rates corresponded well with rates of decay measured in the spectral range from 500 nm – 700 nm where solvent cations absorb. The slower of these observed rates was peculiar given that no similar rate of decay for a solvent cation is present in the radiolysis of pristine DCE. It may suggest an equilibrium exists for a slower decaying solvent cation, or that *p*-terphenyl slows down the reaction which depletes the solvent cation. The spectra at completion of the growths in **Figure 4-33** resembled the spectrum of *p*-terphenyl^{•+} obtained by Arai and coworkers in DCE [101] by radiolytic oxidation. In their study however, the irradiating pulse of $\sim 0.5 \mu\text{s}$ resulted in poorer time resolution relative to the measurement shown here. As both bands of *p*-terphenyl^{•+} are observed decaying with a rate of $1.22 \times 10^5 \text{ s}^{-1}$ while a new band grows in at 550 nm with a rate nearly 3 times faster. The

relationship of the decaying p-terphenyl^{•+} and newly forming species is not clear. The results indicate however that two oxidizing species react with p-terphenyl in the absence of biphenyl as a hole transfer intermediate, and that a side reaction or secondary reaction follows the formation of p-terphenyl^{•+} resulting in an unknown byproduct. The spectrum at 1 μs after pulse is a clear optical signature of the radical cation and no red-shifting is observed during the formation or decay of the species.

A transient absorption spectrum of terthiophene (20 mM) as shown in **Figure 4-34** was found to consist of a band with a peak at 540 nm which rapidly formed within the rise time of the detector. A decay of the 540 nm band was concomitant with growth at 580 nm suggesting conversion of some terthiophene radical cations into a new product - possibly dimer cation based on the similar rates of formation at 580 nm and decay at 540 nm. More experiments were not conducted to verify or eliminate the possibility of this assignment.

The results of radiolytic oxidation for MEH-PPV, p-terphenyl and terthiophene do not exhibit similar trends for red-shifting and it is therefore dubious that redshifting is related generally to systems with delocalized charges. The possibility that redshifting may be specifically an attribute of MEH-PPV cannot be ruled out, and some conceivable mechanisms will be later highlighted in the summary section.

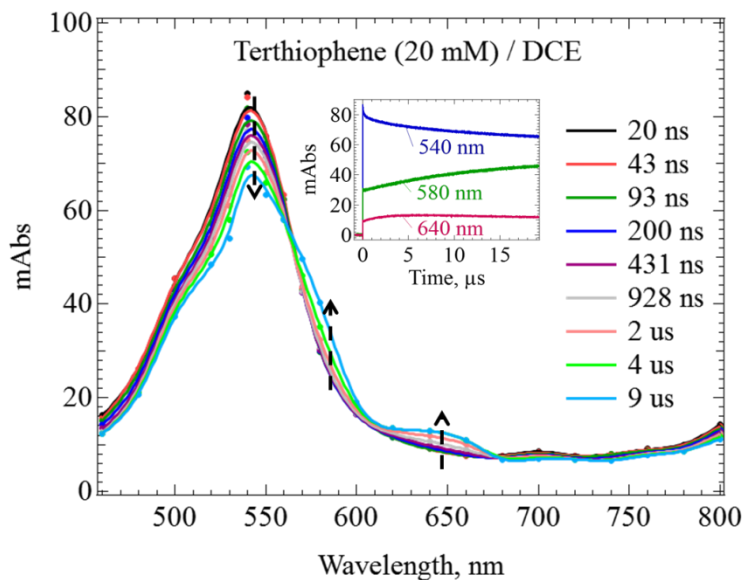


Figure 4-34 Transient absorption spectra following radiolysis of a DCE solution containing terthiophene (20 mM), showing decay of terthiophene^{•+} at 540 nm as new bands form at 580 nm and 650 nm. Absorption transients corresponding to these wavelengths are shown in the inset.

Radiolytic oxidation of other compounds of interest were performed in DCE and compared with results of MEH-PPV. The transient absorption spectrum of perylene diimide (PDI, 1 mM) in DCE, with biphenyl (20 mM) as hole transfer intermediate is shown in **Figure 4-35**. As the spectrum of the biphenyl radical cation (690 nm) is observed decaying from 10 ns after the radiolytic pulse, a concomitant growth is observed at 600 nm with a rate constant of $4.70 \times 10^9 \text{ M}^{-1}\text{s}^{-1}$, which is assigned to PDI^{•+}. A much smaller peak is also observed circa 850 nm. The spectral transformations do not show evidence of redshift, and only a single rate of formation is observed.

The radiolytic oxidation of fSF-PPV via biphenyl radical cation in DCE gives evidence of at least two bands at ~620 nm and ~1450 nm forming at a rate constant of $1.15 \times 10^9 \text{ M}^{-1}\text{s}^{-1}$ per chain ($3.63 \times 10^8 \text{ M}^{-1}\text{s}^{-1}$ pru) as shown in **Figure 4-36**. Due to the overlapping spectra of BP^{•+} and fSF-PPV^{•+} the full decay of BP^{•+} at 690 nm is not observable and only the geminate portion can be seen rapidly decaying. A possible third and smaller band is observed to peak at 1100 nm. As the bands decayed with identical rates, the shape of the high energy band broadened, possibly indicating contribution from a forming degradation byproduct such as deprotonated fSF-PPV.

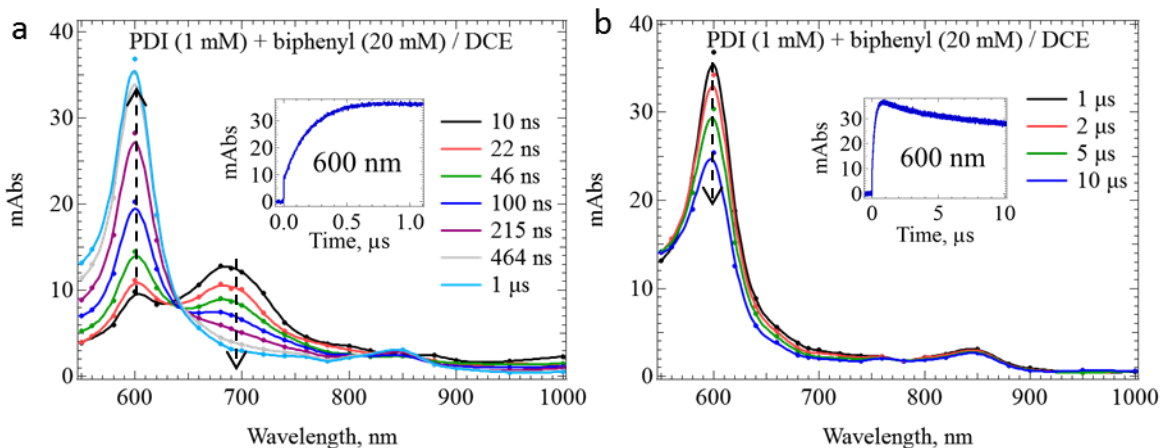


Figure 4-35 Transient absorption spectra following radiolysis of a DCE solution containing PDI (1 mM) and biphenyl (20 mM), showing **a)** growth of a 600 nm band associated with PDI^{•+} concurrent with the decay of a 690 nm band associated biphenyl^{•+} and **b)** decay of the same band. Insets display the 600 nm transients over the timescales of the observed transformations of the corresponding figure.

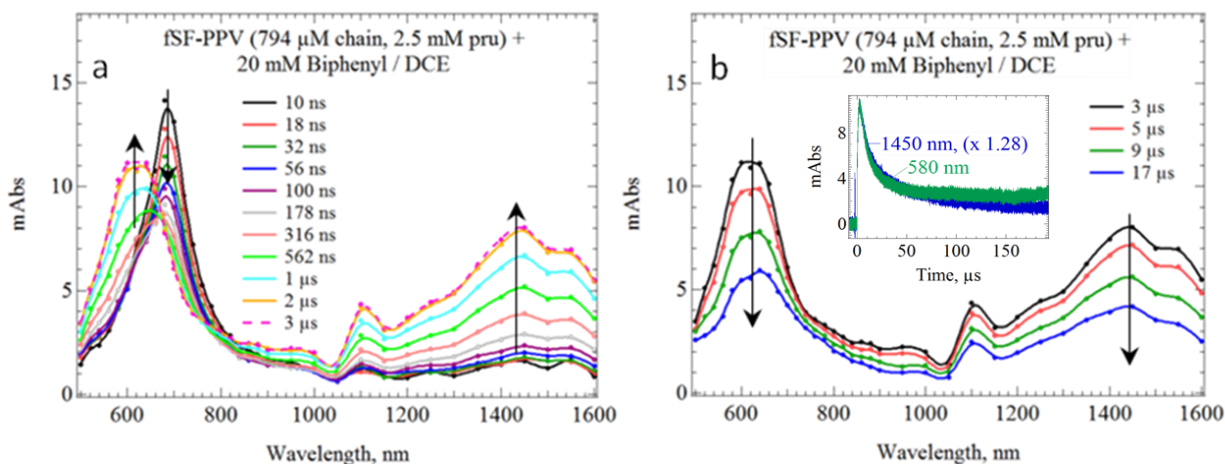


Figure 4-36 Transient absorption spectra following radiolysis of an aerated DCE solution containing fSF-PPV (794 μM, 2.5 mM pru) and biphenyl (20 mM), showing **a)** formation of two bands with peaks at ~620 nm and ~1450 nm associated with fSF-PPV^{•+} which appears to be complete by 2 μs, and **b)** spectral transformations at longer times which involve decay of the bands.

The radiolytic oxidation of pCVPPV via biphenyl radical cation in DCE shows evidence of two radical cation bands circa ~720 nm and ~1450 nm, forming with a rate constant of $2.30 \times 10^{10} \text{ M}^{-1}\text{s}^{-1}$ per chain ($3.00 \times 10^8 \text{ M}^{-1}\text{s}^{-1}$ pru) as shown in **Figure 4-37**. The decay of biphenyl radical

cation is not observable due to the overlapping spectrum of pCVPPV^{•+} which is forming simultaneously. Following the fast rate of formation, a slow spectral transformation is observed which is similar to the spectral transformation observed following the fast oxidation reaction of MEH-PPV. Within the timeframe from 1 μs – 46 μs both of the pCVPPV^{•+} absorption bands are observed redshifting. At the same time, formation of a new species is evident from a growth at 600 nm, but it is unclear whether the two phenomena are correlated.

Radiolytic oxidation of pDPP2FT via biphenyl radical cation in DCE resulted in the formation of a single radical cation band within the allowable range of measurement, with a peak circa 1450 nm. The band is observed to form with a rate of $2.18 \times 10^{10} \text{ M}^{-1}\text{s}^{-1}$ ($6.28 \times 10^8 \text{ M}^{-1}\text{s}^{-1}$ pru). As the 1450 nm band decays a new spectrum with a wavelength under 950 nm forms, a likely degradation byproduct. In the presence of > 1 M toluene, the degradation rate was slowed down by more than an order of magnitude, possibly indicating that the reactant responsible for degradation of pDPP2FT reacts more favorably with toluene, and hence slowing down the rate of reaction with pDPP2FT.

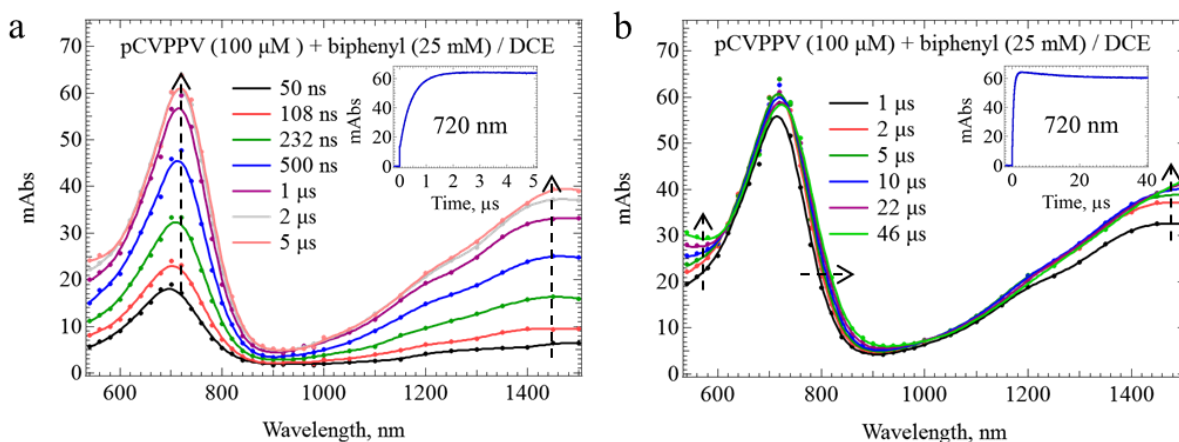


Figure 4-37 Transient absorption spectra following radiolysis of an aerated DCE solution containing pCVPPV (100 μM, 0.7 mM pru) and biphenyl (25 mM), showing **a)** formation of two bands with peaks at 720 nm and ~1450 nm associated with pCVPPV^{•+} which appears to be complete by 2 μs, and **b)** spectral transformations at longer times which involve growth of a new band in the visible and a redshift of the high energy pCVPPV^{•+} band.

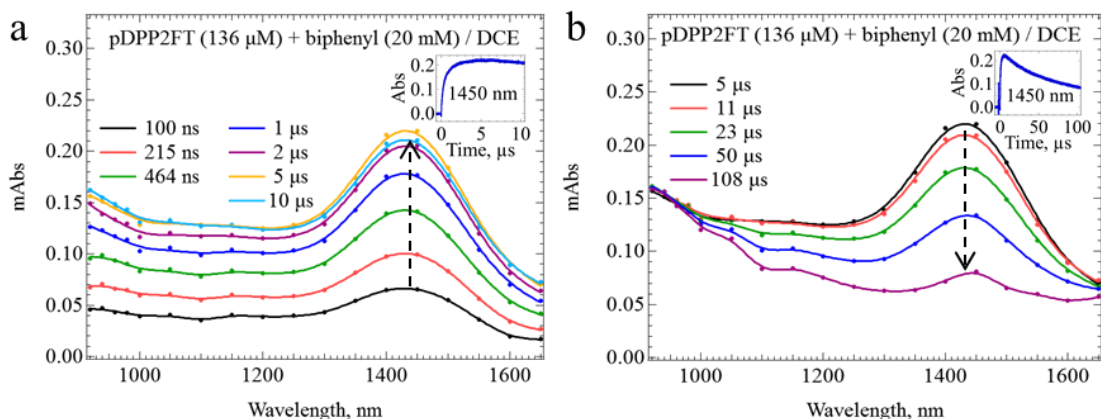


Figure 4-38 Transient absorption spectra following radiolysis of an aertated DCE solution containing pDPP2FT (136 μM , 5 mM pru) and biphenyl (20 mM), showing a) growth of a 1450 nm band associated with pDPP2FT $^{\bullet+}$ and b) decay of the same band. Insets display the 1450 nm transients over the timescales of the observed transformations of the corresponding figure.

Table 4-11 Rate constants of radical cation formation via radiolytic oxidation in DCE and peak wavelengths associated with the formed radical cation.

Solutions in DCE or o-DCB		Species formed (λ_{max})	Rate constant of formation	Diffusion controlled rate constant
Solute of interest	$\text{h}^{\bullet+}$ transfer intermediate			
MEH-PPV in DCE	Biphenyl (20 mM)	MEH-PPV $^{\bullet+}$ (880 nm)	$2.23 \times 10^{10} \text{ M}^{-1}\text{s}^{-1}$ ($9.25 \times 10^8 \text{ M}^{-1}\text{s}^{-1}$ pru)	$2.22 \times 10^{10} \text{ M}^{-1}\text{s}^{-1}$
MEH-PPV in o-DCB	Biphenyl (20 mM)	MEH-PPV $^{\bullet+}$ (890 nm)	$1.49 \times 10^{10} \text{ M}^{-1}\text{s}^{-1}$ ($6.18 \times 10^8 \text{ M}^{-1}\text{s}^{-1}$ pru)	$1.52 \times 10^{10} \text{ M}^{-1}\text{s}^{-1}$
fSF-PPV in DCE	Biphenyl (20 mM)	fSF-PPV $^{\bullet+}$ (540, 1200 nm)	$1.15 \times 10^9 \text{ M}^{-1}\text{s}^{-1}$ ($3.63 \times 10^8 \text{ M}^{-1}\text{s}^{-1}$ pru)	$1.39 \times 10^{10} \text{ M}^{-1}\text{s}^{-1}$
pCVPPV in DCE	Biphenyl (20 mM)	pCVPPV $^{\bullet+}$ (720 nm)	$2.30 \times 10^{10} \text{ M}^{-1}\text{s}^{-1}$ ($2.99 \times 10^9 \text{ M}^{-1}\text{s}^{-1}$ pru)	$> 1.39 \times 10^{10} \text{ M}^{-1}\text{s}^{-1}$ $R(\text{pCVPPV}) > R(\text{fSF})$
pDPP2FT in DCE	Biphenyl (20 mM)	pDPP2FT $^{\bullet+}$ (~1420 nm)	$2.18 \times 10^{10} \text{ M}^{-1}\text{s}^{-1}$ ($6.28 \times 10^8 \text{ M}^{-1}\text{s}^{-1}$ pru)	$1.72 \times 10^{10} \text{ M}^{-1}\text{s}^{-1}$
PDI-hexyl in DCE	Biphenyl (20 mM)	PDI $^{\bullet+}$ (950 nm)	$4.70 \times 10^9 \text{ M}^{-1}\text{s}^{-1}$	$9.96 \times 10^9 \text{ M}^{-1}\text{s}^{-1}$

4.6 Optical signatures of triplets

The radiolysis of benzene produces a high yield of benzene radical ions ($Bz^{\bullet-}$, $Bz^{\bullet+}$) and excited states ($^1Bz^*$, $^3Bz^*$). Due to a large Onsager radius of 25.0 nm which is nearly 4 times larger than that of THF and nearly 5 times larger than that of DCE, ions in benzene rapidly recombine to produce excited states. The principal reactions following radiolysis of pristine benzene are provided in **Table 4-12** and for a benzene solution containing solute "S" are shown in **Table 4-13**. A thorough description of these tabulated reactions is provided below.

Table 4-12 Reactions following radiolysis of Benzene

Reaction step	Reaction	Description
i	$Bz \rightsquigarrow e^{\bullet-} + Bz^{\bullet+}$	Ionization
ii	$Bz \rightsquigarrow ^1Bz^*, ^3Bz^*$	Impact excitation
iii	$e^{\bullet-} + Bz^{\bullet+} \rightarrow ^1Bz^*, ^3Bz^*$	Ion recombination
iv	$^1Bz^* \rightarrow ^3Bz^*$	Intersystem crossing
v	$Bz \rightsquigarrow Bz^{\bullet} + H^{\bullet}$	Benzene fragmentation to phenyl radical & H atom
vi	$Bz + H^{\bullet} \rightarrow BzH^{\bullet}$	Benzene monohydroradical formation
vii	$Bz^{\bullet} + Bz \rightarrow Bz Bz^{\bullet}$	phenyl radical-benzene adduct formation

Table 4-13 Reactions following radiolysis of Benzene solutions containing solute "S"

Reaction step	Reaction	Description
ix	$Bz^* + S \rightarrow S^*$	Energy transfer to solute
x	$Bz^{\bullet+} + S \rightarrow S^{\bullet+}$	Hole transfer to solute
xi	$e^{\bullet-} + S \rightarrow S^{\bullet-}$	Electron transfer to solute
xii	$Bz^{\bullet} + S \rightarrow \text{products}$	Solute degradation

According to the reaction steps shown in **Table 4-12**, radiolysis of benzene ionizes the solvent to produce benzene radical cations and electrons, or to fragment the solvent to

produce phenyl radical and H atom. The total ion yield, $G(\text{ions}) = G(\text{electrons} + \text{Bz}^{+\bullet}) \approx 6.2$ molecules/100 eV [109]. This suggests a G value of 3.1 owing either to electrons or $\text{Bz}^{+\bullet}$ separately. These ions were observed to recombine very rapidly to produce singlet and triplet excited states of Benzene with high efficiency. Cooper and Thomas found that inclusion of biphenyl as a solute resulted in a small yield of biphenyl radical anions and biphenyl radical cations following the 10 ns radiolytic pulse employed. The yield of biphenyl radical anions after pulse was determined as $G(\text{biphenyl}^{\bullet-}) \sim 0.1$ for biphenyl concentrations ranging from 3 mM to 100 mM [109] and would be expected to be equivalent to $G(\text{biphenyl}^{+\bullet})$. This suggests that electrons captured at each concentration of biphenyl belonged to the population having escaped the Onsager radius, which if true, would account for less than 5% of the total population of electrons formed. This result however appears to be at odds with the after-pulse G-value of 1.02 reported by Candeias et. al. for radical cations of N,N,N',N'-tetramethyl-p-phenylenediamine (TMPD) [110] for an oxygen saturated benzene solution of TMPD at 5 mM. The solubility of oxygen in benzene at room temperature and 1 atm is 11.9 mM [110] which is an order of magnitude smaller than the highest concentration of biphenyl used by Cooper and Thomas to determine a $G(\text{biphenyl}^{\bullet-}) \sim 0.1$. The apparent contradiction may be explained in part by differences in the radiolytic pulse length. Substrate conversion efficiency from solvent radical ions to solute radical ions will be limited by the natural lifetime of the solvent ion or by the radiolytic pulse length – whichever is longer. A 10 ns electron pulse width was used in the experiment by Cooper and Thomas and up to 250 ns in the experiment by Candeias et al. A second source of discrepancy may be contributed from the fact that aromatic solutes at sufficiently high concentration may form both geminate radical ions which rapidly recombine, whereas oxygen only scavenges electrons, leaving behind holes to react with other cosolutes.

Fragmentation of benzene via radiolysis produced deprotonated Benzene, $\text{Bz}^{\bullet-}$, and H atom, H^{\bullet} [111]. The yield of radicals, $G(\text{radical}) \approx 0.7$ molecules/100 eV [109], which is approximately $\frac{1}{4}$ of the yield of excited states produced. Both of these byproducts react with neutral benzene to produce other radicals. H atom is rapidly suppressed within 80 ps by reaction with benzene to produce benzene monohydroradical (BzH^{\bullet}) which reacts with the solvent to produce a

phenyl radical-benzene adduct, or may react with an aromatic solute to produce a degradation byproduct.

Table 4-14 Rate constants for radiolytic energy transfer from sensitizing compounds to solutes of interest, and peak wavelengths corresponding to formed triplet products. The hydrodynamic radius of pCVPPV and pDPP2FT in benzene were unknown, but that of pDPP2FT was approximated as equivalent to the estimated value obtained in THF.

Benzene Solution		Species formed (λ_{\max})	Rate constant of formation	Diffusion controlled rate constant
Solute of interest	Triplet sensitizer			
MEH-PPV	Anthracene	$^3\text{MEH-PPV}^*$ (820 nm)	$3.18 \times 10^{10} \text{ M}^{-1}\text{s}^{-1}$ ($1.32 \times 10^9 \text{ M}^{-1}\text{s}^{-1} \text{ pru}$)	$3.30 \times 10^{10} \text{ M}^{-1}\text{s}^{-1}$
fSF-PPV	Biphenyl	$^3\text{fSF-PPV}^*$ (540, 680 nm)	$4.55 \times 10^9 \text{ M}^{-1}\text{s}^{-1}$ ($1.43 \times 10^8 \text{ M}^{-1}\text{s}^{-1} \text{ pru}$)	$\geq 1.22 \times 10^{10} \text{ M}^{-1}\text{s}^{-1}$
pCVPPV	Biphenyl	$^3\text{pCVPPV}^*$ (600 nm)	$9.00 \times 10^9 \text{ M}^{-1}\text{s}^{-1}$ ($1.17 \times 10^9 \text{ M}^{-1}\text{s}^{-1} \text{ pru}$)	N/A
pDPP2FT	Benzophenone	$^3\text{pDPP2FT}^*$ (1050 nm, 1150 nm)	$3.67 \times 10^{10} \text{ M}^{-1}\text{s}^{-1}$ ($1.00 \times 10^9 \text{ M}^{-1}\text{s}^{-1} \text{ pru}$)	$1.61 \times 10^{10} \text{ M}^{-1}\text{s}^{-1}$

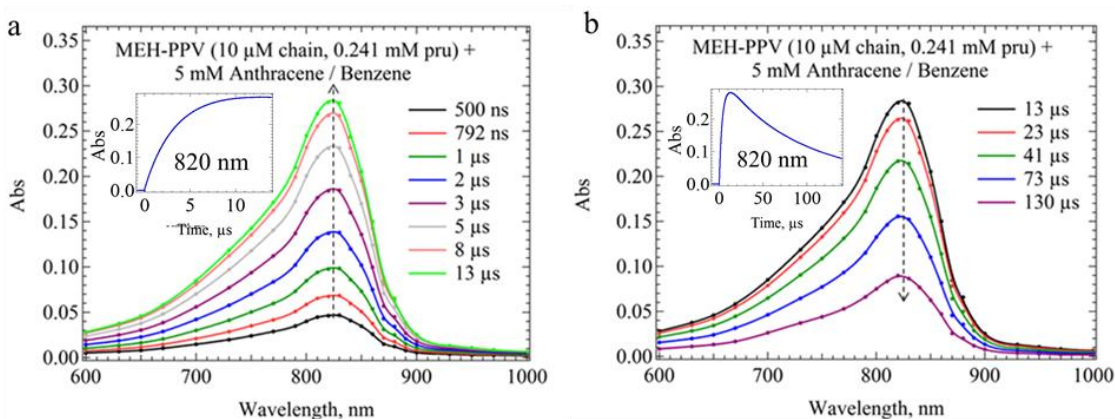


Figure 4-39 Transient absorption spectra at varied time segments following radiolysis of a benzene solution containing MEH-PPV (10 μM chain, 0.241 mM pru) and anthracene (5 mM), showing, (a) formation of an 820 nm band from 500 ns – 13 μs, and (b) decay of the same band from 13 μs – 130 μs.

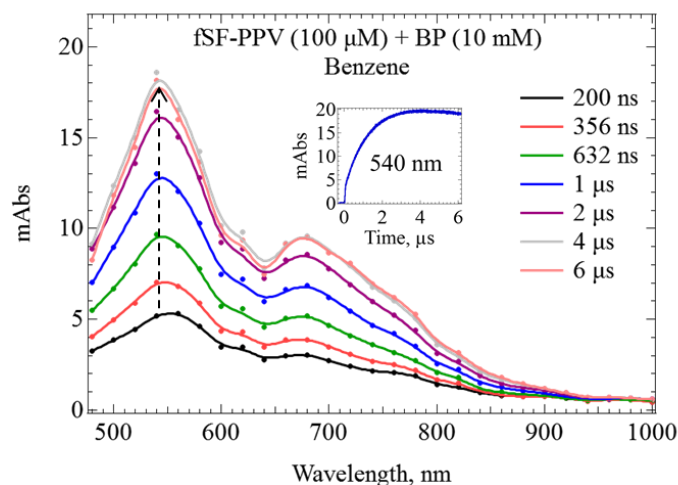


Figure 4-40 Transient absorption spectra at varied time segments following radiolysis of a benzene solution containing fSF-PPV (100 μM chain, 0.315 mM pru) and benzene (10 mM), showing formation of a 540 and 680 nm bands from 200 ns – 6 μs .

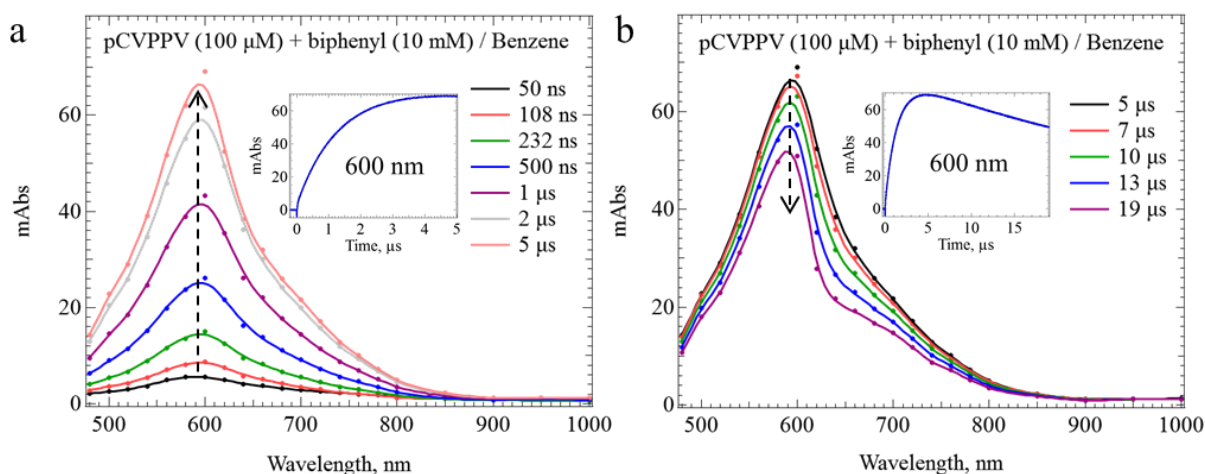


Figure 4-41 Transient absorption spectra at varied time segments following radiolysis of a benzene solution containing pCVPPV (100 μM chain, 0.77 mM pru) and biphenyl (10 mM), showing formation of a 600 nm bands from μs .

The nature of triplets in D-A copolymers have not been well investigated. Triplet energy transfer to pDPP2FT from triplet donors was explored via pulse radiolysis of benzene solutions of the polymer, with and without cosolute sensitizer present.

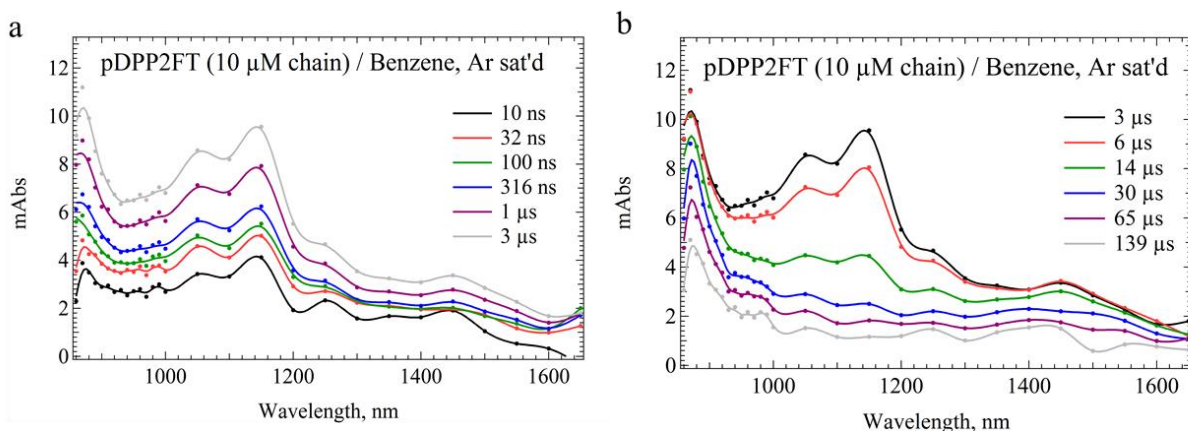


Figure 4-42 Transient absorption spectra collected at varied time segments following radiolysis of 10 μM chain of pDPP2FT in benzene, during (a) growth of three bands (880 nm, 1150 nm, and 1450 nm) and (b) during the decay of those same bands.

Triplet formation of pDPP2FT in the absence of a triplet sensitizer was examined under argon saturated conditions at chain concentration of 10 μM . Under these conditions triplet conversion from $^3\text{Bz}^*$ to $^3\text{pDPP2FT}^*$ is expected but with limited efficiency based on the low concentration of pDPP2FT short lifetime of the $^3\text{Bz}^*$, reported as 2.3 ns [112]. The formation and decay of absorbance bands following radiolytic pulse of the 10 μM solution are shown in **Figure 4-42 (a)** and **Figure 4-42 (b)** respectively.

Three distinct bands are observed with the highest energy band at 800 nm, a mid-energy band with peaks circa 1050 nm and 1150 nm, and a low energy band with a maximum circa 1450 nm. Each of these bands are observed to have nearly identical formation rates as shown in **Figure 4-43** when the absorbance transients are shown with normalized maxima. At 1100 nm growth was observed in three distinct stages: step formation (25%), a fast growth of $1.3 \times 10^8 \text{ s}^{-1}$ (20%) and a slow growth of $9.1 \times 10^5 \text{ s}^{-1}$ (55%). The slowest growth rate seems inconsistent with energy transfer from $^3\text{Bz}^*$ due to the short lifetime of $^3\text{Bz}^*$, and may be an indication of an impurity serving as an intermediate triplet donor.

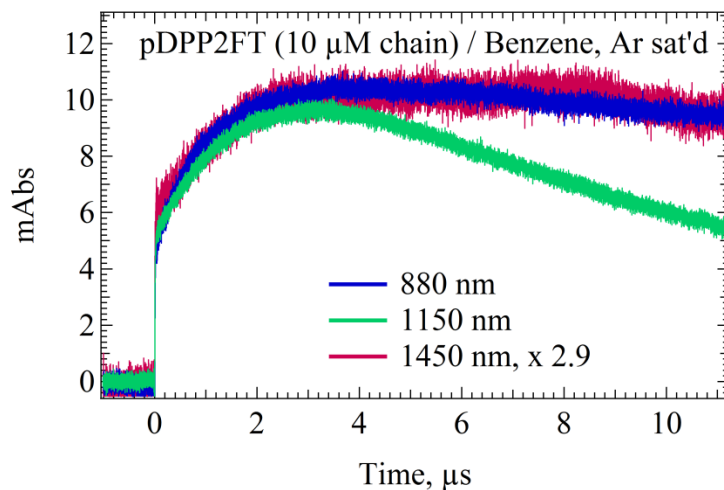


Figure 4-43 Absorption transients collected at 880 nm, 1150 nm, and 1450 nm following radiolysis of an argon saturated benzene solution of pDPP2FT (10 μM chain) showing similar formation kinetics within the first 2 μs after pulse.

In spite of the nearly identical rates of formation at 880 nm, 1150 nm and 1450 nm, the 1150 nm transient was found to exhibit a different decay rate than either the 880 nm or 1450 nm transient, suggesting that the mid energy band is due to a different species than the lower and higher energy bands. In the case of the 10 μM solution, the 1450 nm band resembles that of the radical ions of pDPP2FT.

To further investigate the identities of the three bands, pDPP2FT was prepared at 25 μM chain in benzene to determine the effect of higher polymer concentration on relative yields of each under argon saturated condition. Furthermore, by saturating the same solution with oxygen, the effect of O₂ on the relative yields of the bands at same polymer concentration might also help to elucidate the identities of the species giving rise to each band. The formation and decay of absorbance bands following radiolytic pulse of the 25 μM solution are shown in **Figure 4-44 (a)** and **Figure 4-44 (b)** respectively.

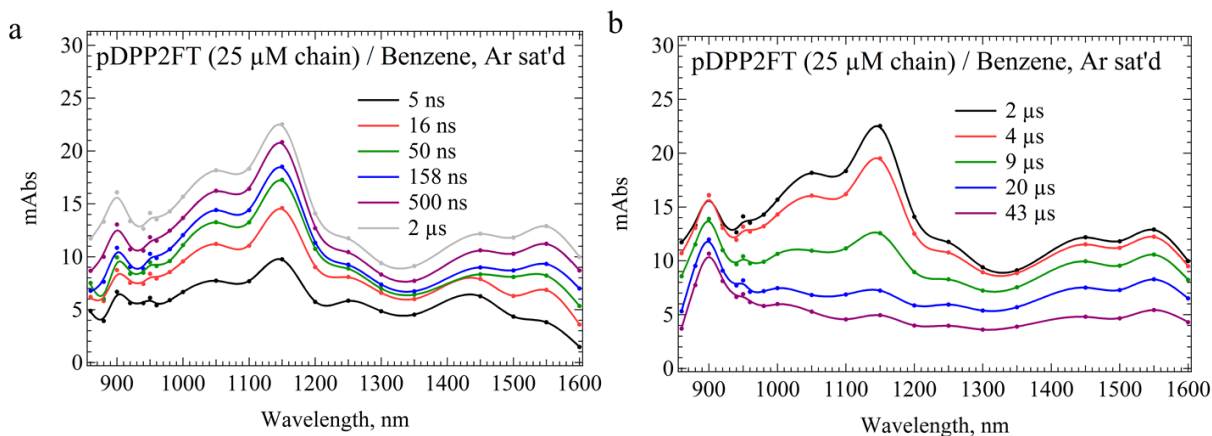


Figure 4-44 Transient absorption spectra following radiolysis of an argon-saturated benzene solution of pDPP2FT (25 μM chain) during (a) the growth at 1150 nm, and (b) decay at 1150 nm.

The 25 μM solution is found to also exhibit three spectral bands but with different relative yields than observed in the 10 μM solution. Once again, in spite of nearly equivalent formation rates at 880 nm, 1150 nm, and 1450 nm, the 1150 nm band is once again observed to exhibit a faster decay than either the 880 nm or 1450 nm bands. In **Figure 4-45**, absorption transients at 880 nm, 1150 nm and 1450 nm are shown for the 10 μM pDPP2FT solution (**a**) and the 25 μM solution (**b**) where the 880 nm transients were rescaled to best match the early kinetics at 1450 nm. By viewing the transients in this way, it seems conceivable that a single slow decaying species is responsible for the slow decaying species at each of these wavelengths. If so, then this would indicate that at the conclusion of the fast decay at 1150 nm, the spectrum owes nearly entirely to that single species.

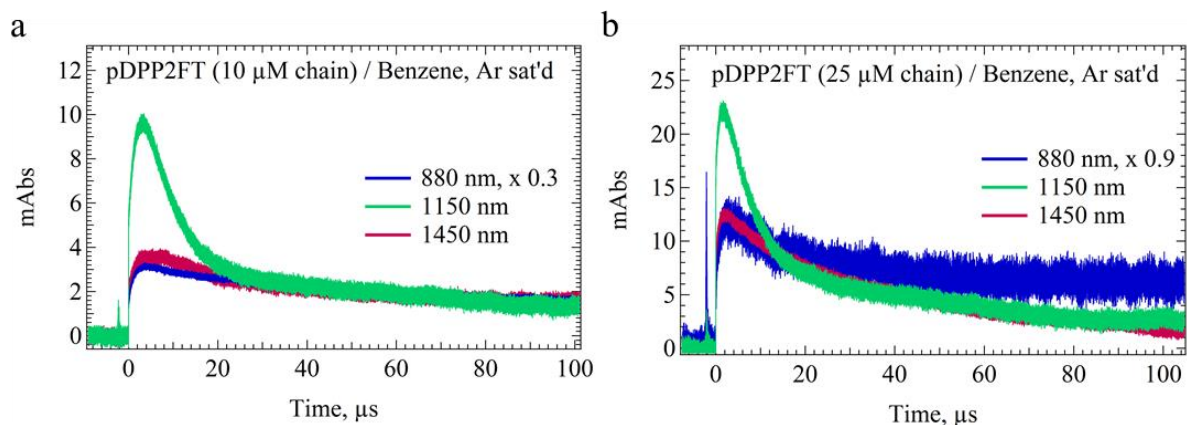


Figure 4-45 The 880 nm, 1150 nm, and 1450 nm absorption transients of argon saturated benzene solutions of pDPP2FT on a 100 μ s timescale, shown at chain concentrations of: (a) 10 μ M and (b) 25 μ M. For either solution, similar slow decays are exhibited at the three wavelengths suggesting a common source for each.

In an attempt to further distinguish the species, benzophenone was used as a triplet sensitizer at 0.1 M in the presence of 25 μ M pDPP2FT. The formation and decay of the absorption bands following radiolytic pulse of this solution are shown in **Figure 4-46 (a)** and **(b)** respectively. The yield of the 1050 nm improved substantially relative to either 880 nm or 1450 nm indicating that 1050 nm species is the likely byproduct of the triplet transfer from benzophenone.

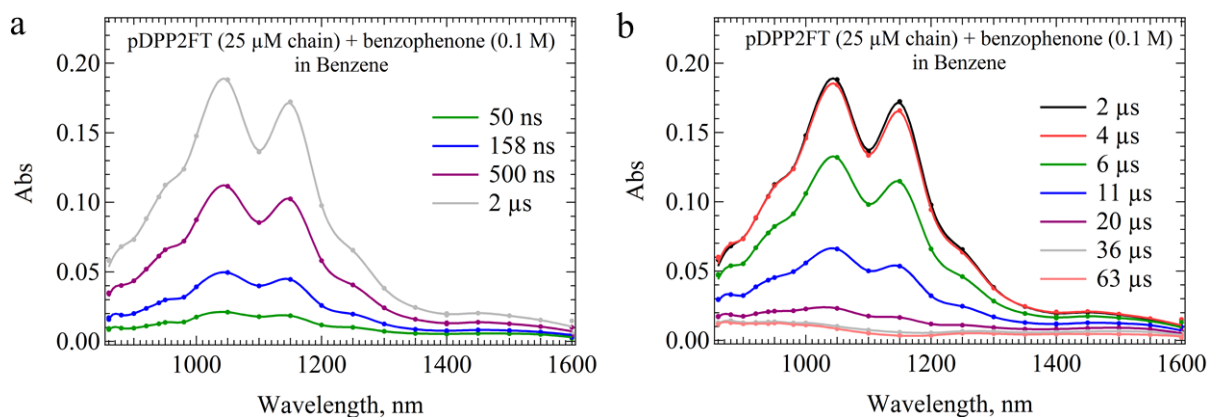


Figure 4-46 The transient absorbance spectra following radiolysis of a benzene solution containing pDPP2FT (25 μ M chain) and benzophenone (0.1 M), shown during: (a) the growth of a spectral band and (b) decay of the same band.

Next, a 25 μM pDPP2FT solution was prepared and O_2 saturated by bubbling with O_2 for one minute and then promptly resealed. The formation and decay of the absorbance bands following radiolytic pulse of this solution are shown in **Figure 4-47 (a)** and **(b)** respectively. The spectra are similar to the ones obtained using benzophenone as a triplet sensitizer in the argon saturated solution.

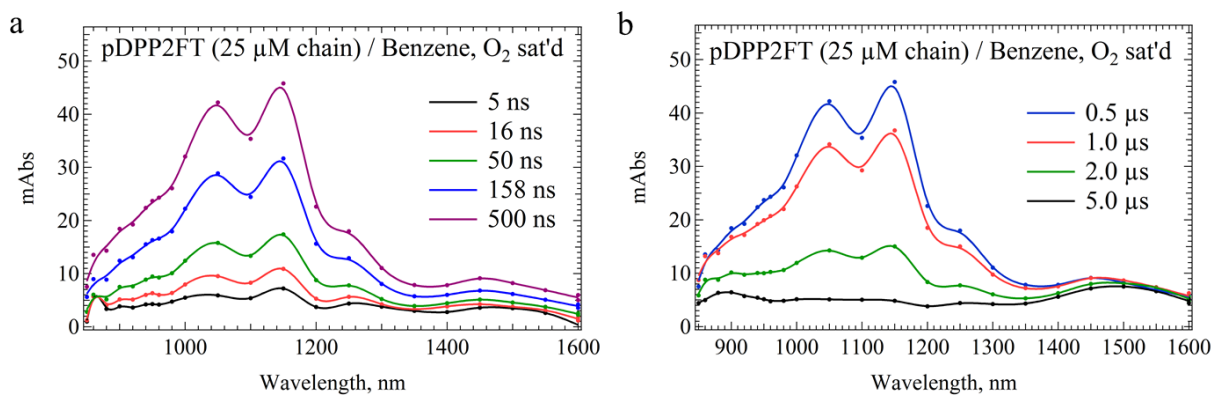


Figure 4-47 The transient absorption spectra following radiolysis of an oxygen saturated benzene solution containing pDPP2FT (25 μM chain), shown during: (a) the growth of a spectral band and (b) decay of the same band.

In **Figure 4-48** the 1150 nm transients corresponding to each of the 25 μM pDPP2FT solutions – argon-saturated without cosolute, argon-saturated with benzophenone, and oxygen saturated are shown. Comparing the yields of $^3\text{pDPP2FT}^*$ in the argon-saturated solutions – with and without benzophenone, gives a ratio of nearly 10:1. Comparing the yields of $^3\text{pDPP2FT}^*$ in the solutions without cosolute – O_2 saturated versus argon saturated, appears to give a ratio of $\sim 2:1$. If true, this would suggest that oxygen acts to both transfer triplets to and deplete triplets from pDPP2FT. This could occur if an equilibrium exists.

In the presence of oxygen, the low energy band at ~ 1500 nm persists, indicating it is likely a cationic species. Oxygen typically functions as an effective electron acceptor and energy acceptor in radiolytic reactions with aromatic compounds. Oxygen typically reacts with radical anions at a diffusion controlled rate, and triplets at $1/9$ the diffusion controlled rate due to spin statistics.

The formation rate of $^3\text{pDPP2FT}^*$ by conversion from $^3\text{benzophenone}^*$ was determined by single exponential fit as $9.17 \times 10^5 \text{ s}^{-1}$ corresponding to a pseudo first order rate constant of $3.67 \times 10^{10} \text{ M}^{-1}\text{s}^{-1}$ which is consistent with a diffusion controlled rate constant. For the oxygen saturated solution, a 2 exponential fit of the rise and decline of the signal provided rates of $3.0 \times 10^6 \text{ s}^{-1}$ and $9.8 \times 10^5 \text{ s}^{-1}$, respectively. Assuming the rise of the signal to be associated with the formation of $^3\text{pDPP2FT}^*$ would give a formation rate constant of $1.2 \times 10^{11} \text{ M}^{-1}\text{s}^{-1}$ which is an order of magnitude greater than diffusion controlled and not feasible.

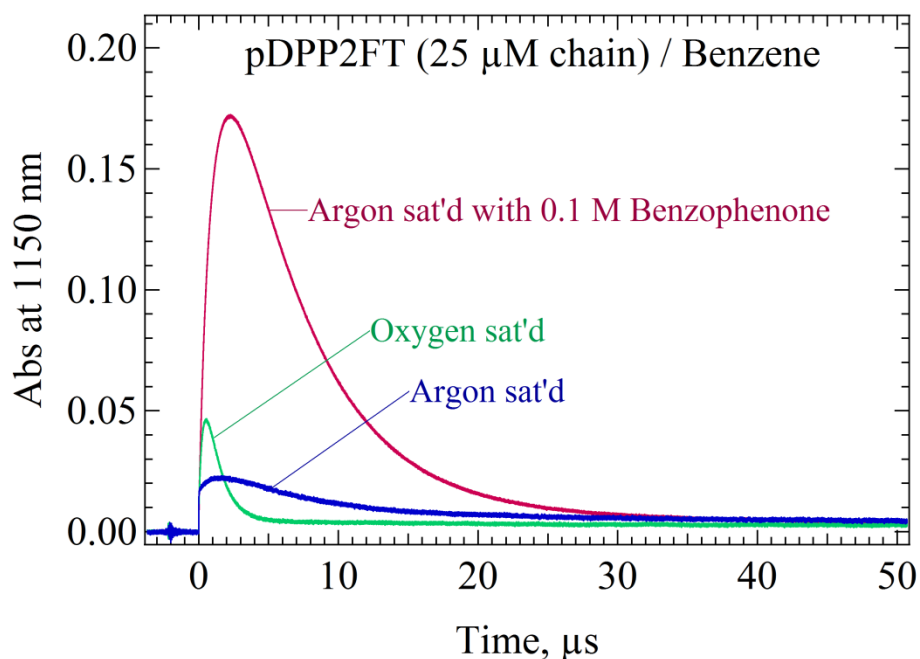


Figure 4-48 The 1150 nm absorbance transients collected following radiolytic pulse of benzene solutions containing 25 μM pDPP2FT collected under argon saturated condition In the absence of a cosolute (blue), argon saturated condition in the presence of 0.1 M benzophenone (red) and oxygen saturated condition in the absence of a cosolute (green).

For a kinetic signal with a rise and decline, the rise of the signal may represent the formation or the decay of a species – whichever is fastest. Conversely, the decline of the signal may represent the formation or decay of a species – whichever is slowest. This scenario is illustrated in **Figure 4-49**. It is therefore plausible that the signal rise corresponds to the decay of $^3\text{pDPP2FT}^*$ and the decline corresponds to the formation of $^3\text{pDPP2FT}^*$. This view would indicate that at 25 μM of pDPP2FT, $^3\text{pDPP2FT}^*$ forms with nearly identical rates in the oxygen

saturated solution as it does in an argon saturated solution with 0.1 M benzophenone, and would indicate that oxygen serves as a triplet sensitizer for pDPP2FT. In this view, the yield of $^3\text{pDPP2FT}^*$ produced in the oxygen-saturated solution can be compared with the yield formed in the argon saturated solution without cosolute by integrating their signals. Performing this integration indicated that the yields were equivalent within 10% in both solutions. This view is favored over the interpretation that $^3\text{pDPP2FT}^*$ forms at an order of magnitude faster than diffusion controlled. Nevertheless, in this interpretation, ironically O_2 it appears is involved in a complicated equilibrium with $^3\text{pDPP2FT}^*$.

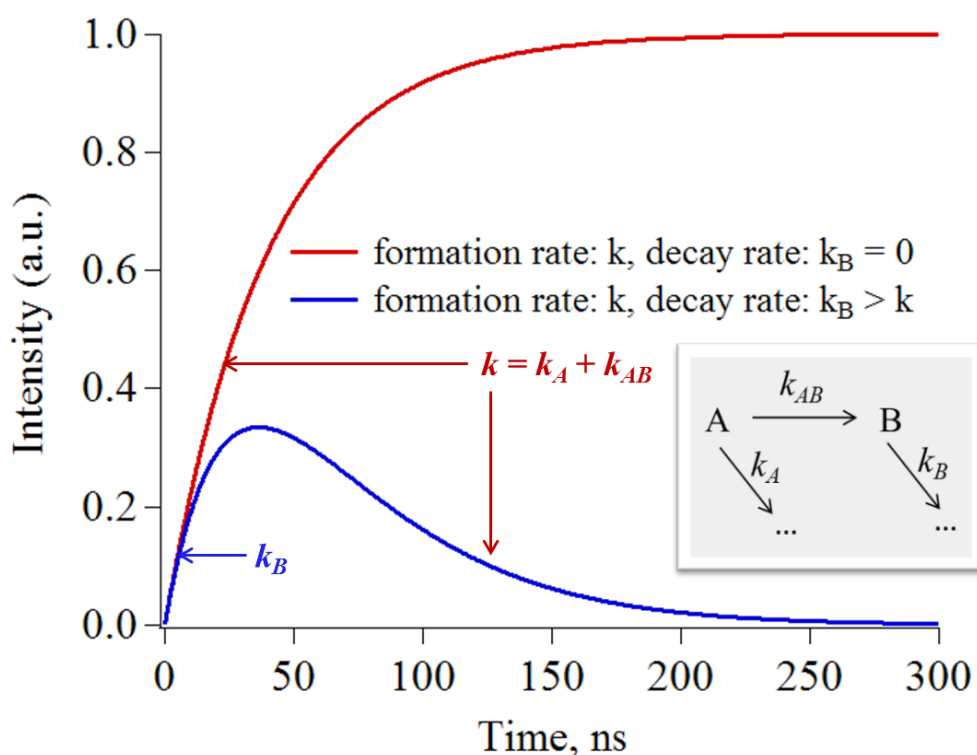


Figure 4-49 Time evolution of a species “B” shown relative to two conditions where its decay rate, k_B is smaller than its observed formation rate, k (shown in red) and for which $k_B > k$ (shown in blue). The reaction scheme shown in the inset, involves conversion of the transient species A into the transient product B, with a rate of k_{AB} . The natural decay rate of A defined as k_A , leads to an observed rate of formation, $k = k_A + k_{AB}$ for B. The time evolution of B will contain a rise which reflects the rate of k or k_B , whichever is largest. In the example shown, rates were assigned as $k_A = 2.0 \times 10^7 \text{ s}^{-1}$, $k_B = 3.0 \times 10^7 \text{ s}^{-1}$, and $k_{AB} = 5.0 \times 10^6 \text{ s}^{-1}$.

In a bimolecular reaction for which one reactant, A is a transient species which may be converted into another transient species B via conversion rate k_{AB} , the observed formation rate

of B, defined as k , will be a sum of k_{AB} and k_A where the latter rate is associated with the natural lifetime of A. If the natural lifetime of the new transient species B is defined as k_B , the observed rise and decay will depend on whether k or k_B is larger. If $k_B > k$, then the rise of the time evolution of B will have a rise which reflects the rate of k_B and a decay that reflects the rate of k . An example of this condition is shown in. Assuming that this condition applies to the observed kinetics for the $^3\text{pDPP2FT}^*$ may suggest O_2 is an effective triplet sensitizer for pDPP2FT, possibly facilitating a reversible triplet transfer. A possible mechanism for this reaction is shown in **Figure 4-50**.

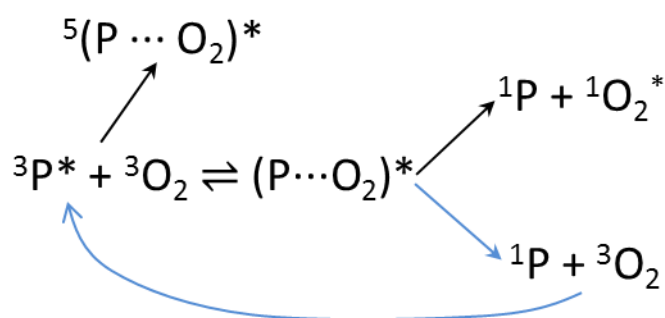


Figure 4-50 A proposed scheme for an equilibrium between a polymer triplet and ground state oxygen triplet.

Based on the interpretation of a rise rate that corresponds with the depletion of $^3\text{pDPP2FT}^*$ and a decay rate that reflects the formation of the species, the depletion of the triplet in the presence of oxygen would be $2.6 \times 10^8 \text{ M}^{-1}\text{s}^{-1}$ while the measured decay rate of $9.8 \times 10^5 \text{ s}^{-1}$ suggests a formation rate constant of $3.9 \times 10^{10} \text{ M}^{-1}\text{s}^{-1}$ for $^3\text{pDPP2FT}^*$, which is near to if not diffusion controlled. If this rate constant is assumed to be equivalent to the rate of encounter between $^3\text{O}_2$ and $^3\text{pDPP2FT}^*$, the expected decay rate would be 1/9 of this, or $4.3 \times 10^9 \text{ M}^{-1}\text{s}^{-1}$ which is 16.5 times faster than the $2.6 \times 10^8 \text{ M}^{-1}\text{s}^{-1}$ rate constant determined. This would suggest that $E(^3\text{pDPP2FT}^*) < E(^1\text{O}_2^*)$ resulting in an equilibrium possibly following a kinetic scheme identified in **Figure 4-50**.

The transient absorption spectra of the oxygenated pDPP2FT solution and argon saturated pDPP2FT solution with 0.1 M benzophenone are similar at maximum yield, but differences are observed. In the solution with benzophenone, the 1050 nm peak is more intense than the 1150

nm peak whereas the opposite is true in the oxygenated solution. This observation was repeatable in separate measurements. At low concentrations, the T-T absorption associated with $^3\text{pDPP2FT}^*$ is more prone to error due to contributing absorption from impurities or unwanted radiolytic byproducts. The degree of error contribution in the spectra is best evaluated by normalizing the peak of a spectrum at lower intensity to the peak of the maximum intensity band and examining the extent of deviation. For both the argon saturated solution with benzophenone and the oxygenated solution without cosolute, spectral shapes at lower yields were found to exhibit strong deviations relative to the respective maximum yield spectra. The possibility was previously considered that for the argon saturated benzene solutions containing only pDPP2FT, that the radiolytic byproduct responsible for the slow decaying component of the 1150 nm transient may also be responsible for the 880 nm and 1450 nm transients and therefore the 1150 nm transient may be corrected by subtracting the contribution of the species. In **Figure 4-51** the 1150 nm and 1450 nm absorbance transients of the argon saturated and oxygen saturated benzene solutions containing pDPP2FT at 25 μM chain, are shown.

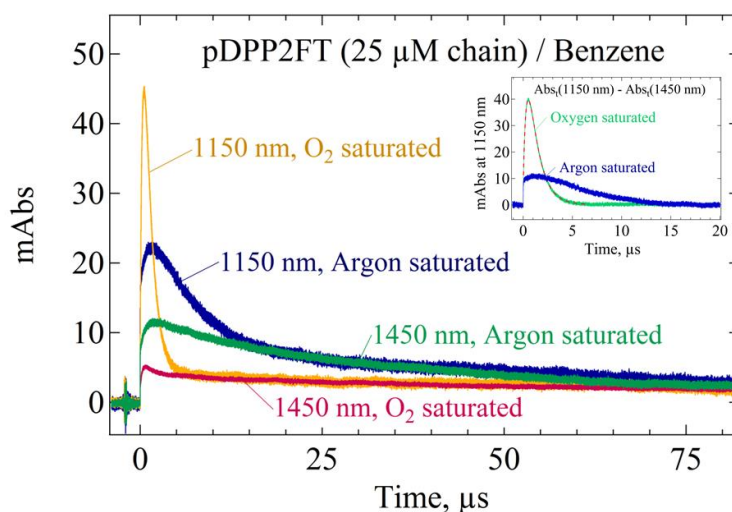


Figure 4-51 The absorbance transients of argon saturated and oxygen saturated benzene solutions of pDPP2FT (25 μM chain) at 1150 nm and 1450 nm. The 1450 nm transient is presumed to be almost entirely due to a byproduct other than $^3\text{pDPP2FT}^*$ and 1150 nm is presumed to contain absorbance contribution of the 1450 nm species and $^3\text{pDPP2FT}^*$. Subtraction of the 1450 nm transients from the 1150 nm transients then resulted in transients which decayed to zero and approximated the time dependence of $^3\text{pDPP2FT}^*$ only.

An inset provides transients corresponding to the 1150 nm transients following subtraction of the 1450 nm transients. Due to the rapid decay of the 1150 nm transient in the oxygen saturated solution, the yield of the 1450 nm species is virtually constant over this time frame. If the 1450 nm and 880 nm transients are due to a single species such as a degradation byproduct, the spectrum of the species must be very broad. For the oxygenated solution the concentration of the unknown species is nearly time invariant at times $\geq 0.5 \mu\text{s}$ following radiolytic pulse but its spectrum not discernible until the complete decay of the fast component of the 1150 nm transient, corresponding to $5.0 \mu\text{s}$. Hence, subtraction of the spectrum at $5.0 \mu\text{s}$ from spectra collected at time segments $\geq 0.5 \mu\text{s}$ should render an accurate spectral shape corresponding to $^3\text{pDPP2FT}^*$, which are time invariant. Corrections to the transient absorption spectra at $0.5 \mu\text{s}$, $1.0 \mu\text{s}$, and $2.0 \mu\text{s}$ after pulse were made using this method and the corrected spectra shown in **Figure 4-52 (a)** as calculated, and **(b)** with normalizing constants. The small deviations in the spectral shapes at the various time segments in **Figure 4-52 (b)** suggest that the spectrum is in fact the proper optical signature of $^3\text{pDPP2FT}^*$. Within the spectral range of measurement allowable, only one spectral band is apparent, with two maxima circa 1050 nm and 1150 nm, and an absorption edge close to 1400 nm.

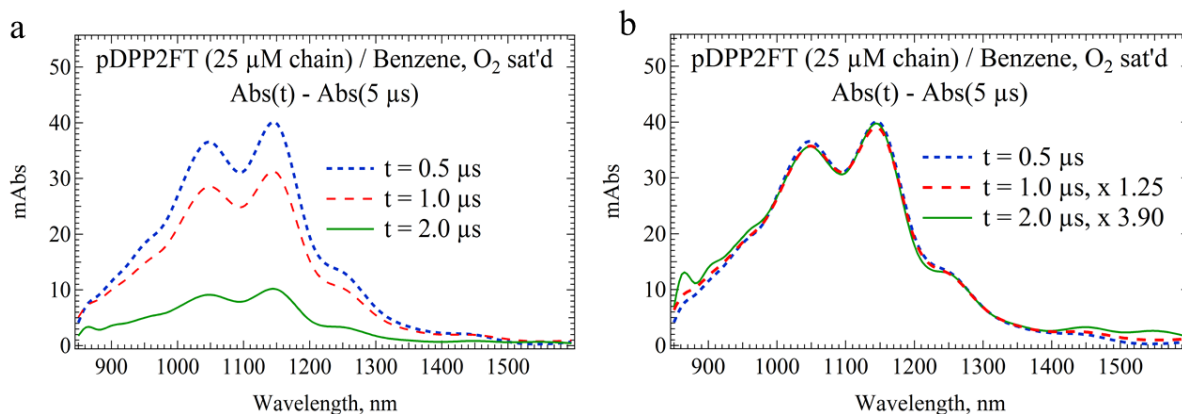


Figure 4-52 The corrected spectra corresponding to $^3\text{pDPP2FT}^*$ produced by subtracting the transient at $5 \mu\text{s}$ associated with a different species which is nearly time invariant in yield at time segments of $0.5 \mu\text{s} \leq t \leq 5 \mu\text{s}$.

4.7 Discussion and Summary

The optical signatures corresponding to radical ions and triplets of MEH-PPV, pCVPPV, and pDPP2FT have been presented, in addition optical signatures of radical ions and triplets of acceptor compounds fSF-PPV, PDI, and PDI-phenyl have been collected and presented, along with others. Transient absorption spectra following radiolysis of THF solutions and benzene solutions were fairly straightforward in most cases, but transient absorption spectra in chlorinated solvents were complicated by multiple oxidants and ambiguous byproducts. Using biphenyl as a hole transfer intermediate for MEH-PPV was found to largely suppress other oxidation pathways and the conversion of biphenyl^{•+} to MEH-PPV^{•+} occurred with a rate that was diffusion controlled according to the Debye-Smoluchowski equation. The spectrum of biphenyl^{•+} in DCE was identical to that identified in literature, giving confidence that the byproduct of conversion would also have a radical cation character. Using biphenyl as a hole transfer intermediate was therefore beneficial and formation of radical cations by transfer from biphenyl could be distinguished from other reactions on the basis of reaction rates. As such, the best condition for determining optical signatures was immediately following completion of the hole transfer reaction from biphenyl.

In the transient absorption spectra of DCE solutions, side reactions or secondary reactions observed following formation of the radical cations of interest were observed as mentioned. The spectral changes occurred during decay of the radical cations of interest and were therefore distinguishable. In the case of terthiophene the similar rate of decay at 540 nm and formation of a product at 580 nm may indicate a degradation byproduct which absorbs in a similar range as the terthiophene^{•+} given the transformation of the spectral band. In the case of p-terphenyl, two rates of formation for the radical cation bands at 450 nm and 950 nm were observed giving evidence of two oxidants, followed by decay of the p-terphenyl^{•+} bands and formation of a new band at 550 nm at a rate three times faster rate. As the 550 nm band grows, no other spectral changes are evident. The new band may correspond to a solvent byproduct in equilibrium with p-terphenyl^{•+} but a solid assignment is inconclusive. Decay of pDPP2FT and PDI radical cations produce what appear to be degradation byproducts which

absorb with maxima blue-shifted relative to the radical cation bands. In none of these transient spectra are redshifts of the initial cation bands discernible. The transient spectra of MEH-PPV and pCVPPV however give evidence of such a redshift, and furthermore exhibit very slow decays – much slower than observed from other radical cations. While blueshifts in spectra of radical ions may correspond to ion-pairing, redshifts are unusual and to our knowledge unprecedented and not cited in literature for conjugated polymers. The redshift was evident for MEH-PPV in DCE and o-DCB – with or without biphenyl present. These results seemingly indicate that the observed redshift is not only real but likely due to some property of MEH-PPV and pCVPPV. A single common quality in MEH-PPV and pCVPPV is the presence of phenylenevinylene. A conceivable source of a redshift then may be a cis-trans isomerization similar to what has been shown to occur following oxidation of some substituted stilbenes [113] but never before for MEH-PPV.

According to the FBC model, two absorption bands are expected of radical ions of aromatic oligomers and polymers. Radical anions and radical cations of PDI and PDI-phenyl exhibited single absorption bands as expected, while MEH-PPV, pCVPPV, and fSF-PPV exhibited two prominent bands. A third smaller band was exhibited in the spectra of radical ions corresponding to fSF-PPV, indicating weakly coupled forbidden transitions. The radical ions of pDPP2FT only exhibited a single optical band within the region of measurement. It may be possible that a second band overlaps the ground state spectrum and was therefore not possible to observe. An alternate possibility may be that the electronic structure of the D-A copolymer results in a deviation from the trends predicted by the FBC model which may be more compatible with conventional conjugated homopolymers.

The bimolecular rate constants for radical ion formation and triplet formation were evaluated with respect to theoretical diffusion controlled rate constants where possible. Assuming the value of hydrodynamic radius for MEH-PPV to be accurate, and radiolytic reduction of MEH-PPV to be diffusion controlled led to an estimate for the reaction radius of the solvated electron, calculated as 0.25 Å. Applying an assumed electron radius of 0.25 Å and the van der Waals radius for perylene diimid in the D-S equation, a theoretical diffusion controlled rate constant for the radiolytic reduction of perylene diimide by a solvated electron

resulted in a value that was within 15% of the experimental value. Based on the self consistency of this result, the estimated reaction radius of the solvated electron in THF seems reasonably accurate. A survey of literature revealed no similar estimate for reaction radius of the electron in THF, indicating this may be the first of its kind. In the case of the 24 monomer MEH-PPV, the hydrodynamic radius was estimated based on the reported hydrodynamic radius of a longer MEH-PPV chain in THF. Using the reaction radius of the solvated electron in THF, and the D-S equation, the reaction radii of other compounds are estimated.

Radiolytic oxidation and radiolytic triplet energy transfer reactions were also found to be near diffusion controlled for almost all compounds. An exception was found for fSF-PPV for which radiolytic oxidation and triplet transfer reactions were significantly slower than diffusion control. A charge or energy transfer reaction which is significantly slower than diffusion controlled can result from an activation energy, and/or reorganization energy which are significant, or due to an equilibrium involving a forward and reverse rate. An equilibrium for a charge transfer reaction would result in an increase in forward reaction rate from the initially charged species to the initially neutral species as the concentration of the initially neutral species is increased, also resulting in an increased yield of charges associated with the initially neutral species. In the slow reaction involving hole transfer from biphenyl^{•+} to fSF-PPV, the possibility of an equilibrium was considered by examining the reaction rates and yields of fSF-PPV^{•+} produced when the starting concentration of fSF-PPV was fixed at 400 μ M while concentrations of biphenyl at 6.5 mM and 55 mM of biphenyl were explored in DCE. At both concentrations of biphenyl, the condition of [biphenyl] \gg [fSF-PPV] ensured that > 90% of the radiolytically formed solvent cations would be scavenged by biphenyl to facilitate the hole transfer reaction.

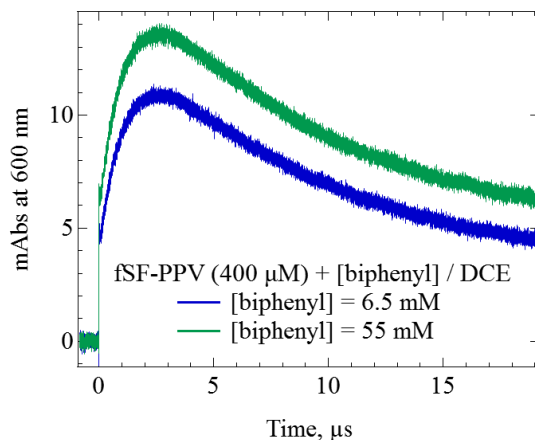


Figure 4-53 Absorption transients at 650 nm following radiolysis of DCE solutions containing 400 μM fSF-PPV + [biphenyl], where [biphenyl] was prepared at 6.5 mM and 55 mM. The rate of formation for fSF-PPV^{•+} was the same in both solutions while the yield improved at 55 mM biphenyl indicating that the hole transfer reaction involved no equilibrium.

An equilibrium would then decrease the yield and forward formation rate of fSF-PPV^{•+} at 55 mM of biphenyl relative to the condition at 6.5 mM. Instead, as observed in **Figure 4-53**, the rate of formation for fSF-PPV^{•+} was invariant with the change in biphenyl concentration, and actually increased in yield with increase in biphenyl concentration indicating that an equilibrium was not present. That the yield of fSF-PPV^{•+} actually increased is explained by the improved efficiency of conversion from solvent radical cations to biphenyl radical cations due to the higher concentration of biphenyl used. As will be shown in the following chapter, a reversible triplet transfer between biphenyl and fSF-PPV could also be ruled out. That reactions of biphenyl^{•+} with compounds with similar energetics as fSF-PPV yielded diffusion controlled reactions indicated that an inverted region was not responsible. Instead, the results may indicate a high reorganization energy is involved in hole transfer and triplet transfer to fSF-PPV from biphenyl.

Chapter 5: Extinction coefficients & energetics

5.1 Methodology for determination of extinction coefficients and energetics

In Chapter 4, radiolysis of solutions containing a solute Q and a transfer intermediate, R for which $[R] \gg [Q]$ were used to form high yields of Q^S . If the decay of R^S in the absence of Q is denoted as $k_{d-}(R^S)$ and is known, and the molar extinction coefficient of R^S denoted as $\varepsilon(R^S)$ is known, then the molar extinction coefficient of Q^S can be determined based on the formation rate of Q^S observed from **Eq 4-3**. The value of $k_{d-}(R^S)$ may be determined from a control solution which only contains R at a concentration equivalent to that found in the binary solution with Q as cosolute. The fraction of R^S that converts to Q^S , must be determined in order to calculate $\varepsilon(Q^S)$ accurately. This fraction will be referred to as the conversion efficiency, ϕ , which can be defined as:

$$\phi = \frac{[Q^S]}{[R^S]} = \frac{k_f[Q]}{k_f[Q] + k_{d-}(R^S)} \quad 5-1$$

Here k_f represents the rate constant of formation for Q^S according to **Eq 4-3**.

Equation 5-1 suggests that R^S decays by a single rate of $k_{d-}(R^S)$ but in a more general case, we may consider that R^S decays by more than one rate, such that a conversion efficiency can be defined for each decay population. If there are n decaying subsets, the decay rate of the n^{th} may be denoted as $k_{d-}(R^S)_n$ and the fraction of this subset relative to the whole denoted as f_n such that the conversion efficiency of the n^{th} subset may be denoted as ϕ_n . The overall conversion efficiency for the entire population can then be defined as a weighted sum of the various efficiencies of the subsets according to:

$$\phi_{total} = \sum_n (f_n * \phi_n) \quad 5-2$$

The conversion of each subset is then defined as:

$$\phi_n = \frac{k_f[Q]}{k_f[Q] + k_{d-}(R^S)_n} \quad 5-3$$

The extinction coefficient of Q^S can then be defined as:

$$\varepsilon(Q^S)_{\lambda_{Q^S}} = \frac{Abs_{tot}(R^S)_{\lambda_{R^S}}}{Abs_{tot}(Q^S)_{\lambda_{Q^S}}} * \frac{\varepsilon(R^S)_{\lambda_{R^S}}}{\phi_{total}} \quad 5-4$$

The term $Abs_{tot}(R^S)_{\lambda_{R^S}}$ is the absorbance associated with total yield of R^S formed in **Eq** Error! Reference source not found. measured at a wavelength λ_{R^S} where R^S absorbs with negligible contribution from other species, and $Abs_{tot}(Q^S)_{\lambda_{Q^S}}$ is the absorbance associated with the full yield of Q^S formed in **Eq 4-3** measured at a wavelength λ_{Q^S} where Q^S absorbs with negligible contribution. The time dependence of the yield of a species such as R^S and Q^S may be defined by an equation of n exponentials from which the values of $Abs_{tot}(R^S)_{\lambda_{R^S}}$ and $Abs_{tot}(Q^S)_{\lambda_{Q^S}}$ can be determined. Such an equation may describe only the formation or decay of the species, or both. To generalize, an equation of n exponentials describing the formation and decay of a species A may be defined as:

$$[A(t)] = [A]_{\infty} + \sum_{i=1}^n [A]_i * exp(-k_i t) \quad 5-5$$

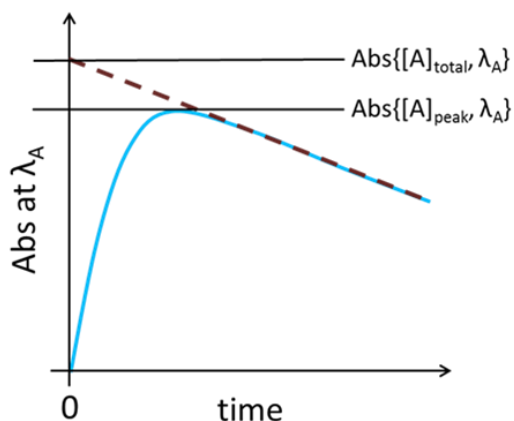


Figure 5-1 An illustration of the formation and decay of species “Q” whose total and peak yields are shown as $Abs([Q]_{total}, \lambda_Q)$ and $Abs([Q]_{peak}, \lambda_Q)$, with the former acquired by a backward extrapolation of the decay back to time zero.

The term $[A(t)]$ is the concentration of A at a given time t , while $[A]_i$ represents a fraction of the total population of A formed which forms or decays with a rate constant k_i , and $[A]_\infty$ represents a residual, non-decaying fraction of A . The total yield of A can be determined by evaluating the decay term(s) at $t = 0$. This is equivalent to extrapolating the fast decay component of $[A(t)]$ back to $t = 0$. An illustration of the absorbance growth and decay of species A is shown in **Figure 5-1** with a relationship between the peak absorbance of the kinetic trace defined by **Eq 5-5** and total absorbance determined at wavelength λ_A where only species A absorbs.

In this work, extinction coefficients of radical ions and triplets are determined using the methodology presented above. The energetics of certain radical ions and triplets were also determined. The energetics were determinable by selecting a compound R with which Q forms an equilibrium of the form:



For such an equilibrium if the energy of R^S , denoted as $E(R^S)$ is known, then the energy of Q^S may be determined as:

$$E(Q^S) = E(R^S) + \Delta G_{RQ}^0 \quad 5-7$$

Here, is define in terms of the equilibrium constant, K_{eq} where $\Delta G_{RQ} = -0.0257 * \ln K_{eq}$ and $K_{eq} = [R][Q^S]/[R^S][Q]$. To determine these equilibria, a wavelength λ_{Q^S} at which Q^S absorbed with negligible contribution of other species was identified, and the relative absorbance of the species monitored at varied concentrations of R .

Using the optical signatures provided in the previous chapter values for $\varepsilon(Q^S)_{\lambda_{Q^S}}$ and $E(Q^S)$ are determined. The following references for extinction coefficient references were used as shown in **Table 5-1**.

Table 5-1 Molar extinction coefficients of species used as references

Reference	$\varepsilon(R^{\bullet})$	λ	Solvent	Literature reference
biphenyl ^{•-}	$1.25 \times 10^4 \text{ M}^{-1}\text{cm}^{-1}$	650 nm	THF	[114]

anthracene ^{•-}	$1.00 \times 10^4 \text{ M}^{-1}\text{cm}^{-1}$	720 nm	THF	[115]
biphenyl ^{•+}	$1.045 \times 10^4 \text{ M}^{-1}\text{cm}^{-1}$	690 nm	DCE	[116]
perylene ^{•+}	$2.70 \times 10^4 \text{ M}^{-1}\text{cm}^{-1}$	550 nm	Benzonitrile	[117]
³ anthracene*	$4.55 \times 10^4 \text{ M}^{-1}\text{cm}^{-1}$	430 nm	Benzene	[118]
³ biphenyl*	$2.71 \times 10^4 \text{ M}^{-1}\text{cm}^{-1}$	370 nm	Benzene	[118]

5.2 Extinction coefficients of radical anions

The extinction coefficients of radical anions determined in this work are tabulated in **Table 5-2**. The corresponding figures showing absorption transients of the reference and the species to which they were converted are shown below.

Table 5-2 Extinction coefficients of radical anions determined by electron transfer from references with known extinction coefficients

Species	Extinction coefficient	Wavelength	Reference
MEH-PPV ^{•-}	$6.9 \times 10^4 \text{ M}^{-1}\text{cm}^{-1}$	900 nm	anthracene ^{•-}
MEH-PPV ^{•-}	$7.0 \times 10^4 \text{ M}^{-1}\text{cm}^{-1}$	1100 nm	e ^{•-} (in THF)
fSF-PPV ^{•-}	$2.6 \times 10^4 \text{ M}^{-1}\text{cm}^{-1}$	650 nm	MEH-PPV ^{•-}
pCVPPV ^{•-}	$8.8 \times 10^4 \text{ M}^{-1}\text{cm}^{-1}$	650 nm	biphenyl ^{•-}
pDPP2FT ^{•-}	$1.1 \times 10^5 \text{ M}^{-1}\text{cm}^{-1}$	1400 nm	anthracene ^{•-}
PDI ^{•-}	$1.4 \times 10^4 \text{ M}^{-1}\text{cm}^{-1}$	950 nm	anthracene ^{•-}

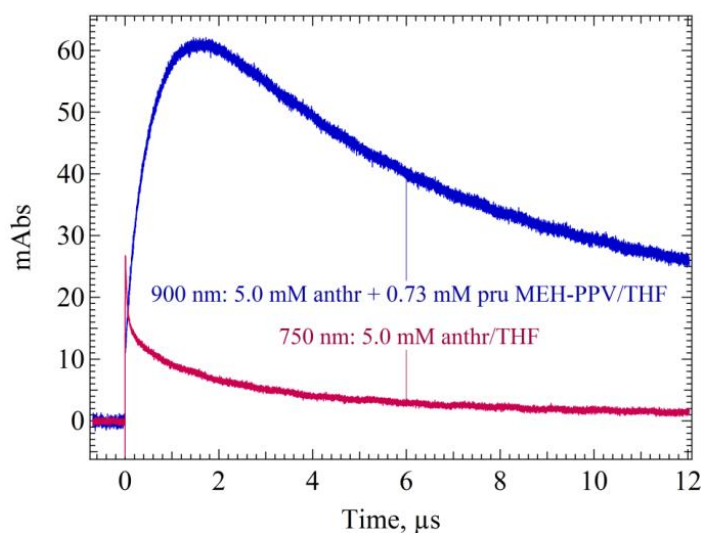


Figure 5-2 A 900 nm absorption transient corresponding to a blend solution of MEH-PPV (0.73 mM pru) and anthracene (5.0 mM) in THF, plotted with a 750 nm absorption transient of a control solution containing anthracene at 5 mM in THF.

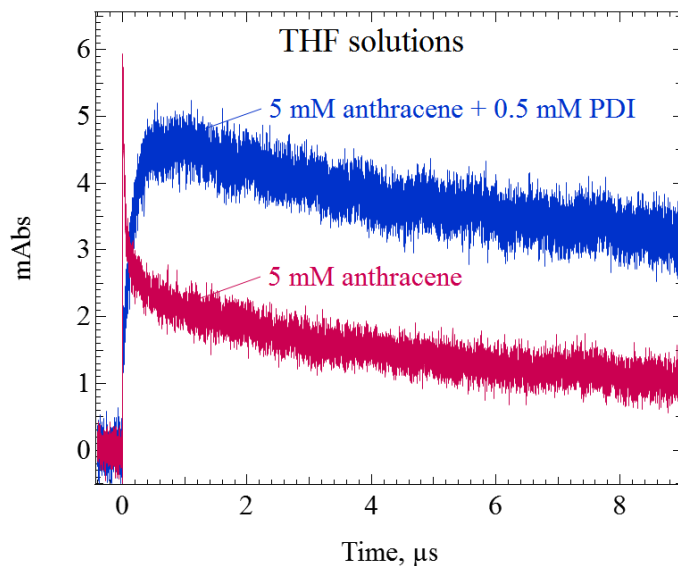


Figure 5-3 A 950 nm absorption transient corresponding to a blend solution of perylene diimide (0.5 mM *pru*) and anthracene (5.0 mM) plotted in THF, with a 750 nm absorption transient of a control solution containing anthracene at 5 mM in THF.

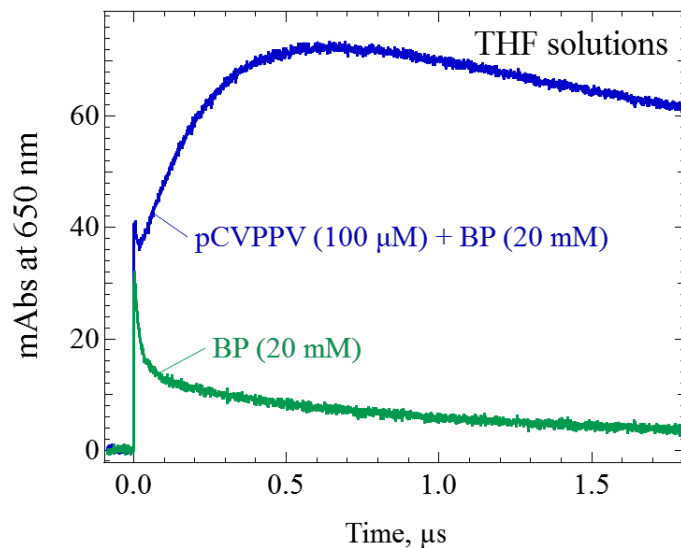


Figure 5-4 A 650 nm absorption transient corresponding to a blend solution of MEH-PPV (0.73 mM *pru*) and anthracene (5.0 mM) in THF, plotted with a 750 nm absorption transient of a control solution containing anthracene at 5 mM in THF.

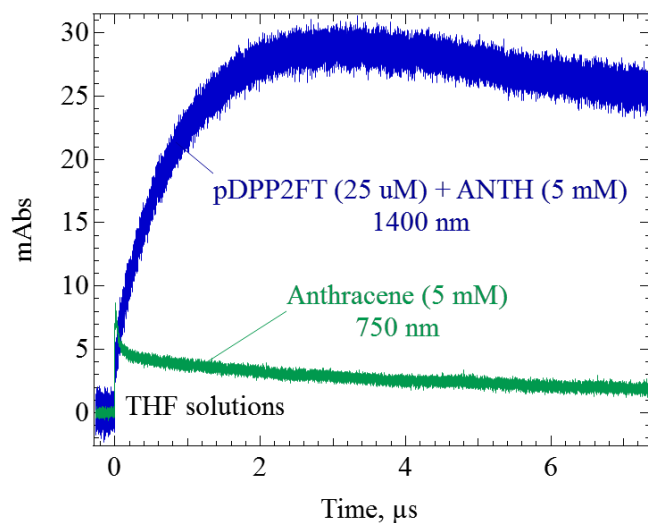


Figure 5-5 A 1400 nm absorption transient corresponding to a blend solution of pDPP2FT (25 μM) and anthracene (5.0 mM) in THF, plotted with a 750 nm absorption transient of a control solution containing anthracene at 5 mM in THF.

5.3 Extinction coefficients & energetics of radical cations

The extinction coefficients of radical cations determined in this work are tabulated in **Table 5-3**. The corresponding figures showing absorption transients of the reference and the species to which they were converted are shown below.

Table 5-3 Extinction coefficients of radical cations determined by hole transfer from references with known extinction coefficients

Species	Extinction coefficient	Wavelength	Reference
MEH-PPV ^{•+}	$1.2 \times 10^5 \text{ M}^{-1}\text{cm}^{-1}$	900 nm	perylene ^{•+}
pCVPPV ^{•+}	$4.6 \times 10^4 \text{ M}^{-1}\text{cm}^{-1}$	650 nm	biphenyl ^{•+}
fSF-PPV ^{•+}	$1.8 \times 10^4 \text{ M}^{-1}\text{cm}^{-1}$	650 nm	biphenyl ^{•+}
pDPP2FT ^{•+}	$1.8 \times 10^5 \text{ M}^{-1}\text{cm}^{-1}$	1400 nm	perylene ^{•+}
pDPP2FT ^{•+}	$1.8 \times 10^5 \text{ M}^{-1}\text{cm}^{-1}$	1400 nm	biphenyl ^{•+}
PDI ^{•+}	$4.5 \times 10^4 \text{ M}^{-1}\text{cm}^{-1}$	600 nm	biphenyl ^{•+}

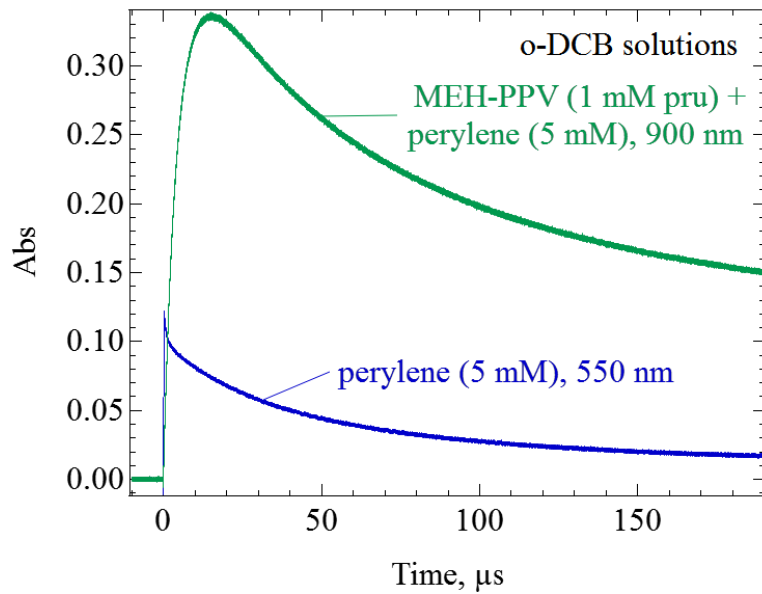


Figure 5-6 The 900 nm absorption transient of a blend solution containing MEH-PPV (1.0 mM pru) and perylene (5.0 mM) in o-DCB, shown with the 550 nm absorption transient of a control solution containing perylene only at 5.0 mM in o-DCB.

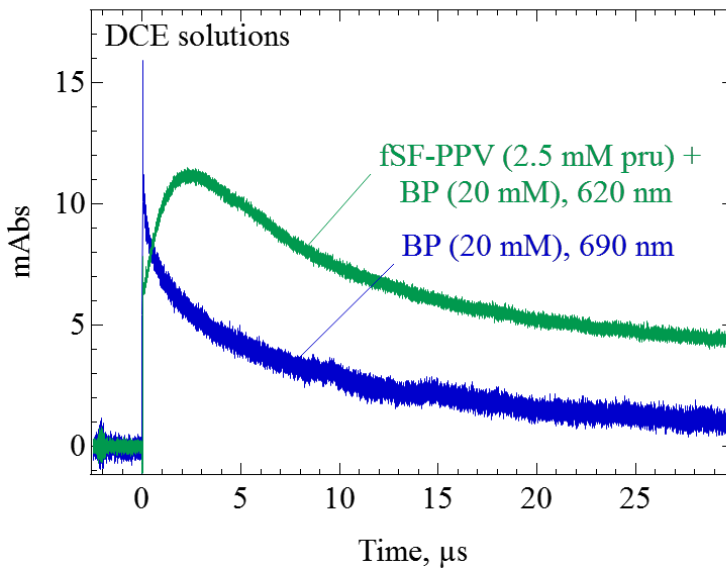


Figure 5-7 The 620 nm absorption transient of a blend solution containing fSF-PPV (2.5 mM pru) and biphenyl (20 mM), shown with the 690 nm absorption transient of a control solution containing perylene only (5.0 mM).

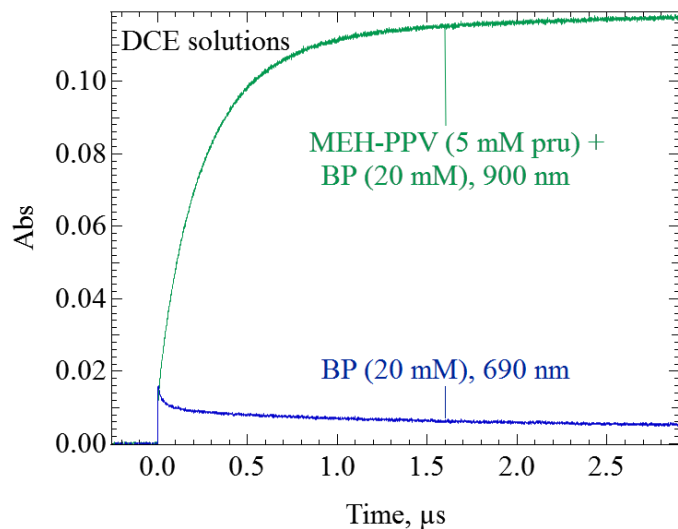


Figure 5-8 The 900 nm absorption transient following radiolysis of a blend solution containing MEH-PPV (5 mM pru) and biphenyl (20 mM) in DCE, shown with the 690 nm absorption transient of a control solution in DCE containing biphenyl only at 20 mM.

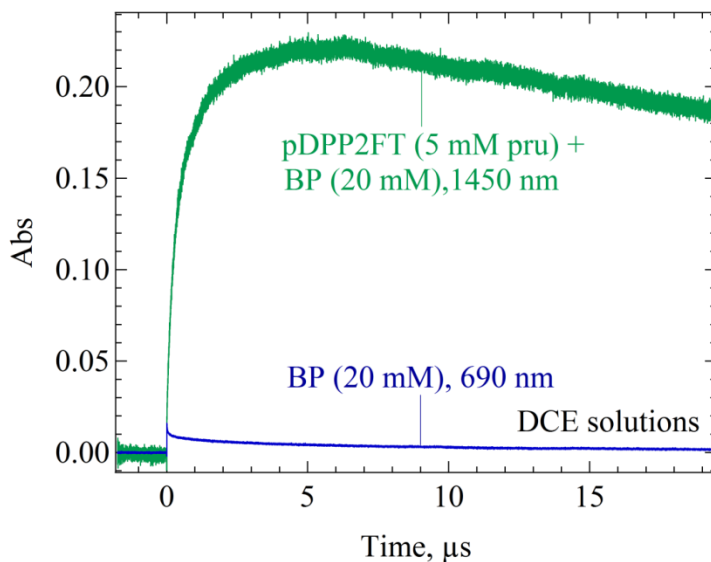


Figure 5-9 The 1450 nm absorption transient following radiolysis of a blend solution containing MEH-PPV (5 mM pru) and biphenyl (20 mM) in DCE, shown with the 690 nm absorption transient of a control solution in DCE containing biphenyl only at 20 mM.

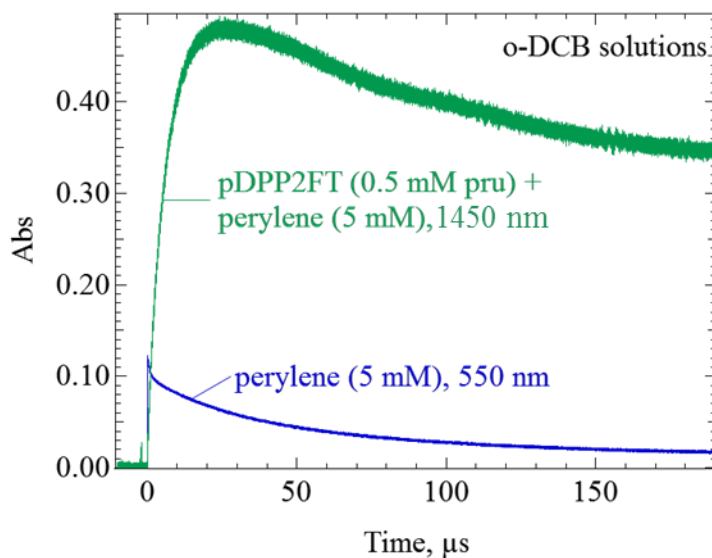


Figure 5-10 The 1400 nm absorption transient following radiolysis of a blend solution containing MEH-PPV (5 mM pru) and biphenyl (20 mM) in *o*-DCB, shown with the 550 nm absorption transient of a control solution in *o*-DCB containing perylene only at 20 mM.

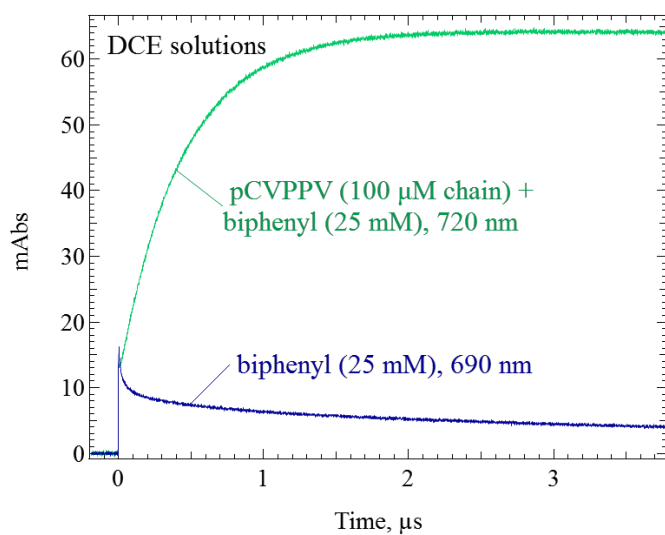


Figure 5-11 The 720 nm absorption transient following radiolysis of a blend solution containing pCVPPV (5 mM pru) and biphenyl (20 mM) in *o*-DCB, shown with the 550 nm absorption transient of a control solution in *o*-DCB containing perylene only at 20 mM.

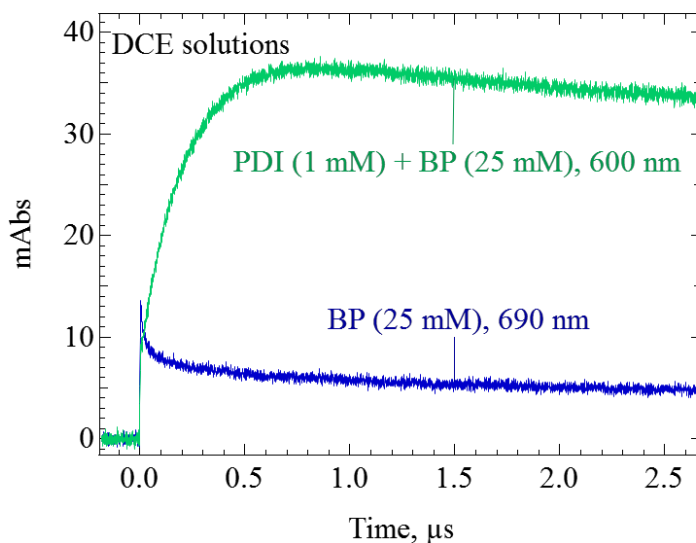


Figure 5-12 The 720 nm absorption transient of a blend solution containing pCVPPV (5 mM) and biphenyl (20 mM) in *o*-DCB, shown with the 550 nm absorption transient of a control solution in *o*-DCB containing perylene only at 20 mM.

5.4 Extinction coefficients of triplets

The extinction coefficients of radical cations determined in this work are tabulated in **Table 5-4**. The corresponding figures showing absorption transients of the reference and the species to which they were converted are shown below.

Table 5-4 Extinction coefficients of triplets determined by triplet transfer from references with known extinction coefficients

Species	Extinction coefficient	Wavelength	Reference
³ MEH-PPV*	$2.4 \times 10^5 \text{ M}^{-1}\text{cm}^{-1}$	820 nm	³ anthracene*
³ pCVPPV*	$8.4 \times 10^4 \text{ M}^{-1}\text{cm}^{-1}$	600 nm	³ biphenyl*
³ fSF-PPV*	$1.0 \times 10^4 \text{ M}^{-1}\text{cm}^{-1}$	540 nm	³ anthracene*

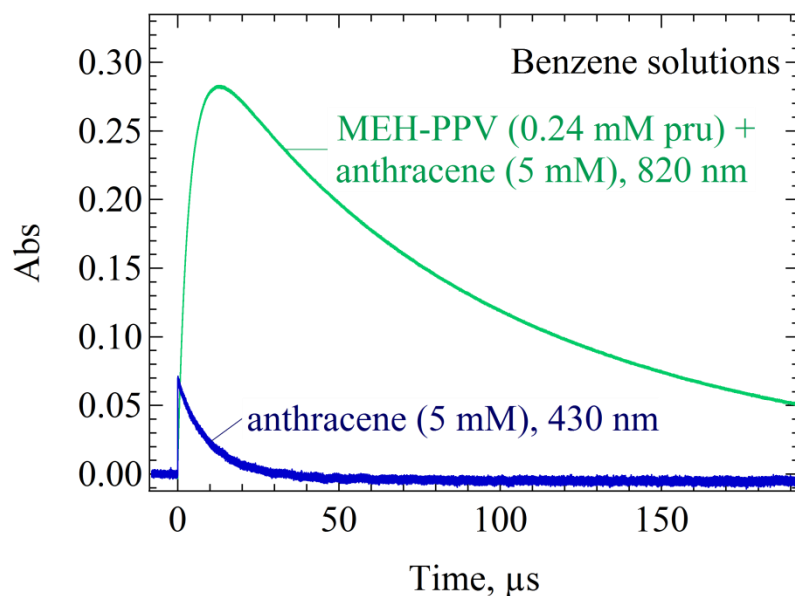


Figure 5-13 The 820 nm absorption transient of a blend solution containing MEH-VPPV (0.241 mM pru) and anthracene (5 mM) in benzene, shown with the 430 nm absorption transient of a control solution in benzene containing antracene only at 5 mM.

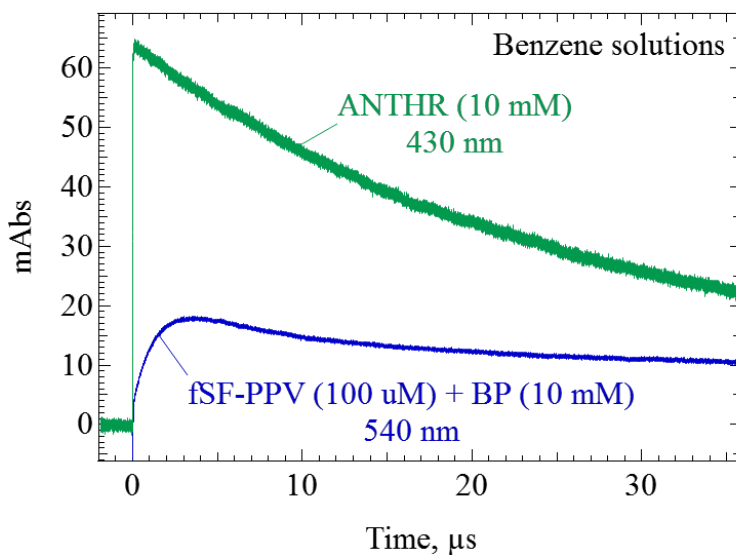


Figure 5-14 The 540 nm absorption transient of a blend solution containing fSF-PPV (0.3 mM pru, 100 μ M) and biphenyl (10 mM) in benzene, shown referenced against the 430 nm absorption transient of a benzene solution containing anthracene only at 10 mM.

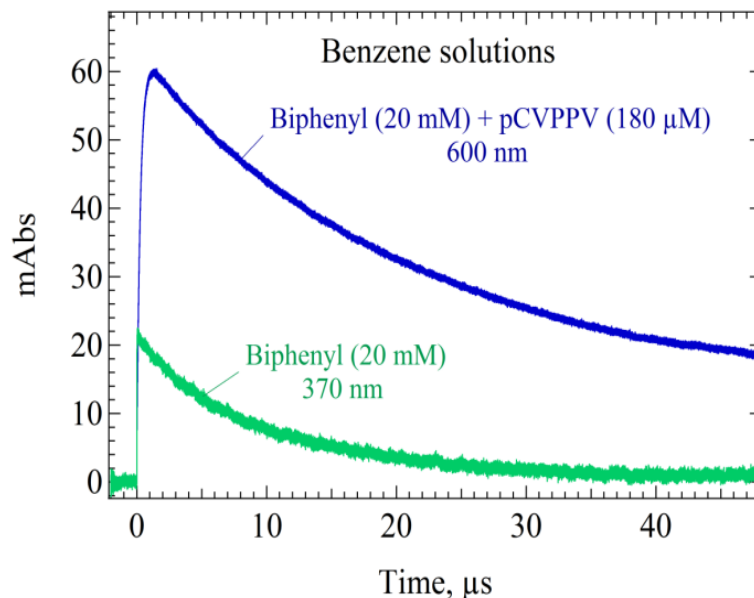


Figure 5-15 The 600 nm absorption transient of a blend solution containing pCVPPV (180 μM) and biphenyl (20 mM) in benzene, shown plotted with the 370 nm absorption transient of a benzene solution containing anthracene only at 10 mM.

5.4 Extinction coefficients of ground state

5.4.1 Phenylenevinylene based compounds

THF solutions of MEH-PPV, fSF-PPV, SF-PPV and a benzene solution of pCVPPV were prepared in quartz cells for collection of their ground state absorbance spectra as shown in **Figure 5-16**, plotted by extinction coefficient versus wavelength. For MEH-PPV maxima were observed at 212 nm, 256 nm, 332 nm, and 500 nm; for fSF-PPV at 220 nm and 380 nm; for SF-PPV at 226 nm, and 380 nm, and for pCVPPV at 337 nm and 417 nm. For spectra corresponding to concentrations ≤ 0.20 mM μru , spectral shapes of each were found to be invariant with concentration, while absorbances varied linearly with concentration in agreement with Beer Lambert's law. These spectra in THF are shown plotted as molar extinction coefficients (per monomer) versus wavelength in **Figure 5-16**. For the ground state absorbance spectra of MEH-PPV, fSF-PPV and SF-PPV, the wavelength at absorbance maximum (λ_{max}), molar extinction coefficient at λ_{max} , and wavelengths at absorption onset (λ_{onset}) were determined and are provided in **Table 5-5**. The excitation energies of the lowest singlet excited state (E_{S_1})

correspond to the wavelengths at absorption onset and are also provided in parentheses. The wavelengths at absorption onset were determined by the method prescribed by Schlaf [119], using the intersection of the line tangent to the long wavelength side of the band, and the corrected baseline.

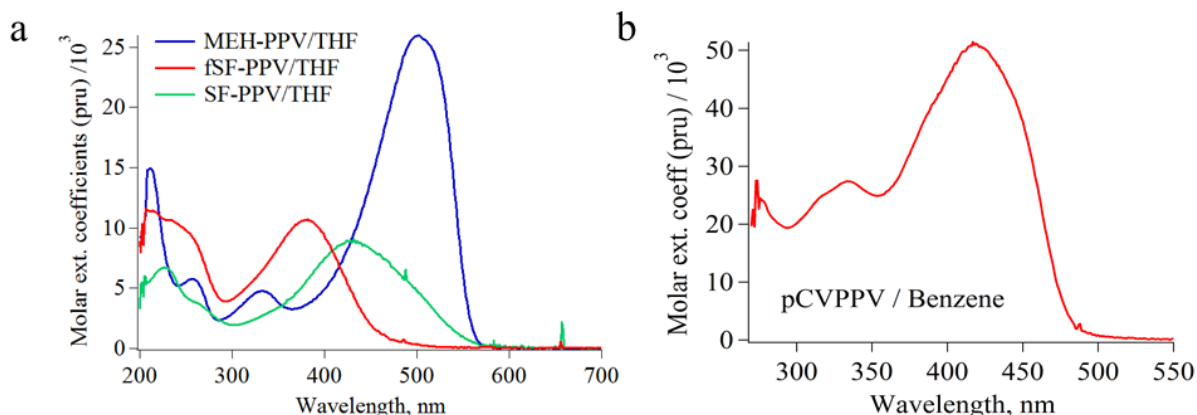


Figure 5-16 Ground state absorbance spectra of a) MEH-PPV, fSF-PPV, and Sf-PPV in THF, and b) pCVPPV in benzene – each plotted as molar extinction coefficients per repeat unit (pru) versus wavelength.

Table 5-5 Molar extinction coefficients at select wavelengths for the ground state absorbance of substituted *p*-phenylenevinylenes

Polymer or oligomer	λ_{\max}	Molar ext. coeff. (per monomer)	λ_{onset}
MEH-PPV	500	$2.59 \times 10^4 \text{ M}^{-1}\text{cm}^{-1}$	558 nm (2.22 eV)
fSF-PPV	380	$1.06 \times 10^4 \text{ M}^{-1}\text{cm}^{-1}$	460 nm (2.70 eV)
SF-PPV	430	$8.84 \times 10^3 \text{ M}^{-1}\text{cm}^{-1}$	568 nm (2.18 eV)
pCVPPV	417	$5.14 \times 10^4 \text{ M}^{-1}\text{cm}^{-1}$	475 nm (2.61 eV)

While spectral shapes and extinction coefficients of MEH-PPV, fSF-PPV, and pCVPPV were found to vary little in THF and chloroform, the ground state spectrum of SF-PPV was found to significantly vary, with a molar extinction coefficient 25% smaller in THF relative to chloroform, and with an onset wavelength of 568 nm (2.18 eV) in THF in contrast with 478 nm (2.59 eV) in chloroform, as shown in **Figure 5-17** Error! Reference source not found..

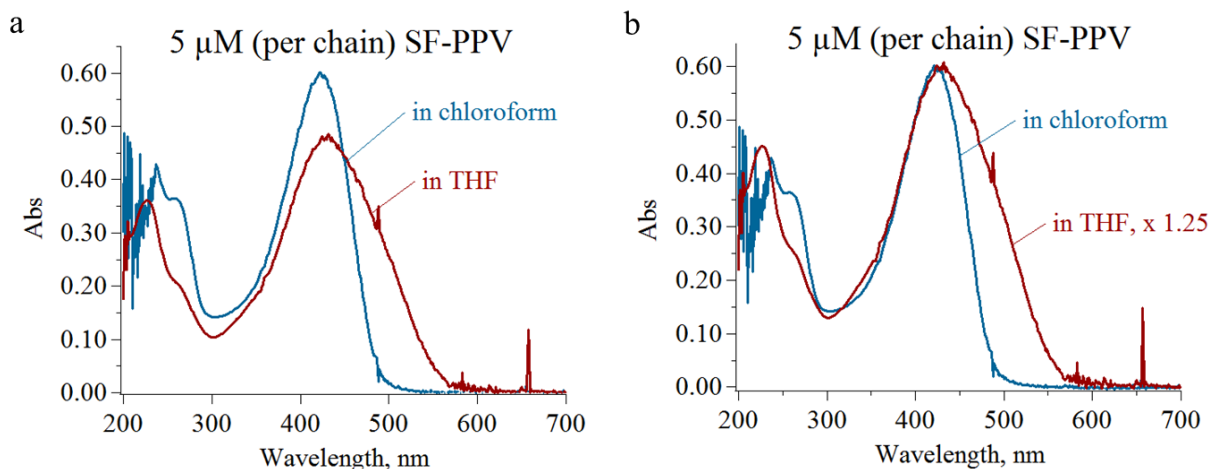


Figure 5-17 Ground state spectra of SF-PPV at 5 μM per chain in chloroform and THF, shown (a) as collected, and (b) with peaks normalized.

5.4.2 pDPP2FT and PDI

D-A copolymers in the ground state have been shown to exhibit two absorption bands – a low energy band (~700 – 800 nm) and a high energy band (~400 – 450 nm). Similar results were obtained via computational studies from which it was found that the lower energy band is due to charge transfer from D to A, and the higher energy band from π - π^* excitation [120] with the oscillator strength of the second transition smaller by more than an order of magnitude

The ground state absorbance spectrum of pDPP2FT collected in chloroform contained at least two bands- a lower energy band with two peaks at 814 nm and 740 nm, and a band at 400 nm. The wavelength corresponding to the greatest absorbance maxima of pDPP2FT and PDI in chloroform were measured as 814 nm and 527 nm, respectively, as shown in **Figure 5-18(a)**. The molar extinction coefficients of PDI and pDPP2FT were determined by our collaborator in chloroform and a determination of extinction coefficient for pDPP2FT in THF was later in our group. The molar extinction coefficients of $9.50 \times 10^4 \text{ M}^{-1} \text{ cm}^{-1}$ and $9.15 \times 10^4 \text{ M}^{-1} \text{ cm}^{-1}$ were determined for pDPP2FT and PDI respectively as shown in **Figure 5-18(b)**. The PL emission of PDI was found to have a mirror image to finely structured ground state absorbance spectrum while no PL emission was measured from pDPP2FT in chloroform.

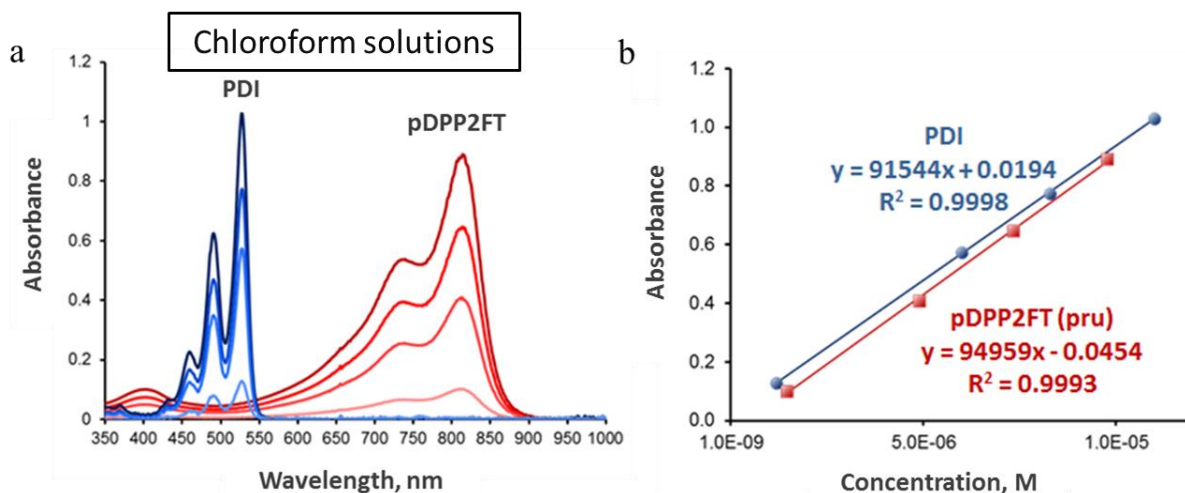


Figure 5-18 Ground state absorbance spectra of pDPP2FT and PDI in chloroform at several concentrations are shown in (a) and corresponding plots of the maximum absorbances versus wavelength from which molar extinction coefficients of $9.50 \times 10^4 \text{ M}^{-1} \text{ cm}^{-1}$ and $9.14 \times 10^4 \text{ M}^{-1} \text{ cm}^{-1}$ respectively were determined, are shown in (b). (Data provided courtesy of Dr. Maxwell Robb).

Measurements of the peak wavelength and molar extinction coefficient of pDPP2FT in THF provided values of 807 nm and $7.78 \times 10^4 \text{ M}^{-1} \text{ cm}^{-1}$, respectively. Due to very small quantity of the, attempts were not made to repeat the measurement to verify the apparent ~20% difference in extinction coefficients in chloroform and THF. The estimates of polaron lengths which will be determined later, depend on the extinction coefficient of the neutral polymer, and for this purpose the pru extinction coefficients determined in chloroform and THF will serve as upper and lower limits respectively. The polymer was found to have an absorption onset of 880 nm, corresponding to 1.40 eV.

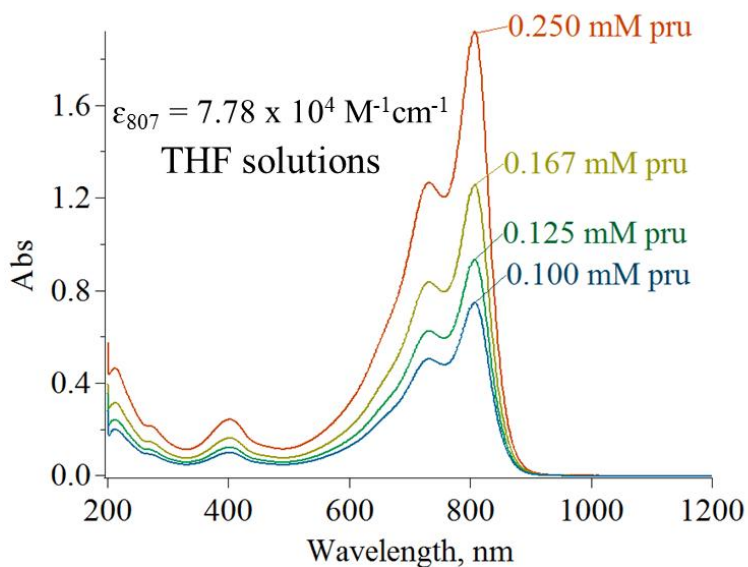


Figure 5-19 Ground state absorbance spectra of pDPP2FT in THF at several monomer concentrations as measured in a cell with 0.1 cm pathlength cell are shown. The pru extinction coefficient at 807 nm was determined by linear fit of the absorbances at 807 nm vs concentration*pathlength.

5.5 Energetics of radical ions by electrochemistry

To predict the favorability of a charge transfer reaction between two compounds, the energies of the initial and final states need to be known. Cyclic voltammetric (CV) methods have been commonly used for determination of reduction and oxidation potentials of various analytes. In the case of many small aromatic molecules, voltammograms typically result in one electron reduction and one electron oxidation, such that the redox potentials can be determined by the average of the potentials at the cathodic and anodic peaks (E_{pc} and E_{pa} , respectively) of the redox couple. Conjugated polymers should be capable of accepting multiple electrons at closely spaced potentials- but quantifying these spacings from cyclic voltammetry alone may prove unfruitful given the broad and ambiguous waves commonly exhibited by conjugated polymers. Through radiolysis, charge transfer reactions can also be studied. Due to the small concentration of charges ($< 3 \mu\text{M}$) produced by radiolysis, a reasonable chain concentration of polymer ($> 10 \mu\text{M}$) ensures that the reaction studied involves

a one-electron redox process. By using a small molecule of known redox potential as an electron donor or electron acceptor capable of reversible charge transfer with such polymer, the one electron reduction (oxidation) potential of the polymer can be determined using the free energy change relative to the potential of the small molecule. In this case, the redox potential of a small molecule serves as a reference for determination of the redox potentials of other compounds for which a reversible charge transfer with the small molecule exists, provided that the same electrolyte conditions are used in both the CV and radiolysis experiments. As common well studied polymers, MEH-PPV and poly(3-dodecylthiophene) (P3DT) were selected to explore in reversible one electron transfer (reduction and oxidation) experiments with small molecules of known redox potentials by CV. The bandgaps and redox potentials for these two polymers have been known to be similar making it possible to employ them in reactions with the same molecules. The use of P3DT was beneficial given that it is commercially produced and a larger batch of it made it possible to use it more extensively for electrochemical measurements.

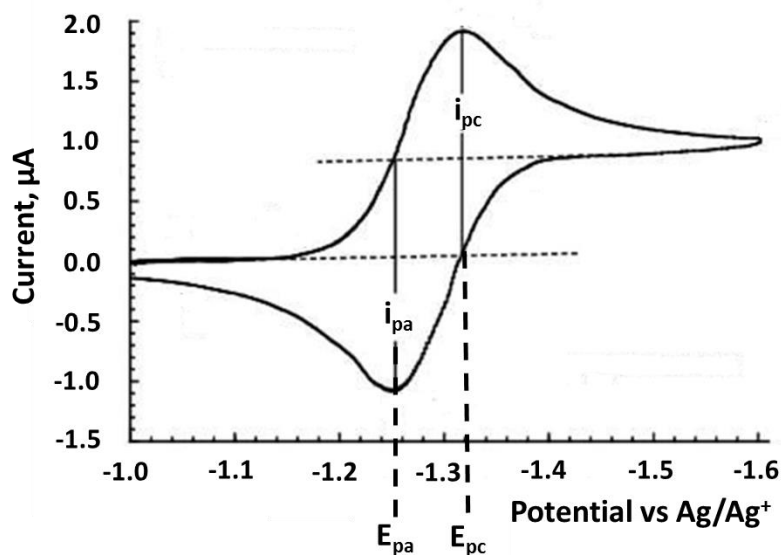


Figure 5-20 An illustration of a voltammogram of an analyte with a reversible redox couple indicated by a peak cathodic current (i_{pc}) and peak anodic current (i_{pa}) whose magnitudes are equivalent. The potentials associated with these currents are the peak anodic potential (E_{pa}) and peak cathodic potential (E_{pc}). The half-wave potential ($E_{1/2} = (E_{pa} + E_{pc})/2$) is

An example of a reversible one-electron redox couple is illustrated in the voltammogram of **Figure 5-20**. Several conventions have been used for displaying voltammograms. The convention used in **Figure 5-20** was the same used in this work. Potentials are shown with increasing negativity from left to right, and currents are shown with increasing positivity from bottom to top. An increase in the negativity (decrease in the positivity) of an analyte indicates that more work is required to add an electron to the analyte. Conversely, an increase in the positivity (decrease in the negativity) indicates that more work is required to remove an electron from it. The measure of negativity and positivity is arbitrarily defined with respect to a reference which is defined to have a potential of zero.

In **Figure 5-20** as the potential of the working electrode is varied more negatively relative to a Ag/Ag^+ reference, from left to right on the x-axis, at a certain point a positive current begins to rise corresponding to the diffusion of an increasing yield of reduced analyte. A maximum (peak) cathodic current, i_{pc} , is reached at the peak cathodic potential, E_{pc} . At some point after the reduction potential of the analyte is reached, the cathodic current will decrease as the concentration of reducible analyte at the working electrode is depleted. This is due to the rate of diffusion for the analyte decreasing relative to the rate of its reduction. As the polarity of the working electrode is scanned in the reverse, oxidation returns the reduced products back to their initial state and a maximum (peak) anodic current i_{pa} is obtained at the peak anodic potential, E_{pa} . A fully reversible one-electron redox couple is symmetric and the peak anodic and cathodic currents in are virtually identical in magnitude.

For one electron redox processes, only one maximum is observed in the cathodic wave and one minimum in the anodic wave. The redox process is considered reversible if the cathodic and anodic waves are symmetric and $i_{pc}/i_{pa} = 1$. The redox potential then can be determined at the potential for which the reduced and oxidized species at the electrode are equal. This corresponds to the average of the anodic and cathodic peak currents and is referred to as the mid potential or half wave potential, denoted by E^0 or $E_{1/2}$. A non-symmetric redox couple may suggest that radical ions formed may in part undergo irreversible reactions.

In **Figure 5-21** cyclic voltammograms of fluoranthene (FLA), perylene (PERYL) and anthracene (ANTHR) prepared at 1 mM in THF with 0.1 M of TBAPF_6 as supporting electrolyte,

are shown. The measurements were collected at a scan rate of 0.1 V/s without compensated resistance, using a 3 electrode system previously described consisting of an Ag/Ag⁺ reference electrode (~0.01 M AgNO₃), glassy carbon working electrode, and platinum wire auxiliary electrode. The redox couple of ferrocene (Fc^{0/+}) was used to calculate and plot the potentials of each compound relative to Fc^{0/+}. The reduction potentials of the compounds are tabulated relative to both Ag/Ag⁺ and Fc^{0/+}. The potentials are presented in **Table 5-6**.

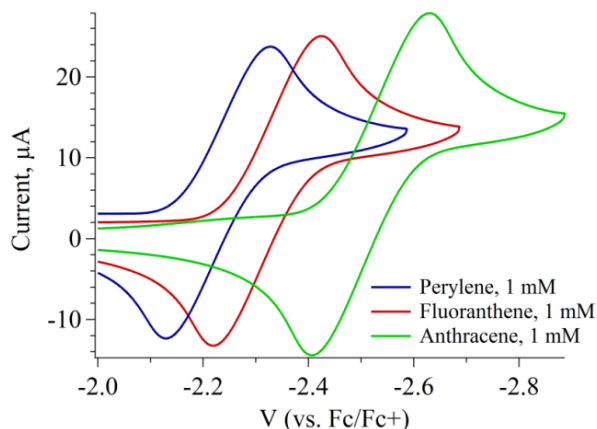


Figure 5-21 CVs of perylene, fluoroanthrene, and anthracene at concentrations of 1 mM vs Fc/Fc⁺.

Table 5-6 Redox potentials associated with redox couples vs Ag/Ag⁺ and Fc/Fc⁺

Compound	Redox Couple	Potential vs Ag/Ag ⁺	Potential vs Fc/Fc ⁺
Ferrocene (Fc)	Fc ^{0/+}	-0.14 ± 0.01	0.00
Perylene (PERYL)	PERYL ^{0/-}	-2.38 ± 0.01	-2.24 ± 0.01
Fluoroanthrene (FLA)	FLA ^{0/-}	-2.47 ± 0.01	-2.33 ± 0.01
Anthracene (ANTHR)	ANTHR ^{0/-}	-2.66 ± 0.01	-2.52 ± 0.01

Cyclic voltammograms of MEH-PPV and P3DT were collected under identical conditions as the small molecules. Presented in **Figure 5-22** are voltammograms of MEH-PPV at 1 mM, 2 mM, and 4 mM. Unlike the small molecules with well defined and symmetric redox couples, the voltammograms of MEH-PPV are neither symmetric nor appear to be fully reversible. Also cathodic and anodic peaks in the CVs of MEH-PPV are not as clearly defined. The current grows in two phases- the first at potentials positive of the quasi peak cathodic current, after which a

slight dip in cathodic current is observed in the current followed by a new growth in the current.

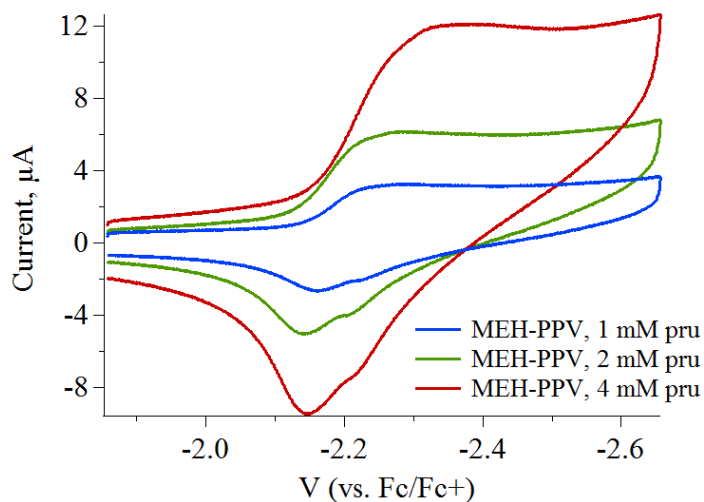


Figure 5-22 CVs of MEH=PPV collected at 1 mM pru, 2 mM pru and 4 mM pru, shown reported vs. Fc/Fc^+ .

The number of electrons added during the CV measurements, can be approximated by using the Randles-Sevcik equation:

$$i_{pc} = 0.4463nFAC(nFvD/RT)^{1/2} \quad 5-8$$

where n is the number of electrons transferred in the redox event, A is the electrode area (0.071 cm^2), F is the Faraday Constant ($9.65 \times 10^4 \text{ C mol}^{-1}$), D is the diffusion coefficient in cm^2/s , C is the concentration in mol/cm^3 , and v is the scan rate (0.1 V/s). Evaluating the voltammogram corresponding to the 4 mM pru ($166 \text{ }\mu\text{M}$ chain) concentration of MEH-PPV, a value of the diffusion coefficient necessary to satisfy **Eq 5-8** at $n = 1$ was determined as $7.72 \times 10^{-5} \text{ cm}^2/\text{s}$. Another estimate for the diffusion coefficient, D , is provided by using the Stokes-Einstein relationship of **Eq 5-9** which defines D in terms of the analyte radius, R , where k is the Boltzmann's constant ($1.38 \times 10^{-23} \text{ J/K}$), T is the temperature in Kelvin, and η is the viscosity in $\text{Pa}\cdot\text{s}$.

$$D = kT/6\pi\eta R \quad 5-9$$

Assuming the previously determined hydrodynamic radius of 3.2 nm for MEH-PPV, $T = 298$ K, and $\eta = 0.00048$ Pa•s, a diffusion coefficient of 1.42×10^{-6} cm²/s, is estimated. Using this value as diffusion coefficient in **Eq 5-8** results in a value of $n = 3.8$ for the number of electrons added per chain in the cathodic wave of the CV for the 24 monomer unit MEH-PPV. Using **Eq 5-9** to determine the diffusion coefficient of anthracene ($R = 3.84$ Å), resulted in a value of 1.18×10^{-5} cm²/s which is 6.5 times smaller than the upper estimate of the diffusion coefficient for MEH-PPV assuming a 1 electron redox process.

This is not physically sensible as the diffusion coefficient of the much smaller anthracene is expected to be significantly larger and is therefore ruled out. This confirms that the redox cycle of MEH-PPV during cyclic voltammetry involves multiple electrons. This also indicates that the reduction potentials of the first few electrons added to MEH-PPV are very closely spaced. The second phase growth of current at potentials negative of the quasi cathodic peak in the CV of MEH-PPV may indicate that beyond some number of electrons, it is feasible to squeeze more electrons onto the chain but with more work required.

The apparent partial reversibility of MEH-PPV redox was similarly observed for P3DT. A redox couple that is not fully symmetric or reversible is typically interpreted as owing to a side reaction in which some fraction of the reduced species is not oxidized back to neutral but instead converted to something else. There are several unique possibilities that can occur in the formation and removal of charges from a conjugated polymer which make the observed phenomenon unclear. It is possible that as electrons are piled onto a chain that it may become energetically favorable for some or all to convert to bipolarons. Bipolarons if formed, may or may not transition back to polarons during the reverse scan but may instead be oxidized directly in a single step at a single potential. The conformation of polymer chains is likely to change as charges are loaded and removed which may alter the diffusion coefficient relative to the neutral chain, especially when considering the effects of ion pairing. It is plausible that these processes contribute to the apparent partial reversibility. The quasi cathodic peaks of these CVs are plotted versus \ln concentrations of MEH-PPV in **Figure 5-23** above. A ratio of 2.3:1.0 is observed in the magnitudes of the slopes of the cathodic currents and anodic currents with respect to \ln concentration of MEH-PPV.

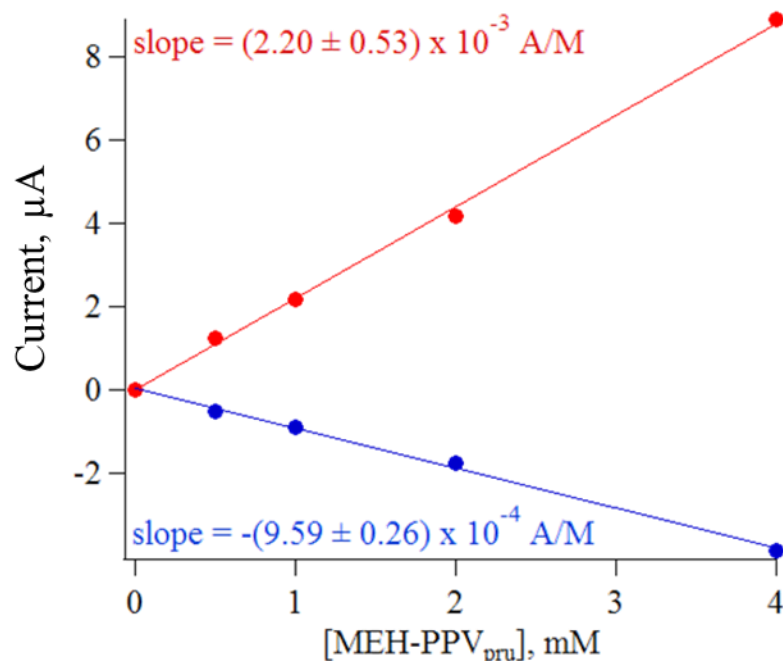


Figure 5-23 The i_{pc} and i_{pa} values plotted versus *pru* concentrations of MEH-PPV with slopes of $(2.20 \pm 0.53) \times 10^{-3}$ A/M and $-(9.59 \pm 0.26) \times 10^{-4}$ A/M show linearity but with values of $i_{pc} \approx 2.3^* i_{pa}$ demonstrating that the redox couple is not fully reversible.

5.6 Energetics of radical anions determined by radiolysis

Reversible electron transfer reactions were used to determine the reduction potentials of a compound *R* relative to a compound *Q* as shown in **Eq 5-10**.



By selecting a wavelength where only one of the anions absorbed, a control could be prepared for which the yield of that anion in the absence of a reversible electron transfer reaction could be obtained. The absorbance loss in the equilibrium condition relative to the control was then used to determine the relative concentrations of the reactants and products in **Eq 5-10**.

Table 5-7 Compounds R and Q used to produce reaction: $R^{\bullet-} + Q \rightleftharpoons R + Q^{\bullet-}$ and calculated K_{eq} and ΔG^0 for reactions (FLA = fluoranthene, 1,4-DCNB = 1,4-dicyanobenzene)

R	Q	K_{eq}	ΔG^0	Electrolyte?
FLA	MEH-PPV	184 ± 82.6	-0.124 ± 0.02 eV	None
FLA	MEH-PPV	22.6 ± 11.3	-0.077 ± 0.012 eV	0.1 M TBAPF ₆
1,4-DCNB	fSF-PPV	1260 ± 203	-0.187 ± 0.04 eV	None
FLA	1,4-DCNB	2800 ± 480	-0.204 ± 0.05 eV	None
O ₂	pDPP2FT	80 ± 6	-0.11 ± 0.02 eV	None
O ₂	PDI	1800	-0.19 eV	None

The data corresponding to these equilibria are shown below with concentrations included.

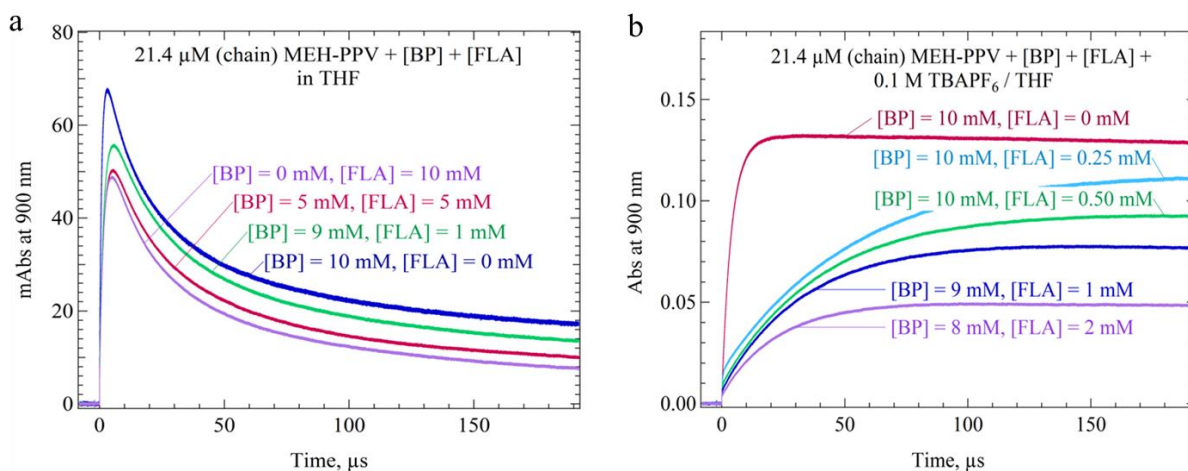


Figure 5-24 The 900 nm absorption transients following radiolysis of THF solutions containing MEH-PPV at 21.4 μM and cosolutes of fluoranthene (FLA) and/or biphenyl (BP) for which FLA was varied and $[\text{FLA}] + [\text{BP}] = 10$ mM, (a) in the absence of electrolyte, and (b) in the presence of 0.1 M TBAPF₆.

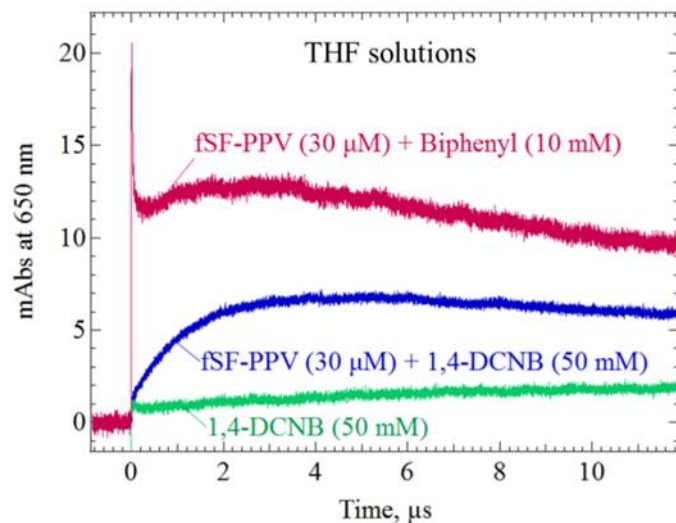


Figure 5-25 The 650 nm absorption transients following radiolysis of THF solutions containing fSF-PPV (30 μM) with and without 1,4-dicyanobenzene (50 mM), and the 650 nm transient corresponding to a solution of 1,4-dicyanobenzene only at 50 mM.

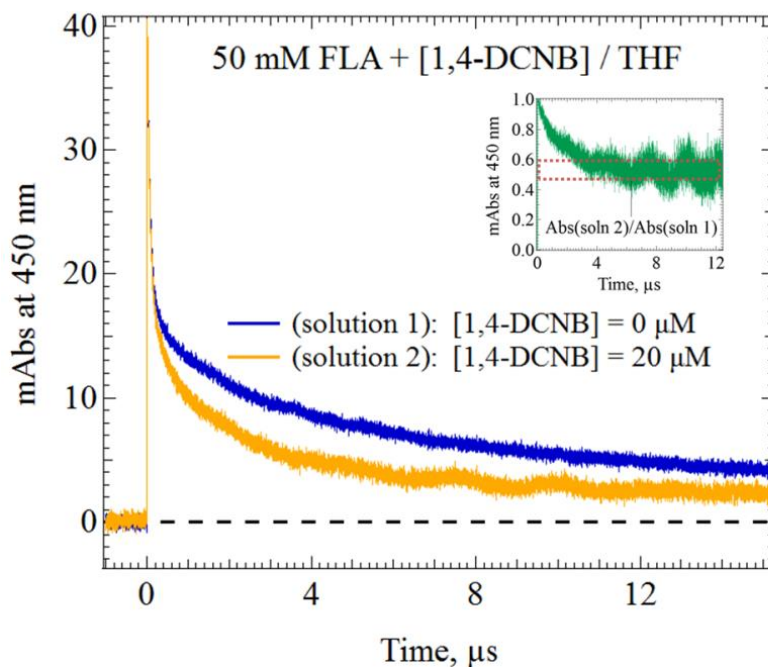


Figure 5-26 The 450 nm absorption transients following radiolysis of THF solutions containing fluoranthene (50 mM) with and without 1,4-dicyanobenzene (20 μM). An inset shows the time-dependent ratios of the absorbance transients which convey the relative ratio of the radical anions shown reaching equilibrium within 8 μs .

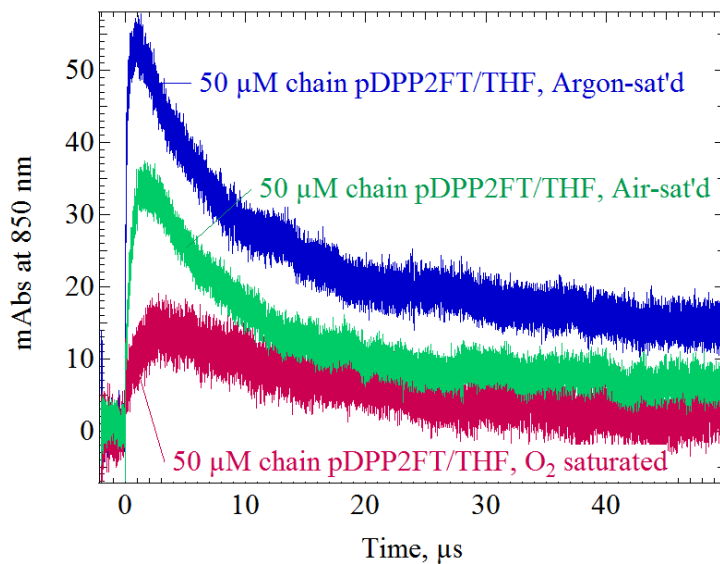


Figure 5-27 The 850 nm absorption transients following radiolysis of a THF solution with pDPP2FT at 50 μM at varied concentrations of oxygen: argons saturated (0 mM O₂), air saturated (2 mM O₂) and oxygen saturated (10 mM O₂).

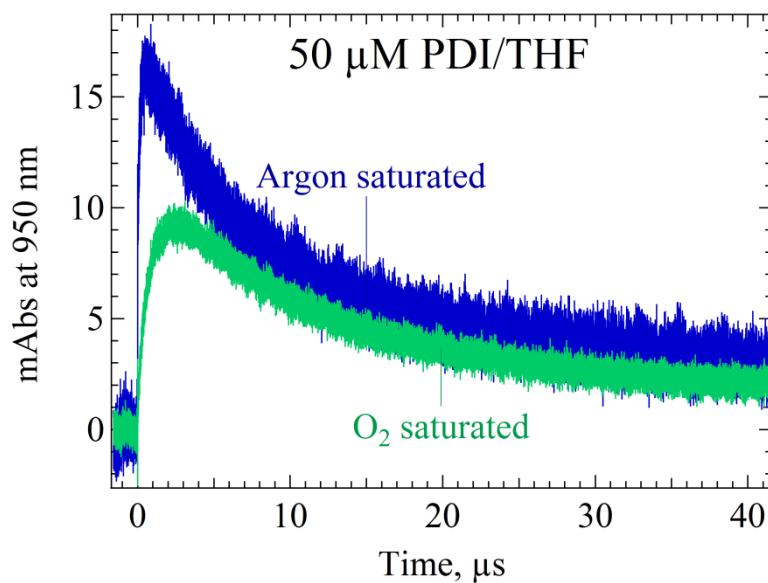


Figure 5-28 The 950 nm absorption transients following radiolysis of a THF solution of perylene diimide (PDI) at 50 μM with varied concentrations no oxygen, and with oxygen saturation (10 mM O₂).

5.7 Energetics of radical cations determined by radiolysis

Reversible hole transfer reactions were used to determine the reduction potentials of a compound R relative to a compound Q as shown in **Eq 5-11**:



Table 5-8 Compounds R and Q used to produce reaction: $R^{*+} + Q \leftrightarrow R + Q^{*+}$ and calculated K_{eq} and ΔG for the reactions

R	Q	K_{eq}	ΔG	Electrolyte?
Fc	MEH-PPV	6.89 ± 0.05	-0.05 ± 0.01 eV	0.1 M TBAPF ₆
Fc	MEH-PPV	15.1	-0.07 eV	None
Anthracene	fSF-PPV	~ 0.1	~ 0.55 eV	None

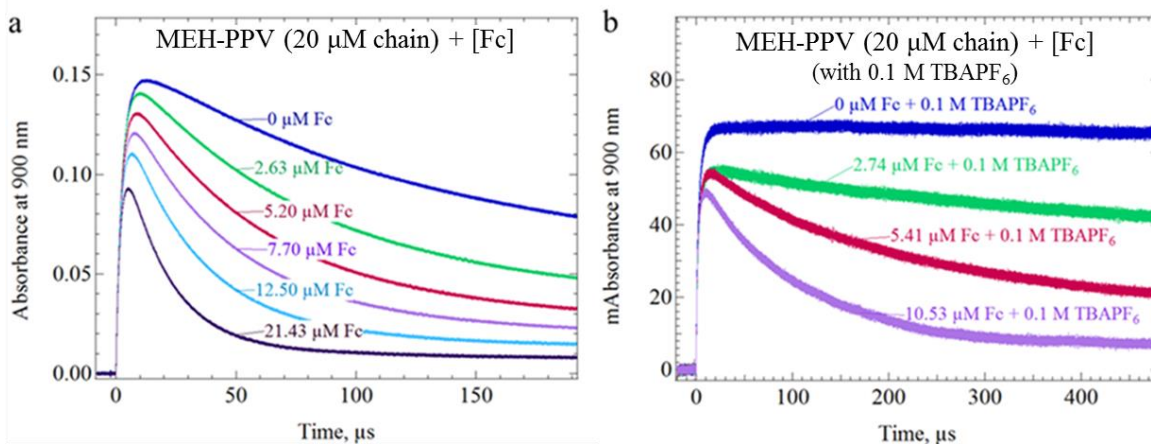


Figure 5-29 Absorption transients following radiolysis of DCE solutions containing MEH-PPV at 20 μM and ferrocene at varied concentrations in: a) without electrolyte cosolute, and b) with 0.1 M TBAPF₆ as cosolute.

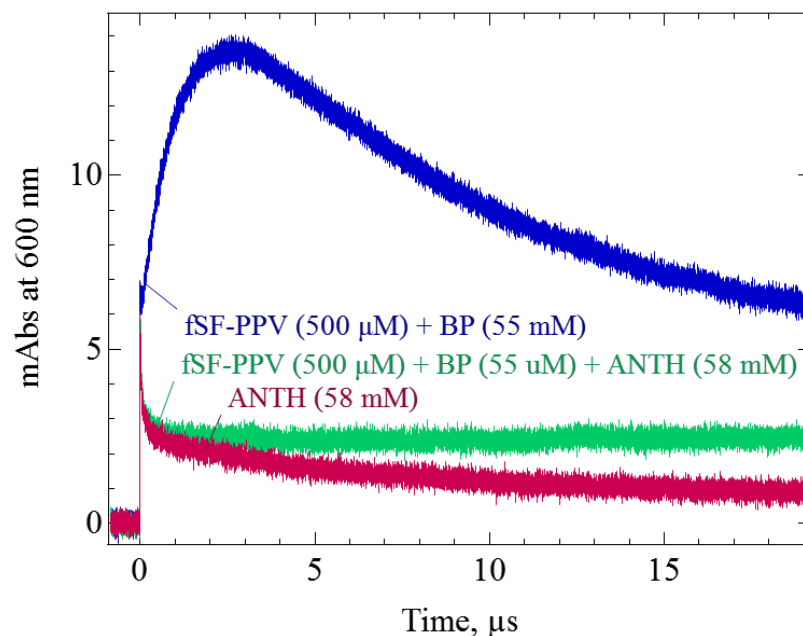


Figure 5-30 The 600 nm absorption transients following radiolysis of DCE solutions containing fSF-PPV (500 μM) and biphenyl (55 mM), with and without anthracene (58 mM), and a 600 nm transient corresponding to a solution of anthracene (58 mM) alone.

5.7 Energetics of triplets

Reversible triplet transfer reactions were used to determine the triplet energy of a compound R relative to a compound Q as shown in **Eq 5-12**:



Table 5-9 Compounds R and Q used to produce reaction: ${}^3R^* + Q \leftrightarrow R + {}^3Q^*$ and calculated K_{eq} and ΔG for the reactions

R	Q	K_{eq}	ΔG	$E_{T1}(R)$	$E_{T1}(Q)$
${}^3\text{Anthracene}^*$	pCVPPV	1628	-0.19 eV	1.845 eV	1.66 eV
${}^3\text{Anthracene}^*$	fSf-PPV	300	-0.146 eV	1.845 eV	1.70 eV

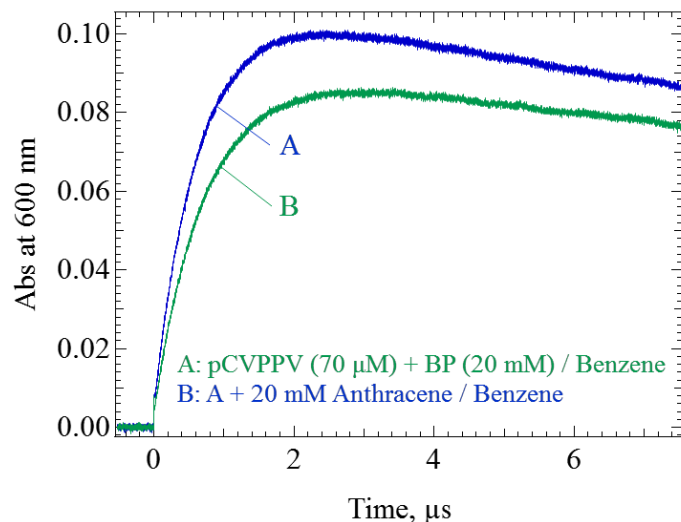


Figure 5-31 600 nm absorbance transients following radiolysis of benzene solutions of fSF-PPV at 50 μM (chain) and a select cosolute (biphenyl, anthracene, and ferrocene) at 10 mM.

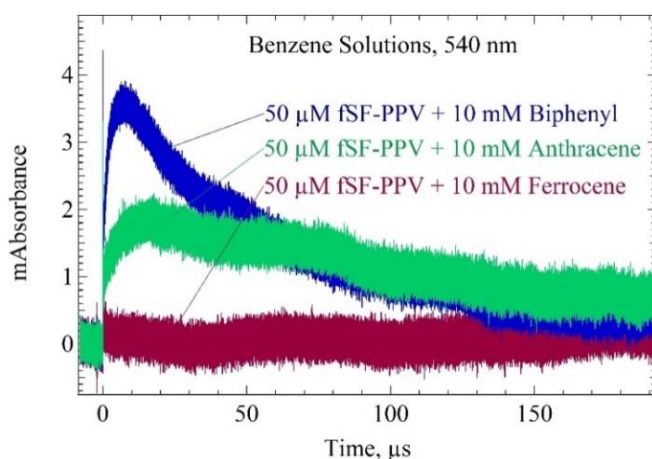


Figure 5-32 540 nm absorbance transients following radiolysis of benzene solutions of fSF-PPV at 50 μM (chain) and a select cosolute (biphenyl, anthracene, and ferrocene) at 10 mM.

5.7.1 Reduction potential of “nth” excess electron of MEH-PPV

It was shown above that during reduction via cyclic voltammetry 24 monomer chain of MEH-PPV appears to gain an excess of ~ 4 electrons suggesting that the redox potentials of the first several electrons added to the chain of MEH-PPV are very close in magnitude. It is of

interest to estimate the differences in the first several added electrons. An experiment was performed to determine the redox potentials at successive steps of MEH-PPV reduction via a reversible electron transfer reaction between MEH-PPV and perylene. This reaction can be shown as:



Equilibria were approximated at various concentrations of the neutrals and radical anions of perylene and MEH-PPV by spectrophotometric measurement given the extinction coefficients of all species. The molar extinction coefficient of ground state perylene was measured to be $3.30 \times 10^4 \text{ M}^{-1}\text{cm}^{-1}$, and the molar extinction coefficient of the radical anion of perylene at 578 nm was reported by Pedersen et al [121] as $5.78 \times 10^4 \text{ M}^{-1}\text{cm}^{-1}$. An average molar extinction coefficient value of $6.95 \times 10^4 \text{ M}^{-1}\text{cm}^{-1}$ was determined for MEH-PPV radical anion based on the upper and lower estimates determined in a previous section. The concentration of MEH-PPV neutral was determined by the decrease in neutral relative to a starting solution containing only $6.7 \text{ }\mu\text{M}$ chain of MEH-PPV and 11 mM of cryptand as reference. The cryptand only contributed to the ground state absorbance spectrum in the UV, outside of the visible spectral range of the neutrals and radical anions of interest. The concentrations of the neutrals and radical anions of MEH-PPV and perylene were determined following additions of aliquots of perylene radical anion solution to the solution of $6.7 \text{ }\mu\text{M}$ of MEH-PPV in THF. From the successive steps of reversible electron transfer, free energies were calculated as shown in **Table 5-10**.

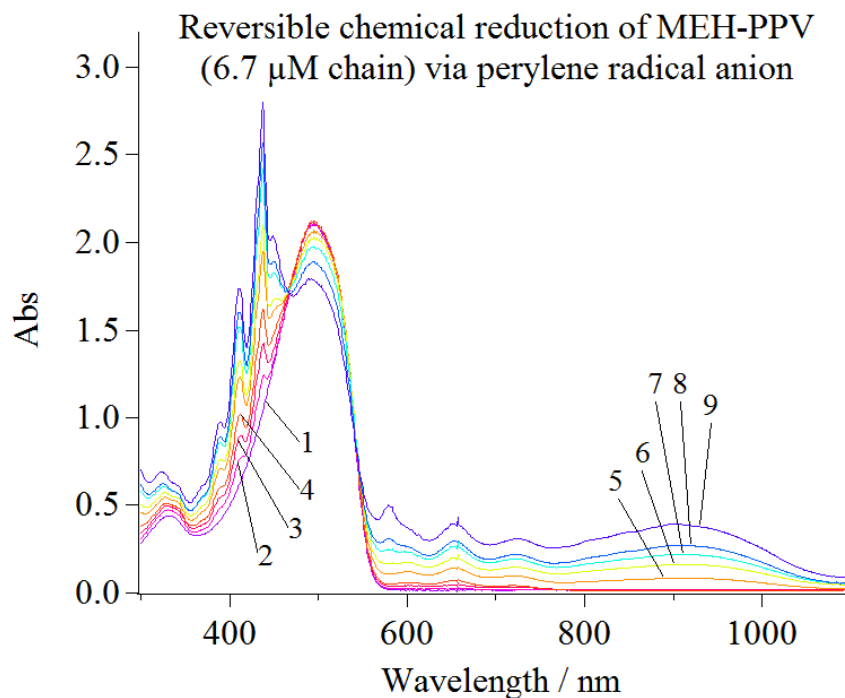


Figure 5-33 The absorbance spectrum of a series of spectrophotometric titrations involving a starting solution of MEH-PPV (6.7 μM chain) and cryptand (11 mM) to which increasing concentrations of perylene $^{\bullet-}$ with chelated Na^+ were added in aliquots.

Table 5-10 K_{eq} and ΔG^0 values measured at steps of reversible MEH-PPV reduction via $\text{PERYL}^{\bullet-}$

Step	[MEH-PPV] μM	[MEH-PPV $^{\bullet-}$] μM	[peryl] μM	[peryl $^{\bullet-}$] μM	K_{eq}	#e $^{\bullet-}$ per chain	ΔG^0
5	6.664	2.28	58.5	3.11	6.436	0.340	0.048
6	6.46	4.52	58.5	3.11	13.161	0.675	0.066
7	6.324	5.92	91.3	5.87	14.560	0.884	0.069
8	6.052	7.08	100.4	7.34	16.002	1.057	0.071
9	5.712	11.57	113.4	12.4	18.524	1.727	0.075

In **Figure 5-34**, the free energy, ΔG^0 , associated with the reaction of **Eq 5-13** is shown plotted versus the number of electrons added per polymer chain. The free energy difference for the last two data points, corresponding to approximately 1 electron per chain ($\Delta G^0 = 71$ meV) and 1.7 electrons per chain ($\Delta G^0 = 75$ meV) indicate a change in potential of ~ 4 meV for the two reduced states of MEH-PPV via perylene radical anion.

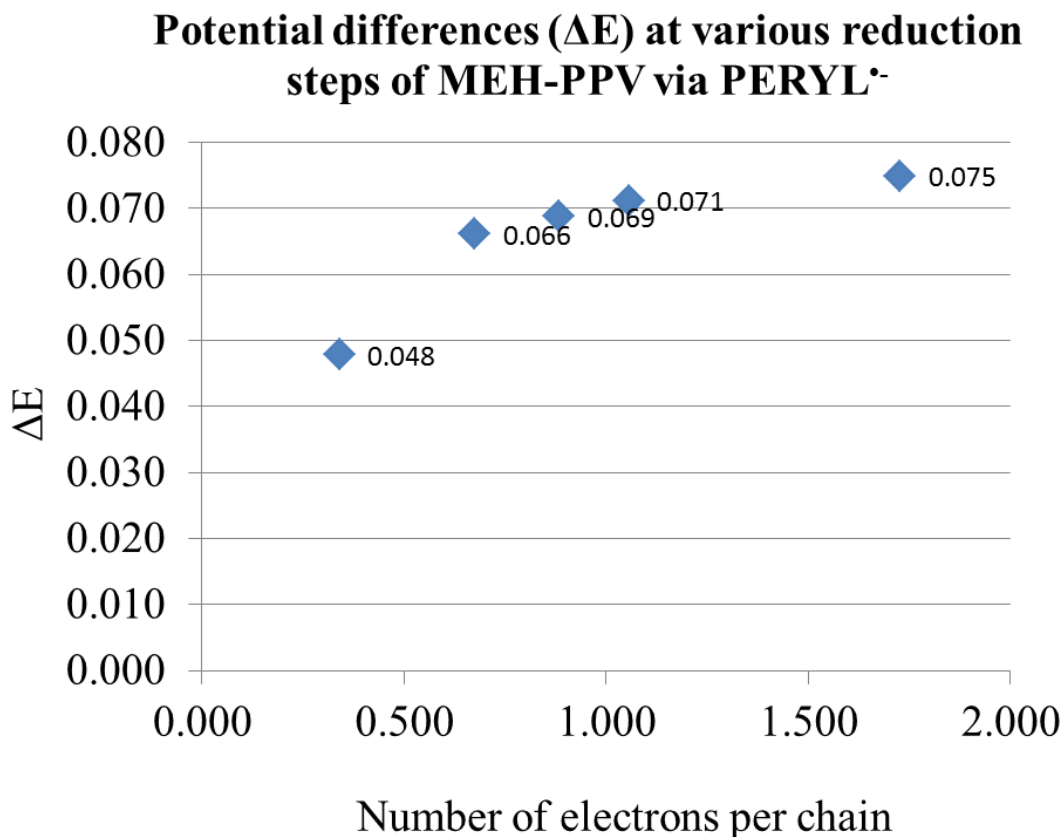


Figure 5-34 ΔG^0 values corresponding to the work done by PERYL⁻ to create a redox state MEH-PPVⁿ⁻ where “n” corresponds to the number of electrons per chain.

5.8 Summary and Discussion

Using the optical signatures collected in Chapter 4, optical probe wavelengths were identified where the absorption yields of radical ions and triplets of compounds of interest could be unambiguously measured and the molar extinction coefficients and energetics of these species determined by comparison with those of known references collected under identical conditions. Based on this method an energy diagram was determined for the phenylenevinylene-containing compounds as shown in **Figure 5-35** below. In the next section, these energetics are used to evaluate the fate of excited states at the interfaces of pCVPPV/MEH-PPV and both charged and excited states at MEH-PPV/fSF-PPV interfaces.

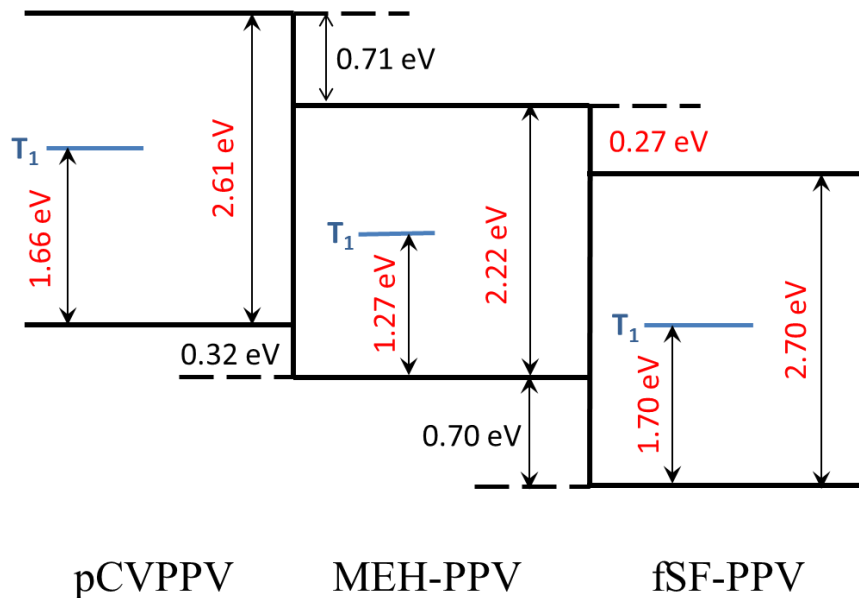


Figure 5-35 Energy diagram based on measurements of energetics of triplet and redox states of pCVPPV, MEH-PPV, and fSF-PPV. Actual experimental measurements are shown in red, while values shown in black indicate calculated values. The T_1 energy levels indicate the lowest lying triplet levels.

Ground state molar extinction coefficients for the compounds were determined by absorption spectrophotometry. The polymers investigated exhibited strong ground state molar extinction coefficients per repeat unit at peak wavelength, and are in order from weakest to strongest: MEH-PPV ($2.59 \times 10^4 \text{ M}^{-1}\text{cm}^{-1}$), pCVPPV ($5.14 \times 10^4 \text{ M}^{-1}\text{cm}^{-1}$), and pDPP2FT ($7.78 \times 10^4 \text{ M}^{-1}\text{cm}^{-1}$). Molar extinction coefficients for ground state absorption have shown to correspond in large part to persistence length [122, 123]. The persistence lengths of each of the polymers were not directly measured and therefore a definitive correlation was not made in this thesis. However, reports of unusually long persistence lengths in DPP containing polymers [122] seem consistent with the results of an unusually large extinction coefficient for pDPP2FT. The intrinsic persistence length of the weakest absorbing of the investigated polymers, MEH-PPV, was reported to be approximately 10 monomers ($\sim 6.0 \text{ nm}$) [124]. A positive correlation between side chain length and persistence length has been reported, but it is also known that longer side chains may also inhibit electronic coupling between neighboring chains in the solid state, and thereby decreasing rates of intermolecular charge transport.

Using the peak anodic current from cyclic voltammetry in conjunction with Randles-Sevcik equation, it was determined that approximately 4 electrons are transferred to a 24 monomer unit chain of MEH-PPV in a CV measurement, corresponding to ~ 1 electron per 6 monomers. The negative polaron length for MEH-PPV was estimated as 5.0 monomer units which predicted a maximum of 4.8 electrons per chain assuming the polaron length to be incompressible. The similar but smaller value obtained experimentally may indicate effects of repulsion between charges. Using the reversible electron transfer experiment in LEAF in the presence of 0.1 M TBAPF₆, an estimated reduction potential for the first added electron was determined as 77 ± 12 meV positive of the reduction potential of fluoranthene in the presence of 0.1 M TBAPF₆. Assuming equivalent free energy changes for the reduction potentials of fluoranthene and perylene in the presence and absence of electrolyte, a reversible electron transfer between perylene and MEH-PPV by chemical reduction was used to evaluate the potentials of various redox states of MEH-PPV and a potential difference of 4 meV was found for adding an average of 1 electron per chain versus adding an average of 1.7 electrons per chain.

Using MEH-PPV, pulse radiolysis has been demonstrated as an effective tool for determining one electron potentials of conjugated polymers in the presence and absence of electrolyte. The effects of ion pairing have been considered and based on assumed binding energies for MEH-PPV and P3DT, a rough approximation of the stabilization energy provided by ion pairing has been determined as 200 ± 50 meV.

In polymer photovoltaics must take into consideration both the energetics and the intrinsic nature of the charged and excited states of the donor and acceptor selected in order to optimize performance. Transfer rates relate directly to energetics, while the transport properties of charges and excited states in conjugated polymers relate directly to their intrinsic nature. The delocalization lengths of charges and excited state are intrinsic physical parameters that relate directly to transport rates and are therefore important characterizations for conjugated polymers. The Marcus hopping model defines the hopping rate of a charge carrier (also applicable to an excited state) as inversely proportional to the reorganization energy [125]. An increase in delocalization of a wave function corresponds to weaker structural relaxation. In the excited state, a wave function delocalized over N carbons, resulting from

promotion of a single electron in a $\pi \rightarrow \pi^*$ (bonding-anti-bonding) transition will cause a change in the bond charge of only $1/N$. The tight binding triplets are generally reported to be much less delocalized than singlets and therefore expected to diffuse at a slower rate along a 1-D lattice. The orders of magnitude longer lifetimes relative to singlets however make triplets advantageous from a perspective of charge generation efficiency due to the fact that diffusion lengths – which are dependent both on diffusion coefficient and excited state lifetime – may be substantially longer for triplets.

Chapter 6: Spectroscopic studies of photoexcitations and charges in DBA type diblocks and at D/A interfaces

6.1 Introduction

Based on the optical signatures for the radical ions and triplets of MEH-PPV, fSF-PPV, and pCVPPV, several experiments were performed to learn about the fate of excitons or ions formed in DBA diblocks and at an MEH-PPV/pCVPPV interface.

6.2 Materials investigated

The series of DBA diblocks were introduced in Chapter 1 but we will be reintroduced here. Each DBA diblock consisted of MEH-PPV as electron donor (D). An acceptor unit in each diblock consisted of either a sulfone-derivatized phenylenevinylene chain, SF-PPV, and all others consisted of a fluorinated SF-PPV, or fSF-PPV. These acceptor compounds are further simplified in notation as “A” and “fA”, respectively. Three batches of MEH-PPV were used to synthesize the various diblocks investigated: a ~21 monomer length chain (D_{21}), a ~24 monomer length chain (D_{24}) and a ~14 monomer length chain (D_{14}). The intervening bridge between the moieties, when present, consisted of an aliphatic and is denoted as “Cn”, where n represents the number ranging from 0 to 6, with 0 indicating that no bridge is present.

A single polymer contained both the D_{21} and the SF-PPV acceptor (A), and is denoted as $D_{21}(C2)A$. This was initially obtained for preliminary from our collaborators who decided to synthesize the next batch of diblocks with fluorinate acceptors for improved free energy change between the donor/acceptor pair. Based on the free energy calculations made earlier from redox equilibria measurements, a free energy difference for the D/fA pair was calculated as -267 ± 11 mV, comparable to an estimate of 260 mV made by our collaborators via electrochemical measurements. The free energy for electron transfer of the D/fA pair was determined in this work from reversible electron transfer measurements in THF, via radiolysis in LEAF.

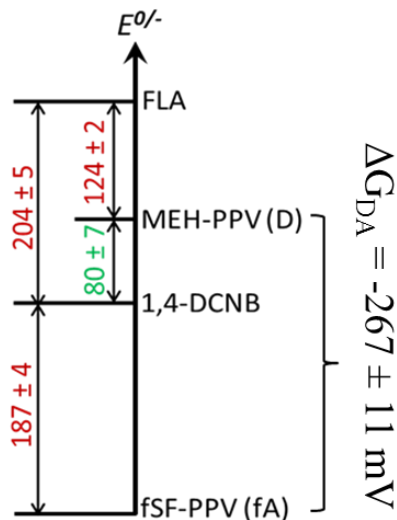


Figure 6-1 Free energy changes for electron transfer from MEH-PPV (D) to fSF-PPV (fA) was calculated as -267 ± 11 mV based on the free energies of electron transfer from fluoranthene (FLA) to MEH-PPV, from FLA to 1,4-dicyanobenzene (1,4-DCNB) and from 1,4-DCNB to fSF-PPV as determined in reversible electron equilibria measurements in THF. Values in indicate measurements, and the value in green indicates a calculation.

In **Table 6-1** a list of all diblock polymers investigated are provided. The names are denoted with indication of monomer length of the MEH-PPV chain. Most of the diblock work discussed in this chapter focuses on D24(Cn)fA polymers, and therefore will be simply denoted as D(Cn)fA. When D₂₁(C2)A or D₁₄(Cn)fA are being referenced, the monomer units will be specified to distinguish from the D(Cn)fA series. Also in **Table 6-1**, are provided the free energy changes expected for dissociation from the D* excited to the D^{•+} + A^{•-} charge separated state, assuming a fully extended bridge and a separation distance defined between the separated charge centers. The calculation was made based on the equation:

$$\Delta G_{CS} = E_{ox}(D) - E_{red}(A) - E_{00} - e^2/(4\pi d\epsilon_0\epsilon_s) \quad 6-1$$

where ϵ_0 is vacuum pervittivity, ϵ_s is the solvent dielectric constant (7.58 for THF), d is distance between the charge centers, and E_{00} is the energy level difference between the relaxed locally excited donor and the zero vibrational level of the ground state (lowest lying singlet).

By converting energy terms to eV and d to angstroms, ΔG_{CS} can be expressed as:

$$\Delta G_{CS} = E_{ox}(D) - E_{red}(A) - E_{00} - 14.40/d\epsilon_s \quad 6-2$$

To compute the charge center to charge center distance requires first knowing the delocalization lengths of the charges which are computed in the following section.

Table 6-1 Maximum separation D-fA separation distance for diblock copolymers investigated

Diblock	Bridge length (Å)	d_{total} (Å)	$\Delta G_{CS}(d)$
D ₂₄ (C0)fA	1.34	29.49	-0.301
D ₂₄ (C1)fA	5.68	33.83	-0.293
D ₂₄ (C2)fA	7.02	35.17	-0.291
D ₂₁ (C2)A	7.02	35.17	-0.291
D ₂₄ (C4)fA	9.70	37.85	-0.287
D ₂₄ (C6)fA	12.38	40.55	-0.284
D ₁₄ (C0)fA	1.34	29.49	-0.301
D ₁₄ (C1)fA	5.68	33.83	-0.293

6.3 Delocalization length estimates

Delocalization lengths are important physical parameters of a conjugated polymer that relate to intrachain mobility. The stronger the lattice distortion induced by a polaron or exciton, the smaller the delocalization length, thus reducing the mobility of the species. The delocalization length of charges are therefore considered as direct indicators for determining the ease of transport along a chain [126].

Based on the assumption that the injection of one charge into a conjugated polymer chain creates an ion which delocalizes over l_n monomer units which consequently no longer have properties of the ground state neutral, the delocalization length can be estimated by the equation:

$$l_n = \frac{\Delta[P^0]}{\Delta[ions]} \quad 6-3$$

where $[P^0]$ represents the concentration of ground state monomer units lost due to occupation by some concentration of ions, $\Delta[ions]$. In principle, this postulate also applies to excited states delocalized over l_n monomer units. The conversion of ground state monomers to ions will then exhibit an absorption band associated with the newly formed ions and a simultaneous

loss of ground state absorption. The measured loss of neutral may be underestimated if ion absorption contributes at the wavelength of the observed loss of neutral.

The delocalization length can be defined in terms of the extinction coefficients and incremental absorption changes of the ion and neutral at wavelengths λ^0 and $\lambda^{-/+}$ where absorbance from the neutral and radical ion, respectively, dominate. By assuming that only ions absorb at $\lambda^{-/+}$ but that absorption at λ^0 contains small contribution from ions, then the incremental change of absorption at λ^0 due to formation of ions will be defined as $\Delta A(total)_{\lambda^0} = \Delta A(P^0)_{\lambda^0} + \Delta A(P^{\bullet-/+})_{\lambda^0}$. The incremental absorbance change at $\lambda^{-/+}$ corresponding to formation of ions is then denoted as $\Delta A(P^{\bullet-/+})_{\lambda^{-/+}}$. Finally, denoting the extinction coefficient of the ion at $\lambda^{-/+}$ as $\varepsilon(P^{\bullet-/+})_{\lambda^{-/+}}$ and the extinction coefficient of monomer neutral at λ^0 as $\varepsilon(P^0)_{\lambda^0}$, the delocalization length, l_n may be defined as:

$$l_n = \frac{\varepsilon(P^{\bullet-/+})_{\lambda^{-/+}}}{\varepsilon(P^0)_{\lambda^0}} \cdot \left(\left| \frac{\Delta A(total)_{\lambda^0}}{\Delta A(P^{\bullet-/+})_{\lambda^{-/+}}} \right| + \frac{\Delta A(P^{\bullet-/+})_{\lambda^0}}{\Delta A(P^{\bullet-/+})_{\lambda^{-/+}}} \right) \quad 6-4$$

The precise value of $\Delta A(P^{\bullet-/+})_{\lambda^0}$ is not easily determined. Assuming λ^0 is near the isosbestic point, $\lambda^{isosbestic}$, it is reasonable to make the approximation that $\Delta A(P^{\bullet-/+})_{\lambda^0} \approx \Delta A(P^{\bullet-/+})_{\lambda^{isosbestic}}$. A lower limiting value can be obtained by assuming $\Delta A(P^{\bullet-/+})_{\lambda^0} \approx 0$.

6.3.1 Negative polaron (Radical anion)

MEH-PPV was chemically reduced in THF using sodium biphenyl (Nabiph) as reductant. The sodium biphenyl solution used came prepared in dimethoxyethane (DME) solvent, but was diluted by mixture with a cryptand solution in THF. The final reductant solution contained Nabiph with 11 mM cryptand in a blend solvent of 80% THF and 20% DME. Cryptand was used for the purpose of chelating the sodium ions to mitigate ion pairing with radical anions.

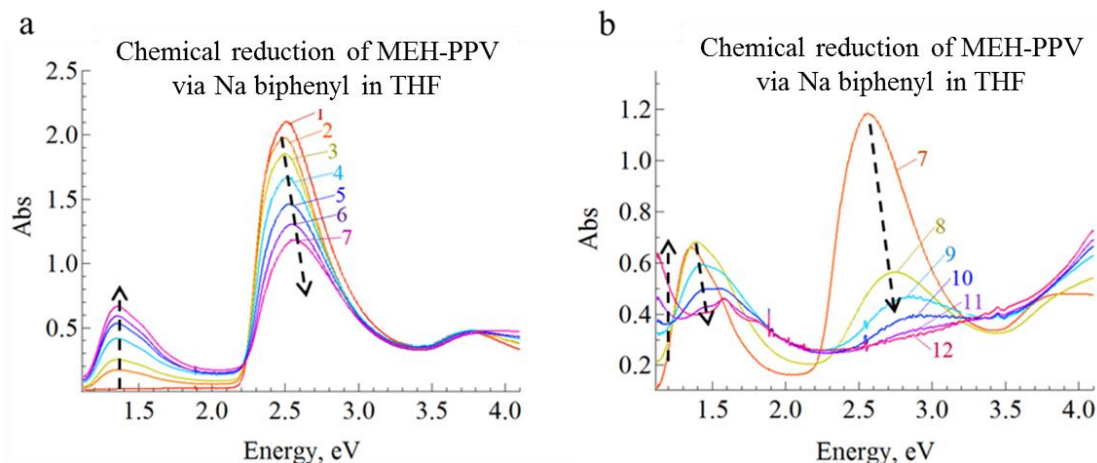


Figure 6-2 Absorbance spectra of MEH-PPV following varied stages of chemical reduction by Na biphenyl in THF, in the presence of 11 mM cryptand, in (a) corresponding to the formation of a radical anion band at 1.365 eV and (b) during the decay of the same band.

In **Figure 6-2** spectral transformations in the visible to NIR regime corresponding to incremental additions of Nabiph solution in aliquots, are shown: in **(a)** during the growth of a 1.362 eV (910 nm) band and, in **(b)** during the decay of the same band. The neutral band of MEH-PPV with peak at 2.500 eV (496 nm) in step 1 undergoes blueshifting in all but the transition from step 1 to 2. The neutral band of step 1 was expected to peak at 2.480 eV (500 nm) but was slightly blue-shifted for reasons that are not clear. Subsequent blueshifting following addition of reductant was due to increasing occupancy of the chain by charges which decrease the average conjugation length of neutral. An isosbestic point at 2.230 eV (556 nm), with a nearly linear relationship observed in the loss of neutral relative to absorption gain of the radical anion band is observed from step 1 through 7. This suggests direct transition of neutral to negative polaron. The transition from step 7 to step 8 a greater suppression of neutral is observed than in prior transitions due to a larger increment of chemical reductant being added. The band of the negative polaron is found to decay in subsequent steps as a quasi-isosbestic point at 1.150 eV (1078 nm) is created due to concomitant formation of a new absorbance band suggesting conversion to negative bipolarons.

In **Figure 6-3** an absorbance spectrum of MEH-PPV^{•-} collected in THF by radiolysis (with maximum at ~ 900 nm) is shown rescaled and overlaying the absorbance spectrum of MEH-PPV^{•-} obtained by chemical reduction in THF with 11 mM cryptand as cosolute. The spectral

shapes are very similar supporting the assignment as the negative polaron. Relative to the spectral shape of the radiolytically formed species, the spectrum corresponding to the chemically reduced species (with maximum at 910 nm) appears to sit on a slope that decreases monotonically with increased wavelength, possibly indicating a small absorbance contributions from cryptand, biphenyl, or impurity, or could be contributed from baseline error due to using different cells for baseline correction and spectral measurement. If the deviation is due to such a source of error, it may also contribute to the apparent ~ 10 nm offset in spectral maxima. Nevertheless, the similarity of these spectra confirms the assignment of the 910 nm band as the negative polaron species of MEH-PPV.

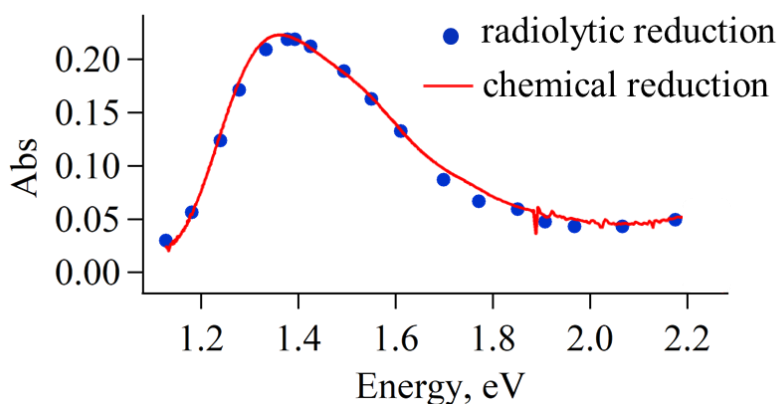


Figure 6-3 Overlaid absorbance spectra of MEH-PPV*⁻ collected by radiolysis (rescaled) and chemical reduction in THF, showing good agreement.

Absorbance difference magnitudes at 910, $|\Delta A(\text{total})_{910}|$, measured at steps 2 – 7 relative to step 1, were plotted against the absorbance difference magnitudes at neutral maximum (circa 500 nm), $|\Delta A(\text{total})_{500}|$, also measured at steps 2 – 7 relative to step 1, and are shown in

Figure 6-4. The ratio of these absorbance changes, $\left| \frac{\Delta A(\text{total})_{500}}{\Delta A(\text{P}^{\bullet-})_{910}} \right|$ are used to calculate the

polaron length of MEH-PPV*⁻, determined as: $\frac{\epsilon(\text{P}^{\bullet-})_{910}}{\epsilon(\text{P}^0)_{500}} \cdot \left(\left| \frac{\Delta A(\text{total})_{500}}{\Delta A(\text{P}^{\bullet-})_{910}} \right| + \frac{\Delta A(\text{P}^{\bullet-})_{500}}{\Delta A(\text{P}^{\bullet-})_{910}} \right)$. The value

of $\left| \frac{\Delta A(\text{total})_{500}}{\Delta A(\text{P}^{\bullet-})_{910}} \right|$ corresponds to the slope of the linear fit in **Figure 6-4**, with a value of 1.76.

Assuming the molar extinction coefficient at 910 nm corresponding to MEH-PPV*⁻ obtained by chemical reduction is the same as the molar extinction coefficient at 900 nm corresponding to

MEH-PPV*⁻ produced radiolytically, then $\frac{\epsilon(\text{P}^{\bullet-})_{910}}{\epsilon(\text{P}^0)_{500}} = \frac{6.95}{2.59} = 2.68$. The value of $\frac{\Delta A(\text{P}^{\bullet-})_{500}}{\Delta A(\text{P}^{\bullet-})_{910}}$ could

not be directly determined but an upper limiting approximation of $\frac{\Delta A(P^{\bullet-})_{500}}{\Delta A(P^{\bullet-})_{910}} \approx \frac{\Delta A(P^{\bullet-})_{580}}{\Delta A(P^{\bullet-})_{910}}$ was made based on the assumption that the extinction coefficient of the radical anion varies little in the range of 500 nm – 580 nm. That neutral MEH-PPV contributes no absorbance at 580 nm makes the calculation of $\frac{\Delta A(P^{\bullet-})_{580}}{\Delta A(P^{\bullet-})_{910}}$ simple. A value of 0.21 was determined as an upper limit for $\frac{\Delta A(P^{\bullet-})_{500}}{\Delta A(P^{\bullet-})_{910}}$. From these parameters, for the delocalization length of the negative polaron limiting values of 4.71 and 5.28 monomers are calculated, giving an average of 5.00 ± 0.28 units. Based on an estimated monomer length of 0.62 nm, the delocalization length of a negative polaron is estimated as 3.10 ± 0.17 nm.

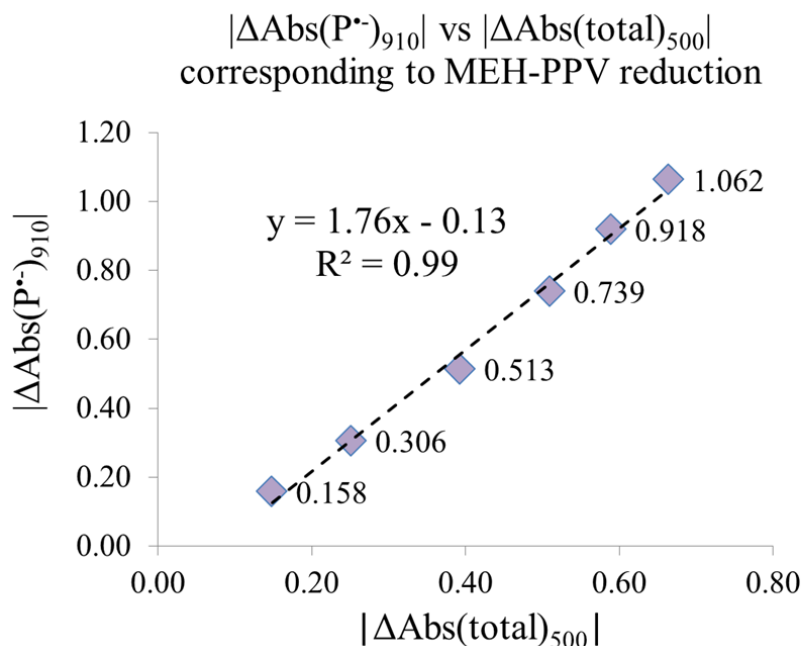


Figure 6-4 A linear relationship was found for the magnitude of absorbance change in the 910 nm band associated with MEH-PPV^{•-} and the corresponding magnitude of absorbance change at 500 nm band where the neutral absorbs.

Radiolysis was also used to acquire an estimate for the negative polaron length by comparing the neutral loss by electron attachment with absorbance gain at the radical anion band. The transient absorption signals of radiolysis are determined by difference absorption measurements, such that loss of neutral is observed as bleach. To observe the change in neutral absorbance, the absorbance prior to radiolysis must be measurable. To satisfy this

requirement the optical density needed to be sufficiently low while maintaining a high enough concentration of the polymer to capture radiolytically formed electrons. These conditions were satisfied by preparing a THF solution of MEH-PPV at a chain concentration of 30 μM in a 0.1 cm pathlength cell. A partial spectrum collected at 316 ns following radiolytic pulse was compared against a difference spectrum obtained from the partial chemical reduction data of **Figure 6-2 (a)** by subtracting step 3 from step 1. These spectra are shown overlaid in **Figure 6-5** with the radiolytic spectrum rescaled to match the reduction spectrum by chemical reduction. The change in absorbances at bleach band maximum and radical anion band maximum are in good agreement suggesting the same result for negative polaron length is obtained with both reduction techniques.

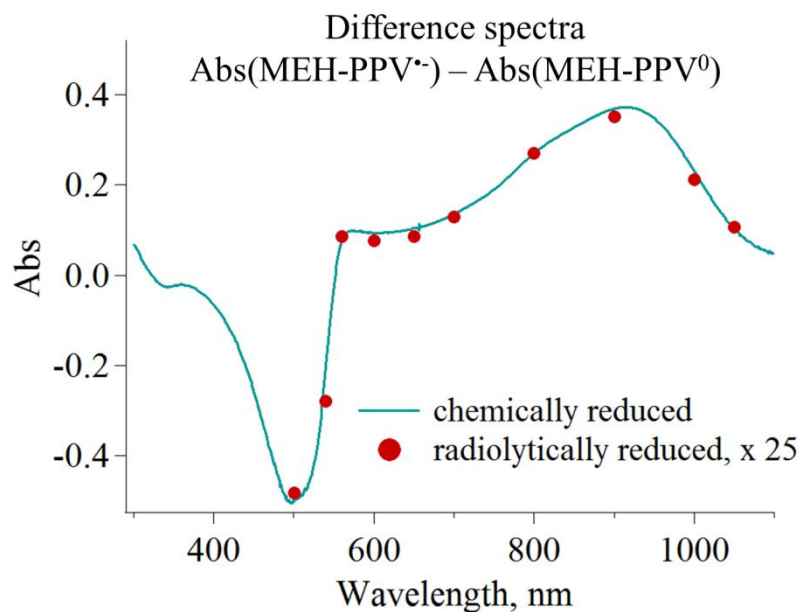


Figure 6-5 Difference absorbance spectra obtained by subtracting the ground state neutral of MEH-PPV from a partially reduced spectrum of MEH-PPV showed good agreement.

6.3.2 Positive polaron

MEH-PPV was chemically oxidized in o-DCB using thianthrenium hexafluorophosphate (ThPF_6) as oxidant. The absorbance spectra corresponding to various stages of oxidation are shown in **Figure 6-6 (a)** numbered according to the order of measurement beginning in step 1 with the ground state neutral spectrum of MEH-PPV (6.7 μM chain) with a peak circa 2.465 eV

(502 nm), and in steps 2 – 10 with increasing loss of neutral as oxidant is added incrementally. The loss of neutral at 2.465 eV corresponds to a redshift of the neutral in all but the first transition, as was observed in the transitions by chemical reduction indicating a decrease in average conjugation length. The decreasing neutral band gives rise to a new band at 1.362 eV which is similar to the spectrum of MEH-PPV^{•+} obtained by radiolysis of MEH-PPV in o-DCB and DCE. This new band is not observed to undergo spectral shifts between steps 2 – 10. An isosbestic point at 2.180 eV (568 nm) and a linearity in neutral loss and absorbance gain at 1.362 eV suggests the new species is MEH-PPV^{•+} directly converted from neutral via chemical oxidation. A deviation from the linearity in neutral loss per absorbance gain at 1.362 eV in steps 8 – 10 indicates a departure from the regime of independent polarons.

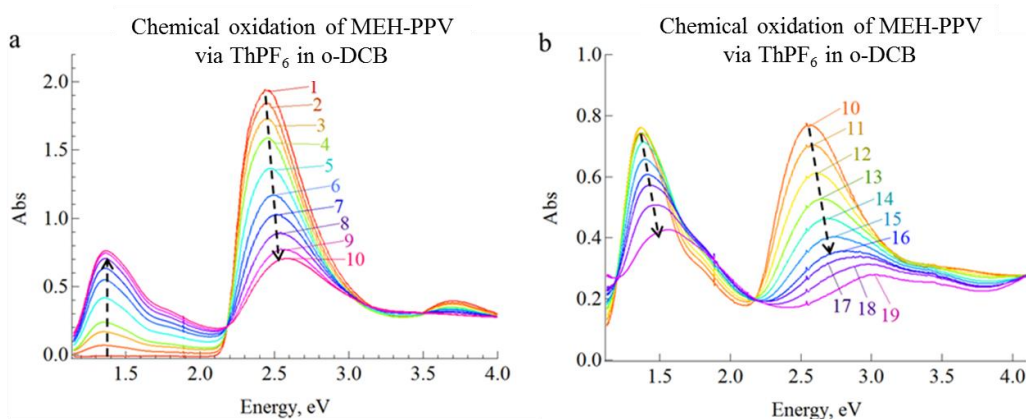


Figure 6-6 Various stages of chemical oxidation of MEH-PPV via thianthrenium hexafluorophosphate (ThPF₆) in o-DCB, shown in **(a)** during formation of a positive polaron band, and **(b)** during suppression of the band as positive bipolarons are formed.

In **Figure 6-6 (b)** the 1.362 eV band is observed decaying and redshifting as neutral continues to decay and redshift as well. The formation of a new quasi-isosbestic point at 1.196 eV signals the conversion of positive polarons (radical cations) into dications (positive bipolarons). An equilibrium of these species is suggested by the presence of remaining neutral. The spectral band of the positive bipolaron band was not possible to acquire due to the limited spectral range of the spectrophotometer used. A spectral overlay of the positive polaron bands acquired via radiolysis of MEH-PPV (at 0.5 μs after pulse) in o-DCB and by chemical oxidation are shown in **Figure 6-7**.

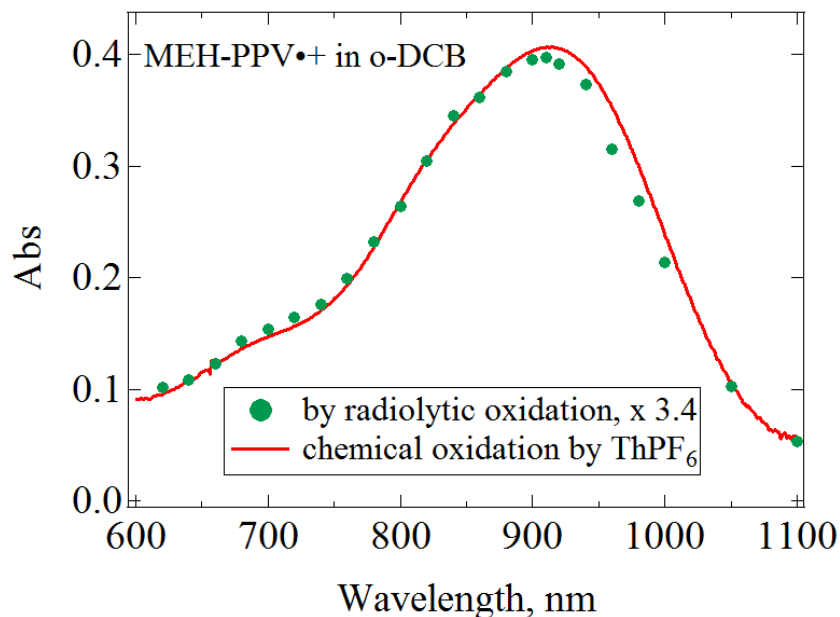


Figure 6-7 A spectrum of MEH-PPV^{•+} collected by radiolysis in o-DCB, shown rescaled to overlay an absorbance spectrum of the same produced by chemical oxidation in o-DCB, showing good agreement.

The positive polaron length was determined by the expression: $\frac{\epsilon(\text{P}^{•+})_{910}}{\epsilon(\text{P}^0)_{500}} \cdot \left(\left| \frac{\Delta A(\text{total})_{500}}{\Delta A(\text{P}^{•+})_{910}} \right| + \frac{\Delta A(\text{P}^{•+})_{500}}{\Delta A(\text{P}^{•+})_{910}} \right)$. Approximating the molar extinction coefficient at 910 nm corresponding to MEH-PPV^{•+} obtained by chemical reduction as equivalent to the molar extinction coefficient at 900 nm corresponding to MEH-PPV^{•+} produced radiolytically, then $\frac{\epsilon(\text{P}^{•+})_{910}}{\epsilon(\text{P}^0)_{500}} = \frac{12.5}{2.59} = 4.82$. As was done in the case of the negative polaron, an approximation of $\frac{\Delta A(\text{P}^{•+})_{500}}{\Delta A(\text{P}^{•+})_{910}} \approx \frac{\Delta A(\text{P}^{•+})_{580}}{\Delta A(\text{P}^{•+})_{910}} \approx 0.28$ was made. A plot of absorbance change at 910 nm vs the absorbance change at 500 nm, provided a linear slope with the value of $\left| \frac{\Delta A(\text{total})_{500}}{\Delta A(\text{P}^{•+})_{910}} \right| = 1.51$. The delocalization length of the positive polaron was calculated as having limiting values of 7.28 and 8.63 monomers, which average to an estimate of 7.95 ± 0.68 monomers. This is equivalent to a length of 4.93 ± 0.42 nm, indicating that the positive polaron of MEH-PPV is 60% larger than the negative polaron.

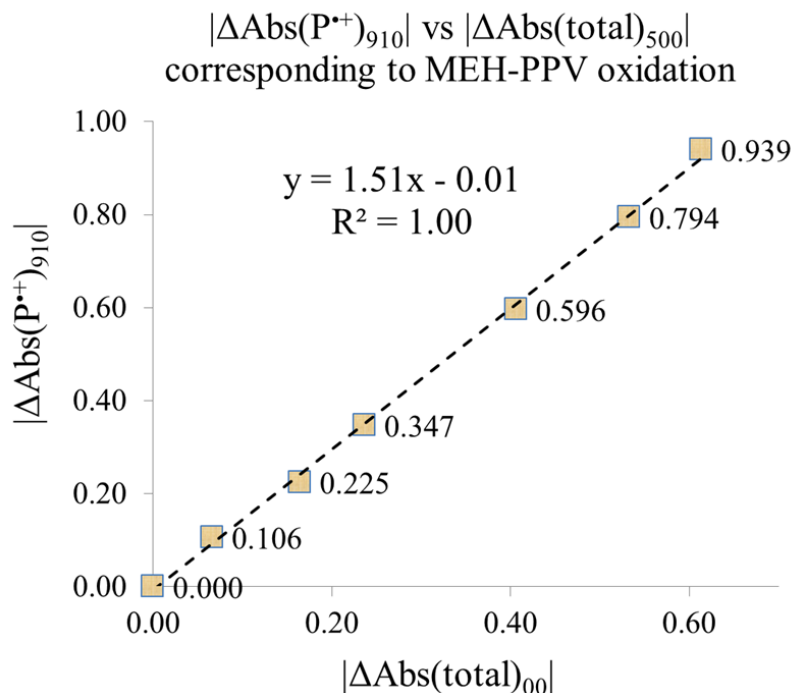


Figure 6-8 A linear relationship was found for the magnitude of absorbance change in the 910 nm band associated with MEH-PPV^{*•} and the corresponding magnitude of absorbance change at 500 nm band where the neutral absorbs.

6.3.3 Triplet

Delocalization of MEH-PPV and pCVPPV triplets were determined from transient absorption spectra containing both triplet-triplet absorption (TTA) and bleach following radiolysis of benzene solutions containing the polymers with biphenyl as triplet sensitizer. To transmit analyzing light at wavelengths where the neutral polymers absorbed a stopcock sealed 1 mm pathlength cuvette attached to solution bulb was used. The blend solutions in benzene consisted of: MEH-PPV (20 μM) and biphenyl (5 mM), and pCVPPV (15 μM) and biphenyl (20 mM). Radiolysis of the solutions resulted in a two-step energy conversion from $^3\text{benzene}^* \rightarrow ^3\text{biphenyl}^* \rightarrow ^3\text{polymer}^*$ due to energetics and satisfying the conditions $[\text{Benzene}] \gg [\text{biphenyl}] \gg [\text{MEH-PPV}]$.

The transient absorption spectrum containing TTA and bleach of MEH-PPV is shown in **Figure 6-9** and the transient absorption spectrum containing TTA and bleach of pCVPPV is shown in **Figure 6-10**. Based on the extinction coefficients of the ground state ($2.6 \times 10^4 \text{ M}^{-1}\text{cm}^{-1}$

¹pru at 500 nm) and triplet ($2.4 \times 10^5 \text{ M}^{-1}\text{cm}^{-1}$ at 820 nm) of MEH-PPV, at 9 μs after pulse, the ratio of the bleach at 520 nm and triplet at 820 nm, was 12/23, corresponding to 4.82 monomers (3.00 nm) of bleach per triplet. This length seems surprising given the reported conjugation length of the singlet in PPV is slightly larger at 6 monomer units and the tight binding of a triplet is expected to correlate with a shorter delocalization length.

Based on the extinction coefficients of the ground state ($5.1 \times 10^4 \text{ M}^{-1}\text{cm}^{-1}$ pru at 500 nm) and triplet ($8.4 \times 10^4 \text{ M}^{-1}\text{cm}^{-1}$ at 660 nm) of pCV-PPV, at 9 μs after pulse, the ratio of the bleach at 420 nm and triplet at 660 nm, was 4.1/7.4, corresponding to 0.92 monomers (1.5 nm) of bleach per triplet. In the transient spectra associated with blends of MEH-PPV and pCV-PPV, the maxima of the observed bleaches were redshifted by ~ 20 nm, possibly due to the summed contributions of the bleach and triplet in both cases. The extinction coefficients determined for the spectra at their maxima were assumed equivalent to the wavelength shifted maxima.

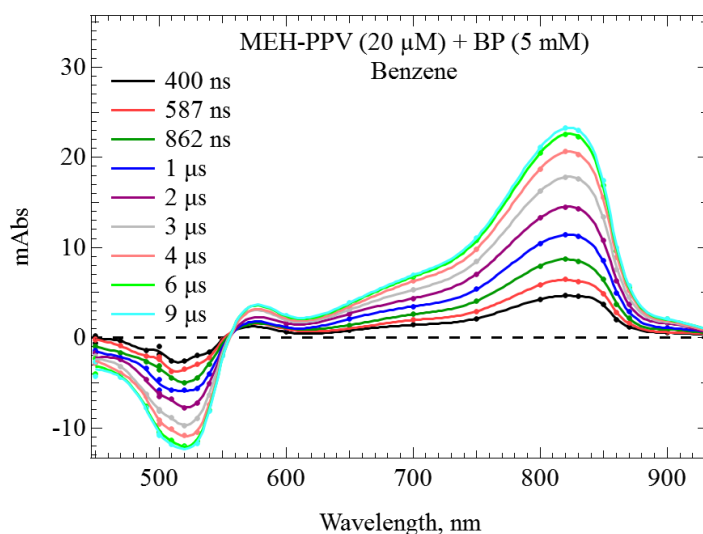


Figure 6-9 Transient absorption spectrum following radiolysis of a benzene solution containing MEH-PPV (20 μM chain) and biphenyl (5 mM) in a 1 mm pathlength cell capable of transmitting light to measure bleach.

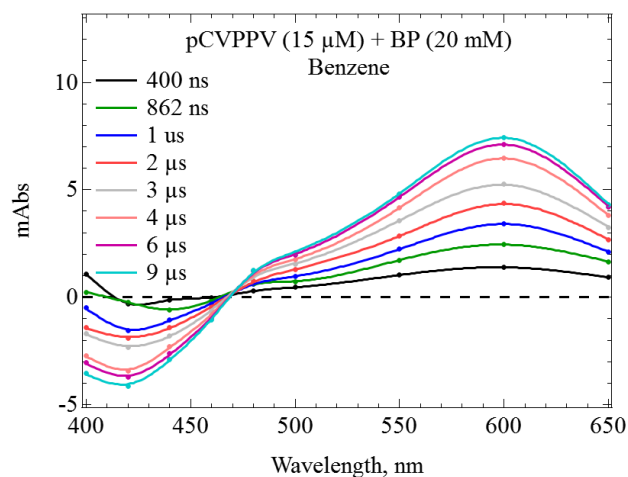


Figure 6-10 Transient absorption spectrum following radiolysis of a benzene solution containing MEH-PPV (15 μM chain) and biphenyl (20 mM) in a 1 mm pathlength cell capable of transmitting light to measure bleach.

6.4 Photophysical properties of moieties

6.4.1 Photoluminescence (PL) spectra

Consideration of the photophysical properties of D/A pairs for photovoltaics is rarely given but important. A type I heterojunction may facilitate energy transfer if strong overlap in the absorption band of one and the emission band of the other. The energy transfer may be competitive with effective electron transfer or may be followed by electron transfer depending on the energetics. Device and material designs should also account for factors such as excited state lifetimes as they limit the exciton diffusion length. Harvesting excitons which cannot reach an effective D/A interface can become a major source of loss.

THF solutions of MEH-PPV and fSF-PPV were prepared for collection of photoluminescence (PL) emission spectra corresponding to excitation at 530 nm and 372 nm, respectively. These wavelengths were not only good for determining the PL quantum yields of each homoblock, but useful for determining quenching of $^1\text{MEH-PPV}^*$ and $^1\text{fSF-PPV}^*$ in solutions containing both. At 530 nm, fSF-PPV absorbs very negligibly, and at 372 nm, the repeat monomer unit extinction

coefficient ratio for $\epsilon(\text{fSF-PPV}_{\text{pru}})/\epsilon(\text{MEH-PPV}_{\text{pru}})$ is at its maximum. The values of $\epsilon_{\lambda}(\text{MEH-PPV}_{\text{pru}})/\epsilon_{\lambda}(\text{fSF-PPV}_{\text{pru}})$ at several wavelengths are shown in **Table 6-2**, with a minimum value obtained at 372 nm.

Table 6-2 Ratio of molar extinction coefficients (pru) for MEH-PPV neutral and fSF-PPV neutral.

λ_{max}	$\epsilon_{\lambda}(\text{MEH-PPV}_{\text{pru}})/\epsilon_{\lambda}(\text{fSF-PPV}_{\text{pru}})$
530	~200
500	86
372	0.32

The photoluminescence quantum yields (ϕ) of MEH-PPV and fSF-PPV were determined from the integration of the PL, using external standards of Rhodamine B in ethanol ($\phi = 0.95$ [127]) at 530 nm, and 9,10-diphenylanthracene (DPA) in ethanol ($\phi = 0.95$ [127] at 372 nm), respectively. The absorbance and PL spectra of these compounds in THF are shown peak normalized in **Figure 6-11**, and the relative quantum yields determined as 0.26 for MEH-PPV and 0.65 for fSF-PPV as shown in **Table 6-3**. The quantum yield for MEH-PPV is similar to the estimate of 0.27 ± 0.01 in THF determined by Nguyen et al [90] relative to a Rhodamine B standard which was assumed to have a quantum yield of unity, rather than 0.95 used in this study. Making a correction for this difference, leads to identical quantum yields for MEH-PPV in this study and Nguyen's. A quantum yield for fSF-PPV has not been previously reported.

That the quantum yield of fSF-PPV is more than double that of MEH-PPV is interesting. It may suggest that the persistence length of fSF-PPV is greater than that of MEH-PPV in spite of the fact that the latter is much longer. In comparing quantum yields of three PPV derivatives of similar length in p-xylene, Gettinger et al [124] suggested a relationship between stiffness and quantum yield, with the stiffest exhibiting a quantum yield of 0.66 ± 0.05 , and the least stiff exhibiting a quantum yield of 0.20 ± 0.05 . These correlations were rationalized on the premise that strong structural relaxations in the excited state requiring multiphonon processes lead to nonradiative decay. Therefore, a higher degree of structural stiffness will enhance probability of radiative photoluminescence by suppressing the multiphonon radiative channel. A similar argument was made by Nguyen who observed that photoluminescence quantum yields of

MEH-PPV measured in different solvents was found to improve with length of hydrodynamic radius, with a quantum yield of 0.27 ± 0.01 in THF compared with 0.39 ± 0.01 in chlorobenzene. The tighter coiling of MEH-PPV in THF is expected to result in increased torsional defects and hence a shorter conjugation length.

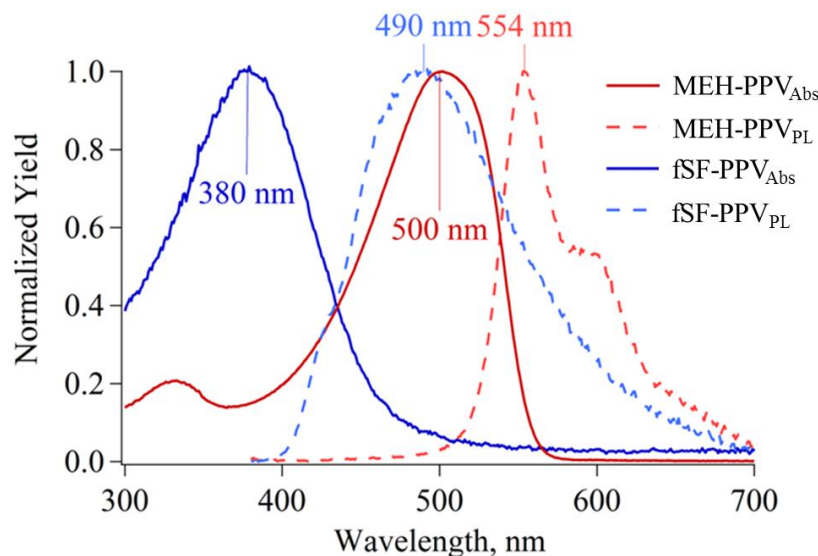


Figure 6-11 The absorbance and PL emission spectra of MEH-PPV and fSF-PPV in THF, plotted with absorbance spectra normalized by $Abs(\lambda)/Abs(\lambda_{max})$ and PL spectra normalized by $PL(\lambda)/PL(\lambda_{max})$.

Table 6-3 Relative quantum yields of MEH-PPV and fSF-PPV measured in THF

Compound	Reference	λ_{exc}	Quantum Yield
MEH-PPV	Rhodamine B	530 nm	0.256
fSF-PPV	Diphenylanthracene	372 nm	0.654

6.5 Determination of MWs by spectral fitting (SF) method

Accurate knowledge of molecular weights for polymers is important for accurate preparation of polymer concentrations from which reaction kinetics can be studied. The synthesis of polymers leads to a polydispersity of molecular weights. The average molecular weights determined by GPC were used to determine concentrations of the homoblocks (MEH-

PPV, SF-PPV, and fSF-PPV). The diblocks were synthesized using the bridge-bound homoblocks of MEH-PPV (DB) and monomers of the acceptors (A and fA) as reagents. The synthetic reaction scheme led to formation of DBA or DBfA involving chain growth of the acceptor moiety only. Consequently, the molecular weights of the donor moieties were equivalent to those of the respective donor homoblocks, while the final lengths of the acceptor moieties were uncertain. GPC measurements had not been collected for the diblock copolymers at the time when materials were originally obtained, but were later provided by our collaborators. To estimate molecular weights, a method which will be referred to as the spectral fitting (SF) method, was used. The SF method assumes that the spectrum of the diblock (absorption or emission) is a linear sum of the spectra of the independent homoblock constituents. The molecular weights estimated by this method were substantially larger than the estimates obtained later by GPC. In this section, the diblock molecular weights as determined by both methods, are presented and compared.

Using the SF method is ideal when no electronic interaction exists between the donor and acceptor constituents, resulting in perfect fits. Weak electronic interaction may produce a spectrum which deviates from a perfect linear sum but which is sufficiently similar to render the approximate fit as reasonable, as was the case for the diblocks in this study. Two approaches of the SF method were used to estimate the number of acceptor monomer units in each diblock.

In the first approach, a reference spectrum of the donor homoblock (D_{ref} spectrum) corresponding to a known concentration, $[D_{ref}]$, and a reference spectrum of the acceptor homoblock (A_{ref} spectrum), corresponding to a known concentration $[A_{ref}]$, were used to produce a composite spectrum, $Diblock_{fit}$ that most closely matched the spectrum of the diblock, through selection of coefficients m and n to satisfy **Eq 6-5**.

$$Diblock_{fit} = m * (D_{ref} \text{ spectrum}) + n * (A_{ref} \text{ spectrum}) \quad 6-5$$

After receiving the molecular weights of all diblocks, a second approach was taken to estimate the number of acceptor monomer units per chain. A reference spectrum of the diblock ($diblock_{ref}$ spectrum) corresponding to a known concentration $[diblock]_{ref}$

(according to MW by GPC), and a reference spectrum of the donor (D_{ref} spectrum) corresponding to known concentration $[D_{ref}]$, were used to acquire a difference spectrum which most resembled the spectral shape of an acceptor reference spectrum, (A_{ref} spectrum) corresponding to a known concentration $[A_{ref}]$. More specifically, the condition $[D_{ref}] = [diblock_{ref}]$ was satisfied, and a coefficient p was selected according to **Eq 6-6** which resulted in a difference spectrum ($diff$ spectrum) whose shape and intensity most closely resembled the byproduct of a coefficient q and A_{ref} spectrum, according to **Eq 6-7**.

$$p * (diblock_{ref} \text{ spectrum}) - (D_{ref} \text{ spectrum}) = diff \text{ spectrum} \quad 6-6$$

$$diff \text{ spectrum} = q * (A_{ref} \text{ spectrum}) \quad 6-7$$

Using the first approach of the SF method, the diblocks D(C2)fA, D(C4)fA and D(C6)fA were fits were generated according to **Eq 6-5**. The diblocks D(C0)fA, D(C1)fA were not available during the initial trial, but were later received and evaluated along with D(C2)fA and D(C2)A, using the second approach of the SF method according to **Eq 6-6** and **Eq 6-7**. In both the initial trial and second trial, absorbance spectra were collected from solutions contained in square quartz cells with pathlengths of 0.5 cm. In the initial trial the donor reference spectrum corresponded to 30.1 μM D pru, and the acceptor reference spectrum corresponded to 9.64 μM of fA pru. The spectral fits of the diblocks were acquired over a spectral range from 300 nm – 600 nm as shown in **Figure 6-12**, **Figure 6-13**, and **Figure 6-14**.

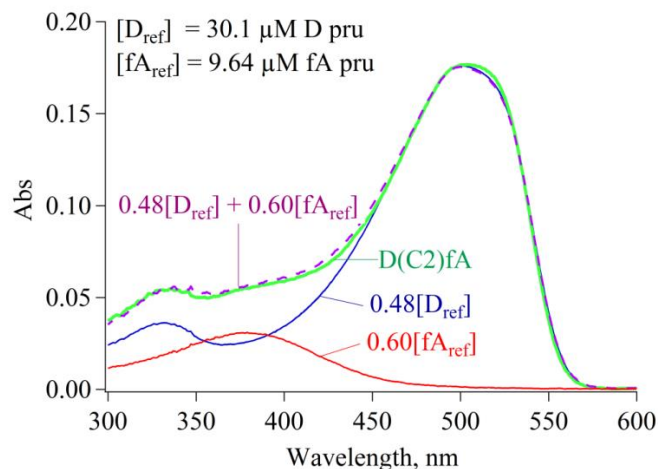


Figure 6-12 The ground state spectrum of $D(C2)fA$ in THF (green) is shown with a best spectral fit (dashed purple) based on the weighted sums of a donor reference spectrum (D_{ref}) and fA reference spectrum (fA_{ref}) defined as: $m*[D_{ref}] + n*[fA_{ref}]$. The spectra corresponding to $m*[D_{ref}]$ (blue) and $n*[fA_{ref}]$ (red) are also shown.

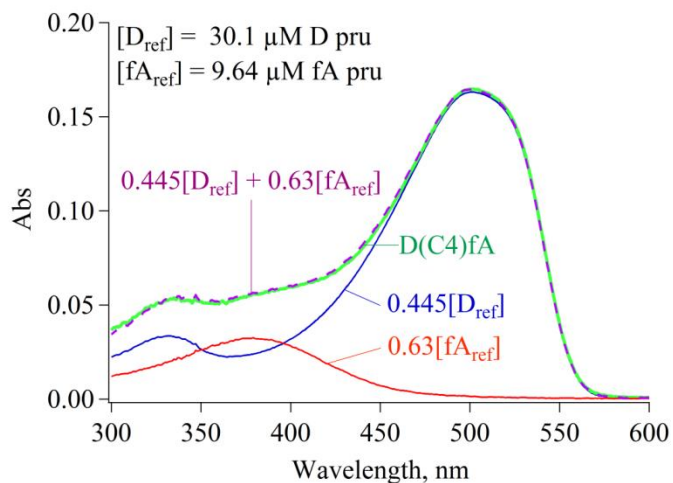


Figure 6-13 The ground state spectrum of $D(C4)fA$ in THF (green) is shown with a best spectral fit (dashed purple) based on the weighted sums of a donor reference spectrum (D_{ref}) and fA reference spectrum (fA_{ref}) defined as: $m*[D_{ref}] + n*[fA_{ref}]$. The spectra corresponding to $m*[D_{ref}]$ (blue) and $n*[fA_{ref}]$ (red) are also shown.

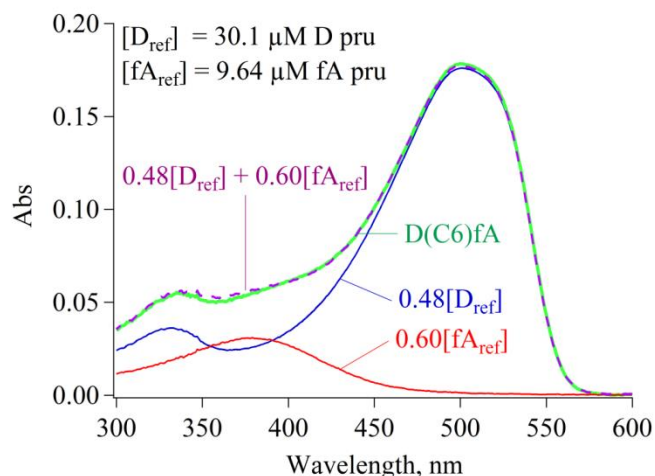


Figure 6-14 The ground state spectrum of D(C6)fA in THF (green) is shown with a best spectral fit (dashed purple) based on the weighted sums of a donor reference spectrum (D_{ref}) and fA reference spectrum (fA_{ref}) defined as: $m*[D_{ref}] + n*[fA_{ref}]$. The spectra corresponding to $m*[D_{ref}]$ (blue) and $n*[fA_{ref}]$ (red) are also shown.

The number of donor monomer units per chain in each of the D(Cn)fA polymers was 24.1. Using the ratio, $n * [A_{ref}]_{pru} / m * [D_{ref}]_{pru}$, the number of acceptor monomers per chain were determined as:

$$(A \text{ monomers per chain}) = (D \text{ monomers per chain}) * \frac{n*[A_{ref}]_{pru}}{m*[D_{ref}]_{pru}} \quad 6-8$$

Based on the spectral fits, **Eq 6-8** was used to determine the number of acceptor monomer units per chain. The molecular weights of the diblocks were then determined as a sum of the molecular weights of the donor moiety ($MW(D)$), bridge ($MW(bridge)$), and terminal groups, ($MW(terminal)$), shown as:

$$MW(diblock) = (MW(A) + MW(D) + MW(bridge) + MW(terminal)) \quad 6-9$$

The number of acceptors per chain and molecular weights of D(C2)fA, D(C4)fA and D(C6)fA as determined in the first trial, are shown in **Table 6-4**.

Table 6-4 Molecular weights of select diblock copolymers determined by SF method in 1st trial

Diblock	Number of fA monomer units per chain of diblock	Molecular weight by SF method	Molecular weight by GPC	MW(SF)/MW(GPC)

D(C2)fA	9.6	16748	10797	1.55
D(C4)fA	10.8	17751	14637	1.21
D(C6)fA	9.6	16804	11142	1.51

In the second trial, ground state absorbance spectra of the diblocks were collected in both THF and chloroform (CHCl₃), over a broader spectral range (from 200 nm – 700 nm). Based on the similarity of D(C2)fA, D(C4)fA, and D(C6)fA observed in the initial trial, only the diblock D(C2)fA was reevaluated in the second trial.

Reference solutions in THF were prepared according to the molecular weights determined by GPC with chain concentrations of: $[diblock]_{ref} = 5 \mu\text{M}$, $[D]_{ref} = 5 \mu\text{M}$, $[A]_{ref} = 5 \mu\text{M}$ (for A), and $[A]_{ref} = 60 \mu\text{M}$ (for fA). The number of acceptor repeat units per diblock chain was then determined by Eq 6-8. In Figure 6-15, *diblock_{ref} spectrum*, *D_{ref} spectrum*, *diff spectrum*, and $q * (A_{ref} \text{ spectrum})$, corresponding to the THF solutions of each of the diblocks are shown. In the cases of D(C0)fA and D(C1)fA, the spectral band associated with the donor moiety were found to be 5 nm blueshifted relative to the 500 nm spectral band of the donor homoblock. The spectral band associated with the donor moiety of diblock D(C2)fA was not shifted relative to spectrum of the donor homoblock however, and by similitude, D(C4)fA and D(C6)fA do not show shifts either. To compensate the blueshift of the donor moieties of D(C0)fA and D(C1)fA relative to the donor homoblock, the *diblock_{ref} spectrum* used in Eq 6-6 for either diblock was redshifted by 5 nm relative to the actual diblock spectrum at the respective concentration. With the exception of D(C2)A, the difference spectra obtained for each diblock using Eq 6-6 were redshifted relative to the reference spectra of the acceptor homoblock. In Figure 6-15 the difference spectra are shown with redshifts applied to match the peaks of the respective acceptor reference spectra. The 5 nm redshift of *diblock_{ref} spectrum* in the case of D(C0)fA and D(C1)fA rendered more accurate matches of the leading edges of the acceptor reference spectra but at the expense of greater inaccuracies at the lower wavelength range as shown in (a) and (b).

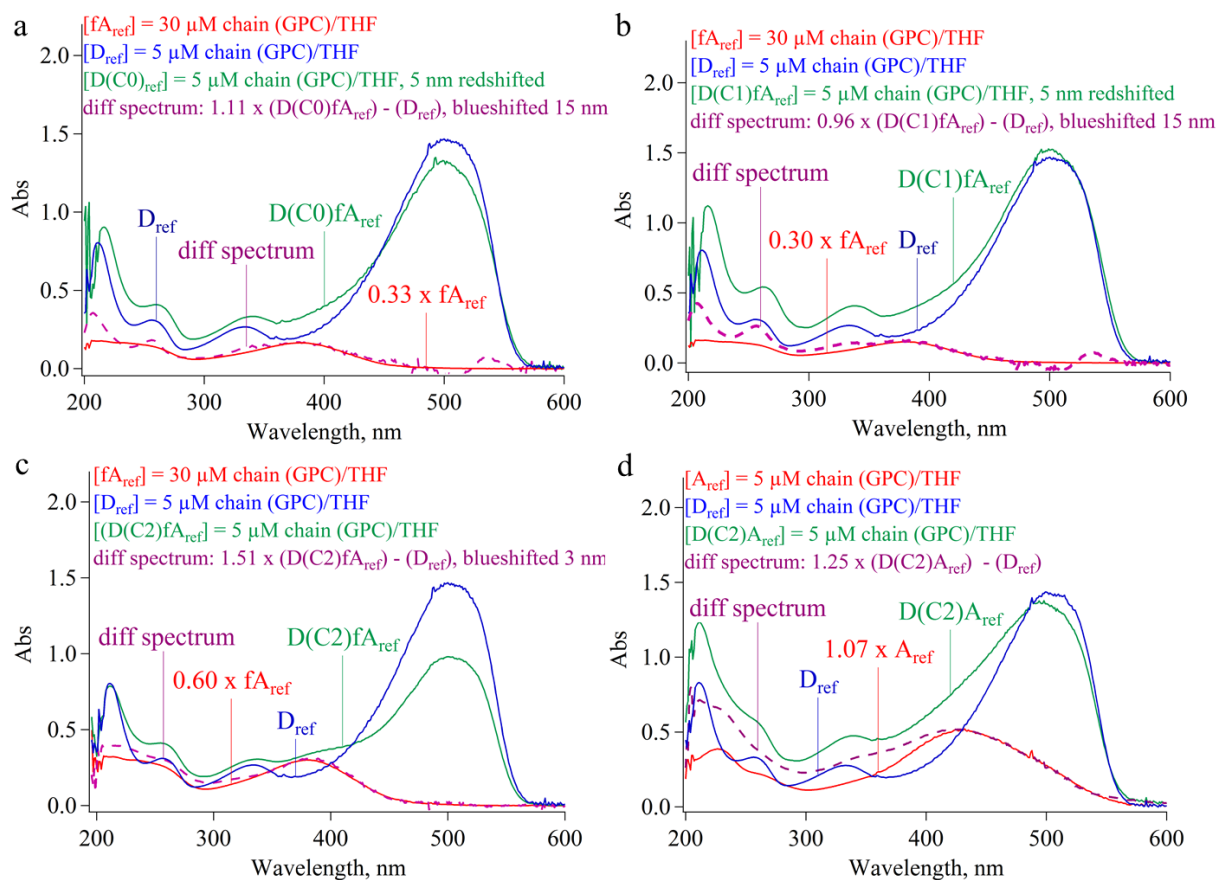


Figure 6-15 Plots of diblock_{ref} spectrum, D_{ref} spectrum, and A_{ref} spectrum corresponding to THF solutions of: a) D(C0)fA, b) D(C1)fA, c) D(C2)fA, and d) D(C2)A.

The amount of blueshift was 15 nm in the case of D(C0)fA and D(C1)fA, and for D(C2)fA was 3 nm. For D(C0)fA and D(C1)fA, the 5 nm blueshift of the donor moiety relative to the donor homoblock, and the 15 nm redshift of the acceptor moiety relative to the acceptor homoblock appears at least in part to be due to a stronger electronic interaction between the donor and acceptor moieties. The donor moieties in each diblock are of the same length and therefore should share the same spectral peaks and molar extinction coefficients if no changes in electronic interactions have occurred. The length of the acceptor moieties are not known and additional contributions to spectral shifts may be due to acceptor moieties being longer than the respective acceptor homoblock. Redshifts have been observed in conjugated oligomers as the number of monomer units increase up to a limiting number of monomers associated with the conjugation length.

If the GPC values of the homoblocks and diblocks are accurate, and if the condition $[diblock]_{ref} = [D]_{ref}$ is satisfied, provided the ground state absorbance spectra of the diblocks can be approximated by linear sums of the homoblock constituents, then the value of p should be ≈ 1 . For the data represented in **Figure 6-15**, the condition $[diblock]_{ref} = [D]_{ref}$ is satisfied, and the ground state absorbance spectra of the diblocks can be approximated by linear sums of the homoblock constituents. With the exception of D(C1)fA, the value of p differs from 1 by more than 5% with values exceeding 1, by 11% (D(C0)fA), 25% (D(C2)A), and 51%, (D(C2)fA). The similarity of D(C2)fA, D(C4)fA and D(C6)fA suggests that the values of p for D(C4)fA and D(C6)fA would also be $\approx 25\%$.

That values of p significantly exceed the value of 1, suggests one of three possibilities: 1) the extinction coefficients of the donor moieties in these diblocks exceed that of the donor homoblock 2) the molecular weights of these diblocks are significantly underestimated, 3) the molecular weights of the homoblock donor is significantly overestimated. The first possibility is not physically possible and is ruled out. Neither the second or third possibility could be completely ruled out, however, it is conceivable that the diblocks due to flexible bridges (with exception of D(C0)fA) may exhibit reduced hydrodynamic volumes which may underestimate their molecular weights. Furthermore, estimates of the molecular weight of the fSF-PPV homoblock by GPC and MALS were virtually identical, which suggests that GPC estimates were accurate for the single component system. For these reasons, we considered the accuracy of the GPC value for the MEH-PPV homoblock more reliable than the GPC values of the diblocks. This assumption also provides an upper estimate for the molecular weights of the diblocks.

The number of acceptor monomers in each diblock chain was estimated from **Eq 6-10** using the value of q obtained from **Eq 6-7**.

$$(A \text{ monomers per chain}) = (D \text{ monomers per chain}) * \frac{q * [A_{ref}]_{pru}}{[D_{ref}]_{pru}} \quad 6-10$$

The molecular weights of the diblocks were once again determined using **Eq 6-9**, based on the assumed accuracy of a 24.1 monomer MEH-PPV in all D(Cn)fA and a 21.5 monomer MEH-PPV in D(C2)A. The molecular weights determined in the second trial of measurements are provided in **Table 6-5**.

Table 6-5 Determined fA monomer units per chain and molecular weights of select diblocks based on application of SF method to ground state absorbance spectra in THF

Diblock	# acceptor monomers per chain	MW _{SF}	MW _{GPC}	MW _{SF} /MW _{GPC}
D(C0)fA	6.2	13979	10987	1.27
D(C1)fA	5.7	13742	11278	1.22
D(C2)fA	11.3	18114	10797	1.68
D(C6)fA	10.2	17293	11142	1.55
D(C2)A	14.8	15299	16022	0.95

As a test of solvent dependence, the SF method was also applied to spectra of the diblock solutions prepared in chloroform as well. Provided that electronic coupling between the donor and acceptor moieties of the diblocks are weak in chloroform, the SF method was expected to render similar results as observed in THF. Chain concentrations of reference solutions in chloroform were prepared according to molecular weights by GPC as: $[diblock]_{ref} = 5 \mu\text{M}$, $[D]_{ref} = 5 \mu\text{M}$, $[A]_{ref} = 5 \mu\text{M}$ (for A) and $[A]_{ref} = 60 \mu\text{M}$ (for fA). The number of acceptor repeat units per diblock chain was then determined by **Eq 6-8**. The diblock reference spectrum (*diblock_{ref} spectrum*), donor reference spectrum (*D_{ref} spectrum*), difference spectrum (*diff spectrum*), and scaled acceptor reference spectrum ($q * (A_{ref} \text{ spectrum})$), corresponding to the chloroform solutions of each of the diblocks are shown in **Figure 6-16**.

As was observed in THF, in the cases of D(C0)fA and D(C1)fA, the spectral band associated with the donor moiety was found to be 5 nm blueshifted relative to the 500 nm spectral band of the donor homoblock. No such shift was evident for diblock D(C2)fA. To compensate for the blueshift of the donor moieties of D(C0)fA and D(C1)fA, the *diblock_{ref} spectrum* used in **Eq 6-6** for either diblock was once again redshifted by 5 nm relative to the actual diblock spectrum. With the exception of D(C2)A, the difference spectra corresponding to each diblock according to **Eq 6-6** were also found to be redshifted relative to the acceptor reference spectra, – 15 nm in the case of D(C0)fA and D(C1)fA, and 3 nm in the case of D(C2)fA, identical to the observations in THF. The difference spectra are shown in **Figure 6-16** blueshifted to match the peak of acceptor reference spectra.

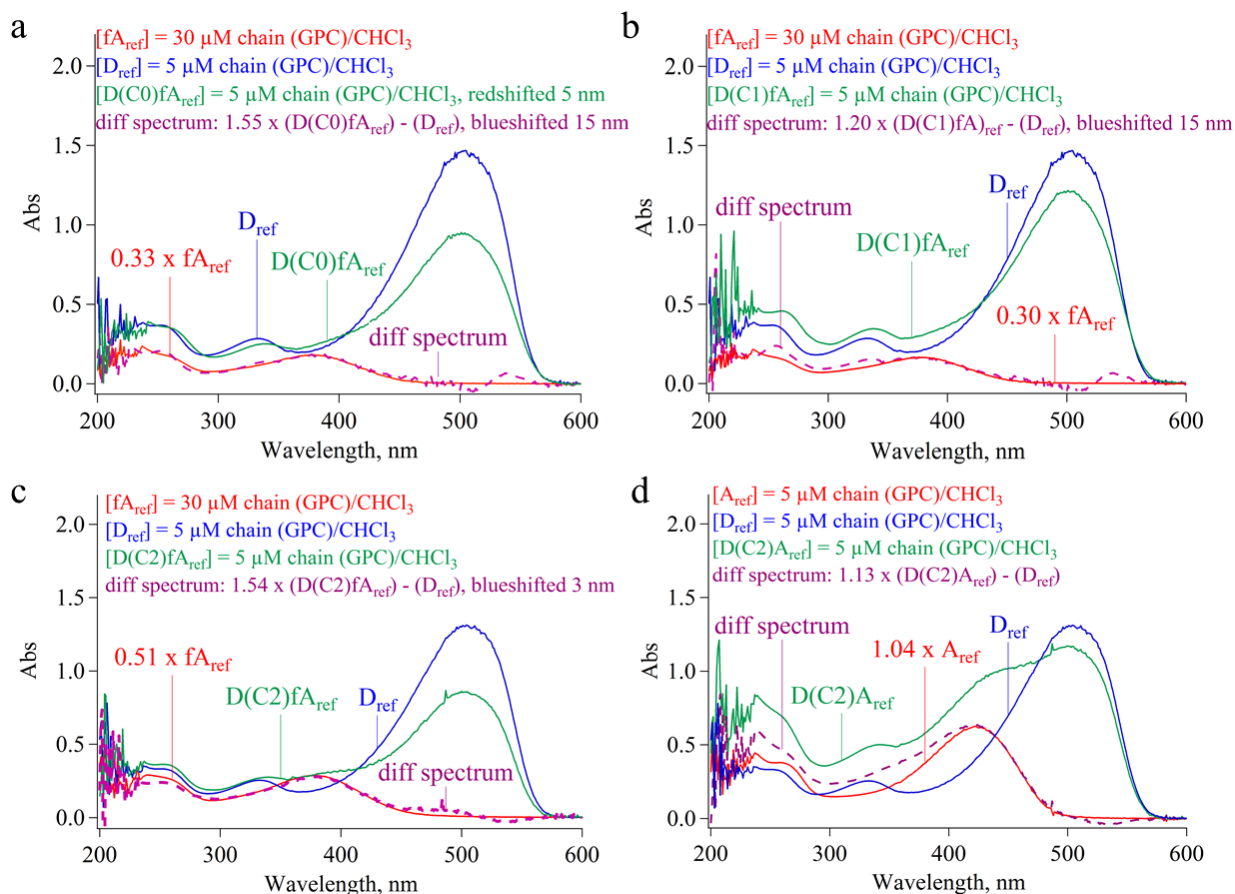


Figure 6-16 Plots of diblock_{ref} spectrum, D_{ref} spectrum, and A_{ref} spectrum corresponding to CHCl₃ solutions of: a) D(C0)fA, b) D(C1)fA, c) D(C2)fA, and d) D(C2)A.

For the diblock spectra in chloroform, the values of p necessary to acquire difference spectra closely resembling the spectrum of the corresponding acceptor homoblock, were ≥ 1.13 , suggesting that the molecular weights of the diblocks were underestimated. However, the values of p obtained for diblocks D(C0)fA and D(C1)A in chloroform exceeded the values obtained for the same diblocks in THF, by 20% and 28% respectively, while values obtained for D(C2)fA and D(C2)A in chloroform were within 10% of the values obtained in THF. The SF method used assumes the concentration corresponding to the donor reference spectrum is accurate, but is insensitive to errors in the concentration of the diblock reference spectrum. For example, a diblock reference spectrum prepared at half the desired concentration will result in a value for p that is twice the value needed for the desired concentration, but resulting in the same value of q in both cases. Assuming the concentrations of the donor homoblock

prepared in both THF and chloroform are accurate, the extinction coefficients of the donor homoblock at maximum were found to decrease by 9% in chloroform relative to THF. As a test of repeatability, a measurement of the donor homoblock (21.5 monomers) at 5 μM chain concentrations was made in chloroform, THF, and a mixed solvent containing 1/6 chloroform and 5/6 THF, and the corresponding ground state absorbance spectra are shown in **Figure 6-17 (a)**.

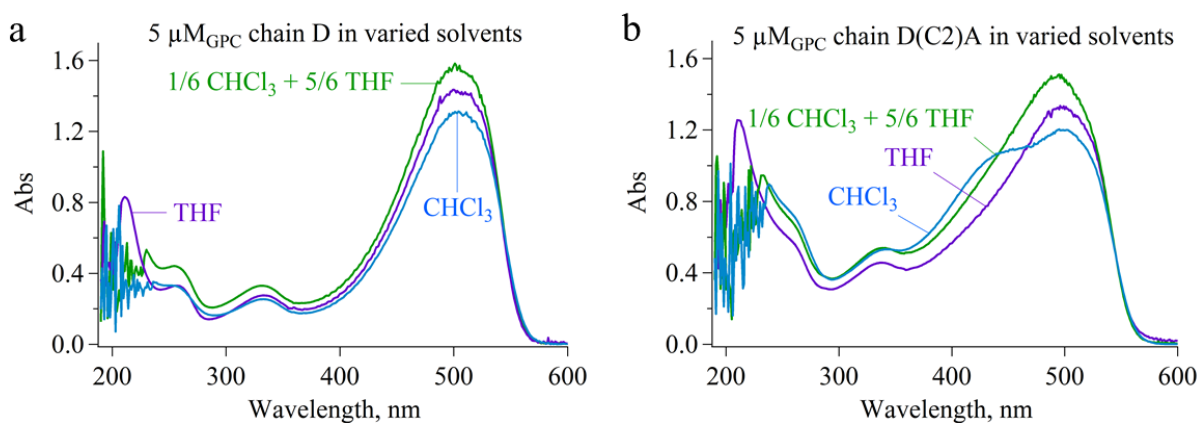


Figure 6-17 Ground state absorbance spectra of: a) D (21.5 monomers) prepared at 5 μM chain (by GPC) in THF, CHCl_3 , and 1/6 CHCl_3 and 5/6 THF, and b) D(C2)A at prepared at 5 μM chain (by GPC) in THF, CHCl_3 , and 1/6 CHCl_3 and 5/6 THF.

The solution in the mixed solvent system was prepared by mixing the respective THF and chloroform solutions of the donor homoblock at volume ratios necessary to acquire 1/6 chloroform and 5/6 THF. It was therefore expected that the extinction coefficient of the donor homoblock in the mixed solvent would be equivalent to the sum of 1/6 the extinction coefficient of donor homoblock in the chloroform solution and 5/6 the extinction coefficient in THF. Surprisingly, the mixed solvent resulted in an extinction coefficient for the donor homoblock that was larger than in either pure solvent. Given the substantial difference in the spectral shape of D(C2)A in THF versus chloroform, the diblock was similarly tested in each of the same solvent systems to determine if the effects on the extinction coefficients of the diblock are similar. The optical densities in the pure and mixed solvents demonstrate a virtually identical dependence of the extinction coefficients of the donor moiety of D(C2)A as observed from the donor homoblock as shown in **Figure 6-17 (b)**. While the solvent tests involved only

three solvent systems, the results suggests that the spectral fitting method is applicable to D(C2)A and likely the other diblocks is independent of solvent choice. A specific for solvent dependence was not performed on D(C0)fA and D(C1)fA, but based on the repeatability of measured extinction coefficients of the donor homoblock moieties in THF and chloroform, it is concluded that the > 10% difference in the value of p measured for these polymers in chloroform versus THF is due to error in the concentrations of the diblock reference spectra which therefore does not affect the reliability of the molecular weight determination. The other alternative would suggest that a substantial difference exists between the extinction coefficients of the donor and acceptor moieties for D(C0)fA and D(C1)fA with respect to their homoblock counterparts. The alternate possibility would suggest the extinction coefficients of the donor and acceptor moieties of D(C0)fA and D(C1)fA are significantly smaller than their homoblock counterparts in chloroform than in THF. Given that the ground state absorbance spectra of the diblocks are well fit by a linear sum of the ground state absorbance spectra of the individual homoblocks, this seems highly improbable.

Table 6-6 Determined fA monomer units per chain and molecular weights of select diblocks based on application of SF method to ground state absorbance spectra in chloroform

Diblock	# fA monomers per chain	MW _{SF}	MW _{GPC}	MW _{SF} /MW _{GPC}
D(C0)fA	6.2	13979	10987	1.27
D(C1)fA	5.7	13742	11278	1.22
D(C2)fA	9.6	16806	10797	1.56
D(C2)A	14.4	15107	16022	0.94

Based on all spectral fits, averages of the number of acceptor monomers per diblock chain, and molecular weights were determined and are presented as shown in **Table 6-7**.

Table 6-7 Fraction of monomer units per chain and corresponding molecular weights of each diblock copolymer as determined by the spectral fit (SF) method. For diblock D(C4)fA, material limitations prevented multiple measurements and for D(C0)fA and D(C1)fA only two measurements were made and both found to be identical. Standard deviations of 5% of the mean are assumed in all of these cases.

Diblock	# fA monomers per chain	MW _{SF}	MW _{GPC}	Fraction of monomers as
---------	-------------------------	------------------	-------------------	-------------------------

				acceptor by SF
D(C0)fA	6.2 ± 0.31	13,980	10,987	0.21 – 0.22
D(C1)fA	5.7 ± 0.28	13,740	11,278	0.19 – 0.20
D(C2)fA	10.2 ± 0.77	17,530	10,797	0.30 – 0.32
D(C4)A	10.8 ± 0.54	17,750	14,637	0.31 – 0.33
D(C6)fA	10.2 ± 0.66	17,312	11,142	0.30 – 0.31
D(C2)A	14.6 ± 0.21	14,840	16,022	0.38 – 0.39

Using the spectral fitting method, THF solutions of D_{14} , $D_{14}(C0)fA$, and $D_{14}(C1)fA$ were used to determine the concentration of fSF-PPV monomer units in $D_{14}(C0)fA$ and $D_{14}(C1)fA$ from by subtracting the peak normalized spectrum of D_{14} . The spectra of $D_{14}(C0)fA$ and $D_{14}(C1)fA$ were virtually identical such that the concentration of fSF-PPV monomers in both could be considered equivalent. The peak absorbance for the $D_{14}(Cn)fA$ chains was at 490 nm, blue shifted by 10 nm relative to the D_{24} chain, but the same monomer extinction coefficient was assumed for D_{14} and D_{24} .

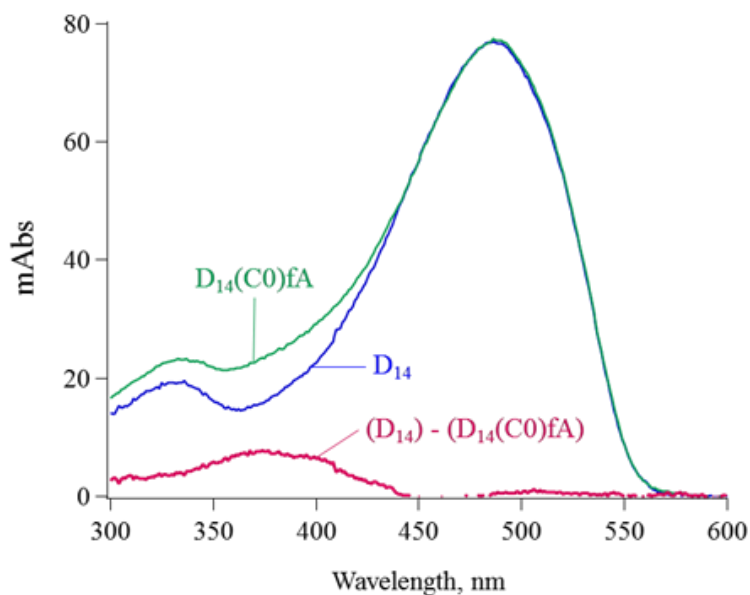


Figure 6-18 A difference spectrum between the ground state absorbance spectrum of D_{14}/THF and $D_{14}(C0)fA/THF$ when normalized at peaks, is assumed to be equivalent to the ground state absorbance spectrum of the fA moiety from which concentration ratios of D:fA can be determined.

As shown in **Figure 6-18** the difference spectrum of $Abs(D_{14}(C0)fA) - Abs(D_{14})$ resulted in a spectrum equivalent to fSF-PPV. Determining monomer concentrations of D and fA at

wavelengths of 490 nm and 380 nm, respectively, molecular weights were estimated and compared with GPC estimates as shown in **Table 6-8**. Based on these estimates, a concentration of 3.4 fA monomers are estimated to be contained per chain of $D_{14}(C0)fA$ and $D_{14}(C1)fA$, leading to a monomer ratio for fA:D of 0.24:1.0.

Table 6-8 Molecular weight estimates for $D_{14}(Cn)FA$ determined by spectral fitting method and compared with GPC determined molecular weights

Compound	D abs at 490 nm	fA abs at 380 nm	[D]mon	[fA]mon	fA per chain	Chain MW by spectral fit	Chain MW by GPC
$D_{14}(C0)fA$	0.0766	0.0075	2.96 μ M	0.71 μ M	3.36	8177	7693
$D_{14}(C1)fA$	0.0766	0.0075	2.96 μ M	0.71 μ M	3.36	8376	7796
D_{14}	N/A	N/A	N/A	N/A	N/A	N/A	5292

6.6 PL emission quenching

A schematic for PL quenching via excited state charge transfer in a DBA system is illustrated in **Figure 6-19**. As shown, an exciton formed on **(a)** the donor moiety or **(b)** the acceptor moiety, may dissociate to a radical ion pair consisting of a radical cation of the donor and radical anion of the acceptor, if it does not first recombine.

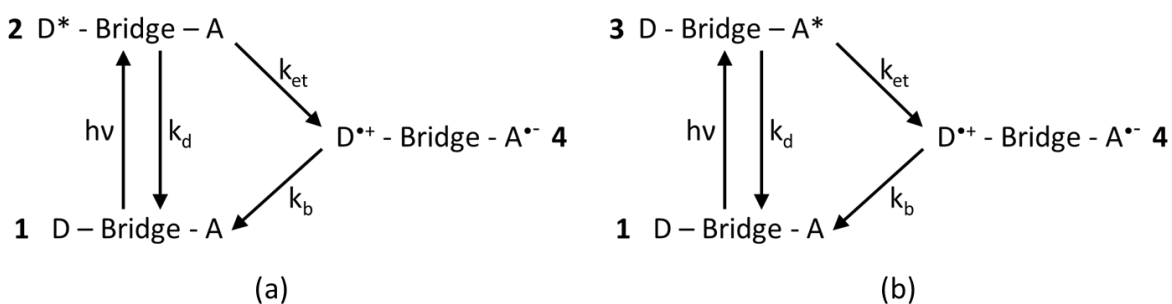


Figure 6-19 Pathways for exciton decay in a DBA system showing competing rates for recombination and dissociation to radical ion pairs.

Photoexcited ps transient absorption spectroscopy and steady state PL spectroscopy were techniques used to investigate charge transfer from the excited state. Optical excitation of a

multichromophoric system may be selective allowing excited states to be preferentially generated on one moiety unlike the distribution of charges generated by radiolysis which depend on the concentrations of the respective moieties. The instantaneous formation of photoexcited states relative to resolution of detectors allows the formation of initial states to be easily distinguished from their decay. The formation of radical ion states from which charge transfer can also occur by diffusive capture is dependent on concentration and may limit the measurement of charge transfer processes which occur more rapidly. Conversely, the lifetime of photoexcited states will limit the measurement of charge transfer processes if the latter occur on a longer time scale. The nature of the excitons formed also means that the nature of charge transfer must account for Coulombic potential of the electron and hole which varies with separation distance.

In the following sections excited state quenching from either photoexcited moiety of D(Cn)fA in THF are explored.

6.6.1 Quenching of $^1fA^*$

Excited state quenching of fA was probed at 372 nm and 370 nm where the ratio of ϵ_{fA}/ϵ_D was at or near its maximum, with ratios of 3.08:1.00 and 3.07:1.00, respectively. THF solutions of the donor homoblock (D), acceptor homoblock (fA), D(C2)fA, D(C4)fA and D(C6)fA were prepared with equivalent ground state absorbances of 0.05 at 372 nm as shown in **Figure 6-20**. This condition ensured that excitation at 372 nm would result in equal numbers of singlet excited states formed in each of the solutions. The ground state absorbance spectra of the donor homoblock and acceptor homoblock were labeled as D_{372Abs} and fA_{372Abs} , respectively. These spectra correspond to concentrations of $[D_{372Abs}] = 1.24 \mu\text{M chain}$ (30.0 $\mu\text{M pru}$) and $[fA_{372Abs}] = 3.08 \mu\text{M chain}$ (9.68 $\mu\text{M pru}$).

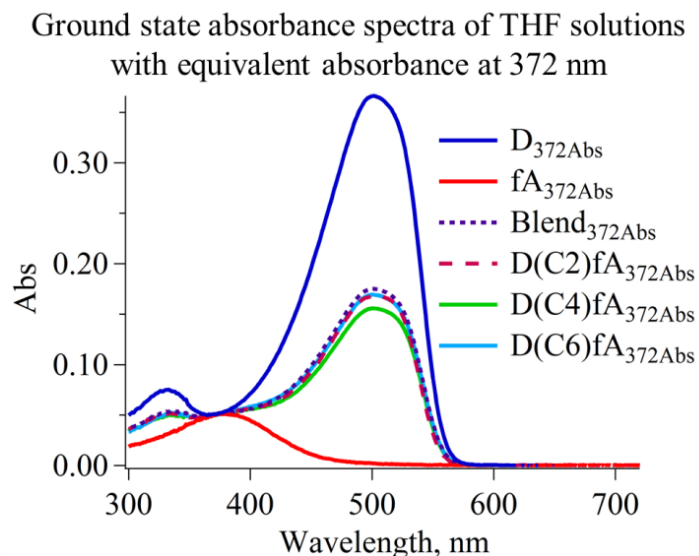


Figure 6-20 Ground state absorbance spectra of THF solutions of homoblocks (*D* and *fA*), blend, and select diblocks, all prepared with an absorbance of 0.05 at 372 nm.

The spectra of the blend ($Blend_{372Abs}$) and diblock ($D(Cn)fA_{372Abs}$) solutions were fitted by linear sums of the homoblock spectra, fA_{372Abs} and D_{372Abs} :

$$Blend_{372Abs} \text{ (or } D(Cn)fA_{372Abs}) = a_{theor} * fA_{372Abs} + b_{theor} * D_{372Abs} \quad 6-11$$

The values of a_{theor} and b_{theor} correspond to the estimated fraction of total excited states in a solution which are of the forms $^1fA^*$ and $^1D^*$ respectively, and should sum to a value of 1. In **Table 6-9**, the values of a_{theor} and b_{theor} corresponding to the blend and diblock solutions are provided.

Table 6-9 Values of a_{theor} and b_{theor} obtained for blend and diblock solutions

Solution (in THF)	a_{theor}	b_{theor}
Blend	0.52	0.48
D(C2)fA	0.55	0.45
D(C4)fA	0.58	0.42
D(C6)fA	0.38	0.66

The photoluminescence (PL) spectra corresponding to 372 nm excitation of the THF solutions of the homoblocks, diblocks, and blend were collected and are shown in **Figure 6-21**. The PL spectra of *D* and *fA* homoblocks shown in **(a)**, are emission yields corresponding to an equal number of singlet excitons for both, the PL yield of *fA* is a factor of 1.38 times greater

than that of D homoblock. By comparison, the PL spectra of the blend and diblock solutions shown in **(b)** contain PL emission from both donor and acceptor moieties. The concentrations corresponding to the PL reference spectra of the homoblocks and their relative emission yields

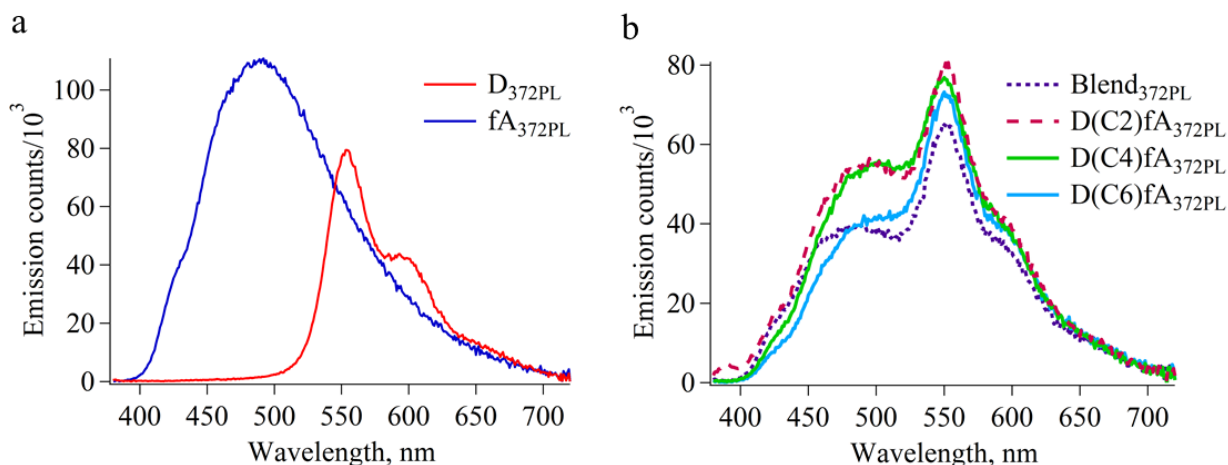


Figure 6-21 Photoluminescence spectra following excitation at 372 nm corresponding to THF solutions of: a) D and fA homoblocks, and b) a D/fA blend, D(C2)fA, D(C4)fA, and D(C6)fA.

Theoretical plots of photoluminescence were determined by using the expression:

$$PL_{theor} = a_{theor} * fA_{372PL} + b_{theor} * D_{372PL} \quad 6-12$$

Here, fA_{372PL} and D_{372PL} are photoluminescence reference spectra resulting from 372 nm excitation of the homoblock solutions fA_{372Abs} and D_{372Abs} , respectively. The theoretical plots are expected plots if energy and charge transfer are negligible and assuming the photoluminescence spectrum of each moiety in the diblock or in the blend is identical to each individual component in isolation.

To evaluate the efficiencies of charge transfer and energy transfer from $^1fA^*$, the PL_{theor} spectra were compared against best fits of the blend and diblock emission spectra obtained by linear sums of the homoblock emission spectra by using the expression:

$$PL_{bestfit} = a_{bestfit} * fA_{372PL} + b_{bestfit} * D_{372PL} \quad 6-13$$

The coefficients $a_{bestfit}$ and $b_{bestfit}$ are determined by trial and result in a composite PL spectrum that most closely resembles that of the blend PL or diblock PL spectrum. Inadequate fits were obtained using this function in the cases of D(C4)fA and D(C6)fA, due to an apparent

redshift in the PL spectrum of the fA moiety with respect to that of the fA homoblock. Furthermore, the sum of $a_{bestfit} + b_{bestfit}$ was found to exceed 1 in all cases but the blend solution. For these reasons, approximations of quenching efficiencies of $^1fA^*$ using **Eq 6-13** was only feasible for the blend solution.

The plots of PL_{theor} and $PL_{bestfit}$ corresponding to the blend and diblock solutions are shown below in **Figure 6-22**.

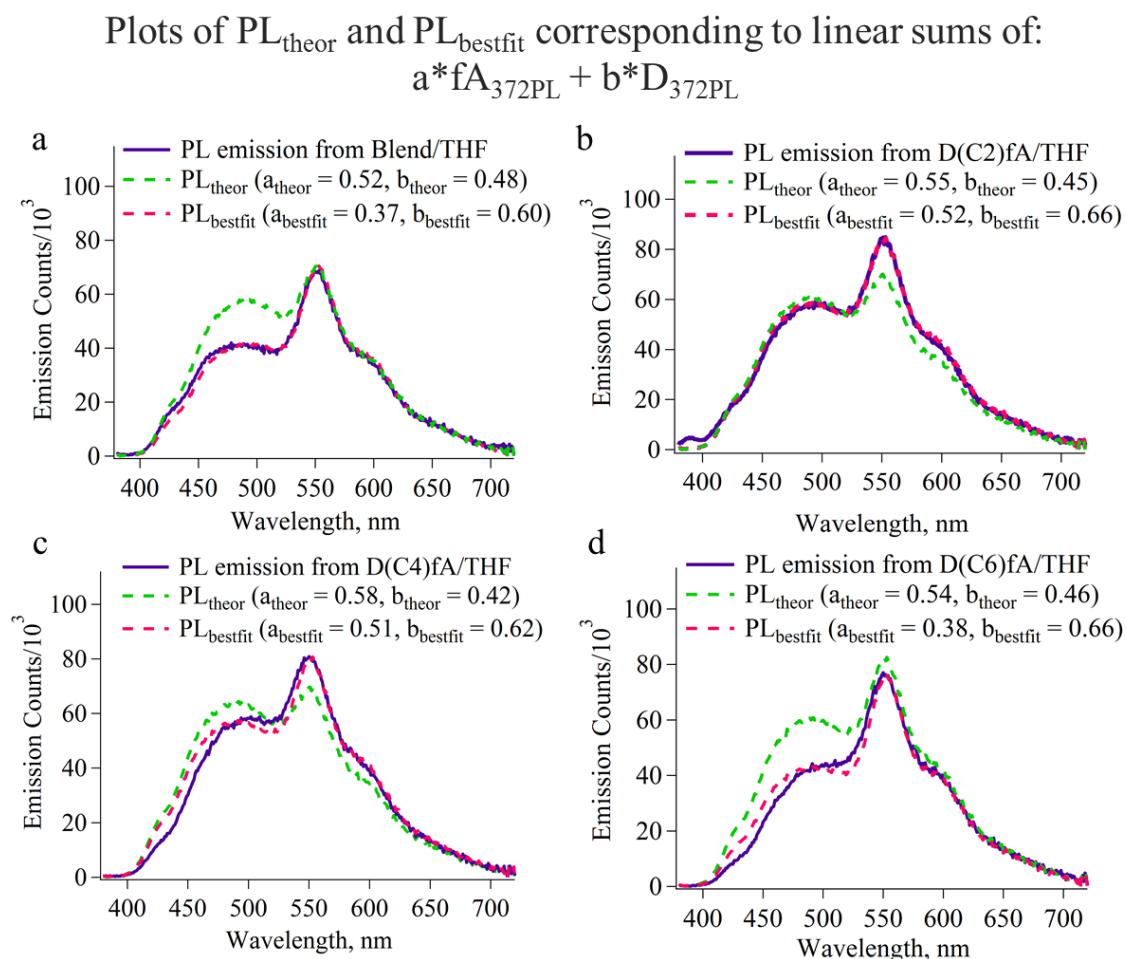


Figure 6-22 Photoluminescence spectra of blend and diblock solutions in THF corresponding to excitation at 372 nm where each contain the same absorbance.

The emission yield of $^1D^*$ from solution D_{372PL} , represented as $N_{homo}^{emit,D}$ is defined as:

$$N_{homo}^{emit,D} = \phi_D \cdot N_{homo}^{total,D} \quad 6-14$$

where ϕ_D is the photoluminescence quantum efficiency of the donor and $N_{homo}^{total,D}$ is the total yield of $^1D^*$ formed by photoexcitation, where $N_{homo}^{total,D} = b_{theor}$. Similarly, the emission yield of $^1fA^*$ from solution fA_{372PL} , represented as $N_{homo}^{emit,fA}$ is defined as:

$$N_{homo}^{emit,fA} = \phi_{fA} \cdot N_{homo}^{total,fA} \quad 6-15$$

where ϕ_{fA} is the photoluminescence quantum efficiency of fA . An upper estimate for the fraction of $^1fA^*$ dissociated can be made based on the following considerations. The yield of emitting $^1fA^*$ states in $Blend_{372PL}$, represented as $N_{blend}^{emit,fA}$ is related to the yield of emitting $^1fA^*$ states in the fA_{372PL} , represented as $N_{homo}^{total,fA}$, by:

$$N_{blend}^{emit,fA} = \phi_{fA} \cdot (N_{homo}^{emit,fA} - N_{fA\ loss}) \quad 6-16$$

where $N_{fA\ loss}$ is the yield of emitting $^1fA^*$ lost in $Blend_{372PL}$ relative to the emission yield of fA_{372PL} . The quantity of $N_{fA\ loss}$ can be determined by:

$$N_{fA\ loss} = a_{theor} - a_{bestfit} \quad 6-17$$

If the fraction of $N_{fA\ loss}$ due to charge transfer from the $^1fA^*$ state, is represented as $N_{CT,fA}$ and the fraction due to energy conversion to $^1D^*$ is represented as N_{conv} , then $N_{fA\ loss}$ can be represented as a sum of these terms:

$$N_{fA\ loss} = N_{conv} + N_{CT,fA} \quad 6-18$$

Therefore $N_{blend}^{emit,fA}$ can be redefined as:

$$N_{blend}^{emit,fA} = \phi_{fA} \cdot (N_{homo}^{emit,fA} - N_{conv} - N_{CT,fA}) \quad 6-19$$

If the charge transfer from the $^1D^*$ state is represented as $N_{CT,D}$, the $N_{blend}^{emit,D}$ can then be defined as:

$$N_{blend}^{emit,D} = \phi_D \cdot (N_{homo}^{total,D} + (N_{fA\ loss} - N_{CT,fA}) - N_{CT,D}) \quad 6-20$$

To acquire an upper limit for $N_{CT,fA}$ we evaluate the condition $N_{CT,D} = 0$. By dividing **Eq 6-20** by $N_{homo}^{total,D}$ and making the substitutions $N_{blend}^{emit,D} = b_{best}$ and $N_{homo}^{total,D} = b_{theor}$ an expression for $N_{CT,fA}$ is obtained as:

$$N_{CT,fA} = (b_{theor} + a_{theor}) - (a_{best} + b_{best}) \quad 6-21$$

The efficiency of energy conversion from ${}^1fA^*$ to ${}^1D^*$, can be expressed in terms of $N_{CT,fA}$ as:

$$N_{conv} = \frac{(a_{theor} - a_{best}) - N_{CT,fA}}{a_{theor}} \quad 6-22$$

Using equation **Eq 6-21**, an upper limit of $N_{CT,fA} = 0.03$, indicating a quenching efficiency of $0\% \leq 3\%$ for dissociation of ${}^1fA^*$ at the concentration of $1.17 \mu\text{M}$ chain of MEH-PPV. At the same concentration of MEH-PPV, the efficiency for quenching ${}^1fA^*$ via energy conversion to ${}^1D^*$, was calculated from **Eq 6-22**, as $N_{conv} = (13.5 \pm 1.5)\%$. The similar concentration ratios of D monomers to fA monomers in the blend and diblocks solutions with equivalent absorbances at 372 nm , suggest that a similar energy conversion yield of ${}^1fA^*$ to ${}^1D^*$ is likely in the diblock solutions. In a solution containing an energy donor (e.g. fA) and energy acceptor (D), energy conversion may occur by collision via Dexter energy transfer, and/or at a distance via Förster energy resonance transfer (FRET). The rate of energy transfer by FRET depends on:

1. The overlap integral, J , as shown in **Figure 6-23** is defined by the spectral overlap between the photoluminescence spectrum of the energy donor and the absorbance spectrum of the acceptor when plotted on a normalized scale;
2. The quantum yield, ϕ_D , of the energy donor;
3. A factor, κ^2 , which describes the relative orientation of the transition dipoles of the energy donor and energy acceptor, and can have a value between 0 and 4, although for molecules undergoing fast isotropic motions, dynamic averaging results in a value of $2/3$.
4. The distance, r , between the energy donor and energy acceptor.

The energy conversion efficiency, N_{conv} , will be dependent on the Förster radius, R_0 , as:

$$N_{conv} = \frac{R_0^6}{R_0^6 + r^6} \quad 6-23$$

Given an index of refraction, n , If the overlap integral, J , is in units of $\text{M}^{-1}\text{cm}^{-1}\text{nm}^4$, then the Förster radius may be determined from:

$$R_0 = 0.0211 * (n^{-4}\phi_D\kappa^2J)^{1/6} \quad 6-24$$

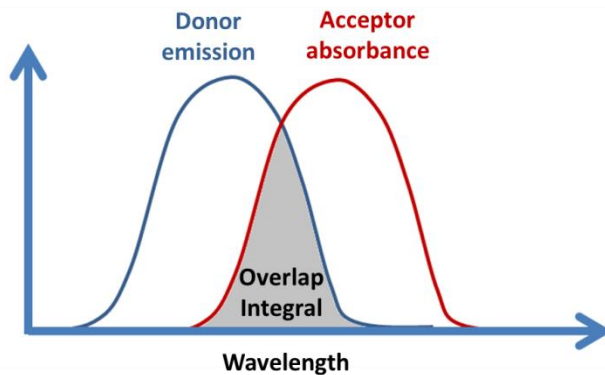


Figure 6-23 The overlap integral is defined by the overlapping spectral regions of the absorbance spectrum of the energy acceptor and the fluorescence spectrum of the energy donor.

Using an index of refraction of 1.407 for THF, and a value of $2/3$ for κ^2 , the overlap integral for D and fA was calculated as $1.91 \times 10^{16} \text{ M}^{-1}\text{cm}^{-1}\text{nm}^4$, resulting in a Förster radius of 7.56 nm. According to **Eq 6-23**, this would suggest a transfer efficiency of 86% in D(C6)fA assuming the transfer distance is equivalent to the bridge length of 1.24 nm. While the sums of the fit coefficients $a_{bestfit} + b_{bestfit}$ for the diblock PL spectra in **Figure 6-22** were greater than 1, which is puzzling, it seems reasonable to conclude from the observation that $a_{bestfit} < a_{theor}$ and $b_{bestfit} < b_{theor}$ for each diblock, that if a branching ratio exists for intramolecular decay of $^1\text{fA}^*$ that energy transfer is the dominant branch, with little to no charge transfer observed.

6.6.2 Quenching of $^1\text{D}^*$

In the previous section MEH-PPV (D) was explored as a PL quencher for $^1\text{fA}^*$. We now evaluate the effectiveness of fA as a PL quencher for $^1\text{D}^*$ via both bimolecular and intramolecular pathways. It was first important to establish the range of concentrations for which PL emission was linear and therefore absent of self-quenching effects. As observed in **Figure 6-24** the emission and absorption are virtually linear over a concentration range of $[\text{MEH-PPV}] \leq 20 \mu\text{M}$ pru.

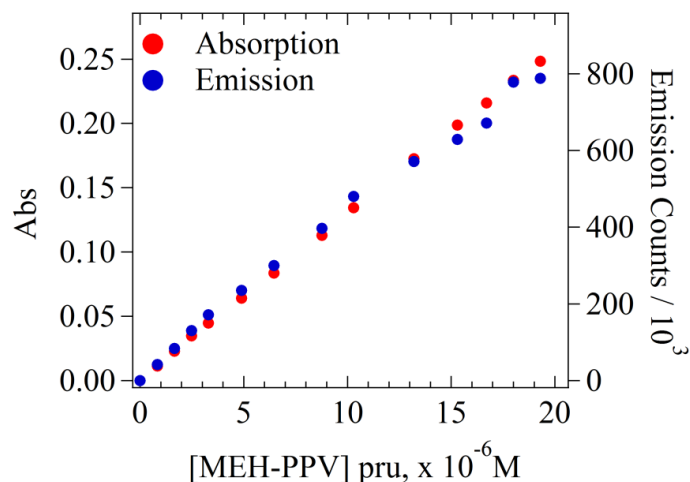


Figure 6-24 A plot of absorbance and PL emission versus pru concentration of MEH-PPV in THF reveals that both are linear over a range of 20 μM pru.

Prior to examining quenching in of $^1\text{D}^*$ in diblock solutions where the donor and acceptor are covalently appended, the quenching due to bimolecular processes needed to be accounted for. In the diblocks, the monomer ratio of [fA]:[D] was at greatest 11:24 or nearly 50%. In this set of experiments, a set of blend solutions in THF for which [MEH-PPV] was held constant at 4.82 μM pru (0.20 μM chain), while [fA] was varied from 0 μM to 28.7 μM pru (9.10 μM chain) resulted in ground state absorbance spectra which were superpositions of the ground state absorbance spectra of the constituting homoblocks as shown in **Figure 6-25 (a)**. In **Figure 6-25 (b)** the corresponding PL emission spectra of these blend solutions as shown are found to be invariant over the concentration range of fA tested indicating that quenching of $^1\text{D}^*$ by bimolecular processes does not occur within the range of concentrations explored for fA. At the highest concentration of fA, the monomer ration of [fA]:[D] was 28.7:4.82 or 6:1, far greater than observed in the diblocks.

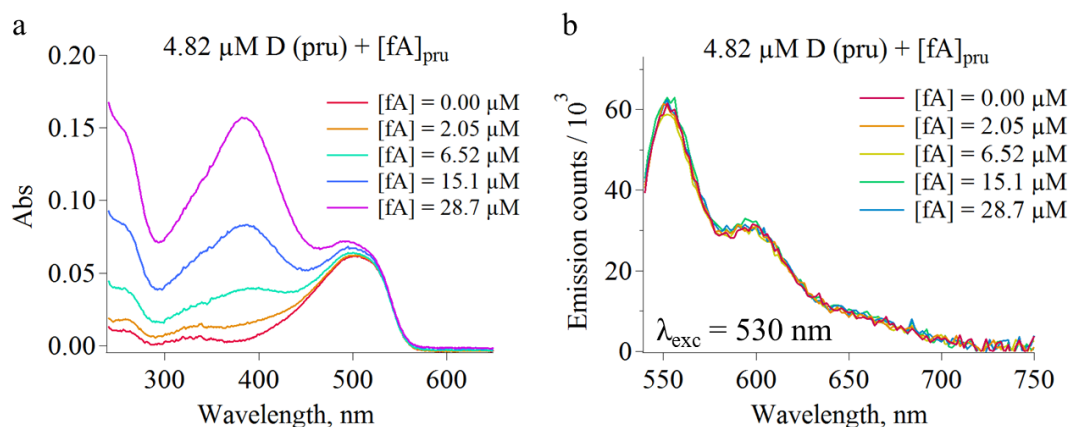


Figure 6-25 (a) Ground state absorbance spectra corresponding to blend solutions of D (4.82 μM pru) and varied concentrations of fA (0 – 28.7 μM pru). In **(b)** excitation at λ=530 nm where only D absorbed resulted in identical PL emission spectra suggesting no collisional quenching occurs.

PL quenching of $^1D^*$ was also examined for the diblocks in THF. In **Figure 6-26** PL emission for the D₂₄ homoblock, D(C2)fA, D(C4)fA and D(C6)fA corresponding to excitation at 530 nm is shown. PL emission measurements were made for the D₂₄ homoblock, D(C0)fA, D(C1)fA, and D(C2)fA corresponding to excitation at 500 nm as shown in **Figure 6-27**. PL quenching from D₁₄(C0)fA and D₁₄(C1)fA by comparison with PL yield of D₁₄ corresponding to excitation at 500 nm was also determined as shown in **Figure 6-28**. In each PL emission experiment, the solutions were prepared with equivalent ground state absorbances at the excitation wavelength as shown in the insets. Negligible absorption from fA at wavelengths ≥ 500 nm resulted in equivalent yields of D* in each PL emission experiment. The PL quenching efficiency of D(C2)fA was measured in both experimental trials and the discrepancy provided an error of 1.9% which is assumed for all PL quenching results. The spectral shape of PL emission from all diblocks excited at 500 and 530 nm as shown in **Figure 6-26** were found to be virtually identical in spectral shape to that of the D homoblock, but with slightly lower yields. By examining the relative decrease in emission intensities of the diblocks relative to the D homoblock, quenching efficiencies were determined as shown in **Table 6-10** below.

Table 6-10 Quenching efficiencies in diblocks observed in THF

Diblock	Quenching efficiency %	λ_{exc} (nm)
D(C0)fA	$(1.3 \pm 1.9) \%$	500
D(C1)fA	$(8.2 \pm 1.9)\%$	500
D(C2)fA	$(2.2 \pm 1.9)\%$	500
D(C2)fA	$(6.0 \pm 1.9) \%$	530
D(C4)fA	$(10.6 \pm 1.9)\%$	530
D(C6)fA	$(4.5 \pm 1.9)\%$	530
D ₁₄ (C0)fA	$(9.0 \pm 1.9)\%$	500
D ₁₄ (C1)fA	$(5.0 \pm 1.9)\%$	500

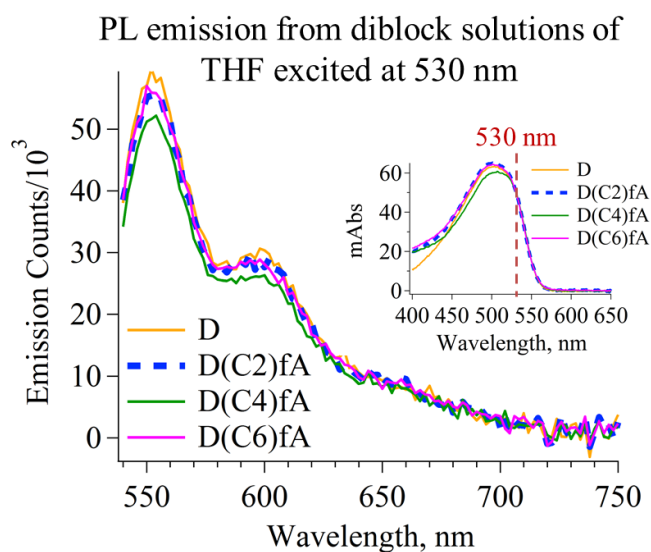


Figure 6-26 Photoluminescence quenching observed from MEH-PPV (D) and diblocks D(C2)fA, D(C4)fA and D(C6)fA excited at 530 nm. The inset shows the ground state absorbance spectra of each solution prepared with same absorbance at 530 nm to ensure equivalent number of photons on each when excited at that wavelength.

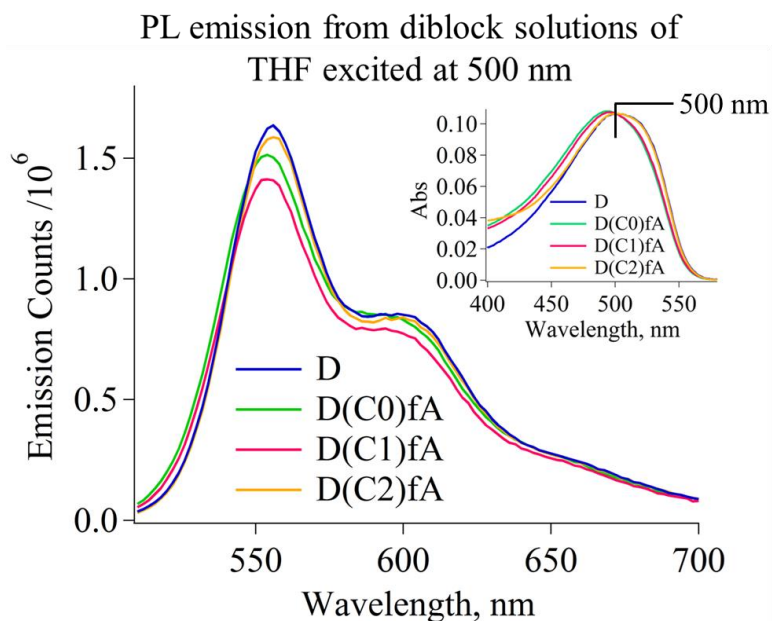


Figure 6-27 Photoluminescence quenching observed from MEH-PPV (D) and diblocks D(C0)fA, D(C1)fA and D(C2)fA excited at 500 nm. The inset shows the ground state absorbance spectra of each solution prepared with same absorbance at 500 nm to ensure equivalent number of photons on each when excited at that wavelength.

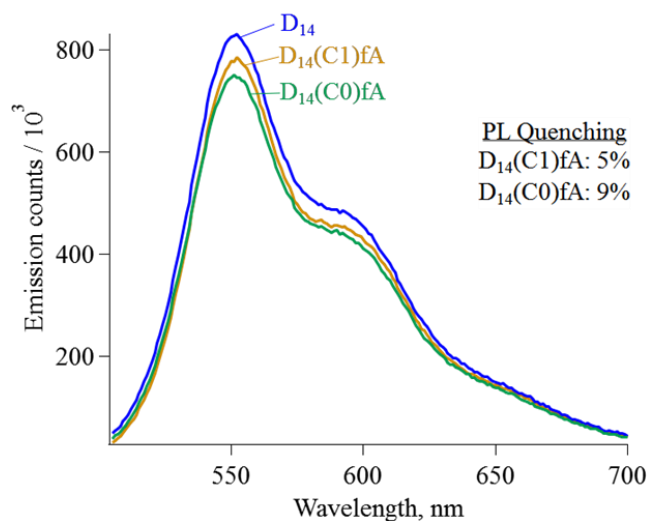


Figure 6-28 Photoluminescence (PL) yields of D_{14} /THF, $D_{14}(C0)fA$ /THF and $D_{14}(C1)fA$ /THF when controlled for number of photons absorbed at 500 nm, exhibited 9% and 5% quenching relative to the PL emission of D_{14} /THF.

6.7 Photoexcited ps transient absorption spectroscopy

Laser-pumped picosecond transient absorption spectroscopy was performed on $D_{21}(C2)A$ as a preliminary investigation of electron transport from the photoexcited state of MEH-PPV. The free energy difference for D/A in the $D_{21}(C2)A$ diblock according to electrochemical measurements from our collaborators was virtually the same as D/fA in the D(Cn)fA diblocks. The transient absorption measurement was collected during preliminary measurements prior to receipt of the D(Cn)fA polymers, and had similar quenching results.

An excited state lifetime of ~ 300 ps has been reported for MEH-PPV in chloroform [128], and similar values measured in other solvents as well [90]. Based on a measured quantum efficiency of 0.256, the radiative lifetime in the absence of non-radiative channels is determined as 1.17 ns. To achieve a quenching efficiency of 10% in steady state PL, which is greater than the observed quenching efficiencies in all but possibly one diblock, an electron transfer rate of $3.70 \times 10^8 \text{ s}^{-1}$ (2.70 ns) would be required. This would facilitate an observed decrease in decay time constant to 270 ps. Chloroform solutions of $\sim 1 \text{ }\mu\text{M}$ per chain were prepared of D_{21} and $D_{21}(C2)A$ and were photoexcited at 530 nm where SF-PPV (A) absorbs negligibly. The $^1\text{MEH-PPV}^*$ state was probed in both cases by monitoring the S_1 - S_2 transition at 795 nm, resulting in single exponential decay profiles with corresponding time constants of 303 ± 6 ps for D_{21} and 289 ± 9 ps for $D_{21}(C2)A$ as shown in **Figure 6-29**. The apparent decrease in lifetime observed for the diblock is marginal within the experimental noise and therefore difficult to know if authentically due to an exciton dissociation pathway.

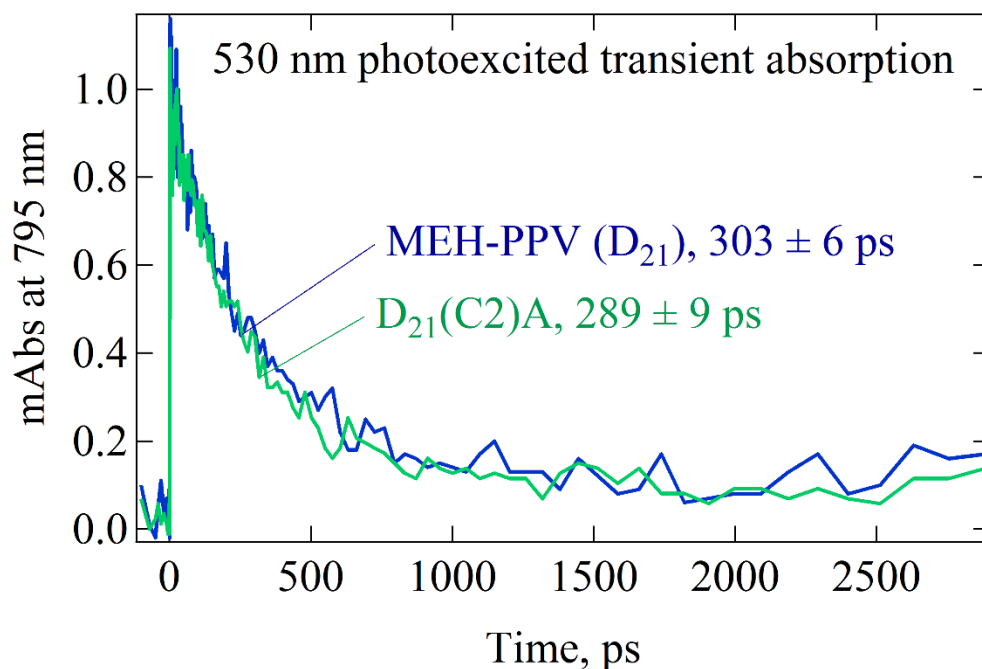


Figure 6-29 Transient absorption following 530 nm photoexcitations of MEH-PPV in D and D(C2)A in CHCl_3 .

Assuming that exciton transport on the MEH-PPV chain is limited dominantly by exciton lifetime and negligibly by chain defects, the exciton dissociation efficiency in a DBA polymer may begin to significantly decline as the MEH-PPV chain length begins to exceed the exciton diffusion length, making it less probable for the exciton to reach or remain at the D/A interface. The diffusion length of 5 – 8 nm (8 – 13 monomers) has been reported for a singlet exciton of MEH-PPV [129] suggesting that the MEH-PPV chains of 21 and 24 monomers are 2 – 3 times longer. For this reason, the 14 monomer length MEH-PPV polymer (D_{14}) was synthesized and used to synthesize $D_{14}(\text{C0})\text{fA}$ and $D_{14}(\text{C1})\text{fA}$. THF solutions of D_{14} , $D_{14}(\text{C0})\text{fA}$ and $D_{14}(\text{C1})\text{fA}$ were excited at 500 nm where they were prepared with equivalent absorbances and the lifetime of the $S_1 \rightarrow S_2$ transitions monitored. In each case, the excited state lifetimes were found to be 270 ± 5 ps, ~30% faster than observed for D_{21} and $D_{21}(\text{C2})\text{A}$. This possibly indicates a chain length dependence of spontaneous emission, but no observable effect of lifetime dependence due to an added decay pathway for exciton dissociation.

6.8 $D^{\bullet-}(Cn)fA \rightarrow D(Cn)fA^{\bullet-}$ reactions via radiolysis

A schematic of charge transfer from a radical ion state of a DBA polymer is shown in **Figure 6-30**. Charge transfer may occur from the radical anion state of a donor moiety as shown in **(a)** or from the radical cation of an acceptor moiety as shown in **(b)**. These reactions may occur via bimolecular or intramolecular rates.

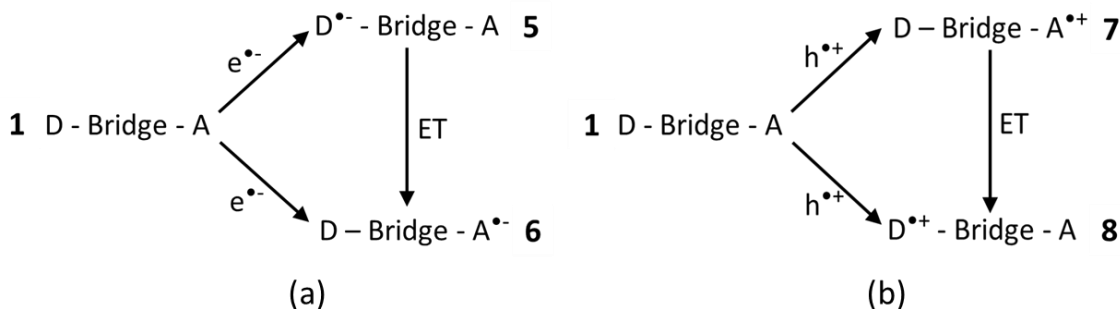


Figure 6-30 Scheme showing charge transfer from a radical ion states of a DBA molecule: $D^{\bullet-}BA$ (a) and $D^{\bullet+}BA$ (b). Charge transfer first is preceded in both cases by non-selective formation of radical ions dependent on relative concentration of the D and A moieties.

Preliminary experiments of electron transfer utilized the first diblock obtained, D(C2)A. The accurate molecular weights were not provided and therefore the A homoblock (SF-PPV), D homoblock (MEH-PPV), and DBA diblock were each prepared at nominal concentrations of 500 μM chain which were later corrected after accurate molecular weights were determined. The transient spectra of MEH-PPV (488 μM chain), SF-PPV (350 μM chain), and D(C2)A (542 μM chain) are shown in **Figure 6-31** over a 500 μs time frame.

As the transient absorbance spectrum of D(C2)A evolves following radiolytic pulse, it transforms towards a spectrum that is similar to that of the $A^{\bullet-}$. The decay of the band at 900 nm where $D^{\bullet-}$ has a maximum is found to decay slowly but at a rate that exceeds the decay observed from the pure D homoblock. The data suggest a transformation from $D^{\bullet-}$ to $A^{\bullet-}$. However, the timescale of this transformation was surprisingly slow by comparison to the < 10 ns intramolecular charge transfer rate constants exhibited by many DBA systems with molecular D and A substituents with rates less than 10 ns. By 500 μs , the transformation from $D^{\bullet-}$ to $A^{\bullet-}$ was still not complete. The radical anion decay was found to be single exponential

and it was not how much if any of the electron transfer was intramolecular but it was apparent that electron transfer was much slower than the formation rate of D^{\bullet} , such that decay during growth could be considered negligible, and the observed decay rate, k_{decay} of D^{\bullet} could then be approximated by the expression:

$$k_{decay} = k_{intra} + k_{bi}[DBA] \quad 6-25$$

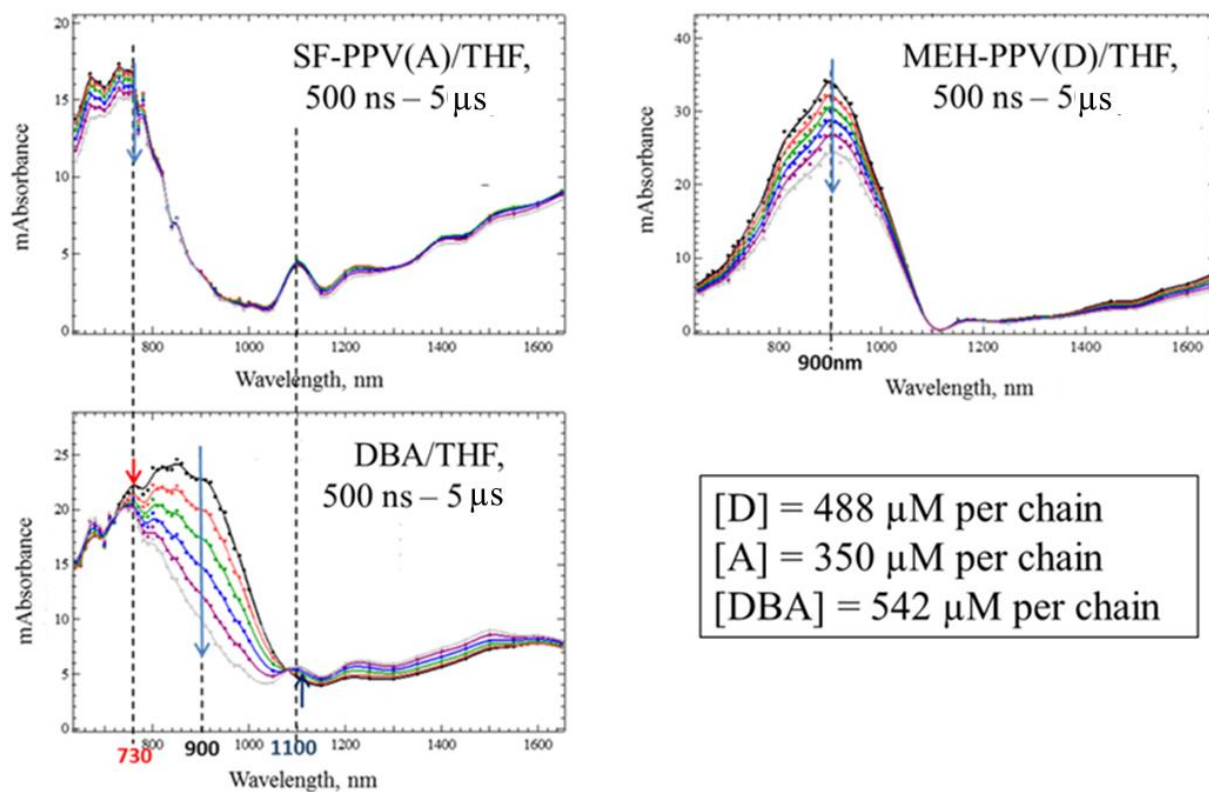


Figure 6-31 Radical anion decays of SF-PPV (A), MEH-PPV (D), and D(C2)A following radiolytic pulse in THF. The radical ion spectrum of DBA has the form of a linear sum of the respective radical anion components, and is found transforming from $D^{\bullet}(C2)A \rightarrow D(C2)A^{\bullet}$.

The synthesis of D(Cn)fA polymers was largely prompted by the initial findings of D(C2)A. Our collaborators who provided D(C2)A believed that electron transfer rates were limited by a weak driving force for electron transfer. Fluorination of the SF-PPV was expected to shift the potential of the compound more positive. However, CV measurements revealed nearly identical reduction potentials for SF-PPV and fSF-PPV. This may be in part due to limited solubility of fSF-PPV which restricted its oligomer length to only 3-4 monomers in the free standing homoblock and slightly larger when bonded to MEH-PPV in a diblock, rather than 14

monomers in SF-PPV. By extending the length of fSF-PPV the bandgap is expected to decrease and the reduction potential to become more positive.

A separate possibility for the ultraslow electron transfer rate is that the bridge length might be the limiting factor in the observed electron transfer rate. For this purpose, bridge lengths for D(Cn)fA were initially prepared at $n = 2, 4,$ and $6,$ and later $n = 0$ and $1.$ For probing the electron transfer kinetics in the D(Cn)fA series, 900 nm was identified as ideal based on the greatest ratio difference between extinction coefficients of $D^{\bullet-}$ or $fA^{\bullet-},$ with a ratio of $22.4/1.0$ as shown in **Figure 6-32.**

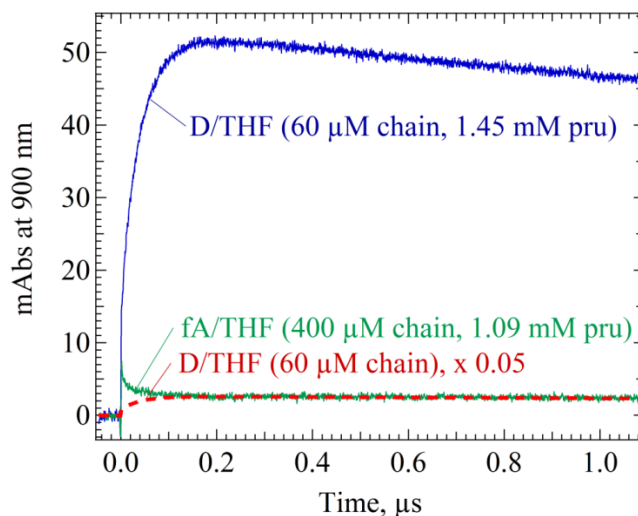


Figure 6-32 Absorbance transients at 900 nm corresponding to radiolysis of D (1.45 mM pru) and fA (1.09 mM pru). Under these conditions, fA captures 12% more electrons suggesting the ratio of anion absorbances of $D:fA$ are less than $20:1.$ This wavelength served as an effective wavelength for monitoring formation and decay kinetics of $D^{\bullet-}$ in the presence of $fA.$

The radical anion spectra of the moieties of D(C2)A appeared to be near identical to those of the homoblocks, and to be certain, transient spectra of D(C0)fA and D(C6)fA were collected to determine if this also held true for all D(Cn)fA. As shown in **Figure 6-33** and **Figure 6-34,** transient spectra of both D(C0)fA and D(C6)fA were well approximated as linear sums of radical anion spectra of D and fA homoblocks. This suggests that the other diblocks are also well approximated by linear sums of the radical anion spectra of the homoblocks. Where concentrations of diblocks are labeled with “SF” indicates that molecular weights according to the SF method were assumed.

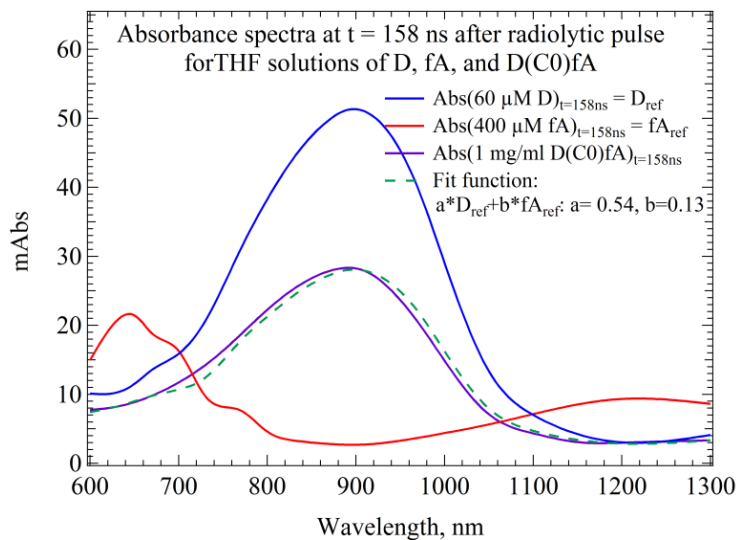


Figure 6-33 Transient spectrum of D(CO)fA (1 mg/ml, purple) near maximum signal following radiolytic pulse, shown with referene spectra of fA^{•-} (red) and D^{•-} (blue) used to find a best linear sum fit of the transient spectrum of D(CO)fA, using $a \cdot D_{\text{ref}} + b \cdot fA_{\text{ref}}$, with $a=0.54$ and $b=0.13$ (dashed green).

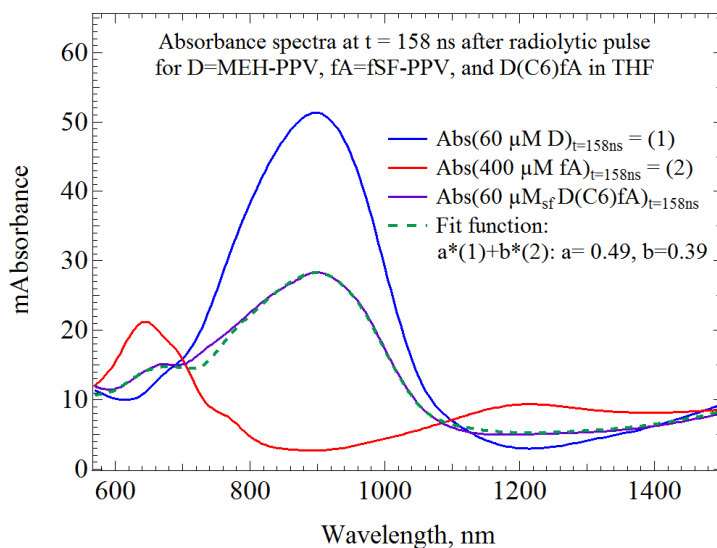


Figure 6-34 Transient spectrum of D(CO)fA ($60 \mu\text{M}_{\text{SF}}$, purple) near maximum signal following radiolytic pulse, shown with referene spectra of fA^{•-} (red) and D^{•-} (blue) used to find a best linear sum fit of the transient spectrum of D(CO)fA, using $a \cdot D_{\text{ref}} + b \cdot fA_{\text{ref}}$, with $a=0.49$ and $b=0.39$ (dashed green).

As with D(C2)A, all of the diblocks in the D(Cn)fA series were observed to exhibit very slow electron transfer rates, even D(C0)fA. The transient spectra during growth are observed in **Figure 6-35 (a)** while decay of the 900 nm band is observed in **Figure 6-35 (b)** with concomitant formation of a 650 nm band inferred from the near constant absorption at 650 nm in spite of absorption loss from $D^{\bullet-}$ at that wavelength. Insets of both figures provide absorbance transients at 900 nm during the growth and decay of the band. The decay transient shows a much slower decay of $D^{\bullet-}$ than formation of the same, such that electron transfer during the formation of $D^{\bullet-}$ can be considered negligible if the entire population of $D^{\bullet-}$ decays via the slow rate(s).

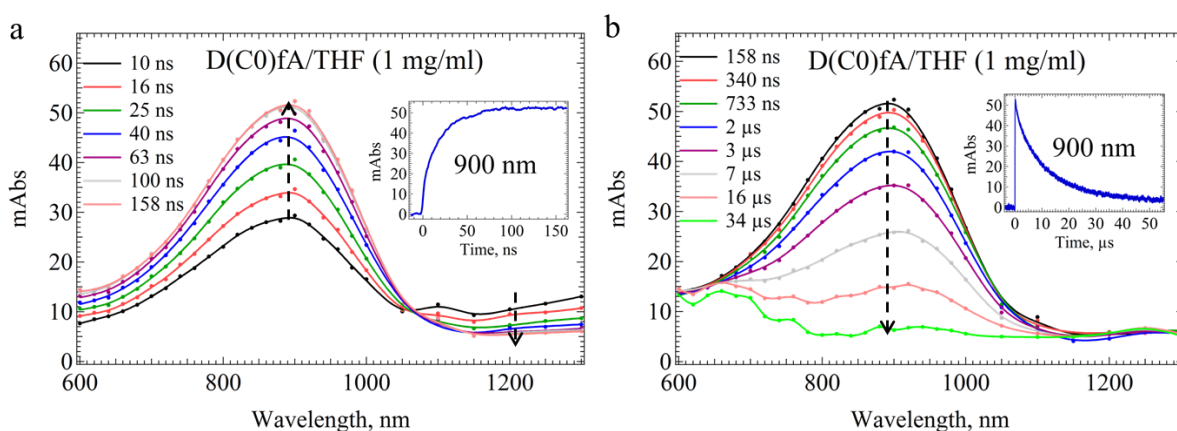


Figure 6-35 Transient absorbance spectra of D(C0)fA (1 mg/ml) in THF shown: a) during the formation of the 900 nm band, and b) during the decay of the 900 nm band.

To accurately determine the time-dependence of $D^{\bullet-}$ depletion in the diblock solution due to the acceptor, the time dependence of $D^{\bullet-}$ depletion due to other mechanisms should be accounted for which is determined by the depletion rate of $D^{\bullet-}$ in the D homoblock solution. Provided that the $D^{\bullet-}$ yields in the diblock and D homoblock solutions at equivalent chain concentrations are normalized for the number of electrons captured by each, the time-dependent ratio of $D^{\bullet-}$ absorbances for the diblock vs homoblock provides a reasonably accurate transient corresponding to the decay rate of $D^{\bullet-}$ due to electron transfer to acceptor A. The accuracy of this method is good at times after all electrons have been captured by the D homoblock, but due to the fact that the concentration of total monomers (D and fA) are greater

for the diblock at equivalent chain concentrations, a faster rate of electron capture is observed for the diblock.

The monomer ratio of fA per chain of each D(Cn)fA was estimated by SF method previously. An estimate may also be rendered by evaluation of the formation rate of D^{\bullet} in the presence of fA, $r_{D/fA}$ relative to the formation rate in the absence of fA, r_D assuming the donor monomer concentration $[D_{mon}]$ is the same in both. Given the electron attachment rate constant of D, the concentration of fA monomers, $[fA_{mon}]$ can then be defined as:

$$[fA_{mon}] = (r_{D/fA} - r_D)/k_{attach,D} \quad 6-26$$

Using this expression, monomer ratio of fA in each diblock was calculated as:

$$f_{fA} = [fA_{mon}]/([fA_{mon}] + [D_{mon}]) \quad 6-27$$

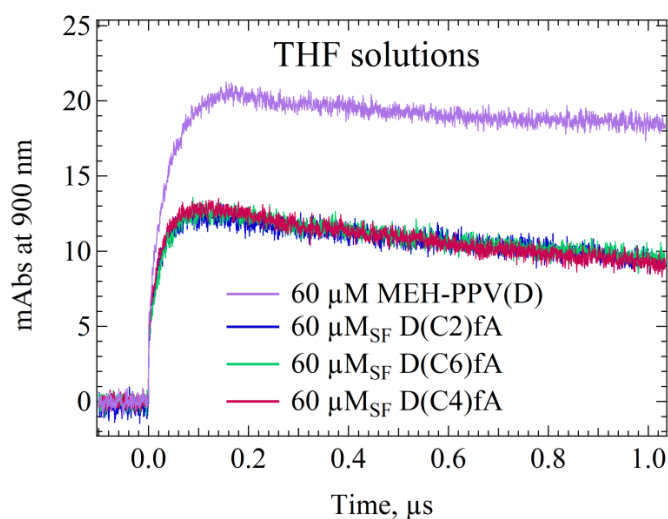


Figure 6-36 Absorbance transients at 900 nm following radiolytic pulse of THF solutions for D(C2)fA, D(C4)fA, and D(C6)fA, each prepared at $60 \mu M_{SF}$. Decay rates are found to be much slower than formation rates suggesting negligible electron transfer during the formation of D^{\bullet} .

In **Figure 6-36** a plot of the 900 nm absorbance transients corresponding to $60 \mu M$ D homoblock and $60 \mu M_{SF}$ of D(C2)fA, D(C4)fA and D(C6)fA are shown following radiolytic pulse. A fast growth is succeeded by much slower decay of D^{\bullet} in each solution. An electron scavenging efficiency of 75% was estimated for the homoblock and 85% for each of the diblocks. After correcting for the differences in electron scavenging efficiency, an estimated 42% of D^{\bullet} is suppressed relative to the yield in the homoblock. Using **Eq 6-26** and **Eq 6-27** the number of fA

monomers per chain and f_{fA} were determined for each diblock solution - D(C2)fA, D(C4)fA and D(C6)fA in **Figure 6-36** and are tabulated below in **Table 6-11**. The number of fA monomers per chain estimated using the “kinetic method” provided values that differed by less than 10% relative to the values obtained using the SF-method. The kinetic method relies on the assumption that the molecular weights determined by the SF method are accurate, and therefore is more of a validation of consistency and supporting the conclusion that the number of fA monomer units in the diblocks are likely ≥ 3 times larger than the estimates determined by GPC.

Table 6-11 Determination of fA_{mon} per chain and f_{fA} for diblocks D(C2)fA, D(C4)fA and D(C6)fA using a “kinetic method” based on formation rate constants for $D^{\bullet-}$ based on presumed equivalence of $[D_{mon}]$ for the D homoblock solution and D(Cn)fA solutions

polymer	Formation rate for $D^{\bullet-}$, s^{-1}	# of fA monomers per chain	f_{fA}	Suppression of $D^{\bullet-}$ relative to $D^{\bullet-}$ yield of homoblock
D	2.33×10^7	0	0	0
D(C2)fA	3.64×10^7	10.85	0.31	0.42
D(C4)fA	3.60×10^7	10.52	0.30	0.42
D(C6)fA	3.66×10^7	11.07	0.31	0.42

The values of f_{fA} estimated were 0.30 – 0.31 however, it was previously determined that the per monomer capture rate of electrons by fA is ~ 1.5 times greater than that of D, which would suggest an estimated electron capture fraction of 0.45 for D(C4)fA and 0.465 for D(C2)fA and D(C6)fA. These fractions are close to the fractional yield of $D^{\bullet-}$ estimated for D(C2)fA, D(C4)fA and D(C6)fA by comparison with the maximum yield of $D^{\bullet-}$ obtained in the D homoblock. The extent of suppression in $D^{\bullet-}$ yield of D(C0)fA and D(C1)fA relative to D homoblock was significantly smaller by an amount that correlated with the estimated values of f_{fA} in those diblocks as well.

Based on these observation, the approximation of **Eq 6-25** can be applied, whereby the fraction of $D^{\bullet-}$ converted to $fA^{\bullet-}$ during growth of $D^{\bullet-}$ can be considered negligible, and therefore virtually if not all electrons transferring from D to A occur during the slow decay process of k_{decay} defined by $k_{decay} = k_{intra} + k_{bi}[DBA]$. To obtain an accurate value of

k_{decay} , the decay of $D^{\bullet-}$ due to other reactions besides conversion of $D^{\bullet-}$ to $fA^{\bullet-}$ should be corrected. The decay of radical anions of the D homoblock in the absence of fA was used as a measure of these decay processes. To correct for these, the absorbance transients of D(Cn)fA were divided by absorbance transients corresponding to D homoblock at the same D monomer concentration, expressed as: $A_t(DBA)/A_t(D)$ where A_t is the absorbance at a time “t” after radiolytic pulse. This decay of the resulting quotient exhibited first order decay characteristics at the concentrations explored. The values of k_{decay} were thus determined from fits of this decay quotient.

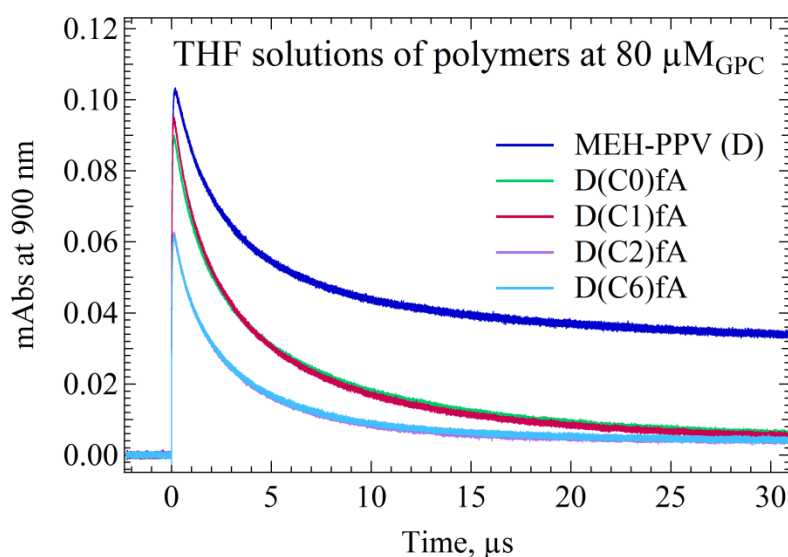


Figure 6-37 Absorbance transients of $D^{\bullet-}$ at 900 nm corresponding to radiolysis of D, D(C0)fA, D(C1)fA, D(C2)fA and D(C6)fA. Transients of D(C2)fA and D(C6)fA were nearly identical and transients of D(C0)fA and D(C1)fA were also nearly identical.

Concentrations of DBA were prepared and tested with the aim of finding a range for which $k_{intra} \geq k_{bi}[DBA]$. This would result in an observed convergence of k_{decay} to a near constant rate at the limiting concentration. For the range of concentrations explored, down to to $5 \mu M_{SF}$ this condition was not achieved. Below $5 \mu M_{SF}$, the efficiency of electron capture is too poor to reliably measure decay rates of $D^{\bullet-}$. To estimate the intramolecular rate constant, a different approach was taken – to plot k_{decay} vs [DBA] and fit the data by an expression of The resulting fit is expected to be linear with a slope equivalent to k_{bi} and a y-intercept equivalent to k_{intra} .

THF solutions of each of the diblocks (except D(C4)fA due to none remaining) were prepared at chain concentrations of 80 μM_{GPC} . Transients at 900 nm following radiolytic pulse were collected for each of the solutions as shown in **Figure 6-37**. Subsequent measurements were made at reduced concentrations prepared by dilution of the 80 μM_{GPC} solutions with THF. The plots of k_{decay} vs $[\text{D}(\text{Cn})\text{fA}]_{\text{GPC}}$ are shown for each of the diblocks in **Figure 6-38** through **Figure 6-41**. The slopes and y-intercept values provided estimated values for k_{bi} and k_{intra} respectively for each of the diblocks. The latter were approximated by the limitations of the error of measurement, which at largest was $\pm 2.33 \times 10^4 \text{ s}^{-1}$ (42.9 μs) in the case of D(C6)fA. This value will be assumed as an upper limit for a slow k_{intra} . Based on the fits of these data, bimolecular and intramolecular rate constants for the diblocks are presented in **Table 6-12**.

Table 6-12 Bimolecular rate constants for electron transfer from $\text{D}^{\bullet}(\text{Cn})\text{fA}$ to $\text{D}(\text{Cn})\text{fA}^{\bullet}$ based on linear fits of k_{decay} vs $[\text{D}(\text{Cn})\text{fA}]$

polymer	k_{Bi} (assuming GPC MWs)	MW _{GPC} /MW _{SF} (5% error assumed)	k_{Bi} (assuming SF MWs)	k_{intra}
D(C0)fA	$1.20 \times 10^9 \text{ M}^{-1}\text{s}^{-1}$	1.27	$1.52 \times 10^9 \text{ M}^{-1}\text{s}^{-1}$	$\leq 9.91 \times 10^3 \text{ s}^{-1}$
D(C1)fA	$1.35 \times 10^9 \text{ M}^{-1}\text{s}^{-1}$	1.21	$1.63 \times 10^9 \text{ M}^{-1}\text{s}^{-1}$	$\leq 8.84 \times 10^3 \text{ s}^{-1}$
D(C2)fA	$2.37 \times 10^9 \text{ M}^{-1}\text{s}^{-1}$	1.59	$3.78 \times 10^9 \text{ M}^{-1}\text{s}^{-1}$	$\leq 1.65 \times 10^4 \text{ s}^{-1}$
D(C6)fA	$2.39 \times 10^9 \text{ M}^{-1}\text{s}^{-1}$	1.55	$3.70 \times 10^9 \text{ M}^{-1}\text{s}^{-1}$	$\leq 2.33 \times 10^4 \text{ s}^{-1}$

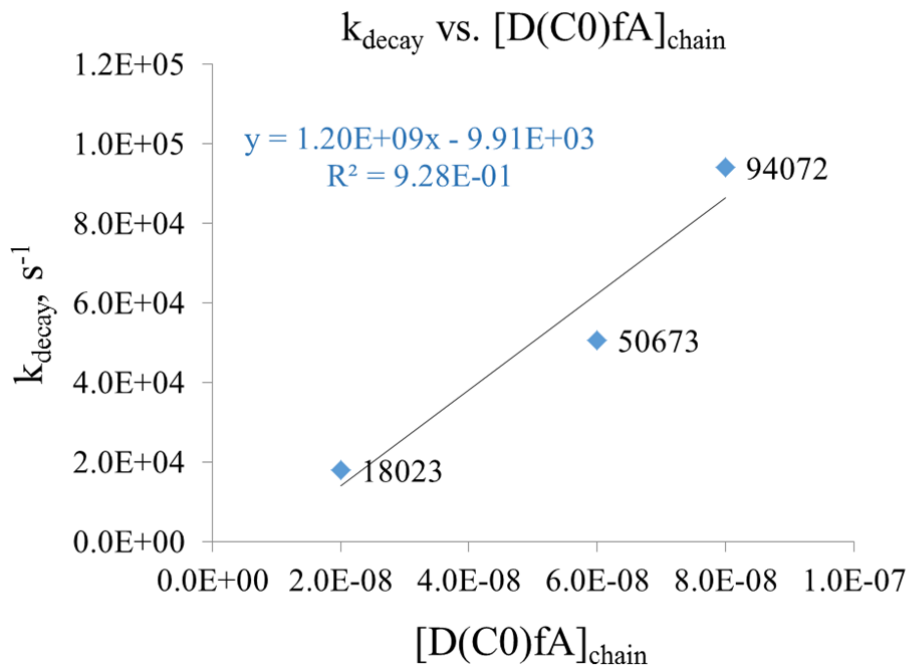


Figure 6-38 The k_{decay} rates for $D^{\bullet}(C0)fA$ plotted versus $[D(C0)fA]$

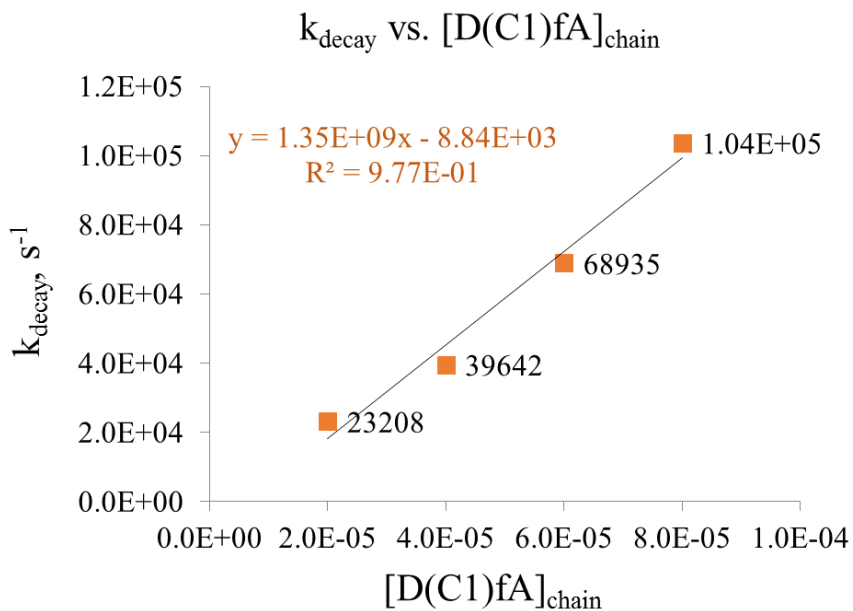


Figure 6-39 The k_{decay} rates for $D^{\bullet}(C1)fA$ plotted versus $[D(C1)fA]$

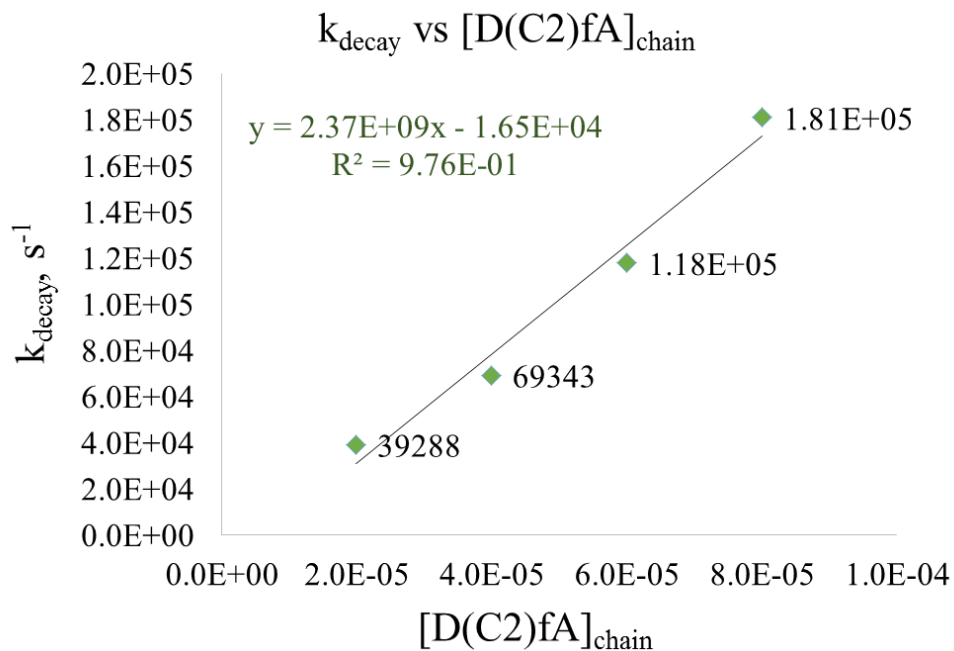


Figure 6-40 The k_{decay} rates for $D^{\bullet}(C2)fA$ plotted versus $[D(C2)fA]$

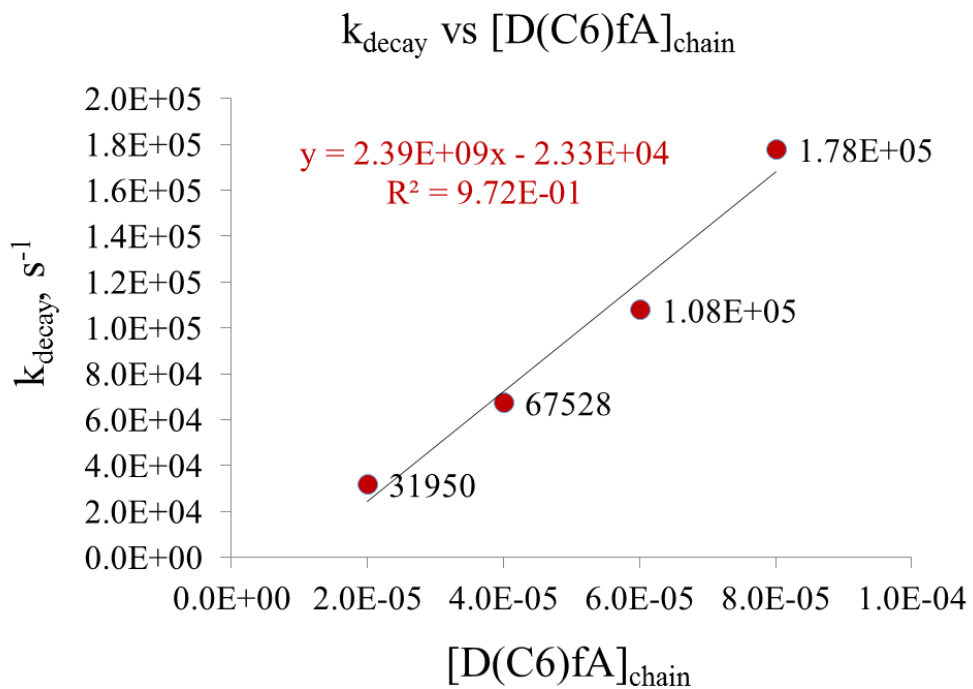


Figure 6-41 The k_{decay} rates for $D^{\bullet}(C6)fA$ plotted versus $[D(C6)fA]$

Another method was used to approximate the bimolecular rate constant of electron transfer in the diblocks. By preparing a blend solution of the D homoblock and a DBA polymer to satisfy the condition that $[D] \gg [DBA] \gg [e^-]$ where $[e^-]$ is the concentration of electrons produced via radiolysis in THF, the following reaction was facilitated and observed at 900 nm:



As most electrons in this condition are captured by the donor homoblock, transfer would necessitate bimolecular interaction with an acceptor on the diblock such that the predominant decay observed was bimolecular in nature. As was done in the previous set of experiments, corrections for other decay routes of $D^{\bullet-}$ were made by dividing the absorbance transient of the blend solution by the one containing only the D homoblock at equivalent monomer concentration. The resulting quotient transient was then fit by first order kinetics, with an obtained rate, r , which relates to k_{Bi} via:

$$k_{Bi} = r/[DBA] \quad 6-29$$

In **Figure 6-42** plots of this kind were generated for various blend solutions of the homoblock with D(C2)fA and the homoblock with D(C4)fA.

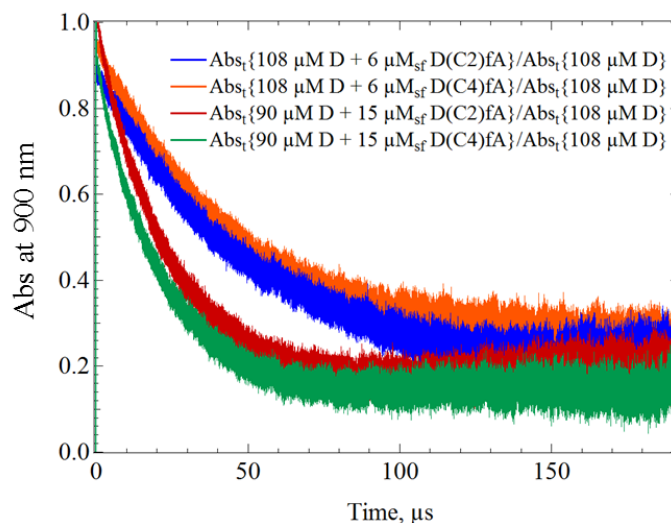


Figure 6-42 Donor radical anion decay rates measured in various blend solutions of D and D(Cn)fA where $[D] \gg [D(Cn)fA]$, and for which neutralization reactions were controlled for by dividing by transients of the donor homoblock solution prepared at similar chain concentrations leading to pseudo first order rates.

The rates of radical anion decay and the corresponding bimolecular rate constants of electron transfer were determined for each solution as shown in **Table 6-13**. An average value of $3.52 \times 10^9 \text{ M}^{-1}\text{s}^{-1}$ was obtained for the blend solutions which is nearly 1.5 times faster than the rate constant measured by linear fit of k_{decay} vs $[\text{D}(\text{Cn})\text{fA}]$. This difference is possibly related to a slightly larger mutual diffusion coefficient in the case of the blend solutions given the smaller molecular weight of the D homoblock relative to the diblock. These results are therefore in good agreement. The average of the bimolecular rate constant was determined as $(3.52 \pm 0.20) \times 10^9 \text{ M}^{-1}\text{s}^{-1}$. This values obtained by linear fits of k_{decay} vs. $[\text{DBA}]_{\text{SF}}$ as shown in **Table 6-12** were virtually identical within < 10% error.

Table 6-13 Bimolecular electron transfer rate constants, k_{Bi} determined using binary solutions of D and D(C2)fA and binary solutions of D and D(C4)fA, providing consistent estimates of $(3.52 \pm 0.20) \times 10^9 \text{ M}^{-1}\text{s}^{-1}$ per chain.

Solution	k_{Bi} (assuming MW by SF)
108 μM D + 6 μM_{SF} D(C2)fA	$3.67 \times 10^9 \text{ M}^{-1}\text{s}^{-1}$
108 μM D + 6 μM_{SF} D(C4)fA	$3.84 \times 10^9 \text{ M}^{-1}\text{s}^{-1}$
90 μM D + 15 μM_{SF} D(C2)fA	$3.22 \times 10^9 \text{ M}^{-1}\text{s}^{-1}$
90 μM D + 15 μM_{SF} D(C4)fA	$3.37 \times 10^9 \text{ M}^{-1}\text{s}^{-1}$

In the presence of 0.1 M TBAPF₆, the bimolecular rate constants for electron transfer were measured as $(1.12 \times 10^4 \text{ s}^{-1}) / (15 \mu\text{M}_{\text{SF}}) = (7.47 \pm 0.1) \times 10^8 \text{ M}^{-1}\text{s}^{-1}$ which was 21% the rate determined in the absence of electrolyte. A slightly faster rate of $(8.80 \pm 0.9) \times 10^8 \text{ M}^{-1}\text{s}^{-1}$ was determined by comparing the lifetimes of $\text{D}^{\bullet-}(\text{C6})\text{fA}$ in THF with and without electrolyte.

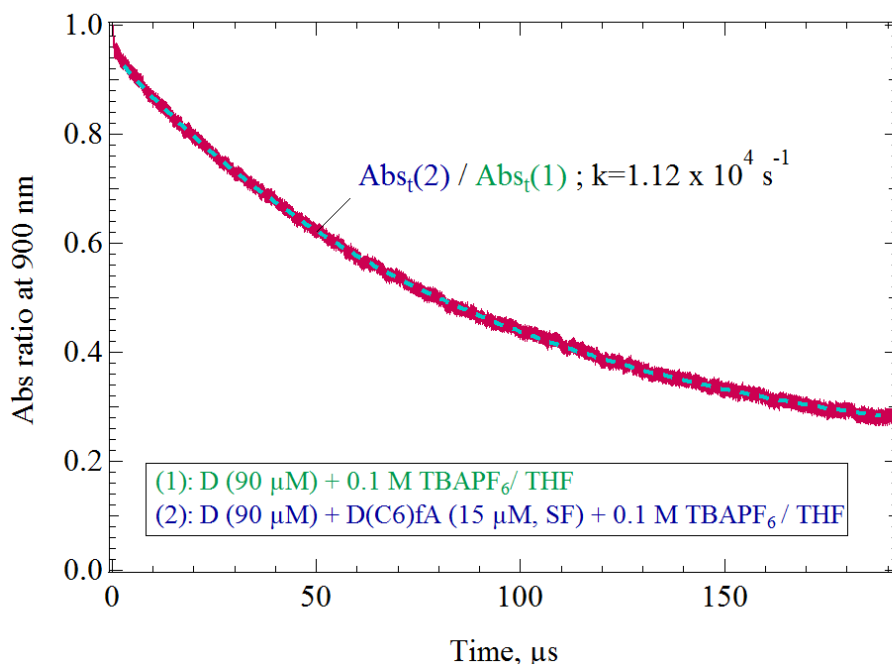


Figure 6-43 The absorbance decay transient associated with the rate of bimolecular electron transfer from $D^*(C6)fA \rightarrow D(C6)fA^*$ in the presence of 0.1 M TBAPF₆. The bimolecular rate in electrolyte was determined by single exponential fit of this decay as $1.12 \times 10^4 \text{ s}^{-1}$, which is likely an underestimate given that the full transient could not be fitted due monitored exceeding the time window of observation.

That the rate of bimolecular electron transfer decreases by a factor of 4.0 in the presence of electrolyte suggests that the electron transfer is energy activated. The presence of electrolyte has negligible effect on the diffusion of polymer anions which are big and bulky, but will affect the diffusion of electrons since the ion to which it pairs is much larger. The most plausible explanation for a reduced electron transfer rate then is that the ion pairing results in an increased activation energy barrier for the reaction. Assuming an Arrhenius form of $k_{bi} = k_{diff} * \exp(-E_a/kT)$ the activation energies of electron transfer in the presence and absence of electrolyte were determined. The k_{bi} values of $3.52 \times 10^9 \text{ M}^{-1}\text{s}^{-1}$ in the absence of electrolyte and $8.8 \times 10^8 \text{ M}^{-1}\text{s}^{-1}$ in the presence of 0.1 M TBAPF₆ were used, and a k_{diff} of $1.20 \times 10^{10} \text{ M}^{-1}\text{s}^{-1}$ calculated based on approximated equivalent radius with MEH-PPV (n=24) of 3.2 nm according to the Debye-Smoluchowski equation. Assuming these rates to be entirely limited by activation energy rather than in part or whole by orientation of encounter, upper limits of activation energies are determined as shown in **Table 6-1**.

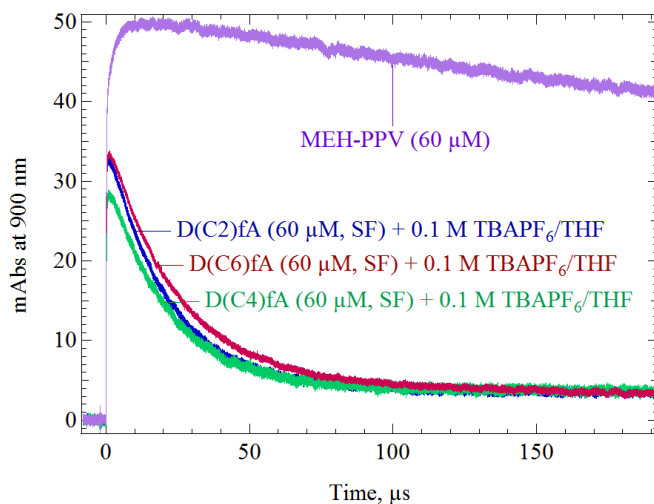


Figure 6-44 Absorbance transients at 900 nm following radiolysis of THF solutions of *D* homoblock, *D*(C2)*fA*, *D*(C4)*fA* and *D*(C6)*fA* prepared at chain concentrations of 60 μM_{SF} with 0.1 M TBAPF_6 .

Table 6-14 Estimated activation energies for bimolecular $\text{D}^*(\text{C6})\text{fA} \rightarrow \text{D}(\text{C6})\text{fA}^*$ in absence and presence of electrolyte

60 μM_{SF} <i>D</i> (C6) <i>fA</i>	K_{bi}	E_{A} required (maximum)
No electrolyte	$3.52 \times 10^9 \text{ M}^{-1}\text{s}^{-1}$	31.5 meV
0.1 M TBAPF_6	$8.8 \times 10^8 \text{ M}^{-1}\text{s}^{-1}$	67.1 meV

It was of interest to determine the effect of chain length on the observed electron transfer rate. A shorter length chain will increase the probability of an electron's proximity to the donor/bridge interface possibly leading to a higher probability of transfer relative to a longer chain. To examine the effect of a shorter length polymer donor, $\text{D}_{14}(\text{C0})\text{fA}$ and $\text{D}_{14}(\text{C1})\text{fA}$ were prepared at 60 μM_{SF} and 120 μM_{SF} and absorption transients collected at 900 nm as shown in **Figure 6-45**. The electron transfer kinetics were similar to the trends observed in the $\text{D}_{24}(\text{Cn})\text{fA}$ series – slow time constants in the microseconds, and concentration dependent. The kinetics of $\text{D}_{14}(\text{C0})\text{fA}$ were even slower than for $\text{D}_{14}(\text{C1})\text{fA}$ and the kinetics of $\text{D}_{14}(\text{C1})\text{fA}$ are therefore used as an upper limit, and bimolecular rate constants of electron attachment at 60 μM_{SF} and 120 μM_{SF} were determined as $1.50 \times 10^9 \text{ M}^{-1}\text{s}^{-1}$ and $1.67 \times 10^9 \text{ M}^{-1}\text{s}^{-1}$, respectively as shown in **Table 6-15**. These average of these values, $(1.59 \pm 0.09) \times 10^9 \text{ M}^{-1}\text{s}^{-1}$ was very similar to the average rate constant of $(1.58 \pm 0.06) \times 10^9 \text{ M}^{-1}\text{s}^{-1}$ measured for $\text{D}_{24}(\text{C0})\text{fA}$ and $\text{D}_{24}(\text{C1})\text{fA}$. in the

absence of electrolyte. The monomer ratios of D:fA were approximately the same in each of these diblocks, providing further indication that observed electron transfer rates are sensitive to D:fA monomer ratio.

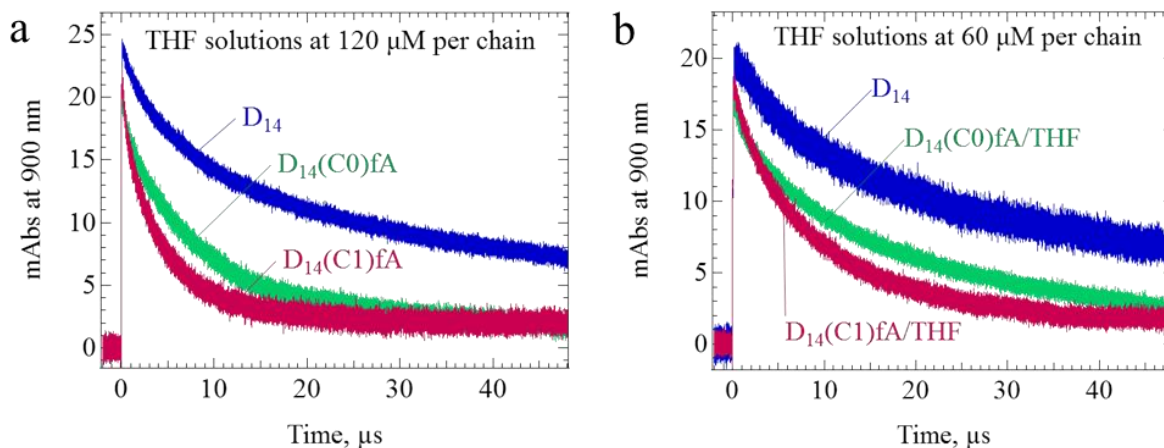


Figure 6-45 900 nm absorption transients of D_{14} /THF, $D_{14}(C0)fA$ /THF, and $D_{14}(C1)fA$ /THF shown at chain concentrations of: a) 120 μM , and b) 60 μM .

Table 6-15 Electron transfer rates of $D^*(C1)fA$ at 60 μM and 120 μM

Polymer	$[D_{14}]/\text{THF}$, per chain	k_{decay} $(D_{14}(C1)fA)_t / (D_{14})_t$	$k_{\text{Bi}} (D^*BA + DBA \rightarrow DBA + D^*BA)$
$D_{14}(C1)fA$	60 μM	$9.0 \times 10^4 \text{ s}^{-1}$	$1.50 \times 10^9 \text{ M}^{-1}\text{s}^{-1}$
$D_{14}(C1)fA$	120 μM	$2.0 \times 10^5 \text{ s}^{-1}$	$1.67 \times 10^9 \text{ M}^{-1}\text{s}^{-1}$

6.9 MEH-PPV triplet neutralization reactions in THF

In the course of conducting experiments aimed at understanding electron transfer in DBA diblocks, an interesting observation was made. The $D^*(Cn)fA \rightarrow D(Cn)fA^*$ transformation should lead to absorbance suppression at 900 nm to a small but positive value. Instead, in the absence of a long pass (LP) optical cutoff filter, small bleach was observed in the transients. The magnitudes of the bleach observed increased to a maximum at 800 nm. Using a cutoff filter was found to remove the bleach as shown in **Figure 6-46**.

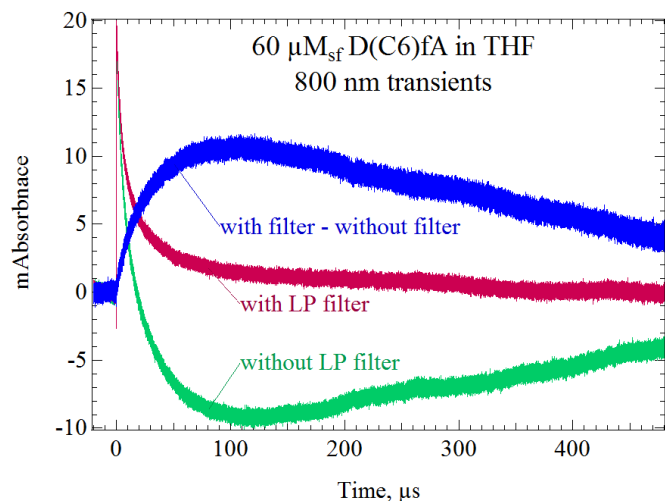


Figure 6-46 800 nm absorbance transients following radiolysis of a THF solution of D(C6)fA ($60 \mu\text{M}_{\text{SF}}$ chain): shown with an optical long pass cutoff filter (red), without an optical filter (blue) and a difference transient (blue) obtained by subtracting the green transient from the red one.

Subtracting the decay transient collected without cutoff filter from the decay in transient collected with cutoff filter, resulted in a difference transient shown in blue in **Figure 6-47**. The growth and decay of this difference transient was fit by two exponentials and found to grow with a rate of $1.97 \times 10^4 \text{ s}^{-1}$, and decay with a rate of $3.12 \times 10^3 \text{ s}^{-1}$. A spectrum of the bleach was obtained as shown in **Figure 6-47**.

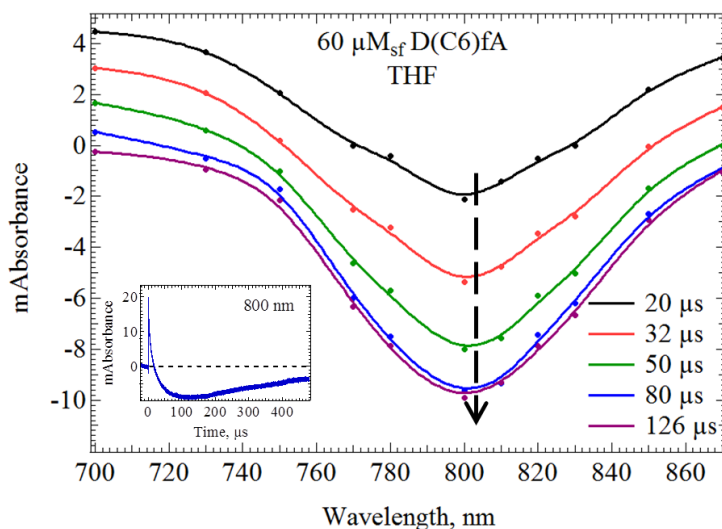


Figure 6-47 Formation of bleach following radiolysis of a THF solution of D(C6)fA ($60 \mu\text{M}_{\text{SF}}$) due to decay of $^3\text{D}^*$ via reaction with radical anions.

This spectrum resembles the triplet-triplet absorption spectrum of MEH-PPV but is blue shifted by 25 ± 5 nm relative to the spectrum obtained in benzene. The growth of the bleach indicates that the triplets formed before radiolytic pulse are being removed. The rate of this triplet removal occurs on a time scale substantially faster than expected from phosphorescence, and given that the energetics of D and fA do not permit conversion of ${}^3\text{D}^* \rightarrow {}^3\text{fA}^*$, nor dissociation at the D/fA interface, this decay must be via reaction with another radiolytic byproduct or a chain defect. Radiolytic byproducts would consist of either $\text{D}^{\bullet-}$ or $\text{fA}^{\bullet-}$. The decay of $\text{D}^{\bullet-}(\text{C6})\text{fA}$ occurs with a bimolecular rate of $2.2 \times 10^5 \text{ s}^{-1}$ which is 9.0 time faster than the decay of ${}^3\text{D}^*$ which suggests that the latter is not due predominantly via reaction with $\text{D}^{\bullet-}$ in this case. However, the same bleach due to decay of ${}^3\text{D}^*$ was observed to occur in solutions of the D homoblock without fA present, suggesting that $\text{fA}^{\bullet-}$ need not be the reactant. The ratio of total radical anion yield (combining $\text{D}^{\bullet-}$ and $\text{fA}^{\bullet-}$) produced in the reaction shown in **Figure 6-47** relative to the ${}^3\text{D}^*$ yield were determined by extinction coefficients as $[\text{radical anions}]:[{}^3\text{D}^*] = 18.3$. Assuming the measured decay rate of $1.97 \times 10^4 \text{ s}^{-1}$ as a pseudo first order reaction rate due to reaction of the triplets with $2.2 \mu\text{M}$ a bimolecular reaction rate of $1.80 \times 10^{10} \text{ M}^{-1}\text{s}^{-1}$ consistent with a near diffusion controlled rate of reaction for which a value of $1.20 \times 10^{10} \text{ M}^{-1}\text{s}^{-1}$ was estimated based on an assumed 3.2 nm radius of the reactants for ${}^3\text{D}^*(\text{C6})\text{fA} + (\text{D}(\text{C6})\text{fA})^{\bullet-} \rightarrow \text{D}(\text{C6})\text{fA} + \text{D}(\text{C6})\text{fA}$. Here, $(\text{D}(\text{C6})\text{fA})^{\bullet-}$ is meant to represent a diblock with the electron on either moiety.

6.10 pCVPPV/MEH-PPV type II heterojunction

Based on the energetics of MEH-PPV and pCVPPV previously presented in Chapter 5, a lower limit of ≥ 390 meV is expected for the electron transfer from the the triplet state of pCVPPV to MEH-PPV. This reaction was investigated on the basis that pCVPPV and MEH-PPV formed a type II heterojunction and because the long triplet lifetimes of both pCVPPV and MEH-PPV allowed the dynamics of these excited states to be explored.

The triplet-triplet absorption spectrum of pCVPPV in benzene at a moderate chain concentration of $100 \mu\text{M}$ as presented earlier was found to have a single peak at 600 nm. In **Figure 6-48**, the transient absorption spectrum of a blend solution in benzene containing

pCVPPV at 450 μM and MEH-PPV at 15 μM is shown. A 600 nm band associated with $^3\text{pCVPPV}^*$ was found to rapidly form, reaching a maximum yield circa 630 ns. At the same time segment a much smaller yield of an absorption band at 820 nm associated with $^3\text{MEH-PPV}$ is observed. As the 600 nm band was observed to decay, the yield of $^3\text{MEH-PPV}$ was observed to form with a nearly equivalent rate of $7.8 \times 10^4 \text{ s}^{-1}$ – equivalent to a bimolecular rate constant of $5.2 \times 10^9 \text{ M}^{-1} \text{ s}^{-1}$ which is slightly slower than diffusion controlled. Concurrent with formation of $^3\text{MEH-PPV}^*$ band at 700 nm is observed to form with a rate of $7.8 \times 10^4 \text{ s}^{-1}$ and decay with a rate of $2.0 \times 10^4 \text{ s}^{-1}$. The species associated with the 700 nm band was unclear but was observed to form in a benzene solution of pCVPPV at 450 μM in the absence of MEH-PPV. The species was not observed to form in a solution of pCVPPV at 100 μM . A possible identity for the species is a triplet dimer, but further exploration was not given to determine it conclusively. In the near IR, no spectral bands were observed to form in the near IR, indicating that radical ions were not formed. The results of the transformation suggest an efficient transfer of triplets from pCVPPV to MEH-PPV while triplet exciton dissociation was non-existent.

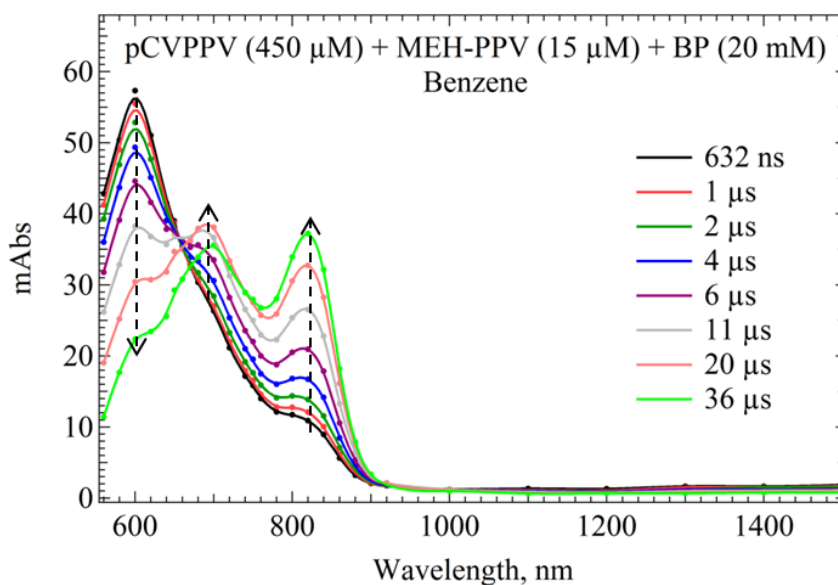


Figure 6-48 Transient absorption spectrum corresponding to a benzene solution of pCVPPV (450 μM chain) and MEH-PPV (15 μM chain) giving indication of a conversion of $^3\text{pCVPPV}^*$ (600 nm) to $^3\text{MEH-PPV}^*$ (820 nm).

6.11 Discussion and Summary

The nature of electron and/or energy transfer at type II heterojunctions were explored in this chapter. To accurately measure free energies of electron transfer at these heterojunctions accurate delocalization lengths of charges are required. Delocalization lengths of charges for MEH-PPV were determined by radiolysis and/or chemical redox titrations. The delocalization lengths of triplets for both MEH-PPV and pCVPPV were also determined. Delocalization lengths of charges and excited states provide a gauge for qualitatively determining ease of transport along chains. MEH-PPV triplets and pCVPPV triplets, were determined as 4.8 monomers (3.0 nm) and 0.92 monomer (1.5 nm), respectively. In the case of MEH-PPV, a triplet delocalization length extending over 4.8 monomers is perhaps surprising given that the conjugation length of 6.0 monomers has been reported for PPV. The delocalization length of pDPP2FT was not determined. Unlike the high energy triplet of pCVPPV, dissociation of pDPP2FT triplets would leave little extractable energy in a device. Delocalization lengths of the negative and positive polaron of MEH-PPV were determined as 5.00 ± 0.28 monomers (3.10 ± 0.17 nm) and 7.95 ± 0.68 monomers (4.93 ± 0.42 nm), respectively. That the positive polaron length exceeds that of the negative polaron is in agreement with computational studies [130] and is further supported by measurements of the zero-field mobilities which for the hole was reported as $(1.0 \pm 0.5) \times 10^{-7}$ cm²/Vs, and larger than that of the electron by an order of magnitude, indicating that while polaron lengths relate to observed mobilities, the relationship is not quantitatively proportional [131].

The compounds SF-PPV (A) and fSF-PPV (fA) were explored as electron acceptors relative to MEH-PPV (D). Using reversible electron transfer reactions in LEAF, the free energy change for the reaction $D^{\bullet-} + fA \rightarrow D + fA^{\bullet-}$ was determined as $-267 + 11$ meV. The reduction potentials of SF-PPV and fSF-PPV as measured by CV were found to be nearly identical and therefore a similar free energy change is expected for $D^{\bullet-} + A \rightarrow D + A^{\bullet-}$. The measured free energy change should be more than sufficient to observe an electron transfer reaction from D to A or D to fA. Diblock copolymers consisting of D and A moieties or D and fA moieties covalently bonded

either directly or via intervening aliphatic bridges, were investigated to explore intramolecular electron transfer rates as a function of donor-acceptor separation distance.

Due to strong absorption of D^{\bullet} at 900 nm and negligible absorption from A^{\bullet} and fA^{\bullet} at 900 nm, the reaction rates of $D^{\bullet}BA \rightarrow DBA$ and $D^{\bullet}BfA \rightarrow DBfA^{\bullet}$ were determined by 900 nm transients following radiolysis of solutions of DBA and DBfA. Time constants were microseconds long, 3 – 4 orders of magnitude longer than electron transfer rates measured in some DBA systems where D and A were molecules, such as a biphenyl-cyclohexane-naphthalene compound for which the intramolecular electron transfer rate was reported as $\sim 10^9 \text{ s}^{-1}$. Within the time resolution of experiments performed, the electron transfer rates for all diblocks were concentration dependent, indicating electron transfer dominantly occurring via bimolecular reaction even at the lowest concentrations explored. Intramolecular electron transfer was rates were approximated by the uncertainty of linear fits to data of electron transfer measurements vs. chain concentration, and an upper limiting value of $\sim 10^{-4} \text{ s}^{-1}$ was determined for all diblocks. This rate for electron transfer by any standard is astonishingly slow and unexpected based on the presumption of scholars who have assumed that these materials provide pathways for rapid exciton dissociation without question.

To estimate the bimolecular reaction rates, accurate molecular weights of the diblocks were required. Estimates of diblock molecular weights measured by GPC were $\geq 20\%$ smaller than molecular weights estimated by assuming accuracy of the molecular weight of the MEH-PPV homoblock but determining the number of fA monomers per chain via optical extinction coefficients. This method, denoted as the spectral fit (SF) method was deemed valid based on the fact that ground state absorption spectra of diblocks could be well fitted by linear sums of the absorption spectra of the D and fA homoblocks, indicating a weak electronic coupling between D and fA. This method was applied to ground state spectra collected in both THF and chloroform, and produced similar estimates for the number of fA monomers in each diblock. A similar spectral fitting technique was also used to fit the absorption transient of $D(C_2)fA$ and $D(C_0)fA$ following radiolysis at a time “t” after pulse, using a linear sum of $f_D^{\bullet} \text{Abs}_t(D^{\bullet}) + f_A^{\bullet} \text{Abs}_t(fA^{\bullet})$ for which f_D/f_A was used as an approximation for the ratio of $[D^{\bullet}bfA]/[DBfA^{\bullet}]$ and ultimately to approximate the ratio of $[D]/[fA]$ based on relative electron attachment rate

constants. For each of the diblocks, the estimated molecular weights determined by the SF method were used to prepare known chain concentrations for which the electron transfer kinetics by radiolysis were determined and plotted versus [DbfA]. Fits of this data were nearly linear with concentration as expected based on the linear sum of intramolecular and bimolecular components. The y-intercept of the best linear fit was used to define an upper limit for intramolecular electron transfer rate which was determined as $\approx 1 \times 10^4 \text{ s}^{-1}$, 5 orders of magnitude slower than observed in biphenyl-cyclohexane-naphthalene [132, 133]. For a DBA construct involving a molecular D and molecular A, if an excess electron is resident on D, it necessarily means that it is also interfaced at the donor/bridge interface. However, if D is an oligomer or polymer of n monomer units, and the electron delocalizes over p units, then the probability of finding the electron at the donor/bridge interface will decrease and result in a substantial decrease in observed rate of transfer. A simplistic approximation might consider the probability for finding the electron at the donor/bridge interface as $1/(n-p+1)$ and due to the electron spreading over p units, this has the potential of decreasing the electronic coupling by a factor of $1/p^{1/2}$ and decreasing the transfer rate by $1/p$. The overall decrease in rate of D_nBA relative to D_1BA is then approximated by an upper limit of $1/(p*(n-p+1))$. For the $D_{24}BfA$ diblocks, the negative polaron is delocalized over 5.0 monomers, and this value is equivalent to $1/(5*20) \approx 1/100$, indicating a rate decrease by 2 orders of magnitude. The delocalization of the electron on fA could not be determined. The fA homoblock was 3.1 monomers in length while spectral fitting suggested nearly double this length for the fA moiety in the DBfA diblocks. It is plausible that accounting for the electron delocalization on fA, that the rate might decrease by an additional order of magnitude, resulting in 3 orders of magnitude decrease. This is still 2 orders of magnitude greater than the fastest possible rate of intramolecular electron transfer estimated from the uncertainty in the electron transfer data, indicating other factors contribute to the very slow rate. Some clues are provided by examining the bimolecular electron transfer rates.

Bimolecular electron transfer rate constants in the $D_{24}(Cn)fA$ series were sensitive to the monomer ratio of D and fA in the diblocks. For $D_{24}(C0)fA$ and $D_{24}(C1)fA$ which contained about 5 - 6 fA monomers, bimolecular rate constants were nearly the same with an average of $(1.58 \pm$

$0.06) \times 10^9 \text{ M}^{-1}\text{s}^{-1}$. This was virtually identical to the rate constant of $(1.59 \pm 0.09) \times 10^9 \text{ M}^{-1}\text{s}^{-1}$ observed for D14(C1)fA which had 3 monomers of fA, making the ratio of [D]:[fA] nearly the same as for D₂₄(C0)fA and D₂₄(C1)fA. The fastest rate constant was obtained from D₂₄(C2)fA, D₂₄(C4)fA, and D₂₄(C6)fA which had 10 - 11 fA monomers, and exhibited an average rate constant of $(3.52 \pm 0.02) \times 10^9 \text{ M}^{-1}\text{s}^{-1}$ in THF. This rate constant is 3.4 times slower than the diffusion controlled rate constant of $1.20 \times 10^{10} \text{ M}^{-1}\text{s}^{-1}$ for encounter of two identical D(Cn)fA chains determined by the Debye-Smoluchowski equation.

The results indicate that contact is required for electron transfer from *D* of one diblock to fA of another. A significantly slower than diffusion controlled rate constant indicates that the reaction either is sensitive to orientation and only proceeds according to the probability coincident with such orientation, involves a high reorganization energy, or is in the inverted region. In the presence of 0.1 M TBAPF₆, the bimolecular rate constant for D₂₄(C2)fA, D₂₄(C4)fA, and D₂₄(C6)fA were found to decrease by a factor of 4. In the presence of the electrolyte, ion-pairing of radical anions and TBA⁺ occurs, but diffusion coefficients of the reacting species are negligibly affected. Ion pairing should decrease the driving force which must then be the mechanism responsible for the observed rate decrease. An increase of the electron transfer rate would indicate the reaction in the absence of electrolyte was in the inverted region.

That the bimolecular electron transfer rate decreased substantially indicates that the reaction involves a large solvent reorganization energy which imposes an activation energy. The solvent reorganization energy is in part dependent on the center-to-center separation distance of D and fA, and this is the only parameter that could possibly change with the inclusion of ion pairing. The reorganization energy decreases as the separation distance decreases. The results are then interpreted as electron transfer occurring via nearly cofacial contact of D and fA moieties. That the rates are concentration dependent indicate that the chains do not fold upon themselves to acquire the requisite morphology for electron transfer. In the absence of electrolyte, the slower than diffusion controlled rate may owe not only to reorganization energy, but also in part to a required orientation of the reactants which may not be satisfied within each encounter of two DBfA chains. The relative contribution owing to an orientation factor is unknown. In order to estimate the reorganization energy responsible for

the activation energy in this reaction, the contribution of an orientation factor is neglected and the slower rate of electron transfer was assumed to owe entirely to an activation energy produced by a large reorganization energy.

The steady state photoluminescence quenching measurements corresponding to the intramolecular reaction $D^*BfA \rightarrow D^{\bullet-}BfA^{\bullet+}$ for the diblocks in THF seem to suggest electron transfer rates faster than the $\leq 1 \times 10^4 \text{ s}^{-1}$ for $D^{\bullet-}BfA \rightarrow DBfA^{\bullet-}$. Quenching magnitudes as large as 10% were measured, suggesting exciton dissociation rates on the scale of $\sim 1 \times 10^7 \text{ s}^{-1}$. A second method of estimating the rate of exciton dissociation was the photoexcited transient absorption spectroscopy. Lifetimes of D^* were investigated for D_{14} , $D_{14}(CO)fA$ and $D_{14}(C1)fA$ and were found in each case to exhibit time constants of $270 \pm 5 \text{ ps}$, suggesting that negligible electron transfer takes place in the diblocks. These results seem contradictory and are difficult to understand. A possible explanation for the discrepancy may lie in the nature of the excited state and its corresponding charge density when situated at the donor/bridge interface which may differ from that of the excess electron.

In a separate measurement, MEH-PPV was used as an acceptor in a type II heterojunction with pCVPPV, to explore the fate of $^3pCVPPV^*$ at the interface. The results indicated that triplet energy transfer was highly efficient and nearly diffusion controlled while no evidence of exciton dissociation was observed. This highlights the importance of pairing donor and acceptor materials not only based on energy offsets but based on limiting overlap integrals and other pathways that make exciton transfer competitive with exciton dissociation.

Chapter 7: Radiolytic investigations of pDPP2FT and perylene-diimide (PDI) capped pDPP2FT

7.1 Photophysical properties of pDPP2FT_x(PDI)

The nomenclature of pDPP2FT_x(PDI) with “PDI” in parentheses is intended as a reference to the collective entity of polymers containing pDPP2FT – the homoblock and the PDI-capped pDPP2FT of varied chain lengths, indicated by “x” as an average number of monomer units per chain. The PDI molecular unit is intended to serve as an electron acceptor. By capping pDPP2FT of varied lengths, our aim is to investigate electron transport as a function of chain length dependence. The pDPP2FT_xPDI were not completely capped with 2 terminating PDI units per every chain, but the number of PDI per chain as determined by NMR decreased with pDPP2FT chain length. The polydispersities of the PDI-capped polymers as determined by GPC using polystyrene standard, and the PDI capping ratios as determined by NMR are presented in **Table 7-1**. To further simplify the naming nomenclature, pDPP2FT will at times be represented as “p” and pDPP2FT_xPDI as “p_xPDI”.

Table 7-1 Properties of pDPP2FT and pDPP2FT_xPDI polymers ^aDetermined by GPC relative to polystyrene standard. ^bThe number averaged molecular weights were determined by end group analysis using ¹H NMR spectroscopy.

Polymer name	Polydispersity (M _w /M _N) ^a	# of PDIs/chain ^b	Chains with PDI End-Cap (%) ^c	M _N (NMR) ^b	n _{NMR} ^b	Maximum fraction of chains uncapped
pDPP2FT (p)	2.47			~21	37	
p ₃₂ PDI	2.19	1.37	90	19.6	32	0.10
p ₂₆ PDI	2.14	1.53	95	16.2	26	0.06
p ₂₀ PDI	1.96	1.67	97	12.8	20	0.02
p ₁₆ PDI	1.85	1.73	98	10.5	16	0.01
p ₁₄ PDI	1.71	1.78	99	9.3	14	0.01

The ground state absorbance spectra of the pDPP2FT_xPDI polymers were also characterized in chloroform and in THF and resulted in ground state absorbance spectra which were superpositions of the ground state absorbance spectra of the constituting polymer homoblock and PDI unit as shown in **Figure 7-1**. This suggests that the polymer donor and molecular acceptor are weakly coupled in the ground state.

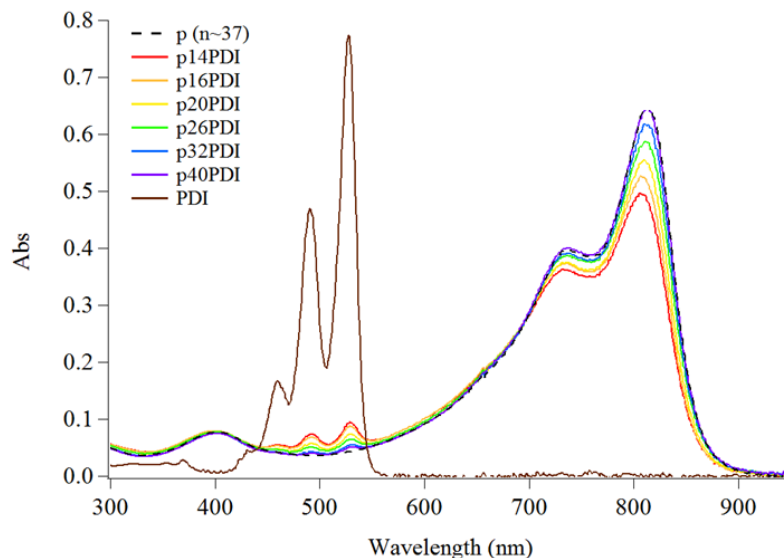


Figure 7-1 Ground state absorbance spectra of PDI and pDPP2FT_xPDI in chloroform. The spectra of pDPP2FT_xPDI are shown with normalized absorbances at 400 nm. In this way, the PDI absorbance is increased relative to the principal band of the pDPP2FT chain as chain length is decreased (Raw data provided courtesy of Dr. Maxwell Robb).

Attempts to measure photoluminescence from steady state emission spectroscopy of pDPP2FT yielded virtually nothing above the optical noise. This condition suggests that decay of ¹pDPP2FT* occurs primarily through nonradiative channels and therefore the rate of nonradiative decay (k_{nr}) greatly exceeds the rate of radiative decay (k_r) such that the fluorescence lifetime (τ_{fl}) can be approximated **Eq 7-1** as:

$$\tau_{fl} = \frac{1}{k_r + k_{nr}} \approx \frac{1}{k_{nr}} \quad 7-1$$

Lifetimes of the ¹pDPP2FT* state in THF were determined by photoexcited ps transient absorption spectroscopy for the homoblock, as well as for p₁₆PDI and p₃₂PDI. The data is shown

in **Figure 7-2** as collected in **(a)** and with peaks normalized in **(b)**. The lifetimes of the singlet excited states for each of the polymers were fit by two exponentials. The fast and slow decay rates for each polymer and the corresponding fraction of total decay attributed to each are shown in. From **Figure 7-2 (b)** it is clear that the decay rates of $^1\text{pDPP2FT}^*$ are virtually identical.

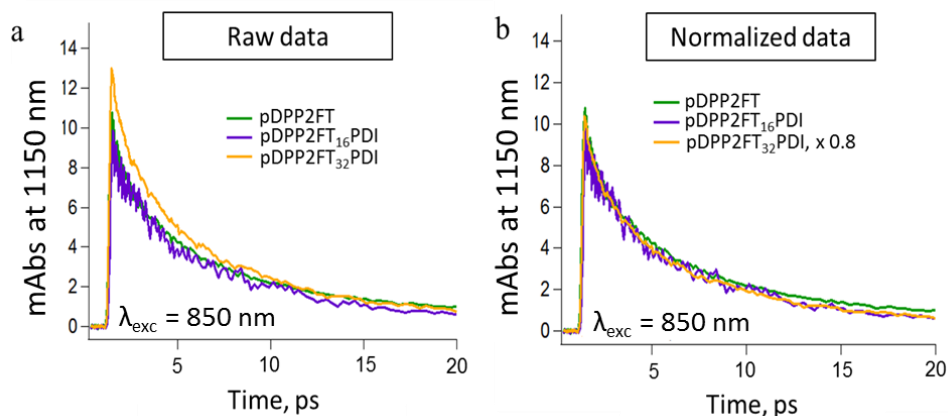


Figure 7-2 Transient absorption signals measured at 1150 nm corresponding to excitation of pDPP2FT , p_{16}PDI and p_{32}PDI at 850 nm.

The time constants and corresponding fraction of photoexcitation decay measured for each polymer are shown in **Table 7-2**. The average time constant, τ_{avg} was calculated as a weighted sum equal to $f_1 \cdot \tau_1 + f_2 \cdot \tau_2$. The mean of the three τ_{avg} values were calculated as 5.05 ± 0.55 ps. The exciton diffusion length of the excited state is not known, but such a short lifetime may suggest the diffusion length is also very short. No transformations were observed in the transient absorbance spectra of the PDI-capped polymer or polymer without capping. The energetic landscape of D-A copolymers creates uncertainty about the possibility of a partially charge separated state. The lack of a spectral transformation does not necessarily exclude the possibility but does not provide evidence for it either.

Table 7-2 Time constants and corresponding fraction of photoexcitation decay

Polymer	τ_1 (ps)	f_1	τ_2 (ps)	f_2	τ_{avg} (ps)
pDPP2FT	0.89	0.34	6.71	0.66	4.73
p ₁₆ PDI	2.10	0.47	9.15	0.53	5.83
p ₃₂ PDI	0.93	0.33	6.42	0.67	4.60

7.2 Redox titrations and polaron length determinations

7.2.1 Negative-polaron

The radical anions of pDPP2FT were prepared by chemical reduction via sodium biphenyl and compared with the earlier result obtained by radiolytic reduction in LEAF. During the course of chemical reduction, four spectral transformations were observed, the first of which is shown in **Figure 7-3**.

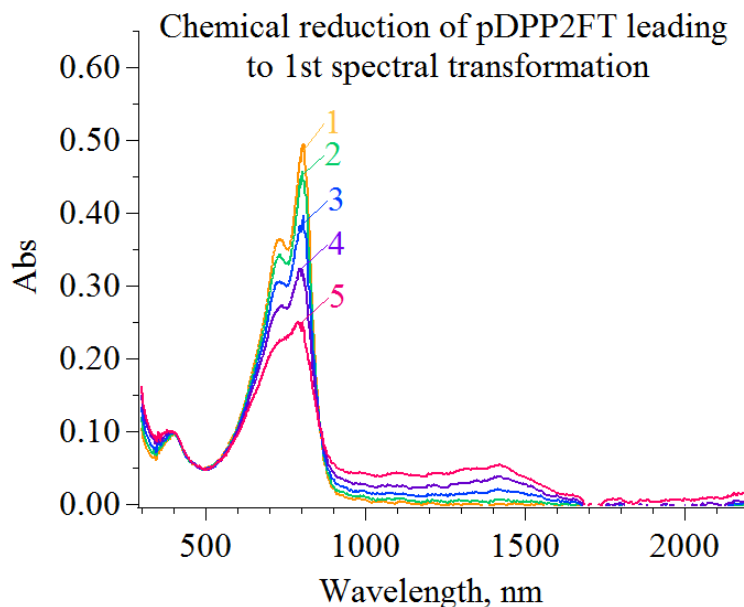


Figure 7-3 Chemical reduction of pDPP2FT (12.8 μM *pru*, 0.35 μM *chain*) via sodium biphenyl in THF results in formation of presumed ($\text{pDPP2FT}^{\bullet-}$, Na^+) with a peak at 1420 nm. In all but step 5, no band is observed above 1600 nm and only the neutral and 1420 nm bands are present.

The formation of a 1420 nm band is observed as pDPP2FT neutral is removed by addition of Na biphenyl in aliquots. Linearity in the neutral loss at 807 nm and absorbance gain at 1420 nm, along with an observed isosbestic point at 828 nm suggesting direct conversion of the neutral to the initial charged state. The spectral shape of the band at 807 nm is observed to transform as reduction occurs as a result of absorption contribution of radical anions. It should be noted that 2,2,2-cryptand was not used. In THF, effective ion pairing of the polymer radical anion and sodium cation is expected in the absence of 2,2,2-cryptand and may therefore lead to shifts in spectra relative to unpaired radical anions. In steps 1 – 4 no absorption band

beyond 1600 nm is observed, however hints of a lower energy band are evident in step 5 signaling formation of a 2nd species giving rise to a new spectral transformation.

In **Figure 7-4** the second spectral transformation is observed. The growth of a lower energy NIR band is observed in conjunction with growth of an 1130 nm band indicating formation of a 2nd species. It is not clear from the spectra whether this species is a result of conversion from the initial one. A difference spectrum obtained by subtracting step 9 from step 6 is provided in the inset. Unlike the initial charged species with a single optical transition, the second species is found to have two. By step 9, the neutral and 2nd species are found to coexist, possibly with the first also present.

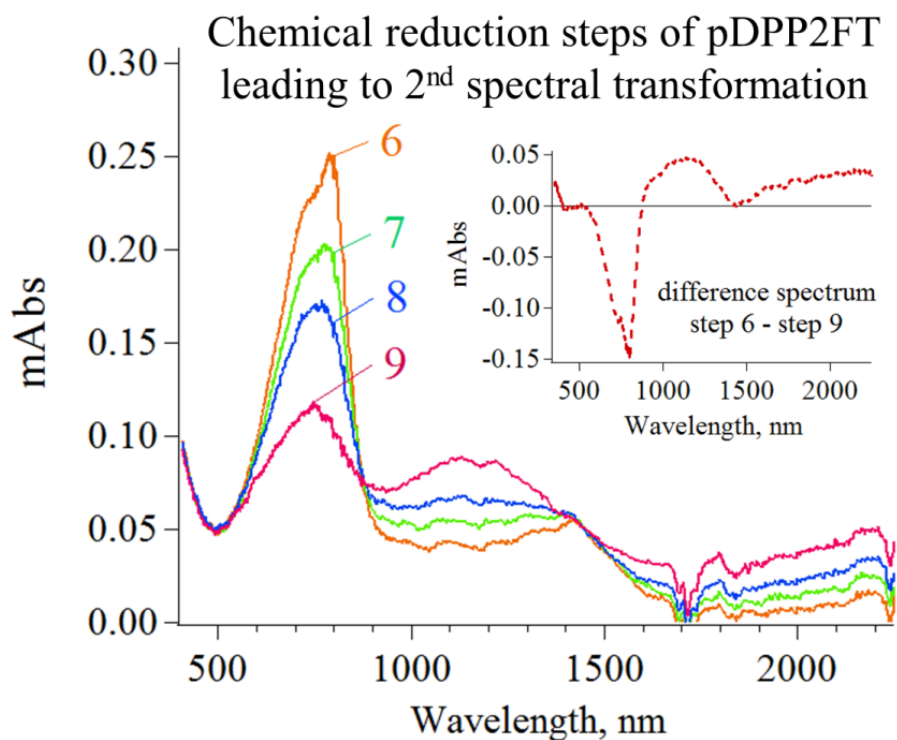


Figure 7-4 As the polymer is further reduced in steps 6 – 9, formation of two new bands are evident: a higher energy band with a maxima circa 1130 nm and a lower energy band that extends beyond the spectral window of observation. A difference spectrum obtained by subtracting step 9 from step 6 provides an approximate spectrum of the new optical transitions as shown in the inset.

Upon further reduction, a third spectral transformation is observed. As shown in **Figure 7-5**, the ground state neutral is further removed in steps 9 – 11 with very little change in yield of the 2nd charged state. As all neutral is removed in the transition from step 11 to 12, a decline in the

yield of the 2nd species is evident by suppression of absorbance at 2000 nm. Simultaneous formation of a new band circa 1350 nm is observed. In steps 13 and 14 the further growth of the 1350 nm band as the lowest energy band decays suggests conversion of the 2nd species into yet a 3rd species.

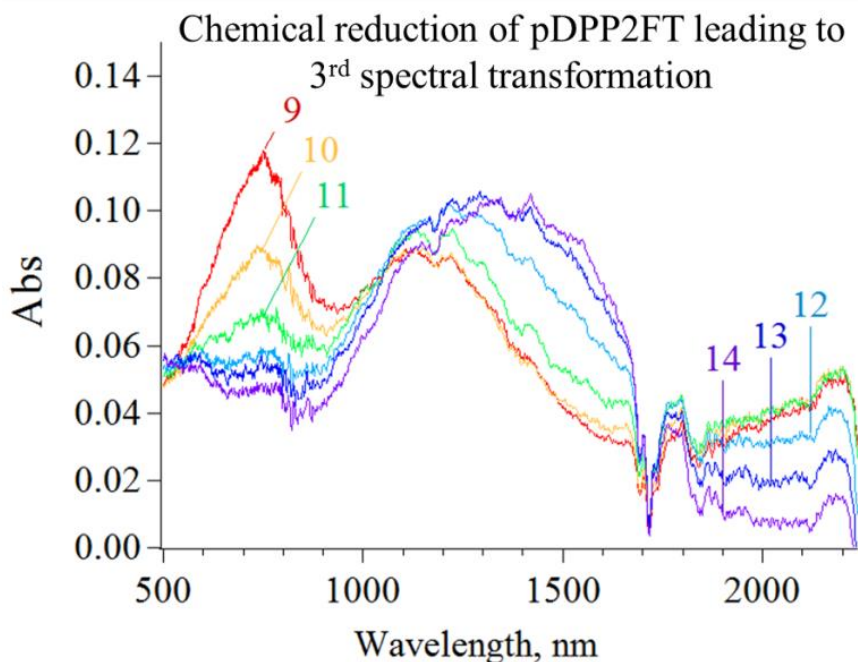


Figure 7-5 Starting with step 9 of the previous figure, a third spectral transformation is identified. Upon further reduction, the neutral is further suppressed in steps 9 – 11 with very little change in the bands associated with the 2nd charged state. In steps 12 – 14 however once the neutral is fully removed, the 2nd charged state begins to decline in yield as a 3rd charged state forms circa 1350 nm.

In the 4th and final transformation only the 2nd and 3rd species are present, and reduction is found to remove the 2nd species by step 17 as evident by full suppression of absorbance at 2000 nm. A difference spectrum obtained by subtracting step 19 from step 17 provides an approximate spectrum associated with this final state. The optical transitions observed in pDPP2FT with one transition associated with the first species, two from a second, and one from a third, differs significantly from the electronic structure of typical nondegenerate conjugated polymers according to the model proposed by Fesser, Bishop and Campbell consisting of a negative polaron with two optically allowed transitions and a negative bipolaron consisting of

one allowed transition. The nature of the electronic structure of pDPP2FT could not be further investigated due to time. The absorbance spectrum of pDPP2FT^{•-} from 1050 nm – 1650 nm, produced by radiolysis is overlaid by a rescaled spectrum of (pDPP2FT^{•-}, Na⁺) produced by chemical reduction via sodium biphenyl and are found to be similar, as shown in **Figure 7-7**.

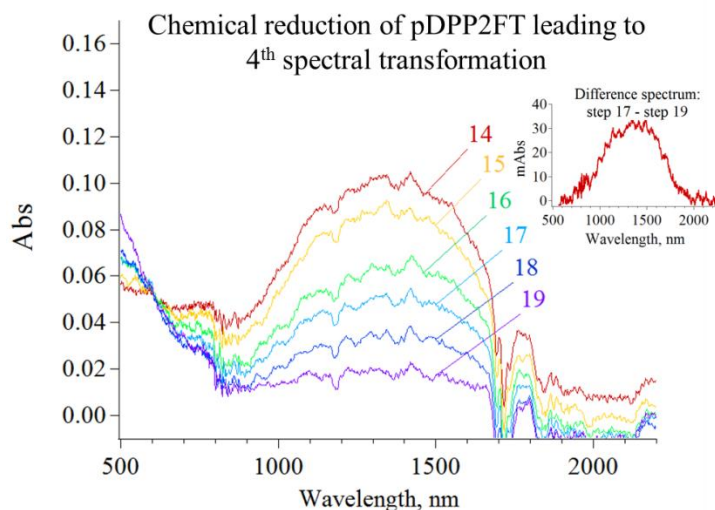


Figure 7-6 The 4th spectral transformation involves removal of the 2nd charged state (evident from suppression at 2000 nm) and eventual removal of the 3rd charged state as well (steps 17 – 19). An approximate spectrum of the 3rd charged state is shown in the inset.

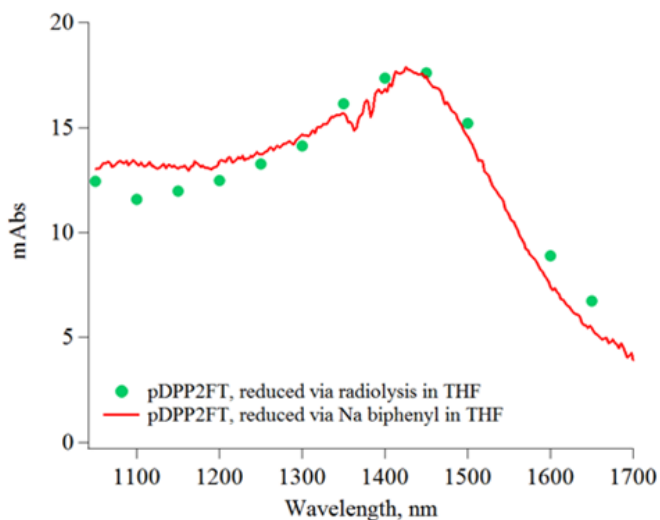


Figure 7-7 The absorbance spectrum of pDPP2FT^{•-} in THF produced via radiolysis, overlaid with a rescaled absorbance spectrum of (pDPP2FT^{•-}, Na⁺) produced by chemical reduction via sodium biphenyl.

The spectra of **Figure 7-3** corresponding to various stages of chemical reduction of pDPP2FT in THF were used to plot absorbance changes at 807 nm against absorbance changes at 1400 nm, and found to have a linear relationship as shown in **Figure 7-8**.

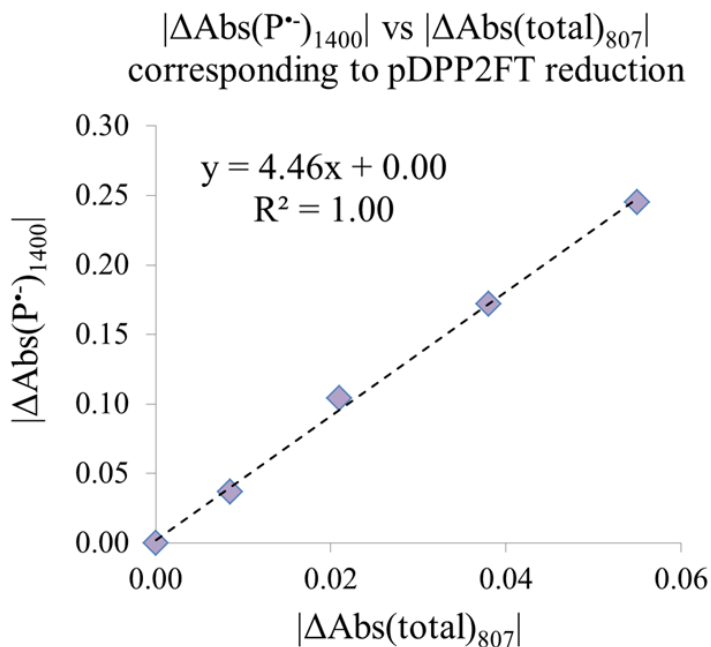


Figure 7-8 The magnitude of absorbance changes at 807 nm and 1400 nm corresponding to stages of partial reduction of pDPP2FT in THF exhibit linearity indicating direct conversion of the neutral into the negative polaronic species for the transitions shown.

The negative polaron length was determined by the expression: $\frac{\epsilon(\text{P}^{\bullet-})_{1400}}{\epsilon(\text{P}^0)_{807}} \cdot \left(\frac{|\Delta\text{A}(\text{total})_{807}|}{\Delta\text{A}(\text{P}^{\bullet-})_{1400}} + \frac{\Delta\text{A}(\text{P}^{\bullet-})_{807}}{\Delta\text{A}(\text{P}^{\bullet-})_{1400}} \right)$. Based on the extinction coefficients of $1.0 \times 10^5 \text{ M}^{-1}\text{cm}^{-1}$ and $7.78 \times 10^4 \text{ M}^{-1}\text{cm}^{-1}$ for $\text{P}^{\bullet-}$ and P^0 , a value of 1.3 is determined for $\frac{\epsilon(\text{P}^{\bullet-})_{1400}}{\epsilon(\text{P}^0)_{807}}$. The value of $\frac{|\Delta\text{A}(\text{total})_{807}|}{\Delta\text{A}(\text{P}^{\bullet-})_{1400}}$ is determined from the slope of **Figure 7-8** as 4.46. Assuming the extinction coefficient of pDPP2FT $^{\bullet-}$ at 950 nm where neutral does not absorb is the same as at 807 nm where neutral peaks, lead to the approximation of $\frac{\Delta\text{A}(\text{P}^{\bullet-})_{807}}{\Delta\text{A}(\text{P}^{\bullet-})_{1400}} \approx \frac{\Delta\text{A}(\text{P}^{\bullet-})_{950}}{\Delta\text{A}(\text{P}^{\bullet-})_{1400}} \approx 0.57$. Based on these calculations, an upper limit of 6.5 monomer units is estimated for the delocalization of the negative polaron, corresponding to a length of 10.9 nm, based on a DPP monomer length of 1.68 nm.

The negative polaron length was also estimated by collecting an absorbance spectrum containing both absorption bands of radical anion and bleach. This spectrum was acquired by radiolysis of a THF solution of pDPP2FT (5.5 μM chain) contained in a 0.1 cm pathlength cuvette allowing transmission at the neutral and is shown in **Figure 7-9**. Based on a value of $\left| \frac{\Delta A(\text{total})_{807}}{\Delta A(\text{P}^{\bullet-})_{1400}} \right| \approx \frac{4.70}{1.40} \approx 3.36$ the negative polaron is approximated to delocalize over 5.1 monomers, corresponding to a polaron length of 8.6 nm. Averaging the two estimates of the negative polaron lengths resulted in delocalization length of 5.8 ± 0.7 monomers, equivalent to 9.8 ± 1.2 nm.

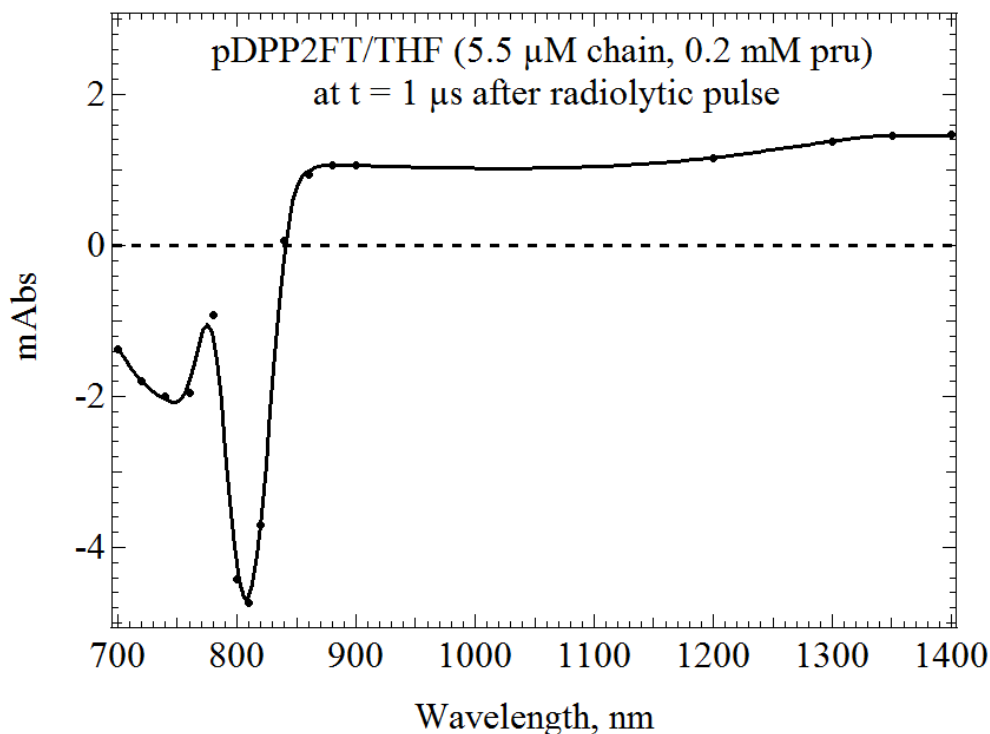


Figure 7-9 Spectrum corresponding to radiolysis of pDPP2FT (5.5 μM chain) in THF, collected at 1.0 μs after pulse, using a 0.1 cm pathlength cuvette.

7.2.2 Positive polaron

Radical cations of pDPP2FT were collected by chemical oxidation via thianthrenium hexafluorophosphate in DCE and by radiolysis of pDPP2FT in DCE. A set of spectra

corresponding to various oxidation states of pDPP2FT are shown in **Figure 7-10**. The early transitions contain no absorption band above 1600 nm and are shown in the inset of the figure. A spectrum shown hashed marking and in green corresponds to a transition between to oxidized species of the polymer – the first with one optical transition at 1450 nm and the second with two transitions, at ~1130 nm and further in the NIR beyond the spectral range of the instrument.

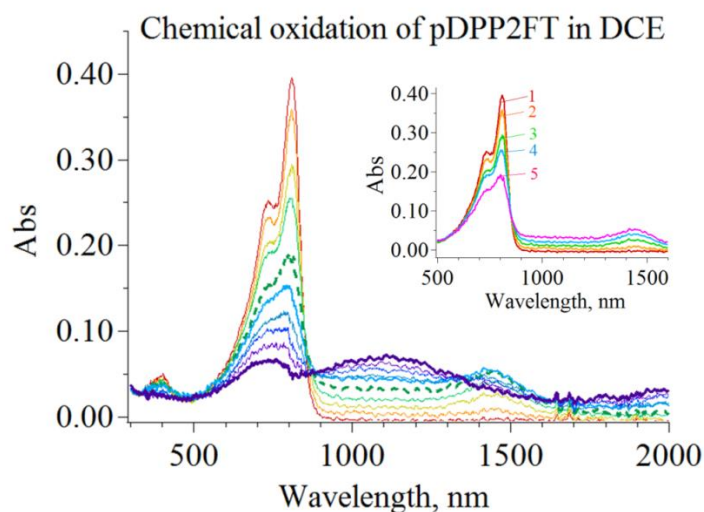


Figure 7-10 Absorbance spectra following various states of oxidation produced chemically via Thianthrenium hexafluorophosphate (ThPF_6) in DCE.

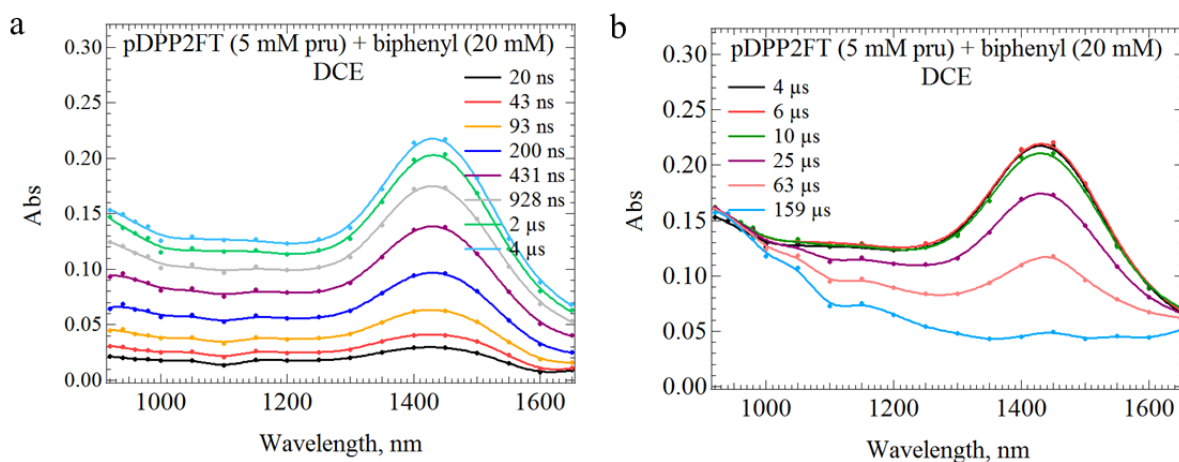


Figure 7-11 Transient absorbance spectra of pDPP2FT^{*+} collected following radiolysis of a DCE solution with biphenyl (20 mM) and pDPP2FT (5 mM pru). Biphenyl^{*+} is rapidly formed and

converted to $pDPP2FT^{\bullet+}$ via efficient hole transfer lead to the growth of a 1450 nm band in (a) and a subsequent decay process removes the band in (b).

Transient absorbance spectra following radiolytic pulse of a blend solution containing biphenyl (20 mM) and $pDPP2FT$ (5 mM) resulted in formation of a 1450 nm band. The growth at 1450 nm was fit by two exponentials with rates of $4.45 \times 10^6 \text{ s}^{-1}$ (80%) and $8.44 \times 10^5 \text{ s}^{-1}$ (20%). The former rate was consistent with a bimolecular hole transfer reaction with biphenyl at a rate constant of $3.23 \times 10^{10} \text{ M}^{-1}\text{s}^{-1}$ while the latter is peculiar. As the 1450 nm band decays a residual band is left remaining. The slower forming growth may have resulted from contribution of the unknown species. Nevertheless, good spectral agreement is found in the spectra of the cationic species at low oxidation steps by chemical oxidation as are obtained during the growth of a 1450 nm band following radiolysis. An overlay of a transient spectrum via radiolysis is shown overlaid by a scaled down spectrum of partially oxidized $pDPP2FT$ in **Figure 7-12**.

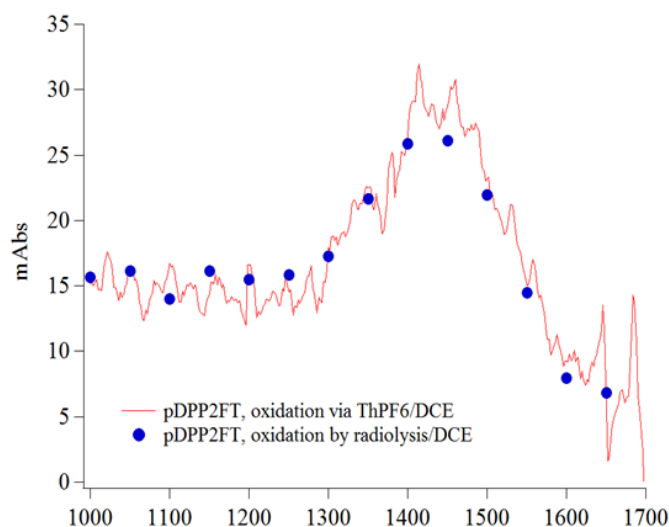


Figure 7-12 A spectrum of chemically oxidized $pDPP2FT$ overlaid by a rescaled spectrum of $pDPP2FT$ oxidized by radiolysis of $pDPP2FT$ in DCE shows good agreement.

Spectral steps of **Figure 7-10** corresponding to various stages of chemical oxidation of $pDPP2FT$ in DCE were used to plot magnitudes of absorbance changes at 807 nm against absorbance changes at 1450 nm where the radical cation band absorbs. This plot is found to

have a linear relationship as shown in **Figure 7-8** indicating direct conversion of neutral into positive polarons.

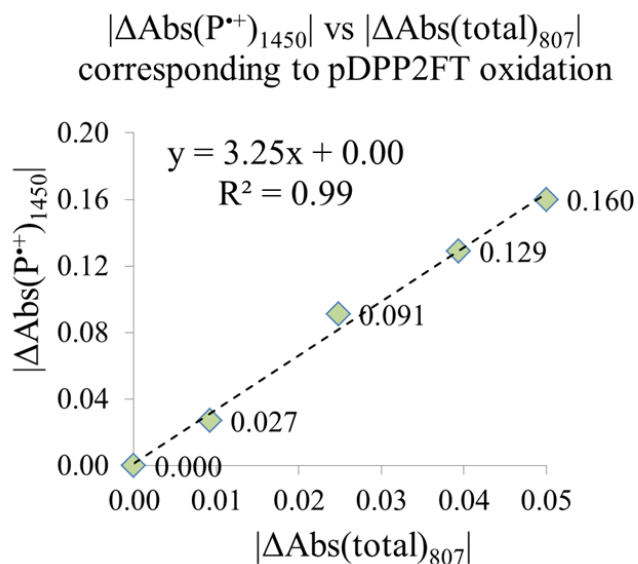


Figure 7-13 The magnitude of absorbance changes at 807 nm and 1450 nm corresponding to stages of partial oxidation of pDPP2FT in DCE exhibit linearity.

The positive polaron length was determined by the expression: $\frac{\varepsilon(\text{P}^{\bullet+})_{1450}}{\varepsilon(\text{P}^0)_{807}} \cdot \left(\frac{|\Delta\text{A}(\text{total})_{807}|}{|\Delta\text{A}(\text{P}^{\bullet+})_{1450}|} + \frac{\Delta\text{A}(\text{P}^{\bullet+})_{807}}{\Delta\text{A}(\text{P}^{\bullet+})_{1450}} \right)$. Based on the extinction coefficients of $1.8 \times 10^5 \text{ M}^{-1}\text{cm}^{-1}$ for $\text{P}^{\bullet+}$ and $7.78 \times 10^4 \text{ M}^{-1}\text{cm}^{-1}$ for P^0 in THF, a value of 2.3 is determined for $\frac{\varepsilon(\text{P}^{\bullet+})_{1450}}{\varepsilon(\text{P}^0)_{807}}$. The value of $\frac{|\Delta\text{A}(\text{total})_{807}|}{|\Delta\text{A}(\text{P}^{\bullet+})_{1450}|}$ is determined from the slope of **Figure 7-13** as 3.25. Assuming the molar extinction coefficient of pDPP2FT $^{\bullet+}$ at 950 nm where neutral does not absorb is the same as at 807 nm at the neutral peak, lead to the approximation of $\frac{\Delta\text{A}(\text{P}^{\bullet+})_{807}}{\Delta\text{A}(\text{P}^{\bullet+})_{1400}} \approx \frac{\Delta\text{A}(\text{P}^{\bullet+})_{950}}{\Delta\text{A}(\text{P}^{\bullet+})_{1400}} \approx 0.68$. The delocalization of positive polaron of pDPP2FT is then calculated as covering 9.0 monomers, equivalent to a length of 15.2 nm. This length is 3.1 times greater than the delocalization length of the positive polaron of MEH-PPV.

7.3 Investigations of electron transport in pDPP2FT_x(PDI)

Electron transfer from a polymer donor to an appended acceptor via intramolecular pathway may be monitored by optical detection if the optical signatures of the polymer radical anion and acceptor radical anion are known and wavelengths exist where one or the other absorbs. Ideally, if a wavelength is known where only the acceptor radical anion absorbs, the formation may be directly measured. It may not be impossible to measure the acceptor radical anion however, in which case, its formation rate may be inferred from monitoring the formation and decay of the polymer radical anion in an acceptor-capped polymer relative to a control polymer without acceptor capping. An effective control will then provide an accurate estimate for the rate constant for electron attachment to the polymer chain ($k_{attachment}$), an approximate fraction for the electrons which directly attach to the acceptor (f_a) versus the fraction that attach to the polymer donor (f_d), and alternative decay paths for the polymer radical anion in the absence of the acceptor ($k_{neutralize}$). An additional pathway of decay for the polymer anion in the presence of the acceptor, is the electron transfer via the bimolecular rate constant (k_{bi}). If the intramolecular rate ($k_{transport}$) is sufficiently fast, a low enough concentration of the polymers may be used to easily distinguish intramolecular and bimolecular electron transfer. The various reaction pathways for an electron attaching to an acceptor-capped polymer donor are shown in **Figure 7-14**.

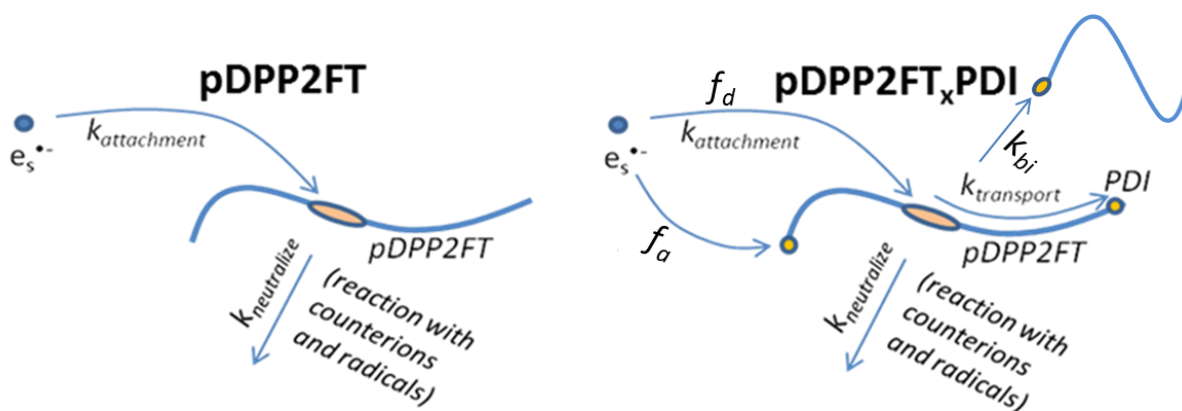


Figure 7-14 A scheme for kinetic parameters involved in radiolysis of a THF solution of pDPP2FT and a THF solution of pDPP2FT_xPDI (shown with 2 PDI end caps).

7.3.1 Overview

The conclusions drawn in this study are based on results obtained among several experimental trials. Achieving consistently repeatable and reliable data was a challenge in some of the earliest measurements, but was to a large extent overcome by determining how to control experimental conditions through improved methods of preparation and handling of solutions. It was discovered that the polymers at even modest concentrations of 0.5 mM per repeat unit would aggregate. The rate of aggregation was very much concentration dependent. At 0.5 mM pru, signs of aggregation were visible after two weeks. At 1.0 mM pru, aggregation was visible after a few days. At concentrations of 1.5 – 2.0 mM pru, signs of aggregation were visible within a day of preparation. In the case of concentrations ≥ 1.5 mM pru, signs of aggregation in THF solutions of pDPP2FT were also detectable via radiolytic reduction, which yielded slower electron attachment rates for measurements made several hours after preparation in contrast with ones made shortly after preparation. Upon reheating the solution, allowing it to cool to room temperature, and recollecting a measurement, the initial electron attachment kinetics could be regained. This result indicated that the slowing rates of electron attachment were the result of a decrease in concentration of isolated single chains with time due to aggregation. To mitigate aggregation effects, a decision was made to only make measurements on solutions directly after preparation when possible. If this was not possible, the solutions would require reheating followed by restoration to room temperature prior to measurement.

In each batch of p_x PDI, there was a distribution of chains with 2 PDI caps, 1 PDI cap, and 0 PDI caps. The fraction of chains with “n” PDI caps will be denoted by f_n . If the percent of chain ends with capping are denoted by P_c , then for a randomized capping process, $f_2 = (P_c)^2$, $f_0 = (1 - P_c)^2$, and $f_1 = 2 * P_c(1 - P_c)$. From NMR, the number of PDI caps per chain, N , were determined. The percent of chain ends with capping, P_c , was then determined as $P_c = N/2$. Based on the values of N measured, the values of P_c and P_n are determined for each of the p_x PDI samples as shown in **Table 7-3** below.

Table 7-3 The fraction of chains with n PDI caps (f_n) calculated based on random capping process, for each batch of p_x PDI based on the measured number of PDI caps per chain (N).

polymer	N (# caps/chain)	Pc	f_2	f_1	f_0
p_{32} PDI	1.37	0.685	0.47	0.43	0.10
p_{26} PDI	1.53	0.765	0.59	0.36	0.06
p_{16} PDI	1.73	0.865	0.75	0.23	0.02
p_{14} PDI	1.78	0.890	0.79	0.20	0.01

In each of the experimental trials, chain concentrations of p_{37} and p_x PDI were held constant. The kinetics of the polymer radical anion for the polymer solutions was monitored at 1400 nm near the maximum extinction coefficient of the polymer radical anion. At 1400 nm the only other strongly absorbing species following radiolysis of the polymer solutions in THF, are the electrons. Following the capture of all electrons, the remaining absorption then should entirely reflect the yields of polymer radical anions in each solution unless some contribution also comes from the radical anion of the end cap. Based on the absorption spectra immediately following radiolysis of PDI and PDI-phenyl, the contribution of the end cap anion is considered negligible at 1400 nm.

Due to the limited solubility of the polymers, exploring a range of polymer concentrations was not possible, but this may help resolve the various kinetic processes in the scheme shown in **Figure 7-14**. For example, at a moderate concentration of an acceptor-capped polymer, the rate of bimolecular electron transfer may be slow enough to resolve bimolecular and intramolecular decay rates for the polymer radical anion, but not sufficiently high to accurately measure the intramolecular rate due to simultaneous electron capture occurring over a similar timescale. At high polymer concentrations, electron transfer kinetics may be well resolved due to an electron capture rate that is significantly faster, but resolving the contributions of bimolecular and intramolecular pathways to the overall electron transfer kinetics may be a challenge. All solutions were prepared in an Argon-saturated glovebox and dispensed into 0.5 cm pathlength cuvette cells and sealed with Teflon stopcocks.

7.3.2 Electron transport study: trials 1 and 2

Absorption transients at 1400 nm for p_{37} and p_x PDI polymers at chain concentrations of 25 μM are shown in **Figure 7-15 (a)** and **(b)**. The data in **(a)** and **(b)** are from separate and independent measurements – the more complete data set in **(b)** was collected last. In the solutions of p_{37} polymer radical anions grow in with a rate of $6.70 \times 10^6 \text{ s}^{-1}$ (149 ns) in **(a)** and $7.30 \times 10^6 \text{ s}^{-1}$ (137 ns) in **(b)** providing an estimate of $(7.00 \pm 0.30) \times 10^6 \text{ s}^{-1}$ ($143 \pm 6 \text{ ns}$). Electron attachment to the polymer in both cases was fully completed by 400 ns. In both sets of data, common observations are found.

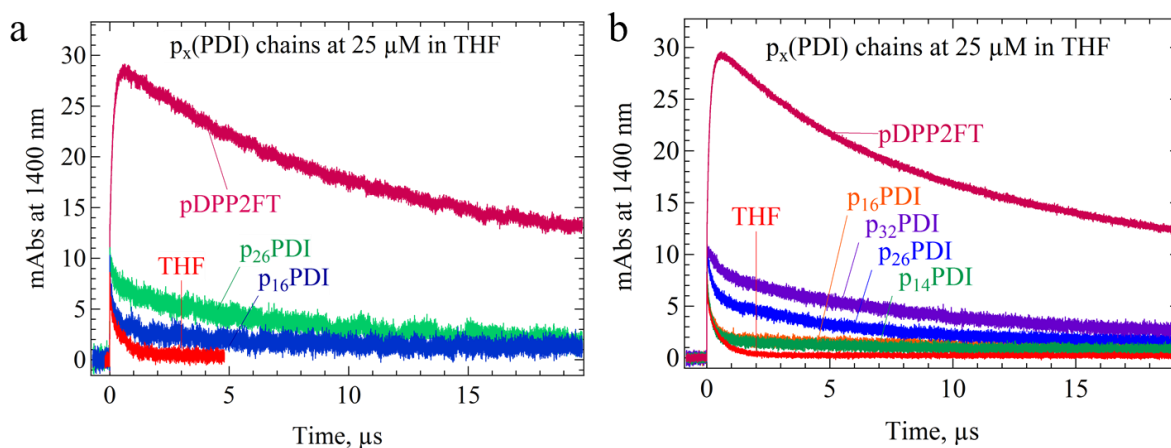


Figure 7-15 1400 nm absorption transients immediately following radiolysis of THF solutions containing p_{37} , and p_x PDI at chain concentrations of 25 μM , where **(a)** and **(b)** correspond to independent experimental trials with **(a)** containing only p_{16} PDI and p_{32} PDI and **(b)** containing p_{14} PDI and p_{32} PDI as well.

During the formation of polymer radical anions in the p_{37} solutions, no growth of polymer radical anions is observed in the p_x PDI solutions. By the completion of the polymer radical anion growth in the p_{37} solution, the absorbance magnitudes corresponding to the p_x PDI solutions are greatly suppressed relative to that of p_{37} , with the extent of suppression increasing with decreasing chain length. At the completion of electron attachment all of the absorption signal is contributed only by polymer radical anions and to a much lesser extent (if at all) from the radical anion of the end cap. This suppression in absorption yield of p_x PDI relative to p_{37} either indicates that only a small fraction of electrons attach to the chain, or that a large fraction attach to the pDPP2FT chain but rapidly transport to PDI end caps with a rate

faster than the rate of electron attachment to the pDPP2FT chain. The possibility of a small electron capture fraction may be evaluated from kinetic considerations. The rate of electron attachment to PDI-phenyl was found to be $1.23 \times 10^{11} \text{ M}^{-1}\text{s}^{-1}$ but this rate should decrease by several factors based on the constrained diffusion coefficient associated with the chain to which PDI is end capped. A study of repeat unit electron attachment rate constants (in the approximately time-independent regime) for oligofluorenes determined that relative to the rate of attachment to a single monomer of oF, the attachment rate slowed by a factor of 3.4 for a 10 monomer chain, and slowed by a factor of 4.6 for a 23 monomer chain. Averaging these rates, suggests for a 16.5 monomer chain, slowing by a factor of 4.0. Taking this rough approximation in rate decrease for PDI which is of similar but slightly larger length than oF suggests that the attachment rate to a single unit in a chain of ~ 16 monomer units of PDI should result in an attachment rate constant of $3.08 \times 10^{10} \text{ M}^{-1}\text{s}^{-1}$. Based on the fact that the per repeat unit attachment rate for pDPP2FT is smaller, suggests that this value is likely an upper limit and possibly even smaller for a PDI end cap terminating 16 monomers of DPP. Based on the rate ratios, the PDI unit would be expected to capture electrons at a rate of 4 times faster per monomer than a DPP unit. The maximum fraction of electrons going directly to the PDI caps without first contacting the pDPP2FT chain is then estimated for each of the p_x PDI chains investigated as shown in **Table 7-4**.

Table 7-4 Max fraction of electrons captured directly by PDI caps assuming 2 PDI caps per chain.

Polymer	Maximum fraction of electrons captured by PDI caps (assuming 2 caps per chain)
p_{14} PDI	36%
p_{16} PDI	33%
p_{26} PDI	24%
p_{32} PDI	20%

It is clear from kinetic considerations that the majority of electrons contact the pDPP2FT portion of the p_x PDI chain before arriving at the end caps. This then indicates that following capture by the chain, electrons rapidly diffuse to the end cap at a rate that exceeds the rate of

attachment. As was demonstrated earlier in **Figure 4-49**, for a kinetic profile corresponding to the formation and decay of a species, the growth will reflect either the rate of formation of the species or its depletion – whichever is fastest. Conversely, the slowest rate will be reflected in the decay of the transient signal. For p₁₄PDI and p₁₆PDI, there the nature of the fast decaying signal is similar to the lifetime of the electron in pristine THF. The yield of radical anions in p_xPDI solutions which are found remaining after electron attachment is complete, decay with a very slow rate which is interpreted as owing to bimolecular electron transfer reactions. The fraction of slow decaying polymer radical anions, denoted as f_{slow} , is determined from the ratio of absorbances of p_xPDI/p₃₇ just after electron attachment is complete. The values of f_{slow} were found to vary in independent experimental trials, but were consistent within a 10% error when data was collected within an hour of sample preparation.

The bimolecular electron transfer rate k_{Bi} for the slow decaying population was determined from first order fits of the slow decay rates of p_xPDI solutions at chain concentrations of 40 μM. An average value of $(1.53 \pm 0.05) \times 10^5 \text{ s}^{-1}$ is determined for the p_xPDI solutions, corresponding to a bimolecular rate constant of $(3.82 \pm 0.13) \times 10^9 \text{ M}^{-1}\text{s}^{-1}$ assuming all chains are capped. In **Figure 7-16** the slow decaying transient of p₃₂PDI is shown. The fraction f_{slow} in each of the p_xPDI solutions was found to exceed the fraction f_0 . This condition of $f_{\text{slow}} > f_0$ is interpreted as owing to a fraction of chains which have PDI caps but also have defects which may confine an electron to the chain. This fraction, denoted $f_{\text{defective}}$ is equivalent to $f_{\text{slow}} - f_0$. This interpretation suggests that the fraction of defective chains then would increase with chain length. The values of f_{slow} and $f_{\text{defective}}$ as determined in the experimental trials shown in **Figure 7-15 (a)** and **(b)** are listed in **Table 7-5** below.

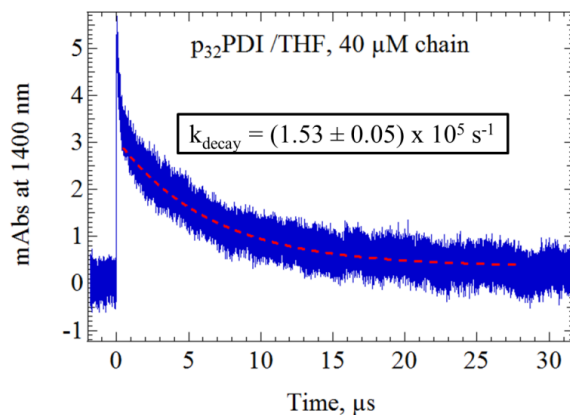


Figure 7-16 The slow decay rate of $p_{32}\text{PDI}/\text{THF}$ at $40\ \mu\text{M}$ chain, associated with bimolecular electron transfer. The decay rates of all $p_x\text{PDI}$ were found to have slow decay rates of $(1.53 \pm 0.05) \times 10^5\ \text{s}^{-1}$.

Table 7-5 Fractions of slow decaying polymer radical anions (f_{slow}), fraction of uncapped chains (f_0), and fraction of defective chains ($f_{\text{defective}}$) for each $p_x\text{PDI}$ batch.

Polymer	Trial #	f_{slow}	f_0	$f_{\text{defective}}$
$p_{14}\text{PDI}$	Trial 2	0.07	0.01	0.06
$p_{16}\text{PDI}$	Trial 1	0.08	0.02	0.06
$p_{16}\text{PDI}$	Trial 2	0.07	0.02	0.05
$p_{26}\text{PDI}$	Trial 1	0.20	0.06	0.14
$p_{26}\text{PDI}$	Trial 2	0.16	0.06	0.10
$p_{32}\text{PDI}$	Trial 2	0.25	0.10	0.15

The 1400 nm kinetics of $p_x\text{PDI}$ solutions contain the absorbance transients of the electron, and the pDPP2FT radical anion corresponding to chains with and without PDI caps. From the present data, it is unclear if and how much polymer radical anion contributes to the fast decaying absorption signals of $p_{14}\text{PDI}$ and $p_{16}\text{PDI}$ at 1400 nm. In one extreme, the fast decay may correspond to the formation rate of polymer radical anions and in the other extreme may correspond to the depletion rate of solvated electrons in the presence of polymer solutes. In either extreme, the rate corresponds to the formation of polymer radical anions. If the time constants of electron attachment to a $p_x\text{PDI}$ chain, and formation of $p_x\text{PDI}^{\bullet-}$ by electron transfer from the chain are denoted as $\tau_f(p_x^{\bullet-}\text{PDI})$ and $\tau_f(p_x\text{PDI}^{\bullet-})$ then the time constant for electron transport, denoted as $\tau_{\text{transport}}$, may be calculated as:

$$\tau_{transport} = \tau_f(p_x^{\bullet}PDI) - \tau_f(p_xPDI^{\bullet}) \quad 7-2$$

The value of $\tau_f(p_x^{\bullet}PDI)$ for $p_{14}PDI$ and $p_{16}PDI$ was determined by the rate of decay corresponding to the fast decay of the 1400 nm transient. Due to the nearly equivalent lengths of p_{37} and $p_{32}PI$, the value of $\tau_f(p_x^{\bullet}PDI)$ for $p_{32}PDI$ was determined from the attachment time constant for p_{37} . The value of $\tau_f(p_x^{\bullet}PDI)$ for $p_{26}PDI$ is estimated by averaging the time constants measured for $p_{16}PDI$ and $p_{32}PDI$. This estimate is a good approximation based on the length dependence of electron attachment rates for polyfluorenes [134]. The values for $\tau_f(p_xPDI^{\bullet})$ were determined by fits of absorbance transients at 950 nm where PDI^{\bullet} absorbs. As with the 1400 nm transients, transients at 950 nm were collected for the solutions prepared both for Trial 1 and Trial 2. At 950 nm, $pDPP2FT^{\bullet}$ and $PDPP2FTH^{\bullet}$ also absorb. Denoting the 950 nm absorption transient for $pDPP2FT$ as $Abs_t(pDPP2FT)_{950}$, to correct for the absorption contributions of $pDPP2FT^{\bullet}$ and $PDPP2FTH^{\bullet}$ the 950 nm transients of each p_xPDI were corrected by subtracting the product $f_0 * Abs_t(pDPP2FT)_{950}$. The corrected 950 nm transients for the p_xPDI solutions along with the 950 nm transients of THF and p_{37} are shown in **Figure 7-17** for Trial 1 and in **Figure 7-18** for Trial 2.

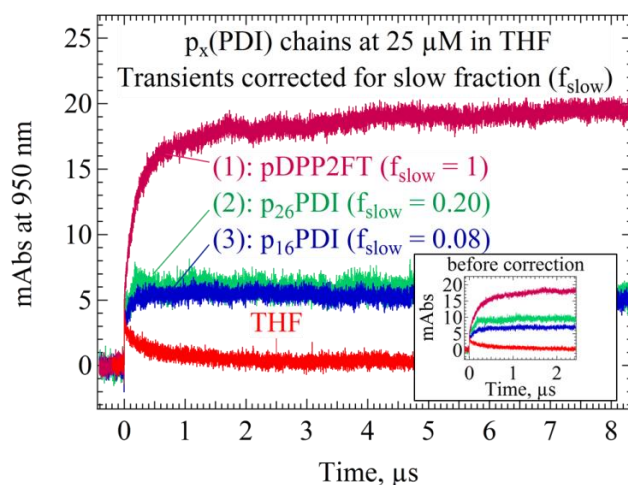


Figure 7-17 Absorption transients at 950 nm following radiolysis corresponding to THF, and solutions of $pDPP2FT$, $p_{16}PDI$ and $p_{26}PDI$ in THF – each at chain concentrations of $25 \mu M$, prepared for Trial 1. The transients of the p_xPDI solutions were corrected by subtracting the f_{slow} contribution.

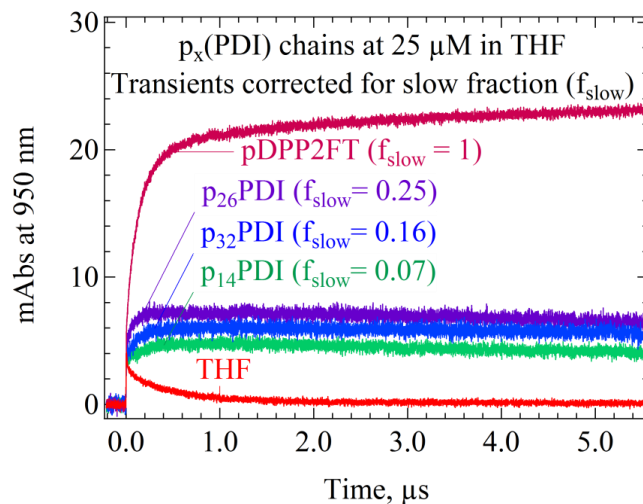


Figure 7-18 Absorption transients at 950 nm following radiolysis of THF, and solutions of pDPP2FT, p₁₄PDI, p₁₆PDI and p₂₆PDI in THF— each at chain concentrations of 25 μM, prepared for Trial 2. The transients of the p_xPDI were corrected by subtracting the f_{slow} contribution.

Table 7-6 Time constants of formation for pDPP2FT^{•-}, PDI^{•-} and calculated times of transport

Polymer	Trial number	$\tau_f(\text{PDPP2FT}^{\bullet-})$	$\tau_f(\text{PDI}^{\bullet-})$	$\tau_{\text{transport}}$
p ₁₄ PDI	Trial 2	187 ± 6 ns	182 ± 6 ns	≤ 7 ns
p ₁₆ PDI	Trial 1	173 ± 6 ns	168 ± 6 ns	≤ 7 ns
p ₂₆ PDI	Trial 1	158 ± 15 ns ^a	168 ± 6 ns	≤ 31 ns
p ₂₆ PDI	Trial 2	158 ± 15 ns ^a	118 ± 6 ns	0 ns
p ₃₂ PDI	Trial 2	143 ± 6 ns	147 ± 6 ns	≤ 16 ns

^a An average was obtained based on the values of p₁₆PDI and p₃₂PDI as upper and lower limits due to difficulty obtaining an accurate fit.

7.3.3 Electron transport study: trial 3

The results of the measurements in the previous section suggest a rapid electron transfer from the pDPP2FT chain to the PDI endcap. A spectral transformation would provide more robust evidence for rapid conversion of chain radical anions to end cap radical anions, but due to observations of radiolytic degradation of the polymer samples as will be shown in the following section, collection of spectral data was very challenging. An attempt was made to define a reasonable exposure limit of radiolytic pulses which might produce negligible

degradation over a series of measurements while still permitting collection of reasonably accurate transient absorption spectra. For this purpose, p_{37} , p_{16} PDI, p_{26} PDI, and p_{32} PDI were prepared at chain concentrations of 25 μ M in THF. An exposure limit of ≤ 12 doses was selected for THF solutions of p_x PDI. To accomplish this, spectra were collected in the range of 850 nm – 1600 nm, using 50 – 100 nm spacings. Rather than averaging multiple measurements at a single wavelength for improved signal/noise, each measurement consisted of only one radiolytic pulse per wavelength. Due to instrumental problems, measurements were not possible on the same day of preparation, but were made instead, several days later. Prior to measurement, the solutions were reheated and allowed to cool back to room temperature.

*Absorption transients of these solutions are shown in **Figure 7-19**.*

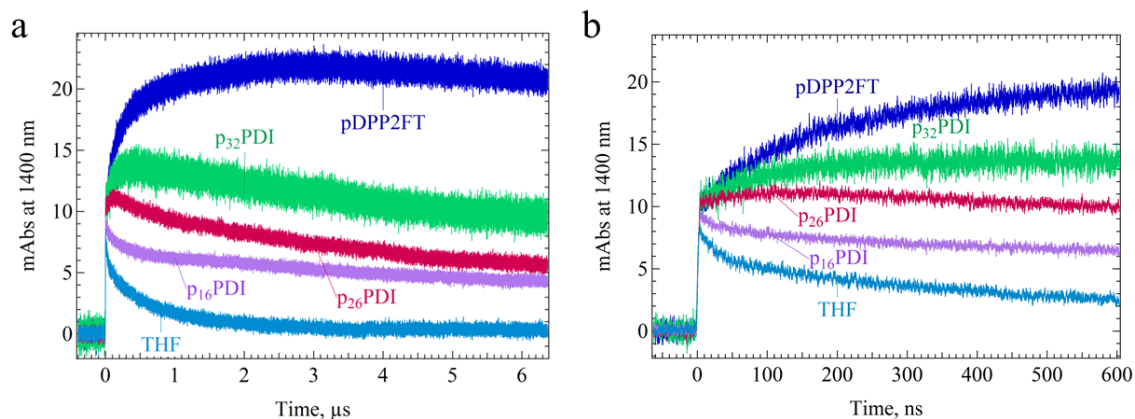


Figure 7-19 Unlike the previous trials for which all p_x PDI solutions exhibited some observable decay, and small values of f_{slow} , in the present trial, only p_{16} PDI is observed to produce a fast decaying transient, and values of f_{slow} in each p_x PDI solution are significantly larger, indicating significantly larger yields of defective chains. Estimates of f_{slow} were determined by comparing the 1400 nm absorption yields of p_{37} and each p_x PDI at 1 μ s after pulse, and are provided in **Table 7-7**. The electron attachment kinetics of pDPP2FT also differed significantly from the previous trials, with two rates rather than one. A fast rate of electron attachment was measured as $5.60 \times 10^6 \text{ s}^{-1}$ (179 ns) accounting for 68%, a slower rate of $1.11 \times 10^6 \text{ s}^{-1}$ (902 ns) accounting for 23% and the remaining 9% attaching via step capture.

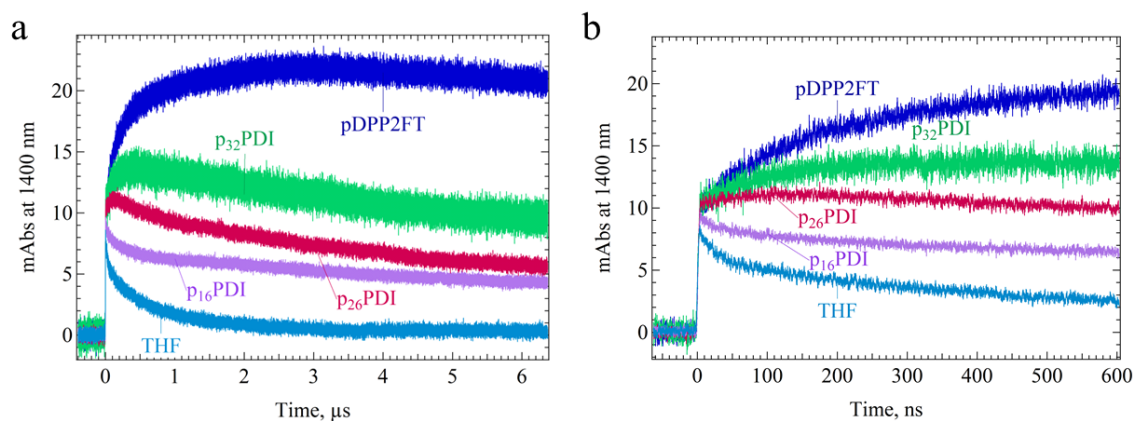


Figure 7-19 Absorption transients at 1400 nm corresponding to radiolysis of THF solutions of pDPP2FT, p₁₆PDI, p₂₆PDI, and p₃₂PDI at chain concentrations of 25 μM following radiolytic pulse, shown on a time scale of (a) 6 μs, and (b) 600 ns.

The reasons for especially high values of defective chains in p_xPDI solutions was unclear but suggests a high proportion of defective chains possibly existed in the pDPP2FT solution and possibly explaining the slower rate of attachment for 23% of captured electrons. That each solution exhibited significantly larger fractions of defective chains suggests that the same mechanism was responsible for each. The only purposeful treatment rendered following the preparation of the solutions was the reheating and cooling. These processes have not been observed to render different kinetics for electron attachment when performed on solutions within the same day of preparation. A plausible explanation for the observed change in electron attachment and yield of defects is solution ageing. One manner in which polymer solutions may be aged may be through reaction with peroxides. The formation rate of peroxides in THF solutions may be dependent on light and oxygen exposure. The amount of light exposure was not well controlled for, although oxygen seepage was minimal by using a teflon stopcock seal. Peroxides may react with polymer to produce degradation of the backbone. Absorption transients collected within hours of preparation always showed evidence of low yields of slow decaying fractions of polymer radical anions. In spite of the higher yields of slow decaying radical anions observed in this trial, as with the previous trials, the loss of absorbance in each p_xPDI solution at 1400 nm relative to the pDPP2FT solution following the completion of electron capture is interpreted as owing to electrons removed from

the polymer chain or electrons which were captured directly by PDI end caps without first touching the chain.

Table 7-7 Values of f_{slow} determined by comparing 1400 nm yields of p_x PDI relative to pDPP2FT at $t = 1.0 \mu s$

Polymer	f_{slow}
P ₁₆ PDI	68%
P ₂₆ PDI	45%
P ₃₂ PDI	31%

As was observed previously, the fast decay in the 1400 nm transient of p_{16} PDI was similar but faster than the decay rate of electrons in THF. In the present set of data, the same observation was made at other wavelengths, such as at 1600 nm. Transients of both p_{16} PDI and THF at 1400 nm and 1600 nm are shown in **Figure 7-20**. The observed kinetics corresponding to the 1600 nm transients are slower than the actual kinetics due to a slow response time of the detector at this wavelength. The similar absorption magnitudes of the p_{16} PDI and THF at very early times at multiple wavelengths – suggests that the fast decaying transient in p_{16} PDI is primarily owing to solvated electrons as they deplete. Due to an extinction coefficient ratio of **8:1** for $\epsilon(pDPP2FT^{\bullet-})/\epsilon(e^{\bullet-})$ at 1400 nm, the fact that the signal of solvated electrons dominate suggests polymer radical anions formed on non-defective polymer chain with PDI end caps are rapidly depleted.

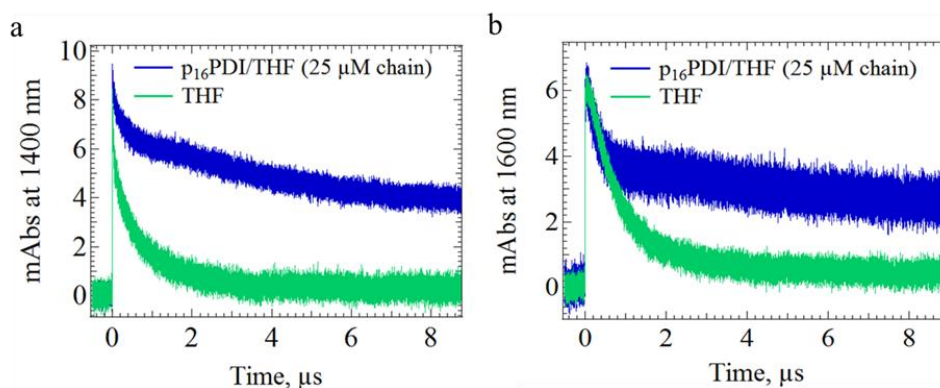


Figure 7-20 Absorbance transients of p_{16} PDI/THF (25 μM chain) and THF at: (a) 1400 nm, and (b) 1600 nm.

The difference in absorption magnitudes of the fast absorption steps of THF and $p_x(\text{PDI})/\text{THF}$ solutions at the same wavelength, may be assumed to owe to step capture of electrons by the polymer chains. Comparing this magnitude with the total yield of polymer radical anions formed provides an estimate of the fraction of total polymer radical anions formed via step capture.

Transient absorption spectra of the solvated electron in THF are shown in **Figure 7-21** over a spectral range extending from 750 nm to 1600 nm. A single exponential fit to the decay transient at 1500 nm provided a time constant of 700 ± 20 ns. The spectral band at 5 ns following the radiolytic pulse of THF, is observed to grow monotonically with increasing wavelength from 750 nm – 1500 nm. At 1600 nm, an apparent deviation from this trend is observed which is due to a slow response from the detector at this wavelength, causing the spectrum of the electron to appear as if it peaks circa 1500 nm. As a result, the spectrum of the electron at wavelengths above 1500 nm is inaccurate at times prior to ~ 100 ns. An additional oddity in the spectrum of the solvated electron is the appearance of a “bump” at 1100 nm – not reported in literature for the solvated electron in THF. That the electron lifetime is quite long indicates that if the peculiar spectral feature owes to an impurity, it would likely be an ion-pairing impurity from an electrolyte. Ion pairing of the electron and tetrabutylammonium cation (TBA^+) has been observed to change the spectrum very little relative to the unpaired electron. It is plausible that such a pairing may result in a vibrational structure but this possibility was not explored. After 100 ns, the spectral shape of the transient spectra are fairly time-invariant from 750 nm – 1600 nm indicating a single species is decaying. suggesting a low yield of impurities in the THF used to prepare the polymer solutions.

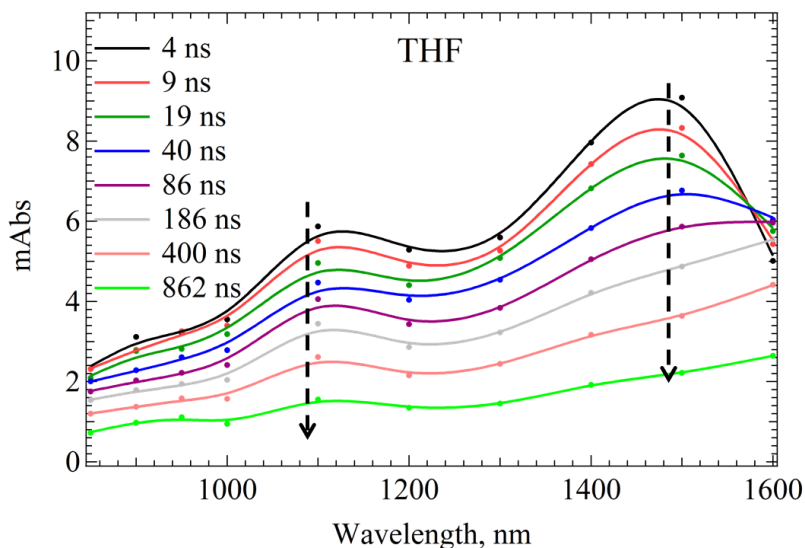


Figure 7-21 Transient absorption spectrum of THF collected immediately following radiolytic pulse.

Transient absorption spectra of pDPP2FT collected immediately after radiolytic pulse were also collected as shown in **Figure 7-22**. The band intensity is found to increase monotonically with wavelength from 1000 nm – 1400 nm peaking circa 1400 nm. Due to the slow response time of the detector at 1600 nm leading to a spectrum of the solvated electron system which appears to have a peak at 1500 nm at early times, and the spectral shapes associated with the solvated electron and pDPP2FT^{•-} are similar at early times. Therefore, the conversion of electrons to pDPP2FT^{•-} is not obvious from spectral transformations and the spectra are nearly time-invariant in the timeframe from 40 ns – 2.0 μ s in spite of the varying contribution of the two species. A slow rate of conversion from pDPP2FT^{•-} to pDPP2FTH[•] is evident at times after 2.0 μ s. A suppression at 1400 nm where pDPP2FT^{•-} is near its maximum, corresponds with concomitant growth at 950 nm where pDPP2FTH[•] was previously shown to absorb. These transformations are shown in dashed markings at 4.0 μ s and 7.0 μ s after pulse in **Figure 7-22**.

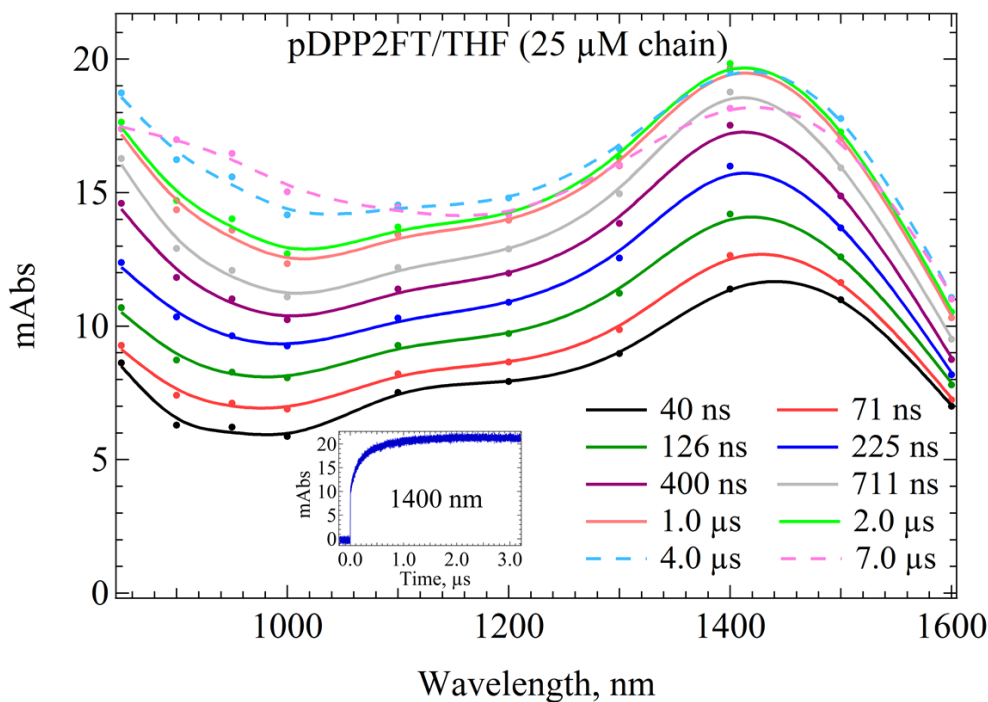


Figure 7-22 Transient absorption spectra of pDPP2FT/THF (25 μM chain) shown over a 7.0 μs time frame following radiolytic pulse. Transient spectra at 4.0 μs and 7.0 μs occur during the decay of pDPP2FT $^{\bullet-}$ and are shown plotted with dashed fits. The decay of pDPP2FT $^{\bullet-}$ by conversion to pDPP2FTH $^{\bullet}$ is indicated by correlated growth at 950 nm associated with the decaying 1400 nm band.

The transient absorbance spectra of p₁₆PDI, p₂₆PDI, and p₃₂PDI are presented in **Figure 7-23**, **Figure 7-24**, and **Figure 7-25**, respectively. In each of these figures, a rapid growth at 950 nm is observed within the first 300 ns. This growth is significantly faster than the observed rate of formation for pDPP2FTH $^{\bullet}$ observed in **Figure 7-22** and is interpreted as formation of PDI $^{\bullet-}$. As was observed in the transient absorption spectra of pDPP2FT, the conversion of electrons into polymer radical anions is not obvious in the p_xPDI solutions due to the similar spectral shapes of the two species. Therefore, as uncapped and defective p_xPDI populations capture electrons to form polymer radical anions, the overall spectral shapes change little.

Though the spectral shapes do not change much over the time frame of 30 – 300 ns, the observed kinetics of the spectral band intensity during this timeframe reflects the relative contributions of $\epsilon(e^{\bullet-})[e^{\bullet-}]$ and $\epsilon(p^{\bullet-})[p^{\bullet-}]$. For p₁₆PDI, the sum of $\epsilon(e^{\bullet-})[e^{\bullet-}] + \epsilon(p^{\bullet-})[p^{\bullet-}]$ results in a net decay of the spectral band during the conversion of electrons to polymer radical

anions due to the condition $\epsilon(e^{\bullet-})[e^{\bullet-}] > \epsilon(p^{\bullet-})[p^{\bullet-}]$. For p_{26} PDI, a relatively invariant band intensity results due to the condition $\epsilon(e^{\bullet-})[e^{\bullet-}] \approx \epsilon(p^{\bullet-})[p^{\bullet-}]$ during the conversion. For p_{32} PDI, an overall growth of the band occurs due to the condition $\epsilon(e^{\bullet-})[e^{\bullet-}] < \epsilon(p^{\bullet-})[p^{\bullet-}]$ during the conversion.

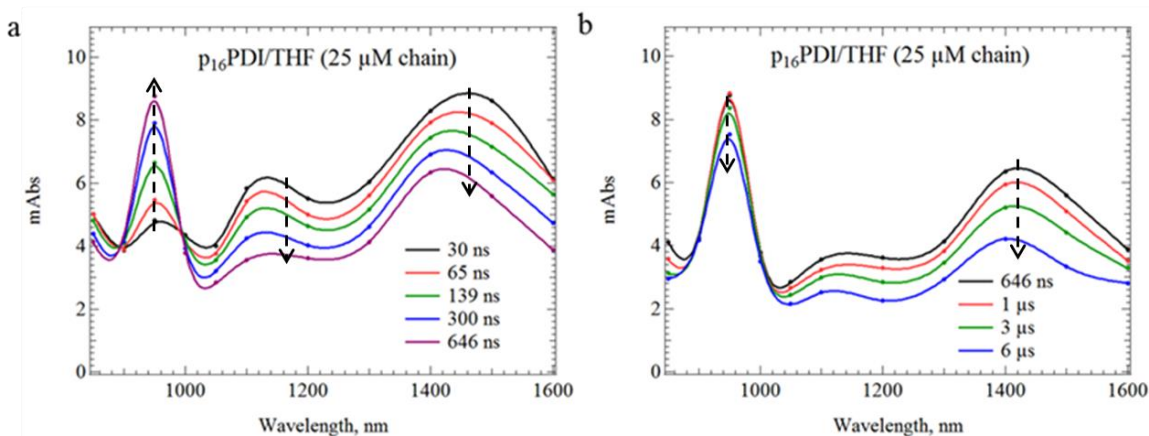


Figure 7-23 Transient absorption spectra of p_{16} PDI/THF (25 μ M chain) shown (a) from 30 ns – 646 ns, and (b) from 646 ns – 6 μ s.

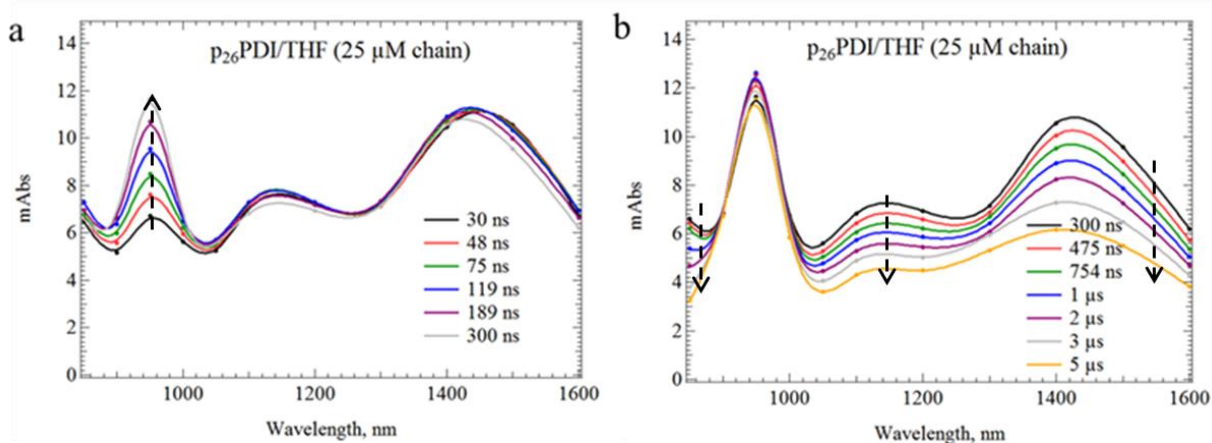


Figure 7-24 Transient absorption spectra of p_{26} PDI/THF (25 μ M chain) shown (a) from 30 ns – 300 ns, and (b) from 300 ns – 5 μ s.

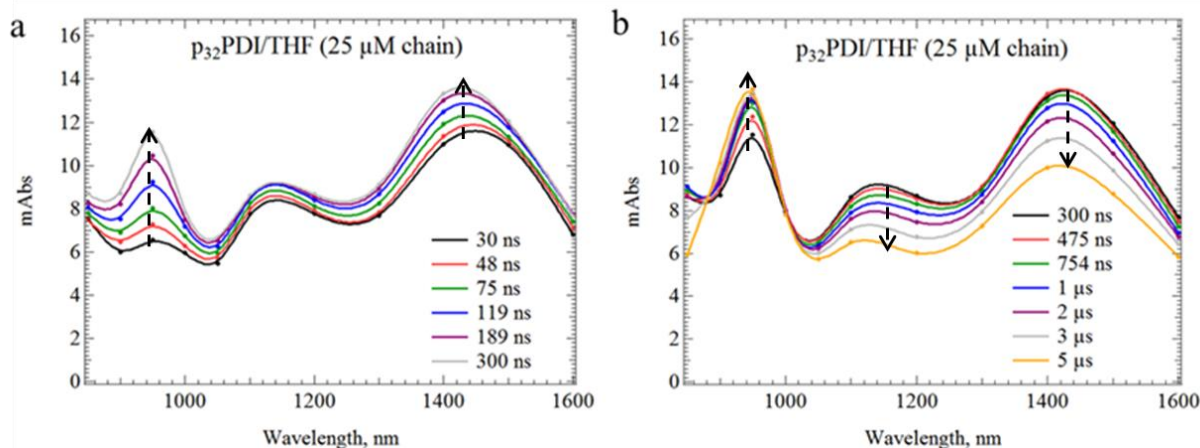


Figure 7-25 Transient absorption spectra of p_{32} PDI/THF (25 μ M chain) shown (a) from 30 ns – 300 ns, and (b) from 300 ns – 5 μ s.

Due to the lower yields of uncapped and defective chains in the p_{16} PDI, the spectral transformation involves an observable suppression of electrons (1400 nm) and corresponding formation of $PDI^{\bullet-}$ (950 nm) with virtually identical rates for both processes, and quasi-isosbestic points at 900 nm and 1000 nm. It was shown in the previous trials that electrons captured by PDI caps primarily contact the polymer chain first rather than entering the PDI caps directly, indicating that the apparent conversion from electrons to $PDI^{\bullet-}$ involve a very rapid intramolecular electron transfer process. The decays of electrons in p_{26} PDI and p_{32} PDI are not observable due to overpowering absorption of polymer radical anions formed on uncapped and defective PDI-capped chains. As was done in the previous trials, values of $\tau_{transport}$ may be determined by the difference of $\tau_f(p_x^{\bullet-}PDI) - \tau_f(p_xPDI^{\bullet-})$ according to **Eq 7-2**. In this trial, $\tau_f(p_x^{\bullet-}PDI)$ for p_{32} PDI was estimated by the fast electron capture rate observed in the solution of p_{37} at 1400 nm, and was estimated based on the rate of observed electron decay in the solution of p_{16} PDI. The 1400 nm transient of p_{16} PDI contained two decay rates – the fastest associated with the electron and the slower associated with polymer radical anions for uncapped and defective chains. For an accurate assessment of the electron decay rate, a biexponential fit of the 1400 nm transient was used. Values for $\tau_f(p_xPDI^{\bullet-})$ were determined by single exponential fits of the p_x PDI solutions at 950 nm. The values for $\tau_f(p_x^{\bullet-}PDI)$ and $\tau_f(p_xPDI^{\bullet-})$ are presented in **Table 7-8**. A reliable estimate for $\tau_f(p_x^{\bullet-}PDI)$ could not be determined.

Table 7-8 Estimates of $\tau_f(p_x^{\bullet}PDI)$ and $\tau_f(p_xPDI^{\bullet-})$, and calculated $\tau_{transport}$ for p_xPDI solutions in Trial 3

Polymer	Trial number	$\tau_f(PDPP2FT^{\bullet-})$	$\tau_f(PDI^{\bullet-})$	$\tau_{transport}$
P ₁₆ PDI	Trial 3	178 ns	191 ± 6 ns	≤ 19 ns
p ₂₆ PDI	Trial 3	N/A	168 ± 6 ns	N/A
p ₃₂ PDI	Trial 3	179 ± 6 ns	184 ± 6 ns	≤ 17 ns

The 950 nm transients of the p₃₇ and p_xPDI solutions are shown in **Figure 7-26**. By 1 μs after pulse, electron capture is nearly complete in each of the p_xPDI solutions. After 1 μs the slow decay of polymer radical anions is observable, in the transient spectra of each p_xPDI solution. The decay of p_x[•]PDI may occur via conversion to either p_xPDI^{•-} or pDPP2FH[•], both of which absorb at 950 nm. In **Figure 7-26**, where a slow growth is observed in the 950 nm transient of p₃₇ after 1 μs, a nearly time-invariant signal is observed in p₃₂PDI and decay is observed in p₂₆PDI and p₁₆PDI, indicating that yields of slow forming pDPP2FH[•] were approximately commensurate with f_{slow} as expected.

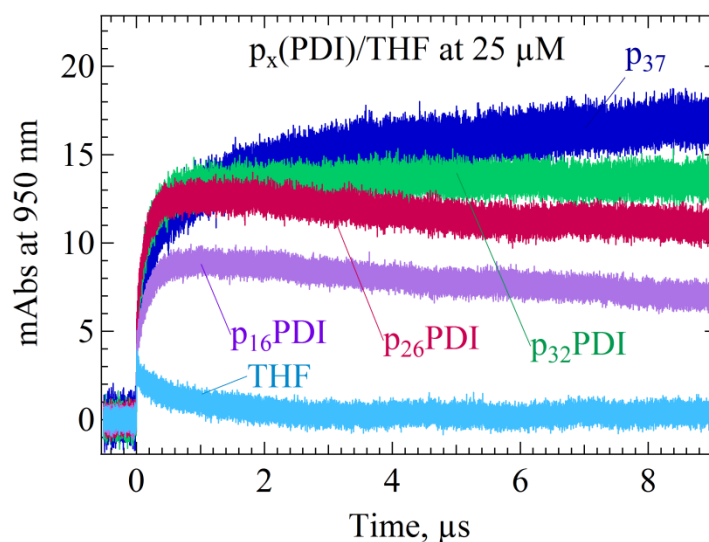


Figure 7-26 Absorbance transients at 950 nm corresponding to THF solutions of p₃₇, p₁₆PDI, p₂₆PDI, and p₃₂PDI collected immediately after radiolytic pulse.

Some uncertainty exists regarding the nature of electron transport within a polaron length of a PDI end cap. To estimate a lower limit for the electron mobility, an assumption was made that electrons within a polaron length of the end cap are instantaneously captured by the cap.

This approximation results in an effective chain length, L_{chain} , that is shortened by twice the polaron length, L_{polaron} . The negative polaron was estimated previously to delocalize over 5.8 monomers. For p_{16} PDI, this results in only 4.4 monomers that the electron must traverse. Defining the mobility over such a short range is not very fruitful. For p_{32} PDI, the effective chain length after accounting for twice the polaron length is 20.4 monomers or a length of 34.3 nm.

The Einstein-Smoluchowski equation provides a relation between the square of a particle's average displacement $\langle \bar{x} \rangle$, within a time τ , and the diffusion coefficient D , for a system with an order of dimensionality of n , expressed as:

$$D = \frac{\langle \bar{x}^2 \rangle}{\tau \cdot 2n} \quad 7-3$$

For a p_{32} PDI chain with 2 PDI caps, $\langle \bar{x} \rangle$ is half the effective chain length, equivalent to 17.15 nm. The electron mobility, μ is related to the diffusion coefficient, D , by the Einstein relation:

$$\mu = \frac{q_e D}{k_B T} \quad 7-4$$

Based on the values of $\tau_f(p_x^{\bullet}\text{PDI})$, $\tau_f(p_x\text{PDI}^{\bullet})$, and $\tau_{\text{transport}}$ estimated for p_{32} PDI, estimates for the diffusion coefficient and zero-field electron mobility were determined as shown in **Table 7-9**. The p_{32} PI chain was the best one to use for estimation of electron mobility as The results suggest that within uncertainty $\tau_f(\text{PDPP2FT}^{\bullet}) \approx \tau_f(\text{PDI}^{\bullet})$ and therefore is approximated by a lower limit defined by the extent of uncertainty. Chain lengths of each polymer are provided based on an estimated DPP monomer length of 1.68 nm.

Table 7-9 Lower limits for the diffusion coefficient (D) and electron mobility (μ) of an electron on a p_{32} PDI chain with 2 PDI caps based on the longest possible $\tau_{\text{transport}}$ of 17 ns.

Polymer	$\tau_{\text{transport}}$	L_{chain}	$L_{\text{chain}} - 2 * L_{\text{polaron}}$	D (cm ² /s)	μ (cm ² /Vs)
p_{32} PDI	≤ 17 ns	53.8 nm	34.3 nm	8.65×10^{-5}	3.37×10^{-3}

7.3.4 Evidence for radiolytic degradation of PDI cap

In the course of collecting radiolytic measurements corresponding p_x PDI solutions in THF, evidence for irreversible degradation of both the polymer chain and end cap were found. Some

evidence presented earlier supported the conclusion of pDPP2FTH[•] formation as a byproduct primarily of the polymer radical anion and protonated THF. Radiolytic degradation of PDI by is likewise presumed to result from formation of PDIH[•] via a reaction of PDI^{•-} and THFH⁺. This conclusion was drawn based on observations of irreversible reactions following radiolysis of THF solutions of p₁₆PDI and p₁₄PDI and evaluation of spectrophotometric measurements of radiation exposed solutions. In **Figure 7-27** absorbance transients at 1400 nm corresponding to a THF solution of p₁₆PDI following specified dosages of radiolytic pulses are presented.

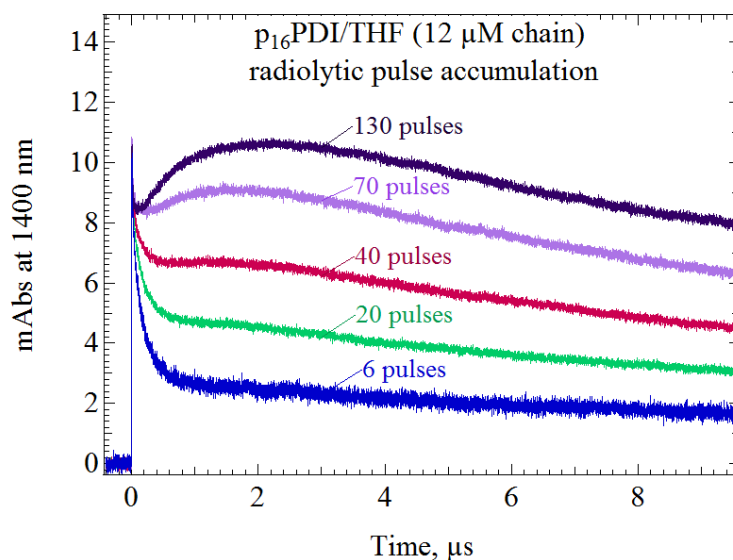


Figure 7-27 Absorbance transients at 1400 nm corresponding to radiolysis of a THF solution containing p₁₆PDI (12 μM chain) following exposure to specified dosages of radiolytic pulses.

It was previously shown that the fast decay observed corresponds to the solvated electron and/or radical anion of capped chains. The residual absorbance following the fast decaying absorbance is polymer radical anion which unlike the majority removed via intramolecular charge transfer, decays through slower bimolecular processes. The increased yields of relatively stable and slow decaying radical anions of pDPP2FT with increased exposure of radiolytic pulses suggest that electrons previously capable of rapidly accessing the PDI caps on certain chains are now incapable of accessing them due to damage created by radiolytic exposure.

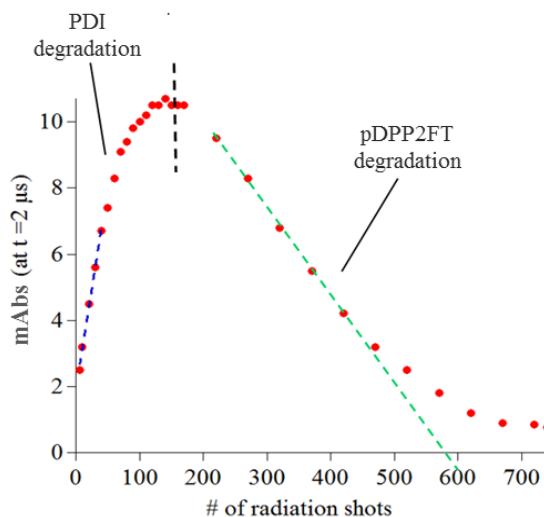


Figure 7-28 A plot of absorbance at $t = 2 \mu\text{s}$ after radiolytic pulse are plotted relative to the number of radiolytic pulses or “shots” delivered to the p_{16} PDI sample, indicating a rise slope that is 7 times faster than the decay slope.

The absorbance values at $2 \mu\text{s}$ after radiolytic pulse were plotted relative to the corresponding number of radiolytic pulses delivered to the $12 \mu\text{M}$ p_{16} PDI solution as shown in **Figure 7-11**. The $\Delta\text{absorbance}/\Delta\text{pulse}$ was found to exhibit linearity over a limited range of initial data points over which absorption was observed to increase, and again linearity was observed in a range of data points corresponding with the decline of absorbance yield. A ratio of the slope corresponding to the absorbance rise and slope of the absorbance decline was found to be 7.2:1.0. This ratio is similar to the 9.0:1.0 ratio obtained for the total number of chain monomers vs PDI molecules if each PDI is treated as a monomer. An interpretation of these results may be that absorption rises as PDI caps are eliminated due to conversion from PDI-capped polymers to polymers which effectively function as chains without PDI caps. The declining absorbance results from conjugation breakage along the backbone of the pDPP2FT chain which removes sites once available for electrons to localize. These results suggest that PDI neutral is removed by degradation at a per dose rate that is ~ 7 times faster than DPP monomers. This rate might be expected to correlate with the ratio of PDI “monomers” relative to the total monomers in a p_{16} PDI chain. A theoretical value of 9.0:1.0 assumes full capping of all chains and no that no chain defects exist which might trap and localize the electron on a chain.

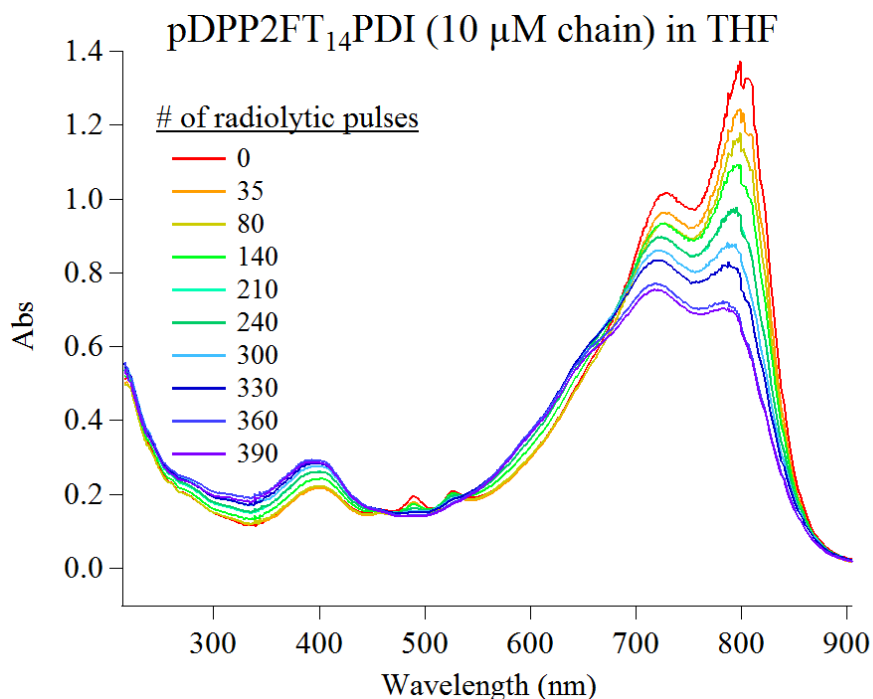


Figure 7-29 Ground state absorbance spectra of pDPP2FT (10 μM chain) in THF following various stages of radiolytic damage according measured by number of accumulated pulses. The bands associated with PDI ground state decay completely after 300 pulses while the principal band of pDPP2FT at 807 nm decays by less than 30% during that same exposure.

A separate test was performed to evaluate the chain and end cap degradation of $p_x\text{PDI}$. This time using $p_{14}\text{PDI}$, a solution containing 10 μM by chain was prepared and spectrophotometric measurements evaluated following exposure to a defined number of radiolytic pulses. As shown in **Figure 7-29** the ground state absorbance spectrum of $p_{14}\text{PDI}$ in THF is shown to evolve in a manner that reflects degradation with suppression of the 807 nm and 727 nm peaks evident. However, these bands have only been suppressed by < 30% after 300 pulses of exposure while the peaks at 490 nm and 520 nm associated with PDI neutral have been completely removed. This supports the prior conclusion that PDI degradation occurs as a result of formation of the PDI radical anion and subsequent reaction with THFH^+ .

7.4 Discussion and Summary

Optical and electronic properties exhibited by pDPP2FT have been investigated. Many of these properties are ideal for photovoltaic application: one of the strongest per monomer

molar extinction coefficients reported for conjugated polymers, very long delocalization lengths for the negative polaron (5.8 ± 0.7 monomers, 9.8 ± 1.2 nm), and positive polaron (9.0 monomers, 15.2 nm), and a reduction potential that indicates that the polymer is less reactive to oxidation degradation and therefore more air stable than most conjugated polymers. The long polaron lengths provide evidence for a fairly uniform energetic landscape. A high degree of planarity from a D-A copolymer may result from alternation between resonance forms as D-A and $D^+=A^-$ [135]. This planarity consequently has the effect of reducing the reorganization energy necessary for facilitating rapid charge transport. Charge mobilities of conjugated polymers have typically been determined from field-dependent measurements in the solid state (e.g. OFETs) or less commonly, have been determined for isolated chains, via field dependent techniques such as microwave conductivity. In this study, zero-field electron mobilities of the pDPP2FT chain were facilitated by PDI-capped pDPP2FT for which 1-D diffusion coefficients of electrons could be approximated by the differences between the formation rates of p_x^*PDI and from formation rates of p_xPDI^* observed at 950 nm. A lower limit for zero-field electron mobility was determined as $3.37 \times 10^{-3} \text{ cm}^2/\text{Vs}$ based on a 32 monomer unit chain. The actual mobility may be significantly higher but the time resolution of the experiment was limited by the attachment rate of electrons to polymer chains. Even so, the lower limiting mobility is several magnitudes faster than the electron mobility of MEH-PPV which is impressive. A recent mobility estimate of $2.5 \text{ cm}^2/\text{Vs}$, among the highest recorded for a conjugated polymer, was obtained in the solid state for a diketopyrrolopyrrole based polymer [136] possibly indicating that the mobility of pDPP2FT may be even several orders of magnitude larger, and may with proper morphological ordering, facilitate band transport within certain temperature regimes [70, 136, 137]. Less attractive qualities of the polymer were poor solubility and a short lifetime of the excited state, limiting the exciton diffusion length. However, long delocalization lengths for the polarons might suggest long delocalization lengths are associated with the excited states as well.

A challenge for this study was mitigating end cap and chain degradation via of monohydroradical formation. It was found that absorption transients corresponding to p_xPDI solutions in THF with NaBPh_4 as cosolute did not exhibit the irreversible degradation trends

observed in THF without electrolyte. However, the effect of ion pairing also slowed the observed diffusion rates for the electron. The electrolyte may have mitigated the reaction of the protonated THF molecule and polymer radical anion by screening the Coulomb potential between them. To improve zero-field mobility measurements using radiolysis of acceptor-capped polymers, effective strategies for mitigating the monohydroradical product should be considered. One possible option is to explore the use of NaAlH_4 , LiAlH_4 or other metallic aluminum hydrides as cosolutes. The AlH_4^- has been shown to neutralize THFH^+ while the metallic cation, pairs with radical anions [99].

The spectral transformations of pDPP2FT at different redox stages gave evidence of optical transitions that were inconsistent with conventional conjugated polymers. The initial transition following light chemical doping or radiolytic doping gave rise to a single observed absorption band which at higher redox states transitioned to a spectrum with two absorption bands. Conventional conjugated polymers typically exhibit two bands for the polaron and one for the bipolaron according to the FBC model. The results indicate pDPP2FT as a D-A copolymer exhibits a different electronic structure than conventional conjugated polymers.

Chapter 8: Conclusion and Outlook

Debate and uncertainty regarding the nature of charges and excited states in conjugated polymers have been a source of confusion and ambiguity. For these species, it is important to have accurate optical signatures, to know how delocalized they are, to understand their energetics, and how quickly they diffuse along isolated chains. These properties are of paramount importance to material and device design considerations for polymeric photovoltaics. Unambiguous optical signatures were obtained for conjugated polymers and acceptor compounds, and these were used to obtain molar extinction coefficients of triplet states and radical ions which are difficult to quantify in yield by other methods that foster ambiguities. Based on the optical signatures, deviations from the theoretical predictions of the FBC model were identified; 3 optical transitions were evident in the radical ion spectra of oligomers f(SF-PPV) instead of only 2 expected, and 1 optical transition was evident in the radical ion spectra of pDPP2FT. Rates of radiolytic oxidation and triplet transfer from biphenyl to fSF-PPV were several factors slower than diffusion controlled, while radiolytic oxidation and triplet transfer reactions involving other compounds were much closer to diffusion controlled.

Two unique studies in this thesis were firsts of their kind: the investigation of electron transfer rate dependence on donor-acceptor separation distance in a DBA diblock copolymer, and the measurement of zero-field electron mobility for a D-A copolymer. To examine rate dependence of electron transfer, selection of a suitable donor and acceptor are often made on the basis of reduction potentials measured by electrochemistry. Unfortunately, free energies are calculated based on reduction potentials made under ion-paired conditions in electrochemistry which may lead to different energy offsets than obtained in electrolyte free conditions. To optimize the conversion of excitons to freed charges, the rate of forward electron transfer at a type II heterojunction should be competitive with backward electron transfer and energy transfer. The competition of these rates may be tuned by the separation distance of the donor and acceptor, often controlled on a molecular level by imposing an

intervening molecular spacer or “bridge” between the donor and acceptor. Charge separation yields as a function of D-A separation distance have previously only been explored for DBA compounds involving a molecular donor and molecular acceptor where the charge on either moiety is immobile. Using MEH-PPV as electron donor, fSF-PPV as electron acceptor, aliphatic bridges (Cn) of varied lengths were utilized to explore the effects of D-A separation distance on electron transfer rates by radiolysis where no competition for back electron transfer exists. Electron transfer rates in solutions of the diblocks were linearly dependent on concentration indicating the reactions were dominantly bimolecular. The uncertainty in these measurements defined the upper limit of intramolecular electron transfer rates, resulting in upper limit values of $\sim 10^{-4} \text{ s}^{-1}$ for all DBA diblocks as well as for the diblock without an intervening bridge. The possibility of bimolecular reaction rates owing to barrier-trapped or defect-trapped electrons at distances far from the D/A interface was considered. Assuming only a fraction of captured electrons were capable of rapid intramolecular transfer from donor to acceptor, this fraction would be expected to increase by a factor of 1.7 for $D_{14}(\text{Cn})\text{fA}$ relative to $D_{24}(\text{Cn})\text{fA}$ after controlling for differences in monomer ratios of D and fA. Instead, the relative donor radical anion yields of $D_{14}(\text{Cn})\text{fA}$ and $D_{24}(\text{Cn})\text{fA}$ were nearly the same after accounting for the differences in monomer ratios of donor and acceptor, and the likelihood of significant trapping of charges at long distances from the D/A interface rendered improbable.

Several plausible contributions to a slower intramolecular transfer rate in the polymeric DBA system relative to DBA systems with molecular donor, molecular acceptor and a rigid insulating hydrocarbon spacer have been considered. The mobile nature of an electron on the polymer donor in the absence of defects suggests that the probability of locating it in a region capable of rapid electron transfer decreases with increasing chain length. Similarly, the total charge density of a delocalized electron at a D/A interface decreases as polaron length increases. The labile nature of the aliphatic bridge also suggests that rate dependence is not strictly defined by bridge length and may be influenced strongly by both the solvent and bridge. That these factors could contribute an order of 4-5 magnitudes slower transfer rate seems unimaginable. A final factor considered is solvent reorganization energy. The solvent reorganization energy exhibits dependence on the separation distance between the charged

donor and neutral acceptor. In a collinear arrangement between a charged donor and acceptor, the minimum distance between the charge center on the donor and acceptor is potentially much larger than in the side-by-side arrangement due to the delocalization length of the electron.

While it is unclear how various factors affect the ultraslow intramolecular electron transfer in isolated DBA diblocks, this work provides evidence that exciton dissociation in such diblocks is not a foregone conclusion as has been the long-held belief. A systematic study of polymer donor length with a fixed acceptor compound, and a systematic study of a fixed oligomer donor and varied acceptor compounds with similar redox potentials were not feasible in this study. These types of studies may elucidate which factors contribute to such incredibly slow rates of intramolecular electron transfer.

In the investigation of electron transport for a D-A copolymer, PDI-capped pDPP2FT was used. Some D-A copolymers have been shown to exhibit high short circuit currents in devices and to exhibit high carrier mobilities in thin films. However, an investigation of charge transport under zero-field conditions along isolated chains in solution had not been previously done. The fast forming PDI radical anions of pDPP2FT_xPDI were interpreted as either owing to electrons directly captured by PDI or captured following transport along the pDPP2FT chain to the end cap. The observed rates were limited by the time resolution of electron capture from the solvent to the polymer chain. A lower limit for electron mobility was determined as $3.34 \times 10^{-3} \text{ cm}^2/\text{Vs}$ which is several orders faster than MEH-PPV [131] and more than an order faster than P3HT [138]. The high mobility seems consistent with the high degree of planarity reported for pDPP2FT [139]. The Marcus hopping model defines the hopping rate of a charge carrier as inversely proportional to the reorganization energy [125]. Increased chain planarity reduces reorganization energy for hopping and improves charge mobility. It has also been shown that DPP-containing polymers exhibit large persistence lengths which potentially contribute to its very large molar extinction coefficients. It has been shown that persistence length is influenced by side chain length [124]. These factors may be investigated in the rational design of future conjugated polymers. Ultimately in devices, intermolecular interactions are affected by side chains and pendant groups which consequently may strongly affect bulk properties of charge

transport [140]. Improvements in these parameters should be balanced against the potential tradeoffs of decreased electronic coupling between adjacent chains which may inhibit intermolecular charge transport.

References

1. ISPRE, *Research and Development on Renewable Energies: A Global Report on Photovoltaic and Wind Energy*. 2009: Paris.
2. Goetzberger, A., Knobloch, J. and Voss, B., *Crystalline silicon solar cells*. 1998: Wiley & Sons.
3. Yoon, B., et al., *Inkjet Printing of Conjugated Polymer Precursors on Paper Substrates for Colorimetric Sensing and Flexible Electrothermochromic Display*. *Advanced Materials*, 2011. **23**(46): p. 5492-5497.
4. Sirringhaus, H., et al., *High-Resolution Inkjet Printing of All-Polymer Transistor Circuits*. *Science*, 2000. **290**(5499): p. 2123-2126.
5. Krebs, F.C., *All solution roll-to-roll processed polymer solar cells free from indium-tin-oxide and vacuum coating steps*. *Organic Electronics*, 2009. **10**(5): p. 761-768.
6. Krebs, F.C., *Polymer solar cell modules prepared using roll-to-roll methods: Knife-over-edge coating, slot-die coating and screen printing*. *Solar Energy Materials and Solar Cells*, 2009. **93**(4): p. 465-475.
7. Forrest, S.R., *The path to ubiquitous and low-cost organic electronic appliances on plastic*. *Nature*, 2004. **428**(6986): p. 911-918.
8. Nielsen, T.D., et al., *Business, market and intellectual property analysis of polymer solar cells*. *Solar Energy Materials and Solar Cells*, 2010. **94**(10): p. 1553-1571.
9. Shaheen, S.E., D.S. Ginley, and G.E. Jabbour, *Organic-Based Photovoltaics: Toward Low-Cost Power Generation*. *MRS Bulletin*, 2005. **30**(1): p. 10-19.
10. Coakley, K.M. and M.D. McGehee, *Conjugated Polymer Photovoltaic Cells*. *Chemistry of Materials*, 2004. **16**(23): p. 4533-4542.
11. Sirringhaus, H., et al., *Mobility enhancement in conjugated polymer field-effect transistors through chain alignment in a liquid-crystalline phase*. *Applied Physics Letters*, 2000. **77**(3): p. 406-408.
12. Ali, K., U. Pietsch, and S. Grigorian, *Enhancement of field-effect mobility due to structural ordering in poly(3-hexylthiophene) films by the dip-coating technique*. *Journal of Applied Crystallography*, 2013. **46**(4): p. 908-911.

13. Sariciftci, N.S., *Primary photoexcitations in conjugated polymers: molecular exciton versus semiconductor band model*. 1998: World Scientific.
14. Pope, M.a.S., C.E., *Electronic Processes in Organic Crystals and Polymers*. 1999: Oxford University Press.
15. Pope, M., Kallmann, H.P., and Magnate P. , J. Chem. Phys., 1963. **38**: p. 2042-2043.
16. Kepler, R.G., Phys. Rev. , 1960. **119**: p. 1226-1229.
17. Leblanc, O.H., J. Chem. Phys., 1960. **33**.
18. Pai, D.M.a.S., B. E. , Rev. Mod. Phys., 1993. **65**: p. 163-211.
19. Bredas, J.L. and G.B. Street, *Polarons, bipolarons, and solitons in conducting polymers*. Accounts of Chemical Research, 1985. **18**(10): p. 309-315.
20. J. H. Burroughes, C.A.J., and R. H. Friend, Nature, 1988. **335**: p. 137-141.
21. Koezuka, H., A. Tsumura, and T. Ando, *Proceedings of the International Conference of Science and Technology of Synthetic Metals Field-effect transistor with polythiophene thin film*. Synthetic Metals, 1987. **18**(1): p. 699-704.
22. Burroughes, J.H., et al., *Light-Emitting-Diodes Based on Conjugated Polymers*. Nature, 1990. **347**(6293): p. 539-541.
23. Karg, S., et al., *Electrical and optical characterization of poly(phenylene-vinylene) light emitting diodes*. Synthetic Metals, 1993. **54**(1-3): p. 427-433.
24. You, J., et al., *A polymer tandem solar cell with 10.6% power conversion efficiency*. Nature Communications, 2013. **4**: p. 1446.
25. Liang, Y., et al., *Highly Efficient Solar Cell Polymers Developed via Fine-Tuning of Structural and Electronic Properties*. Journal of the American Chemical Society, 2009. **131**(22): p. 7792-7799.
26. Carsten, B., et al., *Mediating Solar Cell Performance by Controlling the Internal Dipole Change in Organic Photovoltaic Polymers*. Macromolecules, 2012. **45**(16): p. 6390-6395.
27. Carsten, B., et al., *Examining the effect of the dipole moment on charge separation in donor-acceptor polymers for organic photovoltaic applications*. J Am Chem Soc, 2011. **133**(50): p. 20468-75.

28. Sun, S.-S., *Design of a block copolymer solar cell*. Solar Energy Materials and Solar Cells, 2003. **79**(2): p. 257-264.
29. Miller, J., L. Calcaterra, and G. Closs, *Intramolecular long-distance electron transfer in radical anions. The effects of free energy and solvent on the reaction rates*. J. Am. Chem. Soc.:(United States), 1984. **106**(10).
30. Closs, G.L. and J.R. Miller, *Intramolecular long-distance electron transfer in organic molecules*. Science, 1988. **240**(4851): p. 440-7.
31. Marcus, R.A., *On the Theory of Oxidation-Reduction Reactions Involving Electron Transfer. I*. The Journal of Chemical Physics, 1956. **24**(5): p. 966-978.
32. Marcus, R.A., *Electrostatic Free Energy and Other Properties of States Having Nonequilibrium Polarization. I*. The Journal of Chemical Physics, 1956. **24**(5): p. 979-989.
33. Johnson, M.D., et al., *Distance dependence of intramolecular hole and electron transfer in organic radical ions*. The Journal of Physical Chemistry, 1989. **93**(4): p. 1173-1176.
34. Oevering, H., et al., *Long-range photoinduced through-bond electron transfer and radiative recombination via rigid nonconjugated bridges: distance and solvent dependence*. J. Am. Chem. Soc.:(United States), 1987. **109**(11).
35. Sun, S.-S., T. Nguyen, and J. Brooks. *Fluorinated polyphenylenevinylene (PPV) block copolymers for nanophotonics*. 2013.
36. Nguyen, T., Hasib, M., Wang, D., Sun, S.-S., *Design, Synthesis, Characterizations, and Processing of a Novel c-Donor-nc-Bridge-cf-Acceptor Type Block Copolymer for Optoelectronic Applications*. Journal of Research Updates in Polymer Science, 2016. **5**(1): p. 18-38.
37. David, T.M.S., W. Arasho, and S.-S. Sun, *Synthesis and structure-optoelectronic property relationships of a series of PPV and SFTV derived polymers*. Journal of Polymer Science Part A: Polymer Chemistry, 2015. **53**(19): p. 2202-2213.
38. Chen, J.W.C., Y., Acc. Chem. Res., 2009. **42**: p. 1709-1718.
39. Cheng, Y.J.Y., S. H.; Hsu, C. S., Chem. Rev., 2009. **109**: p. 5868-5923.
40. Morvillo, P., et al., *Low band gap polymers for application in solar cells: synthesis and characterization of thienothiophene-thiophene copolymers*. Polymer Chemistry, 2014. **5**(7): p. 2391-2400.

41. Keshtov, M.L., et al., *New low bandgap near-IR conjugated D-A copolymers for BHJ polymer solar cell applications*. Physical Chemistry Chemical Physics, 2016. **18**(12): p. 8389-8400.
42. Nunzi, J.-M., *Organic photovoltaic materials and devices*. Comptes Rendus Physique, 2002. **3**(4): p. 523-542.
43. Dou, L., et al., *Low-Bandgap Near-IR Conjugated Polymers/Molecules for Organic Electronics*. Chemical Reviews, 2015. **115**(23): p. 12633-12665.
44. Bijleveld, J.C., et al., *Poly(diketopyrrolopyrrole-terthiophene) for Ambipolar Logic and Photovoltaics*. Journal of the American Chemical Society, 2009. **131**(46): p. 16616-16617.
45. Woo, C.H., et al., *Incorporation of Furan into Low Band-Gap Polymers for Efficient Solar Cells*. Journal of the American Chemical Society, 2010. **132**(44): p. 15547-15549.
46. Bittner, E. and J. Ramon, *Exciton and Charge-Transfer Dynamics in Polymer Semiconductors*, in *Quantum Dynamics of Complex Molecular Systems*, D. Micha and I. Burghardt, Editors. 2007, Springer Berlin Heidelberg. p. 57-85.
47. Meier, H., U. Stalmach, and H. Kolshorn, *Effective conjugation length and UV/vis spectra of oligomers*. Acta Polymerica, 1997. **48**(9): p. 379-384.
48. Peierls, R., *Quantum Theory of Solids*. 1955, Oxford: Oxford University Press.
49. Fesser, K., A.R. Bishop, and D.K. Campbell, *Optical absorption from polarons in a model of polyacetylene*. Physical Review B, 1983. **27**(8): p. 4804-4825.
50. Conwell, E.M., *Definition of exciton binding energy for conducting polymers*. Synthetic Metals, 1996. **83**(2): p. 101-102.
51. Cornil, J., D. Beljonne, and J.L. Brédas, *Nature of optical transitions in conjugated oligomers. I. Theoretical characterization of neutral and doped oligo(phenylenevinylene)s*. The Journal of Chemical Physics, 1995. **103**(2): p. 834-841.
52. Lima, M.P. and G. Magela e Silva, *Dynamical evolution of polaron to bipolaron in conjugated polymers*. Physical Review B, 2006. **74**(22): p. 224304.
53. Brédas, J.L., et al., *Polarons and bipolarons in polypyrrole: Evolution of the band structure and optical spectrum upon doping*. Physical Review B, 1984. **30**(2): p. 1023-1025.
54. Shimoi, Y. and S. Abe, *Competition between polarons and bipolarons in nondegenerate conjugated polymers*. Physical Review B, 1994. **50**(20): p. 14781-14784.

55. Tol, A.J.W., *The instability of a bipolaron versus two polarons: charge localization in cyclo-dodecathiophene*. Synthetic Metals, 1995. **74**(1): p. 95-98.
56. Magela e Silva, G., *Electric-field effects on the competition between polarons and bipolarons in conjugated polymers*. Physical Review B, 2000. **61**(16): p. 10777-10781.
57. Saxena, A., et al., *Stability of bipolarons in conjugated polymers*. Synthetic Metals, 1999. **101**(1): p. 325-326.
58. Gribkovskii, V.P., *Theory of Luminescence*, in *Luminescence of Solids*, D.R. Vij, Editor. 1998, Springer US. p. 1-43.
59. Takeda, N., S. Asaoka, and J.R. Miller, *Nature and energies of electrons and holes in a conjugated polymer, polyfluorene*. J Am Chem Soc, 2006. **128**(50): p. 16073-82.
60. Graham, S.C., et al., *Raman and photoluminescence spectra of PPV oligomers*. Synthetic Metals, 1991. **41**(3): p. 1277-1280.
61. List, E.J.W., Partree, J., Shinar, J., Scherf, U., Mullen, K., Zojer, E., Petritsch, K., Leising, G., and Graupner, W., Phys. Rev. B, 2000. **61**: p. 10807 - 10814.
62. Teraoka, I., *Polymer Solutions: An Introduction to Physical Properties*. 2002: Wiley.
63. Cook, A.R., et al., *Sudden, "Step" Electron Capture by Conjugated Polymers*. The Journal of Physical Chemistry A, 2011. **115**(42): p. 11615-11623.
64. Cook, A.R., et al., *Rapid "Step Capture" of Holes in Chloroform during Pulse Radiolysis*. The Journal of Physical Chemistry A, 2013. **117**(33): p. 7712-7720.
65. Debye, P., *Reaction Rates in Ionic Solutions*. Transactions of The Electrochemical Society, 1942. **82**(1): p. 265-272.
66. Bässler, H., Enkelmann, V. Sixl, H. Cantow, H.-J. , *Polydiacetylenes*. Advances in polymer science. Vol. 63. 1984, Berlin: Springer.
67. Blum, T. and H. Bässler, *Reinvestigation of generation and transport of charge carriers in crystalline polydiacetylenes (PDAs)*. Chemical Physics, 1988. **123**(3): p. 431-441.
68. Karl, N. and J. Marktanner, *Electron and Hole Mobilities in High Purity Anthracene Single Crystals*. Molecular Crystals and Liquid Crystals Science and Technology. Section A. Molecular Crystals and Liquid Crystals, 2001. **355**(1): p. 149-173.

69. Bittner, E.R. and J.G.S. Ramon, *Exciton and Charge-Transfer Dynamics in Polymer Semiconductors*, in *Quantum Dynamics of Complex Molecular Systems*, D.A. Micha and I. Burghardt, Editors. 2007, Springer Berlin Heidelberg: Berlin, Heidelberg. p. 57-85.
70. Yamashita, Y., et al., *Mobility Exceeding 10 cm²/(V·s) in Donor–Acceptor Polymer Transistors with Band-like Charge Transport*. *Chemistry of Materials*, 2016. **28**(2): p. 420-424.
71. Shinar, J., *Organic light-emitting devices : a survey*. 2004, New York: Springer.
72. Demas, J.N., and Crosby, G. , *Journal of Physical Chemistry*, 1971. **75**: p. 991.
73. Martini, I.B., E.R. Barthel, and B.J. Schwartz, *Mechanisms of the ultrafast production and recombination of solvated electrons in weakly polar fluids: Comparison of multiphoton ionization and detachment via the charge-transfer-to-solvent transition of Na⁻ in THF*. *The Journal of Chemical Physics*, 2000. **113**(24): p. 11245-11257.
74. Funston, A.M. and J.R. Miller, *Increased yields of radical cations by arene addition to irradiated 1,2-dichloroethane*. *Radiation Physics and Chemistry*, 2005. **72**(5): p. 601-611.
75. Choppin, G.R., J.-O. Liljenzin, and J.A.N. Rydberg, *CHAPTER 7 - Radiation Effects on Matter**, in *Radiochemistry and Nuclear Chemistry (Second Edition)*. 1995, Butterworth-Heinemann: Oxford. p. 166-191.
76. Wardman, P., *Excited States and Free Radicals in Biology and Medicine. Contributions from Flash Photolysis and Pulse Radiolysis*. *British Journal of Cancer*, 1994. **69**(4): p. 255.
77. Wilkinson, F., W.P. Helman, and A.B. Ross, *Quantum Yields for the Photosensitized Formation of the Lowest Electronically Excited Singlet State of Molecular Oxygen in Solution*. *Journal of Physical and Chemical Reference Data*, 1993. **22**(1): p. 113-262.
78. Gijzeman, O.L.J. and F. Kaufman, *Oxygen quenching of aromatic triplet states in solution. Part 2*. *Journal of the Chemical Society, Faraday Transactions 2: Molecular and Chemical Physics*, 1973. **69**(0): p. 721-726.
79. Wilkinson, F. and A.A. Abdel-Shafi, *Mechanism of Quenching of Triplet States by Molecular Oxygen: Biphenyl Derivatives in Different Solvents*. *The Journal of Physical Chemistry A*, 1999. **103**(28): p. 5425-5435.
80. Stevens, M.A., et al., *Exciton dissociation mechanisms in the polymeric semiconductors poly(9,9-dioctylfluorene) and poly(9,9-dioctylfluorene-co-benzothiadiazole)*. *Physical Review B*, 2001. **63**(16): p. 165213.

81. Tong, M., et al., *Photoexcitation dynamics and laser action in solutions and films of PPE-PPV copolymer*. Physical Review B, 2004. **69**(15): p. 155211.
82. Nishihara, Y., et al., *Origin of Free Charge Carrier Generation of the Second-order Process Photocurrent in Conjugated Polymer Studied by Two-Correlated-Pulse Technique*. Synthetic Metals, 2005. **154**(1–3): p. 101-104.
83. Dyakonov, V. and E. Frankevich, *On the role played by polaron pairs in photophysical processes in semiconducting polymers*. Chemical Physics, 1998. **227**(1–2): p. 203-217.
84. Spangler, C.W., et al., *Speciality Polymers '88 Polaron and bipolaron formation in model oligomeric extended π -electron systems: studies towards the rational design of electroactive polymers for non-linear optics applications*. Polymer, 1989. **30**(6): p. 1166-1169.
85. Deussen, M. and H. Bässler, *Anion and cation absorption spectra of conjugated oligomers and polymers*. Chemical Physics, 1992. **164**(2): p. 247-257.
86. Kira, A., S. Arai, and M. Imamura, *Pulse radiolysis study of dimer cation formation of aromatic hydrocarbons in benzonitrile solution*. The Journal of Physical Chemistry, 1972. **76**(8): p. 1119-1124.
87. Romanovskii, Y.V. and H. Bässler, *Phosphorescence from a ladder-type conjugated polymer in solid solutions at low temperature*. Chemical Physics Letters, 2000. **326**(1–2): p. 51-57.
88. Monkman, A.P., et al., *The triplet state of the ladder-type methyl-poly(p-phenylene) as seen by pulse radiolysis-energy transfer*. Chemical Physics Letters, 2000. **327**(1–2): p. 111-116.
89. Wishart, J.F., A.R. Cook, and J.R. Miller, *The LEAF picosecond pulse radiolysis facility at Brookhaven National Laboratory*. Review of Scientific Instruments, 2004. **75**(11): p. 4359-4366.
90. Nguyen, T.-Q., V. Doan, and B.J. Schwartz, *Conjugated polymer aggregates in solution: control of interchain interactions*. The Journal of chemical physics, 1999. **110**(8): p. 4068-4078.
91. Burrows, H.D., et al., *Triplet state dynamics on isolated conjugated polymer chains*. Chemical Physics, 2002. **285**(1): p. 3-11.
92. Jou, F.Y. and L.M. Dorfman, *Pulse radiolysis studies. XXI. Optical absorption spectrum of the solvated electron in ethers and in binary solutions of these ethers*. The Journal of Chemical Physics, 1973. **58**(11): p. 4715-4723.

93. Salmon, G.A., W.A. Seddon, and J.W. Fletcher, *Pulse Radiolytic Formation of Solvated Electrons, Ion-pairs, and Alkali Metal Anions in Tetrahydrofuran*. Canadian Journal of Chemistry, 1974. **52**(18): p. 3259-3268.
94. Campbell, D.K., A.R. Bishop, and K. Fesser, *Polarons in quasi-one-dimensional systems*. Physical Review B, 1982. **26**(12): p. 6862-6874.
95. Das, T.N. and K.I. Priyadarsini, *Transients formed during reduction of polynuclear aromatics: a pulse radiolysis study*. Journal of the Chemical Society, Perkin Transactions 2, 1993(4): p. 733-739.
96. Burrows, H.D., et al., *Transient absorption spectra of triplet states and charge carriers of conjugated polymers*. Journal of Molecular Structure, 2001. **563-564**: p. 41-50.
97. Aoyama, T., Y. Yamamoto, and K. Hayashi, *Pulse radiolysis study of ion pairing of diphenylpolyene radical anions with tetrabutylammonium and sodium cations in tetrahydrofuran*. Journal of the Chemical Society, Faraday Transactions 1: Physical Chemistry in Condensed Phases, 1989. **85**(10): p. 3353-3358.
98. Robinson, M.G. and G.R. Freeman, *Charge Scavenging vs Hydrogen Atom Scavenging in the Radiolysis of Liquid Saturated Hydrocarbons*. The Journal of Chemical Physics, 1968. **48**(3): p. 983-989.
99. Salmon, G.A. and W.A. Seddon, *Production of solvated electrons, ion-pairs and alkali metal anions in tetrahydrofuran studied by pulse radiolysis*. Chemical Physics Letters, 1974. **24**(3): p. 366-368.
100. Rappoport, Z., *The Chemistry of Phenols, 2 Volume Set*. 2004: Wiley.
101. Arai, S., et al., *Pulse-Radiolysis Observation of Molecular Cations of Aromatic Compounds in Halogenated Liquids*. The Journal of Chemical Physics, 1969. **50**(3): p. 1072-1077.
102. Sumiyoshi, T., et al., *Pulse Radiolysis Studies of Solvent Radical Cations in Liquid 1,2-Dichloroethane*. Bulletin of the Chemical Society of Japan, 1988. **61**(9): p. 3055-3059.
103. Truszkowski, S. and A.G. Shostenko, *Radiolysis of chloroalkanes*. High Energy Chemistry, 2008. **42**(2): p. 89-91.
104. Anklam, E., K.-D. Asmus, and L.W. Robertson, *Radical cations of polychlorinated and polybrominated biphenyls in 1,2-dichloroethane: a pulse radiolysis study*. Journal of the Chemical Society, Perkin Transactions 2, 1989(10): p. 1573-1576.

105. Ueda, H., *Formation and Decay of the Transient Species in Radiation Chemistry. Radiolysis of Alkyl Halide Systems*. Bulletin of the Chemical Society of Japan, 1968. **41**(11): p. 2578-2586.
106. Alfassi, Z.B., S. Mosseri, and P. Neta, *Reactivities of chlorine atoms and peroxy radicals formed in the radiolysis of dichloromethane*. The Journal of Physical Chemistry, 1989. **93**(4): p. 1380-1385.
107. S.G. Lias, H.M.R., K. Draxl, B.W. Steiner, J.T. Herron, J.L. Holmes, R.D. Levin, J.F. Liebman, S.A. Kafafi Available from: webbook.nist.gov/chemistry.
108. Wang, Y., J.J. Tria, and L.M. Dorfman, *Identity and yield of positive charge centers in irradiated chloro hydrocarbon liquids and the rates of their interaction with solute molecules*. The Journal of Physical Chemistry, 1979. **83**(15): p. 1946-1951.
109. Cooper, R. and J.K. Thomas, *Formation of Excited States in the Nanosecond-Pulse Radiolysis of Solutions of Benzene and Toluene*. The Journal of Chemical Physics, 1968. **48**(11): p. 5097-5102.
110. Candeias, L.P., et al., *Pulse Radiolysis–Optical Absorption Studies on the Triplet States of p-Phenylenevinylene Oligomers in Solution*. The Journal of Physical Chemistry B, 2000. **104**(35): p. 8366-8371.
111. LaVerne, J.A. and M.S. Araos, *Radical production in the radiolysis of liquid benzene*. Radiation Physics and Chemistry, 1999. **55**(5–6): p. 525-528.
112. Baxendale, J.H. and M. Fiti, *Yield of triplet state benzene in the pulse radiolysis of solutions of some aromatics*. Journal of the Chemical Society, Faraday Transactions 2: Molecular and Chemical Physics, 1972. **68**(0): p. 218-222.
113. Tokumaru, K., et al., *HIGHLY SPECIFIC ISOMERIZATION OF AROMATIC OLEFIN RADICAL CATIONS PRODUCED BY PHOTSENSITIZED ELECTRON TRANSFER A2 - Honda, Kenichi*, in *Photochemical Processes in Organized Molecular Systems*. 1991, Elsevier: Amsterdam. p. 199-211.
114. Jagur-Grodzinski, J., et al., *Electron Affinities of Aromatic Hydrocarbons in Tetrahydrofuran Solution*. The Journal of Physical Chemistry, 1965. **69**(2): p. 628-635.
115. Gill, D., J. Jagur-Grodzinski, and M. Szwarc, *Chemistry of radical-ions. Electron-transfer reactions: -DD-+dimethyl anthracene and -DD-+pyrene*. Transactions of the Faraday Society, 1964. **60**(0): p. 1424-1431.

116. Shank, N.E. and L.M. Dorfman, *Pulse Radiolysis Studies. XVII. Reaction Kinetics of Molecular Cations of Aromatic Compounds in Dichloroethane Solution*. The Journal of Chemical Physics, 1970. **52**(9): p. 4441-4447.
117. Veldkamp, B.S., et al., *Photoinitiated multi-step charge separation and ultrafast charge transfer induced dissociation in a pyridyl-linked photosensitizer-cobaloxime assembly*. Energy & Environmental Science, 2013. **6**(6): p. 1917-1928.
118. Carmichael, I., W.P. Helman, and G.L. Hug, *Extinction Coefficients of Triplet-Triplet Absorption Spectra of Organic Molecules in Condensed Phases: A Least-Squares Analysis*. Journal of Physical and Chemical Reference Data, 1987. **16**(2): p. 239-260.
119. Schlaf, R., et al., *Determination of interface dipole and band bending at the Ag/tris (8-hydroxyquinolino) gallium organic Schottky contact by ultraviolet photoemission spectroscopy*. Surface Science, 2000. **450**(1-2): p. 142-152.
120. Aryanpour, K., et al., *Theory of Primary Photoexcitations in Donor-Acceptor Copolymers*. Phys Rev Lett, 2015. **115**(26): p. 267401.
121. Pedersen, S.U., et al., *New methods for the accurate determination of extinction and diffusion coefficients of aromatic and heteroaromatic radical anions in N,N-dimethylformamide*. Journal of Electroanalytical Chemistry, 1998. **454**(1-2): p. 123-143.
122. Grey, J., *Organic photovoltaics: Strong absorption in stiff polymers*. Nat Mater, 2016. **15**(7): p. 705-706.
123. Vezie, M.S., et al., *Exploring the origin of high optical absorption in conjugated polymers*. Nat Mater, 2016. **15**(7): p. 746-53.
124. Gettinger, C.L., et al., *A photoluminescence study of poly(phenylene vinylene) derivatives: The effect of intrinsic persistence length*. The Journal of Chemical Physics, 1994. **101**(2): p. 1673-1678.
125. Marcus, R.A., *Electron transfer reactions in chemistry. Theory and experiment*. Reviews of Modern Physics, 1993. **65**(3): p. 599-610.
126. Baumgarten, M. and K. Müllen, *Radical ions: Where organic chemistry meets materials sciences*, in *Electron Transfer I*, J. Mattay, Editor. 1994, Springer Berlin Heidelberg: Berlin, Heidelberg. p. 1-103.
127. Brouwer, A.M., *Standards for photoluminescence quantum yield measurements in solution (IUPAC Technical Report)*. Pure Appl. Chem, 2011. **83**(12): p. 2213-2228.

128. Samuel, I.D.W., et al., *The efficiency and time-dependence of luminescence from poly (p-phenylene vinylene) and derivatives*. Chemical Physics Letters, 1993. **213**(5–6): p. 472-478.
129. Lewis, A.J., et al., *Singlet exciton diffusion in MEH-PPV films studied by exciton–exciton annihilation*. Organic Electronics, 2006. **7**(6): p. 452-456.
130. Nayyar, I.H., et al., *Effect of trans- and cis-isomeric defects on the localization of the charged excitations in π -conjugated organic polymers*. Journal of Polymer Science Part B: Polymer Physics, 2013. **51**(12): p. 935-942.
131. Bozano, L., et al., *Temperature- and field-dependent electron and hole mobilities in polymer light-emitting diodes*. Applied Physics Letters, 1999. **74**(8): p. 1132-1134.
132. Miller, J.R., *Through-Bond Electronic Couplings in Intramolecular Electron Transfer Reactions*, in *Supramolecular Photochemistry*, V. Balzani, Editor. 1987, Springer Netherlands: Dordrecht. p. 241-254.
133. A. Curtiss, L., C. Naleway, and J. R. Miller, *Superexchange Pathway Calculation of Electronic Coupling through Cyclohexane Spacers*. Vol. 99. 1995.
134. Sreearunothai, P., et al., *Length and Time-Dependent Rates in Diffusion-Controlled Reactions with Conjugated Polymers*. The Journal of Physical Chemistry A, 2009. **113**(12): p. 2786-2795.
135. Chen, M., et al., *1 micron wavelength photo- and electroluminescence from a conjugated polymer*. Applied Physics Letters, 2004. **84**(18): p. 3570-3572.
136. Senanayak, S.P., et al., *Room-temperature bandlike transport and Hall effect in a high-mobility ambipolar polymer*. Physical Review B, 2015. **91**(11): p. 115302.
137. Yamashita, Y., et al., *Transition Between Band and Hopping Transport in Polymer Field-Effect Transistors*. Advanced Materials, 2014. **26**(48): p. 8169-8173.
138. Woo, C.H.K., *Conjugated Polymer Design and Engineering for Organic Electronics*, in *Chemical Engineering*. 2011, University of California, Berkeley: Berkeley, California. p. 121.
139. Chen, M.S., et al., *Enhanced Solid-State Order and Field-Effect Hole Mobility through Control of Nanoscale Polymer Aggregation*. Journal of the American Chemical Society, 2013. **135**(51): p. 19229-19236.

140. Wang, H., et al., *Structure and Morphology Control in Thin Films of Conjugated Polymers for an Improved Charge Transport*. *Polymers*, 2013. **5**(4): p. 1272.